Convection Calibration of Schmidt-Boelter Heat Flux Gages in Shear and Stagnation Air Flow

Andreas Frank Hoffie

Thesis submitted to the Faculty
of the Virginia Polytechnic Institute and State University
in partial fulfilment of the requirements for the degree of

Master of Science

in

Mechanical Engineering

Prof. Dr. Thomas E. Diller, chair man
Prof. Dr. Pavlos Vlachos, committee member
Prof. Dr. Scott Huxtable, committee member

December 19, 2006
Blacksburg, Virginia, USA

Key words:
Heat transfer, heat flux,
Schmidt-Boelter gages,
convection calibration

Convection Calibration of Schmidt-Boelter Heat Flux Gages in Shear and Stagnation Air Flow

Andreas Hoffie,
Prof. Dr. Thomas E. Diller
Mechanical Engineering

Abstract

This work reports the convection calibration of Schmidt-Boelter heat flux gages in shear and stagnation air flow. The gages were provided by Sandia National Laboratories and included two one-inch diameter and two one-and-one-half-inch diameter Schmidt-Boelter heat flux gages. In order to calibrate the sensors a convection calibration facility has been designed, including a shear test stand, a stagnation test stand, an air heater and a data acquisition system.

The current physical model for a combined radiation and convection heat transfer environment uses an additional thermal resistance around the heat flux gage. This model clearly predicts a non-linear dependency of the gage sensitivity over a range of heat transfer coefficients. A major scope of this work was to experimentally verify the relation found by the model assumptions.

Since the actual heat sink temperature is not known and cannot be measured, three different cases have been examined resulting in three different sensitivities for one pressure value, which is the gage sensitivity for the not cooled case and the gage sensitivity for the cooled case, based on the plate temperature or on the cooling water temperature.

All of the measured sensitivities for shear as well as for stagnation flow fit well in the theory and show the non-linear decay for increasing heat transfer coefficient values. However, the obtained data shows an offset in the intersection with the sensitivity at zero heat transfer coefficient. This offset might arise from different radiation calibration techniques and different surface coatings of test gage and reference standard.

Acknowledgements

This work is dedicated to all of the great and helpful people
I have gotten to known and who have gotten to known me at this special place, Virginia Tech, and in this special country, the U.S.A., each of whom made a contribution to my success in pursuing my degree and in the completion of this work.

In particular, I have to thank *Sandia National Laboratories* for the financial support. I thank *Justin Dominic* for his contribution and his help taking the stagnation stand data, I thank *Samuel Raben* for a night of PIV data taking and for his experienced skills in handling the PIV setup, and I want to thank *John Charonko* for numerous hours giving me a crash course in PIV data evaluation and his countless ideas and helpful inputs. Moreover, I want to thank all of *my colleagues* in the Complex Thermo Fluids Systems Laboratory, who are creating a good and healthy work environment, where great achievements are made possible!

I also want to thank all of *my friends, international or local*, I got to know here at Tech and in the U.S., who supported me whenever they could and who created a temporary family, giving me the understanding that professional success is not possible without a balanced private life.

I give special thanks to *Cathy Hill*, working in the graduate program recourse office in the mechanical engineering department, who helped me when I was struggling through the paper work to obtain my degree and switch my status from exchange to full degree graduate

student; and never got tired of answering thousands of questions. Thanks very much for the great help.

I also give special thanks to *Jerrod Ewing*, a fellow graduate student who told me about the possibility of working as a research assistant, which had a major impact on my career at Tech. I am also grateful for his continuous advice during my graduate studies.

I also want to express my special thanks to *Andrew Gifford*, PhD student in the CTFS Lab, for his continuous and valuable advice. I have to thank him for his ideas and skills to realize things. I also appreciated the countless and generative discussions we had, necessary to accomplish this work. Without his support, I would not have been able to accomplish, what I have accomplished in this short amount of time. Thanks for everything!

Special thanks and appreciation is given to my committee *Dr. Pavlos Vlachos* and *Dr. Scott Huxtable;* appreciation to Dr. Scott Huxtable for his positive attitude, his support and the confidence in me; appreciation to Dr. Pavlos Vlachos for giving me the opportunity to study the PIV technique and also for his confidence in me. There was no one else, who understood my situation as an exchange student as quickly as he did.

Most of all, I want to express my deepest gratitude to my advisor, *Dr. Thomas Diller*, for giving me the opportunity to work for him as a graduate research assistant and thus enabling me the perspective to pursue the M.S. degree. I want to thank him for being my mentor, for his advice, time and his always open ears, for his financial and moral support, his confidence and trust in me; for his endurance, patience and his dedication for a common goal. Obtaining this degree was an important milestone in my life. I will always be indebted to him for giving me that opportunity and I will never forget!

I will be forever deeply grateful to my parents, *Hans* and *Annemarie Hoffie*, who supported me whenever they could and who will always be there for me.

I am carrying my Virginia Tech Master of Science degree with honours. I will always remember my graduate student time at Tech and the great help I have received.

With utmost appreciation to all of the individuals included and mentioned above,
Ut Prosim.

Blacksburg, VA, USA, December 2006 Andreas Hoffie

Contents Overview

Table of Contents

List of Figures

Chapter 2

Chapter 3

Chapter 4

Appendix A

Appendix B2

Appendix C2

Appendix D

List of Tables

Chapter 2

Chapter 3

Chapter 4

Appendix A

Appendix E

Nomenclature

Letter Symbols & Abbreviations

Symbol/Abbreviation	Description	Unit/Value
□	Place holder	any
a	Speed of sound	m/s
A	Area	m²
$b(x_i)$	Bias error of measurand x_i	any
Bi	Biot number	-
c_f	Friction coefficient	-
$c_{f,x}$	Friction coefficient as a function of x	-
$\overline{c_{f,L}}$	Mean friction coefficient over length L	-
c_p	Specific heat for constant pressure	J/(kgK)
CPU	Central Processing Unit	-
Cu	Copper	-
d	Thickness	m
D	Drag	N
DAQ	Data aquisition unit	-
E	Voltage output	V
$F_{a\rightarrow b}$	View factor from object a to b	-
h	Heat transfer coefficient	W/(cm²K)
HFM	Heat flux microsensor	-
$J(x)$	Jet momentum	Ns
J_s	Original jet momentum	Ns
k	Thermal konductivity	W/K
K	von Kármán constant	-

Symbol/Abbreviation	Description	Unit/Value
L	Length	m
m	Mass	kg
Ma	Mach number	-
N_1	Nozzle 1	-
N_2	Nozzle 2	-
Ni	Nicel	-
Nu	Nusselt number	-
$q“$	Heat flux	W/m²
q	Heat transfer	W = J/s
Q	Thermal energy (heat)	J
p	Pressure	N/m², respectively psi
p_{dyn}	Dynamic pressure	N/m²
$p(x_i)$	Precision error of measurand x_i	any
Pr	Prandtl number	-
Pr_t	Turbulent Prandtl number	-
r	Radius	m
r_f	Recovery factor	-
$R“$	Thermal Resistance	cm²K/W
Re_x	Reynolds number based on x	-
Re_L	Reynolds number based on L	-
R_S	Specific gas constant	J/(kgK)
St	Stanton number	-
Stk	Stokes number	-
t	Time	s
t_r	Relaxation time	s
S	Sensitivity	mV/(W/cm ²)
SB	Schmidt-Boelter gage	-
$SHEAR$	Shear flow stand	-
$STAG$	Stagnation flow stand	-
T	Temperature	K respectively °C
T_r	Recovery temperature	K
u_t	Friction velocity	m/s
u	Horizontal velocity component	m/s
$u_c(x_i)$	Uncertainty of measurand x_i	any
v	Vertical velocity component	m/s
V	Valve	-
u_{max}	Maximum velocity	m/s
U	Internal energy	J
w	Width	m
W	Work	J
x	Horizontal coordinate	m
y	Vertical coordinate	m
$y_{1/2}$	Position, wher mean velocity is equal to one half of the maximum velocity	
z	Coordinate of the third dimension	m

Subscripts

Symbol/Abbreviation	Description	Unit/Value
1	at junction 1	-
2	at junction 2	-
∞	surroundings	-
abs	absorbed	-
cond	conduction	-
conv	convection	-
det	detector	-
dyn	dynamic	-
fluid	fluid	-
g	gage	-
i	index	-
incident	incident	-
j	index	-
lam	laminar	-
net	netto	-
N	number, limit	-
plate	plate	-
ref	reflection	-
req	required	-
rad	radiation	-
sur	surroundings	-
surf	surface	-
trans	transmition	-
turb	turbulent	-

Superscripts

Symbol	Description	Unit/Value
—	Mean	-
′	Fluctuation (in turbulence)	-
+	Wall coordinates/velocies	-

Greek

Symbol	Description	Unit/Value
α_r	Apsortivity for radiation	-
α	Thermal diffusivity	m²/s
$\delta(x)$	Velocity boundary layer thickness	m
$\delta_t(x)$	Thermal boundary layer thickness	m
Δ	Delta	any
ε_r	Emissivity for radiation	-
ε_M	Momentum diffusivity	-
ε_H	Thermal diffusivity	-
ϕ	Angle	°
γ	Adiabatic coefficient	-
μ	Dynamic viscosity	kg/(ms)
ν	Kinematic viscosity	m/s
π	Number	3.14159
ρ_r	Reflectivity for radiation	-
ρ	Densitiy	kg/m³
σ	Stefan-Boltzmann-Constant	$5.67051 \cdot 10^{-8} W/(m^2K^4)$
σ_T	Seebeck coefficient	V/K
σ_υ	Standart deviation	-
Σ	Sum	-
τ_r	Transmissivity for radiation	-
τ	Shear stress	N/m²

Operators

Symbol	Description	Unit/Value
$\partial\square/\partial\square$	Partial derivative	-
∇	Del-Operator (3D)	-

1 Introduction

Measurement of heat flux in addition to temperature gives a more complete understanding of a thermodynamic system, because it provides additional information about thermal energy transfer and heat paths. Due to higher quality standards and an increase in the load limits of materials, it is necessary to make accurate heat flux measurements. In order to make accurate measurements, it is important to calibrate heat flux sensors for real applications and to understand how heat flux sensors work. This paper explains how heat flux sensors work, what theory they are based on and more important, how they can be calibrated.

Examples for applications of heat flux sensors cover a broad variety, starting from heat flux measurement in turbo jet engines (monitoring of thermal stresses in combustion chambers, turbine vanes), applications in construction engineering (fire protection and detection, thermal insulation), geothermal applications, biomedicine and physiology.

Chapter two gives further details why heat flux measurement is so important in complex and advanced engineering as well as in our daily life. This chapter also discusses the required fundamentals in radiation convection and conduction. It then carries this knowledge over to explain the functionality of heat flux sensors and how combined convection and conduction affects the sensor sensitivity. The resulting model and associated equation predict a non-linear decrease of the gage sensitivity for increasing heat transfer coefficients. The major scope of this work was to experimentally verify those predictions, if there really was an influence of convection heat transfer components on the gage sensitivity.

Chapter three explains the convection calibration facility specifically designed to calibrate the four Schmidt-Boelter heat flux sensors, the air heater, the test stands, the test procedures, the data acquisition system and the programs used. Data reduction and uncertainty analysis is also explained in the last section of this chapter.

Chapter four presents the experimental results found in chapter three and discusses them, which are then concluded in Chapter five and followed by some recommendations.

The second major part of this work covered the PIV analysis of the left nozzle (in flow direction) of the shear stand. Although not part of the calibration work, the PIV was used to obtain an insight of the flow field provided by the nozzles.

An air property data, design data and MATLAB programs used for this work can be found in the appendices.

2 Fundamentals

2.1 Why Heat Flux Measurements?

Thermal management of materials and temperature control of industrial processes is becoming more important in order to achieve higher quality standards. An example would be to monitor thermal stresses in ceramics and thin films. Moreover, in our daily life, proper heating and cooling of living spaces is desired for maximum comfort. Temperature control requires controlled energy transfer. To ensure controlled energy transfer, a proper design of the equipment, such as heaters, heat exchangers, boilers and condensers is very important.

Measuring the temperature only of a thermodynamic system might not be sufficient for a complete understanding of the processes in all of the cases. Measuring heat flux instead, gives additional information of how, where, and how much thermal energy is being transferred or dissipated. Furthermore, maximizing and minimizing thermal energy transfer of many thermal systems in practical use is crucial to their optimum performance. The challenge now is to measure heat flux. Consequently, gages, capable of sensing heat flux directly and in real time become suddenly very important. The fundamentals chapter gives a review of important heat transfer characteristics and the basics heat flux relies on. The basic principles are then carried over to applications in heat flux sensor design. Thus, the third part (2.3) gives an

overview of different types of heat flux sensors and the fourth part (2.4) explains radiation calibration of sensors.

2.2 Heat Transfer Fundamentals

Diller [1] gives a brief and complete summary of heat transfer fundamentals and its three basic modes of conduction, convection and radiation: “Heat” is the movement of thermal energy and “heat transfer” is the rate of which heat is transferred in matter. The symbol for heat is Q with unit Joule, the symbol for heat transfer is q with unit Watts (Joules per second). Heat transfer per unit area is then termed as heat flux with symbol q'' and unit Watts per square meter. In some cases, the overall heat transfer of a system is of importance. In other cases the spatial and temporal variation of the heat flux is important for performance enhancements. This chapter discusses the measuring of spatial or temporal distribution of heat flux. Simultaneous measurements of spatial and temporal changes of heat flux are not feasible at this time.

The fundamental principle, which thermodynamics and heat transfer is based on, is the first law of thermodynamics, which states that energy can not be abolished – energy is conserved and transformed from one state to another:

$$dU = dQ + dW \ , \tag{2.1}$$

where U is the inner energy of the system, Q is the heat and W is the work done on the system. If the work done on the system is zero, the first law of thermodynamics (2.1) reduces to:

$$dU = dQ \tag{2.2}$$

Thus, changes of the inner energy of a thermodynamic system are equal to changes in Q. And the changes in Q include all three modes of heat transfer – conduction, convection and radiation. Figure 2.1 shows a heat flux gage in a thermodynamic environment, with the three modes of energy transfer acting on it.

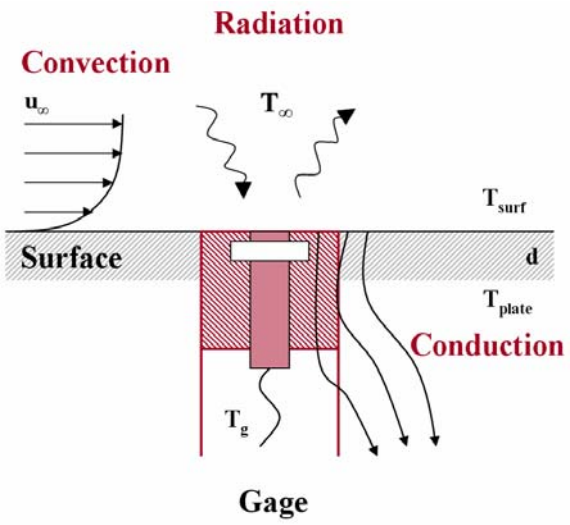

Figure 2.1: Heat flux sensor in a thermodynamic environment with the three modes of energy transfer conduction, convection and radiation acting on it.

Figure 2.2 illustrates a simple thermodynamic system with a control volume (CV) around such a heat flux sensor. The energy balance, applied on the example as a function of time and with positive incoming quantities and negative outgoing quantities can be expressed as:

$$\frac{\partial}{\partial t}(Q) = \frac{\partial}{\partial t}(mc_pT) \overset{!}{=} q_{net} = q_{convection} + q_{radiation} - q_{conduction}\,, \tag{2.3}$$

or:

$$c_p\left(m\frac{\partial T}{\partial t} + T\frac{\partial m}{\partial t}\right) = q_{conv} + q_{rad} - q_{cond}\,. \tag{2.4}$$

if the mass m of the system is constant, one obtains:

$$c_p m\frac{\partial T}{\partial t} = q_{conv} + q_{rad} - q_{cond}\,, \tag{2.5}$$

where c_p is the specific heat with units in Joule per kilogram and Kelvin, T is the temperature in Kelvin and q is the heat transfer. The thermal capacitance (c_pm) causes a time lag in the temperature response of the material to a change in heat transfer. For steady-state heat transfer, one gets:

$$q_{cond} = q_{conv} + q_{rad} \tag{2.6}$$

In the following sections, convection, radiation and conduction will be explained briefly. Conduction takes place within the material, where convection and radiation are on the surface of the material and are the quantities of interest to measure with a heat flux sensor.

Both convection and radiation are present on the surface, although in most of the cases one effect is negligible compared to the other.

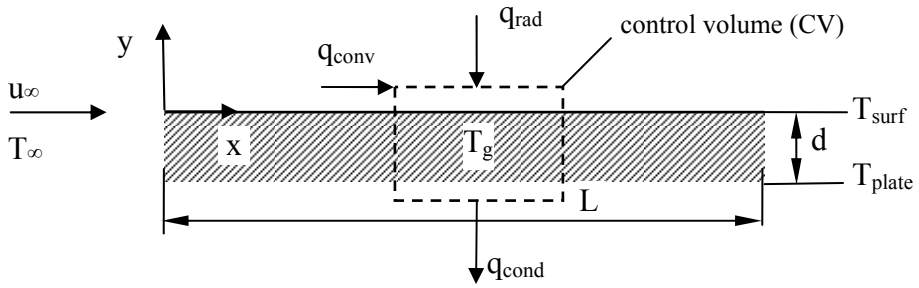

Figure 2.2: Energy balance on a thermodynamic system (for example a temperature sensor) with control volume (CV). The thin plate case is achieved in the limit of d→0.

2.2.1 Radiation Heat Transfer

"Heat transfer by radiation occurs by electromagnetic emission and absorption of photons" (Diller [1]). Radiation thus does not rely on a medium for transmission of the energy hence it is very different from conduction or convection. The characteristics of the emitting or absorbing surface material determine the spectrum of wavelengths that are transmitted through radiation. Hence, the absorption characteristics can be controlled by changing the surface characteristics. For that reason, the surface of a radiation sensor is often coated with high absorptive paint or graphite. The fraction of the spectrum (or energy) emitted, is called the emittance or emissivity ε_r. The fraction of the spectrum absorbed is the absorptance or absorptivity α_r. The reflectance or reflectivity ρ_r defines the fraction of energy, which is reflected by the material. Analogous is the fraction of energy which is transmitted through the material characterized by the transmittance or transmissivity τ_r. Consequently, it must be:

$$\alpha_r + \rho_r + \tau_r = 1 \tag{2.7}$$

For a grey body radiator the emittance is equal to the absorbtance ($\alpha_r = \varepsilon_r$). For a black body radiator, both are equal and are hundred percent ($\alpha_r = \varepsilon_r = 1$). The energy emitted from the surface is proportional to the fourth power of the (absolute) temperature of the body. Since this is the case, the emitted energy from the detector is often negligible compared to the emitted energy. In this case, the temperature distribution of the sensor is not important. The following development of equation (2.10) shows the mathematical relation to this physical effect. For a view factor between radiator and detector of equal to one, and the grey body assumption, with $\alpha_r = \varepsilon_r$, the net heat flux between radiator and detector is given through the Stefan-Boltzmann-Equation for radiation

$$q''_{net} = \varepsilon_r \sigma \left(T_{rad}^4 - T_{det}^4 \right), \tag{2.8}$$

where σ is the Stefan-Boltzmann-Constant, given by $\sigma = 5.67051 \cdot 10^{-8} \mathrm{W/(m^2K^4)}$. The view factor between radiator and detector is obtained by

$$F_{rad \to det} = \iint \frac{\cos(\varphi_{rad}) \cos(\varphi_{det})}{\pi r^2} dA_{rad} dA_{det} \tag{2.9}$$

φ_{rad} determines the orientation of the area dA_{rad} of the radiator in space. φ_{det} determines the orientation of the area of the detector dA_{det} in space and r is the distance between them. Figure 2.3 illustrates the geometry and the relative orientation between radiator and detector. Not all of the radiated energy will be captured by the detector. The heat flux which the detector will see, is dependent on the orientation of the radiator relative to the detector. This effect is taken care of by the view factor.

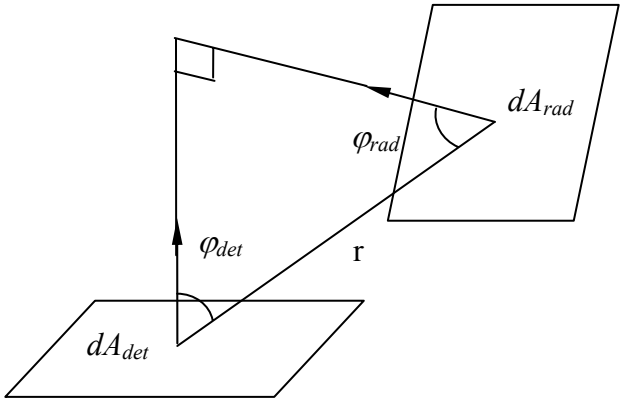

Figure 2.3: Relative orientation between radiator and detector in space

Typically, the temperature of the detector (e.g. the heat flux gage) is much smaller than the temperature of the radiator and thus negligible. If the radiator is the surrounding, the last relation simplifies further to:

$$\boxed{q''_{net} = \varepsilon_r \sigma T_\infty^4} \tag{2.10}$$

The fact that the energy absorbed by the detector (sensor) is negligible against the emitted energy by the radiator, is a big advantage over convection measurements for which Diller [1] states that the temperature distribution on the surface has a big influence on the measurement. The major scope of this work is to show this influence of convection to the output of the heat flux sensor.

From equation (2.7) we can further deduce:

$$\begin{aligned} \alpha_r q''_{rad} + \rho_r q''_{rad} + \tau_r q''_{rad} &= q''_{rad} \qquad \text{(a)} \\ q''_{abs} + q''_{ref} + q''_{trans} &= q''_{rad} \qquad \text{(b)} \end{aligned} \tag{2.11}$$

If for the material of the detector ρ and τ is zero, it will absorb the whole spectrum (black body radiator) thus we can conclude from comparison of equations (2.11) (a)&(b):

$$q''_{abs} = \alpha_r q''_{rad} \tag{2.12}$$

For the actual incident heat flux on the detector we get:

$$q''_{incident} = F_{rad \to det} q''_{rad}\,, \tag{2.13}$$

So that equation (2.12) with a view factor of one truly is:

$$\boxed{q''_{abs} = \alpha_r q''_{incident}} \tag{2.14}$$

This finding will be used later on in this text.

2.2.2 Conduction Heat Transfer

Heat transfer through stationary materials by electrons and photons is called conduction. Fourier's law relates heat flux with the temperature gradient, where the heat flux vector is in the opposite direction of the temperature gradient and *k* is the thermal conductivity of the material in Watts per Kelvin:

$$\vec{q}''_{cond} = -k\nabla T \tag{2.15}$$

If we want to measure the temperature response of a system to determine the heat transfer, we can use equations (2.5) with q_{conv} and q_{rad} zero and (2.15) as

$$q_{cond} = -k\left(\frac{\partial}{\partial x}\left(\frac{\partial T}{\partial x}\right)+\frac{\partial}{\partial y}\left(\frac{\partial T}{\partial y}\right)+\frac{\partial}{\partial y}\left(\frac{\partial T}{\partial y}\right)\right)\partial x\partial y\partial z \tag{2.16}$$

and get:

$$\frac{\partial T}{\partial t} = \alpha\left(\frac{\partial^2 T}{\partial^2 x}+\frac{\partial^2 T}{\partial^2 y}+\frac{\partial^2 T}{\partial^2 z}\right), \tag{2.17}$$

or:

$$\frac{\partial T}{\partial t} = \alpha(\nabla^2 \cdot T) \tag{2.18}$$

where

$$\alpha = \frac{k}{\rho c_p} \tag{2.19}$$

is the thermal diffusivity with the density ρ of the material in kilogram per cubic meter. (2.18) is known as the classic heat diffusion equation. Determining the heat transfer from the heat diffusion equation can get quite complicated, if multidimensional effects are present.

For steady-state, one-dimensional heat transfer, and the thickness *d* of the material (Figure 2.2), equation (2.15) reduces to: $q''_{cond} = -k\frac{\partial T}{\partial y} = -k\frac{\Delta T}{\Delta y}$, (2.20)

or simply:

$$\boxed{q''_{cond} = \frac{-k}{d}(T_{plate} - T_{surf})}, \tag{2.21}$$

This is the equation which heat flux sensors based on the spatial temperature gradient follow. The utilization of this equation will be explained in the following sections.

2.2.3 Convection Heat Transfer and Boundary Layer Theory

Convective heat transfer takes place between a fluid and a surface, where the fluid is free or forced to move relative to the surface with a velocity u_∞ (Figure 2.2). Due to frictional stresses, caused by the fluid motion across the surface, given by:

$$\tau_{surf} = \mu \left(\frac{\partial u}{\partial y} \right)_{y=0} \tag{2.22}$$

the velocity very close to the surface at $y = 0$ is zero. μ is the dynamic viscosity of the fluid in kilogram per meter and second, given by:

$$\mu = \nu \rho, \tag{2.23}$$

with ν, the kinematic viscosity of the fluid in square meters per second and ρ, the density of the fluid. A skin friction coefficient can be obtained by relating the surface stresses to the dynamic pressure p_{dyn}, based on the free stream velocity u_∞:

$$c_f = \frac{\tau_{surf}}{p_{dyn}} = \frac{\mu \left(\frac{\partial u}{\partial y} \right)_{y=0}}{\frac{1}{2} \rho u_\infty^2}, \tag{2.24}$$

Utilizing the skin friction coefficient, it is possible to calculate the drag force acting on the plate in Figure 2.4, assuming the drag is caused by frictional forces only and the width of the plate is unity ($w = 1$):

$$\begin{aligned} D &= \int_0^L \tau_{surf} w dx = \int_0^L c_{f,x} p_{dyn} w dx \\ \frac{D}{w} &= \frac{1}{2} \rho u_\infty^2 L \cdot \left[\frac{1}{L} \int_0^L c_{f,x} dx \right] \\ \frac{D}{w} &= \frac{1}{2} \rho u_\infty^2 L \cdot \overline{c_{f,L}} \end{aligned} \quad , \tag{2.25}$$

which means in order to obtain the drag force or shear stress acting on the plate, it is necessary to know the friction coefficient for our problem. $\overline{c_{f,L}}$ is the average friction coefficient. Determining the flow quantities for the simple boundary layer problem, given in Figure 2.2 for the laminar and the turbulent case, is the scope of this section. Once the desired quantities are known, we can make an estimate about the heat transfer, which will take place, in case the

fluid crossing the plate is heated. As a consequence there will be heat transfer going from the fluid into the plate, which is related to the skin friction.

Figure 2.4 shows the developing velocity and thermal boundary layers from the leading edge. At the edge of the velocity boundary layer, for $y=\delta(x)$ the fluid velocity is equal to 99% of u_∞ and at the edge of the thermal boundary layer, for $y=\delta_t(x)$ the temperature difference $(T-T_w)$ is equal to 99% of $(T_\infty-T_w)$. The thicknesses of the boundary layers are given by $\delta(x)$ for the velocity and $\delta_t(x)$ for the temperature respectively.

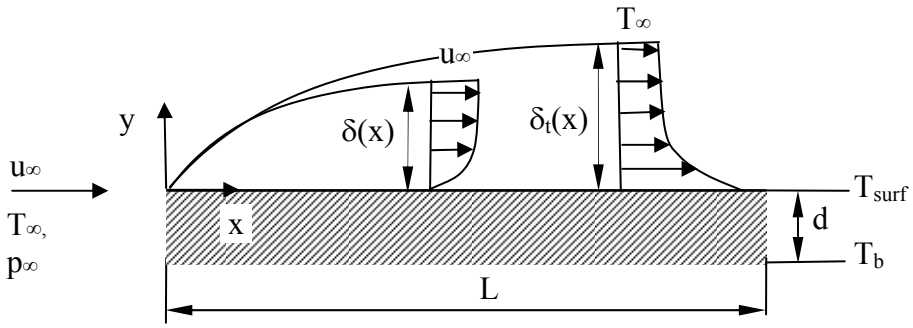

Figure 2.4: Velocity and thermal boundary layers on a flat plate.

Laminar boundary layer flow becomes turbulent after a threshold value, characterized by a dimensionless number, has been exceeded. This value is known as the Reynolds number, which is defined as

$$\mathrm{Re}_x = \frac{u_\infty x}{\nu} \tag{2.26}$$

For a laminar flow over a flat plate, the critical Reynolds number (Re_{x_c}, with x_c as critical length) has been determined to be between $2\cdot10^4$ … 10^6, depending on a number of different factors. Between regions of purely laminar and fully developed turbulent flow, there is an intermediate state, called the transition region (Figure 2.5).

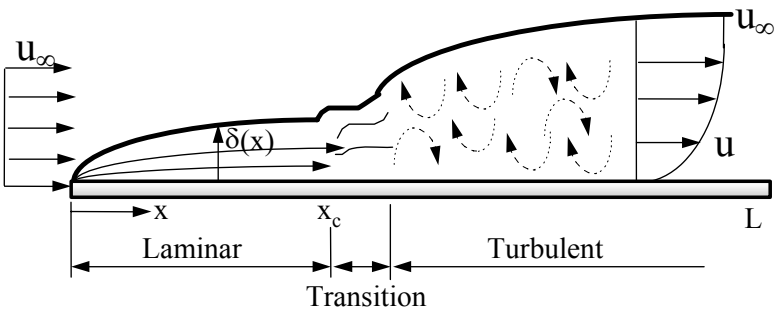

Figure 2.5: Laminar, transition and turbulent region of a flow over a flat plate.

As a consequence of the complexity and unavailability of exact analytical solutions to the Navier-Stokes equations (especially for the turbulent cases), fluid motion and heat transfer are decoupled by the introduction of a heat transfer coefficient *h* (units in Watts per Kelvin and per centimetre squared). The heat transfer is then calculated from Newton's law of cooling:

$$\boxed{q''_{conv} = -h(T_{surf} - T_{fluid})} \tag{2.27}$$

Unlike *k*, the heat transfer coefficient *h* is not only a property of the fluid. It also incorporates surface conditions and fluid flow effects.

For high speed applications, that is for Mach numbers greater or equal to 0.5, compressibility becomes important. The Mach number is defined by:

$$Ma = \frac{u_\infty}{a} = \frac{u_\infty}{\sqrt{\gamma R_s T_\infty}}, \tag{2.28}$$

with *a* as sound speed in meters per second, γ as the dimensionless adiabatic coefficient of the fluid and R_s as the specific gas constant of the fluid, with units of Joules per kilogram and Kelvin. The work done on the thermodynamic system is not negligible anymore. Thus, the temperature of the fluid is then represented by the recovery temperature T_r, often also termed as the adiabatic wall temperature. The recovery temperature takes into account the effect of frictional heating, caused by the dissipative term $\mu\phi$ in the energy equation:

$$\mu\phi = \mu\left(\frac{\partial u}{\partial y}\right)^2 \tag{2.29}$$

The recovery temperature can then be obtained from (as given by Schetz [2] and others)

$$T_r = T_\infty + r_f \frac{u_\infty^2}{2c_p} \tag{2.30}$$

The recovery factor r_f is obtained from the Prandtl number of the fluid, by:

$$r_f = \sqrt{\Pr} \tag{2.31}$$

and the Prandtl number is defined as:

$$\Pr = \frac{\mu c_p}{k} = \frac{\nu}{\alpha}. \tag{2.32}$$

Finally equation (2.27) becomes:

$$q''_{conv} = -h(T_{surf} - T_r). \tag{2.33}$$

For low-speed flows equation (2.27) simply becomes:

$$\boxed{q''_{conv} = -h(T_{surf} - T_\infty)} \tag{2.34}$$

Using equations (2.20) and (2.34) an equation for h can be obtained:

$$h = \frac{-k\left(\frac{\partial T}{\partial y}\right)_{y=0}}{-(T_{surf} - T_\infty)} \approx \frac{k}{\delta_t} \tag{2.35}$$

Since h is dimensional, it is usually grouped to a dimensionless quantity, known as the Nusselt number, which represents a dimensionless heat transfer number at the wall and becomes with using equation (2.35):

$$Nu(x) = \frac{hx}{k} \approx \frac{x}{\delta_t} \tag{2.36}$$

The problem given in Figure 2.4 is completely described by the three governing equations – conservation of mass, momentum and energy. For the laminar, two-dimensional, incompressible but unsteady case, the governing equations reduce to, assuming constant c_p, ρ, μ and k and no body forces

Continuity Equation:
$$\frac{\partial u}{\partial x} + \frac{\partial v}{\partial y} = 0 \tag{2.37}$$

Momentum Equation:
$$\frac{\partial u}{\partial t} + u\frac{\partial u}{\partial x} + v\frac{\partial u}{\partial y} = -\frac{1}{\rho}\frac{\partial p}{\partial x} + \nu\left(\frac{\partial^2 u}{\partial x^2} + \frac{\partial^2 u}{\partial y^2}\right) \tag{2.38}$$

Energy Equation: $$\frac{\partial T}{\partial t}+u\frac{\partial T}{\partial x}+v\frac{\partial T}{\partial y}=\alpha\left(\frac{\partial^2 T}{\partial x^2}+\frac{\partial^2 T}{\partial y^2}\right)+\frac{\mu}{\rho c_p}\phi \tag{2.39}$$

$$\text{with } \phi=2\left[\left(\frac{\partial u}{\partial x}\right)^2+\left(\frac{\partial v}{\partial y}\right)^2\right]+\left(\frac{\partial u}{\partial y}+\frac{\partial v}{\partial x}\right)^2. \tag{2.40}$$

For steady-state flow, and applying the boundary layer simplifications, given by Schetz [2] or Bejan [3]

Momentum Equation: $$u\frac{\partial u}{\partial x}+v\frac{\partial u}{\partial y}=-\frac{1}{\rho}\frac{\partial p_\infty}{\partial x}+\nu\left(\frac{\partial^2 u}{\partial y^2}\right) \tag{2.41}$$

Energy Equation: $$u\frac{\partial T}{\partial x}+v\frac{\partial T}{\partial y}=\alpha\frac{\partial^2 T}{\partial y^2}+\frac{\mu}{\rho c_p}\left(\frac{\partial u}{\partial y}\right)^2 \tag{2.42}$$

A solution to equations (2.41) and (2.42) with the boundary conditions given in Figure 2.4 can be obtained by using the momentum and energy integral method. The integral method however, gives only an approximate solution, since the velocity and temperature profiles are approximated with polynomials. For the flat plate case, the similarity solution (Blasius, 1908) reveals the exact solution of the governing equations for Pr ≈ 1 and assuming uniform surface temperature (T_{surf}):

Thickness of the velocity boundary layer:

$$\delta(x)=4.92x\,\mathrm{Re}_x^{-1/2} \tag{2.43}$$

Skin friction coefficient: $$c_{f,x}=0.664\,\mathrm{Re}_x^{-1/2} \tag{2.44}$$

The average friction coefficient will thus be:

$$\bar{c}_{f,x}=\frac{1}{x'}\int_0^{x'} c_{f,x}dx=1.328\,\mathrm{Re}_x^{-1/2} \tag{2.45}$$

Since the velocity and the thermal boundary layer thickness scale as:

$$\frac{\delta_t}{\delta}=\mathrm{Pr}^{-1/3} \tag{2.46}$$

we get for the thermal boundary layer thickness:

$$\delta_t=4.92x\,\mathrm{Re}_x^{-1/2}\,\mathrm{Pr}^{-1/3}.$$

Utilizing (2.36), we get the Nusselt number:

$$Nu(x) = 0.332\,\mathrm{Re}_x^{1/2}\,\mathrm{Pr}^{1/3}, \tag{2.47}$$

where the average Nusselt number becomes:

$$\overline{Nu(x)} = \frac{1}{x'}\int_0^{x'} Nu(x)dx = 0.664\,\mathrm{Re}_x^{1/2}\,\mathrm{Pr}^{1/3} \tag{2.48}$$

Another important dimensionless quantity in heat transfer is the Stanton number, which combines all dimensionless quantities that have been introduced so far:

$$St = \frac{Nu}{\mathrm{Re}\cdot\,\mathrm{Pr}} = \frac{h}{\rho u_\infty c_p} = \frac{1}{2}c_{f,x}\,\mathrm{Pr}^{-2/3} \tag{2.49}$$

and thus, we have obtained a useful and direct relation between skin friction and heat transfer. The last part of equation (2.49) is called the Reynolds-analogy. One further similarity number, characterizing the flow is the Stokes number, defined as:

$$Stk = \frac{t_r u_\infty}{d}, \tag{2.50}$$

this number gives the ratio of the stopping distance of a particle to a characteristic dimension of the obstacle, where t_r is the relaxation time in seconds, and d is the characteristic dimension of the obstacle. This number will become important for the PIV analysis done on a similar geometry as given in Figure 2.2 and is part of this work (see appendix A1).

In turbulent flow however, one has to deal with fluctuations of the fluid particles over time. So far, it has been impossible to determine the turbulent flow solution at any point in space and time by applying the mass, momentum and energy conservation equations. Through time-averaging of the continuity equations, however, we can get rid of the complications of instantaneous turbulent flow. Instead of looking at the instantaneous behaviour, we can look at the mean behaviour averaged over a long enough period. Reynolds discovered this simpler way to think about turbulent flows. The flow quantities are now given by a time averaged part and a fluctuation part:

$$\begin{aligned} u &= \bar{u} + u' \quad \text{(a)} \\ v &= \bar{v} + v' \quad \text{(b)} \\ p &= \bar{p} + p' \quad \text{(c)} \\ T &= \bar{T} + T' \quad \text{(d)} \end{aligned} \tag{2.51}$$

Plugging equations (2.51) (a-d) back into the continuity equations simplified for our boundary layer problem, equations (2.37), (2.41), (2.42) and notifying that $\overline{u'} = 0$, we obtain the time-averaged continuity equations, also known as Reynolds-averaged equations:

Time averaged Continuity Equation $$\frac{\partial \bar{u}}{\partial x} + \frac{\partial \bar{v}}{\partial y} = 0, \tag{2.52}$$

Similarly, $$\frac{\partial u'}{\partial x} + \frac{\partial v'}{\partial y} = 0 \tag{2.53}$$

Momentum Equation: $$\bar{u}\frac{\partial \bar{u}}{\partial x} + \bar{v}\frac{\partial \bar{u}}{\partial y} = -\frac{1}{\rho}\frac{\partial \bar{p}}{\partial x} + \nu\left(\frac{\partial^2 \bar{u}}{\partial y^2}\right) - \frac{\partial(\overline{u'v'})}{\partial y} \tag{2.54}$$

Energy Equation: $$\bar{u}\frac{\partial \bar{T}}{\partial x} + \bar{v}\frac{\partial \bar{T}}{\partial y} = \alpha\frac{\partial^2 \bar{T}}{\partial y^2} + \frac{\partial\left(\overline{v'T'}\right)}{\partial y} \tag{2.55}$$

Unfortunately now, our problem is governed still by three equations but five unknowns which are $\bar{u}, \bar{v}, \bar{T}, \overline{u'v'}, \overline{v'T'}$. This is known as the closure problem. The expression $\overline{u'v'}$ is called the turbulent stress, also known as the Reynolds stress. $\overline{v'T'}$ represents the turbulent contribution to the heat transfer. In order to solve the equations, we would have to model these terms. Rewriting equations (2.54), (2.55):

Momentum Equation: $$\bar{u}\frac{\partial \bar{u}}{\partial x} + \bar{v}\frac{\partial \bar{u}}{\partial y} = -\frac{1}{\rho}\frac{\partial \bar{p}}{\partial x} + \frac{1}{\rho c_p}\frac{\partial}{\partial y}\left[\mu\frac{\partial \bar{u}}{\partial y} - \rho\overline{u'v'}\right] \tag{2.56}$$

Energy Equation: $$\bar{u}\frac{\partial \bar{T}}{\partial x} + \bar{v}\frac{\partial \bar{T}}{\partial y} = \frac{1}{\rho c_p}\frac{\partial}{\partial y}\left[k\frac{\partial \bar{T}}{\partial y} - \rho c_p\overline{v'T'}\right] \tag{2.57}$$

Shear stress and heat transfer are now obtained from:

Apparent shear stress:

$$\tau_{app} = \tau_{molec} + \tau_{turb} = \mu\frac{\partial \bar{u}}{\partial y} - \rho\overline{u'v'} = \rho\left[\left(\nu + \varepsilon_M\right)\frac{\partial \bar{u}}{\partial y}\right] \tag{2.58}$$

Apparent heat transfer:

$$-q''_{app} = -q''_{molec} - q''_{turb} = k\frac{\partial \bar{T}}{\partial y} - \rho c_p\overline{v'T'} = \rho c_p\left[\left(\alpha + \varepsilon_H\right)\frac{\partial \bar{T}}{\partial y}\right], \tag{2.59}$$

where ε_M is the momentum diffusivity and ε_H is the thermal diffusivity. Both are purely flow parameters have and units of square meters per second. This puts us in the position to define a turbulent Prandtl number:

$$\mathrm{Pr}_t = \frac{\varepsilon_M}{\varepsilon_H}, \tag{2.60}$$

The challenge now is to find the correct modelling for these parameters. A simple but good approximation has been developed by van Driest, which includes Prandtl's Mixing Length Model and the Deissler Model, which takes care of damping effects as a function of the distance to the wall (constant properties and zero pressure gradient assumed):

$$\varepsilon_M = K^2 y^2 \left|\frac{\partial \bar{u}}{\partial y}\right| \left[1 - \exp\left(-\frac{y}{A}\right)\right]^2, \tag{2.61}$$

where K is the von Kármán constant with $K=0.4$ and

$$A = 26\frac{\nu}{u_\tau} \tag{2.62}$$

and u_τ is the friction velocity defined as: $u_\tau = \left(\frac{\tau_{surf}}{\rho}\right)^{1/2}$. (2.63)

The next step is to express everything in dimensionless wall coordinates based on the friction velocity u_τ:

$$\begin{aligned} u^+ &= \frac{\bar{u}}{u_\tau} \quad \text{(a1)} & v^+ &= \frac{v}{u_\tau} \quad \text{(a2)} \\ x^+ &= \frac{u_\tau}{\nu} x \quad \text{(b1)} & y^+ &= \frac{u_\tau}{\nu} y \quad \text{(b2)} \end{aligned} \tag{2.64}$$

Very close to the wall, the inertia terms may be neglected. The momentum equation (2.56) using equation (2.58) with no pressure gradient reduces to:

$$\frac{\tau_{surf}}{\rho} = \left(\nu + \varepsilon_M\right)\frac{\partial \bar{u}}{\partial y} \tag{2.65}$$

Finally, one obtains a dimensionless velocity for each turbulent layer. The solution is a composition of all velocities in each sub-layer. Those solutions are discussed in detail by Schetz [2] and Bejan [3] and summarized in Table 2.2. Different researchers found different results for the layers dependent on their assumptions. The different regions in a turbulent boundary layer are given by Table 2.1 (Pope [4]).

To estimate the thermal diffusivity, we can directly use the expression for the turbulent Prandtl number provided by equation (2.60), for most cases the turbulent Prandtl number is 0.8 Schetz [2] or of the order of unity Bejan [3] and Pope [4]. In order to solve equation (2.57), we can go further and say, that very close to the wall, there are no convective contributions to the heat transfer, thus equation (2.57) simplifies to:

$$\frac{-q''_{cond}}{\rho c_p} = \left(\alpha + \varepsilon_H\right)\frac{\partial \overline{T}}{\partial y}, \tag{2.66}$$

Note the analogy to equation (2.65). Likewise the velocity, this equation has to be analyzed for each turbulent layer. Finally, one obtains a dimensionless temperature for each turbulent layer. The solution is a composition of all temperatures in each sub layer. Those solutions are discussed in detail by Bejan [3] and summarized in Table 2.3. Different researchers found different results for the layers dependent on their assumptions.

Other models utilize the turbulent kinetic energy in order to model ε_M and ε_H. One of these is the famous (K,ε)-Model.

Region	**Location**	**Defining property**
Inner layer	$y/\delta < 1$	$\overline{u}$ determined by ut and y^+, independent of U0 and d
Viscous wall region	$y^+ < 50$	Viscous contribution to shear stress significant
Viscous sublayer	$y^+ < 5$	Reynolds shear stress negligible compared to viscous stress
Outer layer	$y^+ > 50$	Direct effects of viscosity on $\overline{u}$ are negligible.
Overlap region	$y^+ > 50$, $y/\delta < 0.1$	Region of overlap between inner and outer layers (at large Re numbers)
Log-law region	$y^+ > 30$, $y/d < 0.3$	The log law holds
Buffer layer	$5 < y^+ < 30$	The region between the viscous sublayer an the log-law region

Table 2.1: Wall regions, layers and their defining properties, Pope [4].

$u^+(y^+)$	Name of the relation	Range	Researcher
$u^+ = y^+$ $u^+ = 2.5 \ln y^+ + 5.5$	Law of the Wall	$0 < y^+ < 11.6$ $y^+ > 11.6$	Prandtl and Taylor
$u^+ = y^+$ $u^+ = 5 \ln y^+ - 3.05$ $u^+ = 2.5 \ln y^+ + 5.5$	Law of the Wall	$0 < y^+ < 5$ $5 < y^+ < 30$ $y^+ > 30$	von Karman
$u^+ = 14.53 \tanh(y^+/14.53)$ $u^+ = 2.5 \ln y^+ + 5.5$	Law of the Wall	$0 < y^+ < 27.5$ $y^+ > 27.5$	Rannie
$\frac{du^+}{dy^+} = \frac{2}{1+\left[1+4\kappa^2 y^{+2}\left[1-exp\left(-y^+/A^+\right)\right]^2\right]^{1/2}}$ $\kappa = 0.4 \quad A^+ = 26$		$all\ y^+$	van Driest
$u^+ = 2.5 \ln(1+0.4\, y^+)$ $+7.8[1 - exp(-y^+/11)$ $-(y^+/11)exp(-0.33y^+)]$		$all\ y$	Reichardt
$\frac{du^+}{dy^+} = \frac{1}{1+n^2 u^+ y^+\left[1-exp\left(-n^2 u^+ y^+\right)\right]}$ $n = 0.124$ $u^+ = 2.78 \ln y^+ + 3.8$		$0 < y^+ < 26$ $y^+ > 26$	Deissler
$y^+ = u^+ + A[exp\, Bu^+ - 1 - Bu^+ - ½(Bu^+)^2$ $-1/6\,(Bu^+)^3 - 1/24\,(Bu^+)^4]$ $A = 0.1108$ $B = 0.4$		$all\ y^+$	Spalding

Table 2.2: Summary of lateral velocity expressions for the inner region of a turbulent boundary layer Bejan [3].

$u^+(y^+)$	Name of the relation	Range	Researcher
$T^+ = Pr \cdot y^+$	Conduction Sublayer	$0 < y^+ < y^+_{csl}$	
$T^+ = \Pr \cdot y^+_{csl} + \frac{\Pr_t}{K} \ln\left(\frac{y^+}{y^+_{csl}}\right)$	Fully Turbulent Sublayer	$y^+ > y^+_{csl}$	

Table 2.3: Two-part formula for T^+, the "thermal law of the wall" of a turbulent boundary layer from Bejan [3]. In the range of $0.5 < Pr < 5$ the formulas indicate $Pr_t \approx 0.9$, $K \approx 0.41$, $y^+_{csl} = 13.2$.

By utilizing Prandtl's one-seventh power law, which represents a curve fit for the $u^+(y^+)$ data and is given by Bejan [3]:

$$u^+ = 8.74(y^+)^{1/7} \tag{2.67}$$

we are able to obtain an expression for the boundary layer thickness and the equations can be solved. First, we have to substitute in u^+ and y^+ with equations (2.64) (a1)&(b2). Replace for $y=\delta$, $u=u_\infty$ and obtain an expression for the surface shear stress as:

$$\tau_{surf} = 0.228\rho u_\infty \,\mathrm{Re}_\delta^{-1/4} \tag{2.68}$$

Also:

$$\frac{\bar{u}}{u_\infty} = \left(\frac{y}{\delta}\right)^{1/7}, \tag{2.69}$$

putting this and (2.68) into the momentum integral equation:

$$\frac{d}{dx}\left[\int_0^\delta \bar{u}(u_\infty - \bar{u})dy\right] = \frac{\tau_{surf}}{\rho}, \tag{2.70}$$

and solving, finally one obtains an expression for the velocity boundary layer thickness:

$$\delta_{turb}(x) = 0.37x\,\mathrm{Re}_x^{-1/5} \tag{2.71}$$

Using (2.24) and (2.68), the local turbulent friction coefficient turns out to be:

$$c_{f,x,turb} = 0.0592\,\mathrm{Re}_x^{-1/5} \tag{2.72}$$

The average friction coefficient is:

$$\bar{c}_{f,x,turb} = \frac{1}{x}\left[\int_0^{x_c} c_{f,x,lam}dx + \int_{x_c}^{x} c_{f,x,turb}dx\right], \tag{2.73}$$

$$\bar{c}_{f,x,turb} = 0.074\,\mathrm{Re}_x^{-1/5} - 1.742\,\mathrm{Re}_x^{-1}$$

where $\mathrm{Re}_{xc}=5\cdot10^5$ was used.

Since the mechanism of transport for both, heat and momentum in the turbulent sublayer is due almost entirely to the turbulent eddies, the turbulent Prandtl number given by equation (2.60) can assumed to be constant. Hence,

$$\frac{\delta_t}{\delta} \sim 1, \tag{2.74}$$

Through the Reynolds analogy, equation (2.49), it is possible to calculate the local Nusselt number, to:

$$Nu_{turb}(x) = \frac{1}{2} c_{f,x,turb} \operatorname{Re}_x \operatorname{Pr}^{1/3} = 0.0296 \operatorname{Re}_x^{4/5} \operatorname{Pr}^{1/3} \tag{2.75}$$

The average Nusselt number will then be:

$$\overline{Nu}_{turb}(x) = \frac{1}{x}\left[\int_0^{x_c} Nu_{lam}(x)dx + \int_{x_c}^{x} Nu_{turb}(x)dx\right], \tag{2.76}$$
$$\overline{Nu}_{turb}(x) = 0.037 \operatorname{Re}_x^{4/5} \operatorname{Pr}^{1/3} - 871 \operatorname{Pr}^{1/3}$$

where $R_{xc}=5\cdot10^5$ has been used. Table 2.4 shows a summary of laminar and turbulent findings.

Quantity	Laminar	Turbulent
$\delta(x)$	$4.92x \operatorname{Re}_x^{-1/2}$	$0.3700x \operatorname{Re}_x^{-1/5}$
$\delta_t(x)$	$4.92x \operatorname{Re}_x^{-1/2} \operatorname{Pr}^{-1/3}$	$\delta(x)$
$c_{f,x}$	$0.664 \operatorname{Re}_x^{-1/2}$	$0.0592 \operatorname{Re}_x^{-1/5}$
$\bar{c}_{f,x}$	$1.328 \operatorname{Re}_x^{-1/2}$	$0.074 \operatorname{Re}_x^{-1/5} - 1.742 \operatorname{Re}_x^{-1}$
$Nu(x)$	$0.332 \operatorname{Re}_x^{1/2} \operatorname{Pr}^{1/3}$	$0.0296 \operatorname{Re}_x^{4/5} \operatorname{Pr}^{1/3}$
$\overline{Nu}(x)$	$0.664 \operatorname{Re}_x^{-1/2} \operatorname{Pr}^{1/3}$	$0.037 \operatorname{Re}_x^{4/5} \operatorname{Pr}^{1/3} - 871 \operatorname{Pr}^{1/3}$

Table 2.4: Summary of laminar and turbulent findings. $R_{xc}=5\cdot10^5$.

2.3 Heat Flux Measurement

Most methods for measuring heat flux are based on temperature measurements on the surface or close to the surface of a solid material. This involves insertion of a sensor either onto the surface or into the material, which can cause physical and thermal disruption of the surface. Consequently, the goal must be to minimize the disruption. The more that is known about the disruptions caused by a gage, the more accurate the measurement will be, when these effects are taken into account. Hence, it is important to understand the disruptions. Also important for good heat flux measurements, is to use the correct type of sensor with the proper operating range. This section gives an overview of different sensor types.

2.3.1 Sensors Based on Spatial Temperature Gradient

By utilizing Fourier's Law, equation (2.15), the heat flux can be found, if the temperature gradient is known. Since it is difficult to mount the sensor in the material, it is either mounted on the surface or in a hole in the material. Different types of sensors, based on the spatial temperature gradient follow. The different gages may vary in how the temperature difference is measured, the thickness of the thermal resistance layer used, and how the sensing element is mounted in the gage. These three aspects of each different type of gage are discussed along with the implications for measurements.

2.3.1.1 One-Dimensional Planar Sensors

The simplest heat flux gage concept is based on steady-state and one-dimensional heat conduction. In this case, the heat flux can be found directly from the simplified Fourier's law found in section 2.2.2, equation (2.21)

$$\boxed{q_g'' = \frac{k_g}{d_g}(T_1 - T_2)} \tag{2.77}$$

Temperature difference is measured across a thermal resistance layer of thickness d_g by temperature sensors – k_g is the thermal conductivity of the gage or more correctly, the resistance layer. This working principle is illustrated by Figure 2.6. A further parameter characterizing the resistance layer is the thermal diffusivity α.

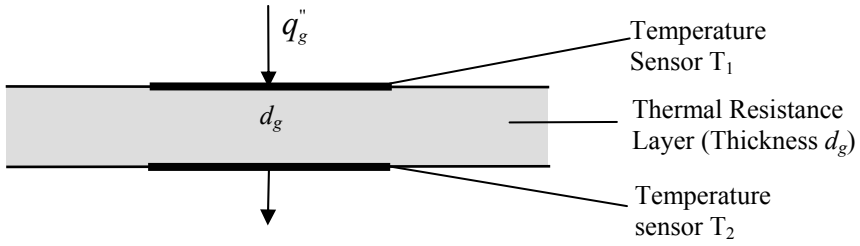

Figure 2.6: One-dimensional planar sensor concept [5].

The temperature difference across the thermal resistance layer is commonly measured by thermocouples. The big advantage of thermocouples is that they generate their own voltage output (E) corresponding to the temperature difference (T_1-T_2) between two junctions. The output signal will be increased, if the thermocouples are put in series to form a thermopile. Figure 2.7 illustrates a thermopile for measuring a temperature difference. Figure 2.8 shows a Thermopile heat flux sensor. For the legs of the sensor (the output leads) any good conductor material can be used. However they must be of the same material in order to prevent forming another thermocouple junction. A good material for example is a copper.

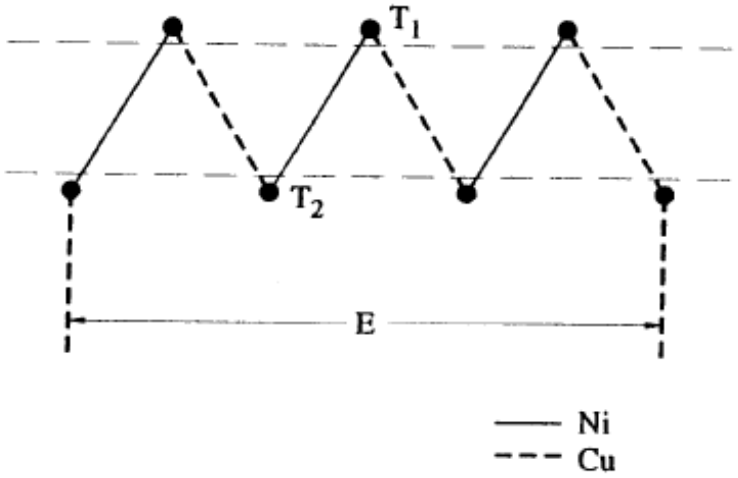

Figure 2.7: Thermopile for differential temperature measurements [5].

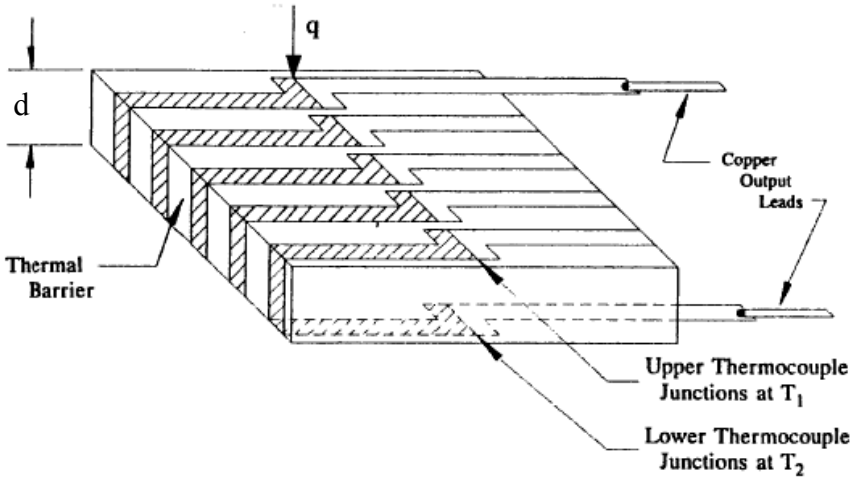

Figure 2.8: Thermopile heat flux sensor [5].

The voltage output of the sensor, can be obtained by using the Seebeck coefficient σ_T, which represents the thermoelectric sensitivity of the materials, with units of volts per degree Celsius, as given by Diller [5]:

$$E = N\sigma_T (T_1 - T_2). \tag{2.78}$$

N is the number of thermocouple junction pairs. The corresponding sensitivity of the heat flux sensor is then:

$$\boxed{S_g = \frac{E}{q_g''} = N\sigma_T \frac{d}{k}}. \tag{2.79}$$

Although the sensitivity of a sensor is determined in practice from a direct calibration, equation (2.79) can be used for design purposes.

The transient response of the gage is a function of the thermal resistance layer thickness and the thermal diffusivity of the material. The time required for 98% response is [5]:

$$t = \frac{3}{2}\frac{d^2}{\alpha} \tag{2.80}$$

The sensitivity increases linearly with the thermal resistance layer thickness (2.79), but the time response increases as the square of the thickness. Consequently, sensitivity versus time response increases as the square of the thickness. Consequently, sensitivity versus time response is one of the major trade-offs in the design of the gages.

The other factor is the temperature disruption of the surface. To minimize errors due to this disruption the temperature change across the gage should be small

$$\frac{T_g - T_{surf}}{T_\infty - T_{surf}} \ll 1. \tag{2.81}$$

If the heat transfer is pure convection, equation (2.81) can be expressed as:

$$\frac{hd}{k} \ll 1 \tag{2.82}$$

Already available on the market is a very thin thermopile sensor, called the Heat Flux Micro-sensor (HFM). The entire sensor is less than 2μm thick. The use of high temperature-temperature thermocouple materials allow operating temperatures over 800°C and heat flux up over 1 kW/m², with no practical upper limit. Because of the thin sensor design, the thermal response time is less than 10 μs so that the frequency response is well above 1 kHz. The high temperature and fast time response capabilities are useful for aerodynamic applications, like combusting flows in jet engines and other propulsion systems but also for capturing high speed events such as shock-waves [7].

For a heat flux gage mounted into the surface, a thermal resistance of the gage can now be defined and is represented by the letter R_g'':

$$R_g'' = \frac{T_1 - T_2}{q_g''} = \frac{d_g}{k_g} \tag{2.83}$$

In order to accurately attach the sensor to the surface, an adhesive layer between the sensor and the material may also be required. In case the sensor is mechanically attached to the surface (for example by a flange and a tightening nut and so forth), there might also be an air gap. Adhesive and air gaps add additional thermal resistances to the system and increase the thermal disruption for the system. Thermal resistances caused by other factors than the sensor are grouped together as the resistance of the surroundings R_{sur}''. The thermal resistance has units of square meters and Kelvin per Watts. The total thermal resistance is then found by assuming a series connection of thermal resistances:

$$R'' = R_g'' + R_{sur}''. \tag{2.84}$$

The thermal resistance through materials (conduction) is defined as:

$$R''_{cond} = \frac{\Delta T}{q''_{cond}} = \frac{d}{k}, \tag{2.85}$$

which can be easily seen in comparison with equation (2.20). The thermal resistance caused by air gaps (convection) on the other hand is given by and can be found by using equation (2.27):

$$R''_{conv} = \frac{\Delta T}{q''_{conv}} = \frac{1}{h}, \tag{2.86}$$

Thus for the resistance of the surroundings it is:

$$R''_{sur} = R''_{cond} + R''_{conv} = \frac{d}{k} + \frac{1}{h}, \tag{2.87}$$

The thermal resistance can also be quantified by measurements. This is done by measuring the sensor temperature and the temperature of the undisturbed surroundings.

For a heat transfer case with fluid temperature T_∞, plate temperature T_{plate} and gage temperature T_g, as shown in Figure 2.9, one can find the heat flux from the plate to the gage by using the total thermal resistance found in equation (2.84) as:

$$q''_{g,cond} = \frac{T_g - T_{plate}}{R''} \tag{2.88}$$

The system shown in Figure 2.9 can thus be modelled as a series connection of two thermal resistances, shown in Figure 2.10.

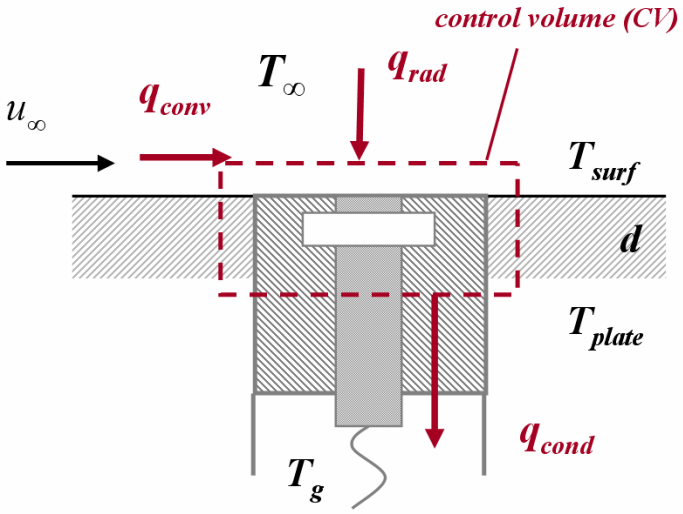

Figure 2.9: Control surface around the heat flux sensor in a combined conduction, convection and radiation environment.

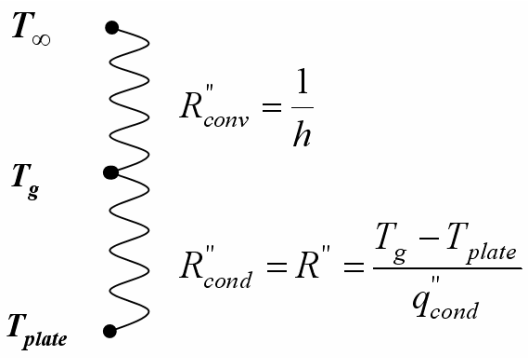

Figure 2.10: Thermal resistance model.

For this combined conduction, convection and radiation heat transfer case, the heat flux to the gage is on the other hand, according to equations (2.6) and (2.8):

$$q''_{g,cond} = h(T_\infty - T_g) + \varepsilon_r \sigma (T_\infty^4 - T_g^4) \tag{2.89}$$

Similarly, the heat flux to the plate is determined by:

$$q''_{plate,cond} = h(T_\infty - T_{plate}) + \varepsilon_r \sigma (T_\infty^4 - T_{plate}^4) \tag{2.90}$$

since T_g and T_{plate} are negligible against T_∞, the radiation contributions from the plate are negligible. Substituting the expression for T_g from equation (2.88) into equation (2.89), we can find through comparison with equation (2.90):

$$\boxed{q''_g = \frac{q''_{plate}}{1 + hR''}} \tag{2.91}$$

A well designed heat flux gage will keep the temperature difference between the gage surface and the plate heat sink to a minimum, because a temperature difference between gage and plate will increase the local heat transfer coefficient, which then will increase the measurement error, which is definitely not desired.

A similar and very important relation as (2.91) can be found for the sensitivity S_g of the sensor. First, from the radiation calibration equations (2.14) and the first part of (2.79):

$$S_{abs} = \frac{S_{incident}}{\alpha}. \tag{2.92}$$

Further, for a combined conduction and convection case it is:

$$S_g = \frac{E_g}{q''_{plate}} \tag{2.93}$$

and $$S_{abs} = \frac{E_g}{q''_g}. \tag{2.94}$$

Thus, combining equations (2.94), (2.93) and (2.91) one obtains.

$$S_g = \frac{S_{abs}}{1 + hR''} \tag{2.95}$$

This equation represents the major scope of this work. It has been tried through stagnation and shear tests to verify this relation.

2.3.1.2 The Schmidt-Boelter Gage

Although the Schmidt-Boelter Gage is a one-dimensional planar heat flux sensor based on the spatial temperature gradient, it is given special consideration in this text, since these type of gages were the major scope of this work. Thus, the Schmidt-Boelter Gages are mentioned in a separate subchapter.

It is credited to E. Schmidt, to make use of the thermoelectric effect in 1924 for the first time, with a sensor that relied on the similar principle as the Schmidt-Boelter gage does today. Practical implementation of the method of temperature measurement in the Schmidt-Boelter gage is generally attributed L. M. K. Boelter in the mid 1950s.

As mentioned above, the Schmidt-Boelter gage represents another method to measure the temperature difference across the thermal resistance layer, which is made of electrically insulating material. The specialty about the Schmidt-Boelter gage is that bare constantan wire, of usually about $2 \cdot 10^{-3}$ inches in diameter is wrapped around the thermal resistance layer, or wafer. For that reason, the sensor is also known as Wire-Wound gage. The wafer is usually made of anodized aluminum. This geometry is illustrated in Figure 2.11.

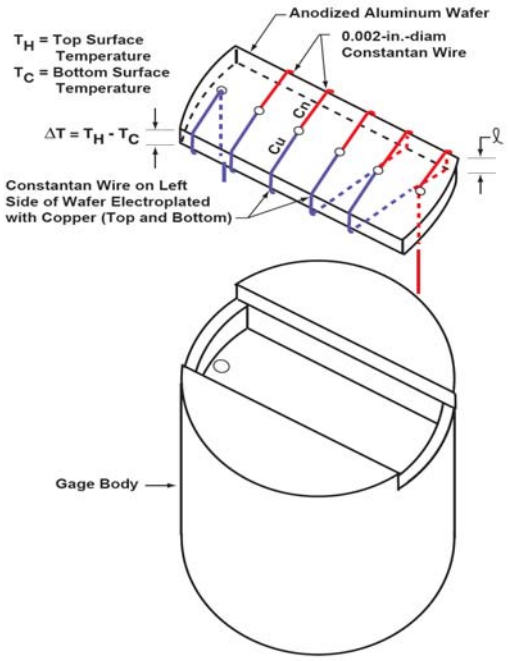

Figure 2.11: Concept sketch of the Schmidt-Boelter gage [6].

The wire/wafer assembly is electroplated with copper, on one side (top and bottom), because copper is one metal besides silver that is thermoelectrically compatible with constantan thermocouple wire. Anodized aluminum has a high thermal conductivity. After plating, the wafer with the wire is placed into the gage body, which works as a heat sink for the sensor. The entire wafer is then surrounded by a potting material (Syncast® 2762) to give a smooth surface to the top of the gage.

Figure 2.12 shows the interior design of the Schmidt-Boelter gage. The basic heat flux sensing mechanism is a temperature gradient developed between the top and the bottom surface of the wafer. The sensitivity is directly proportional to the number of turns of constantan wire wound around the wafer. For N number of turns, we achieve N pairs of thermocouple junctions, i.e. N/2 thermocouples, forming a thermopile. The junctions end and start where the electroplating ends and starts, namely at the top and bottom surface.

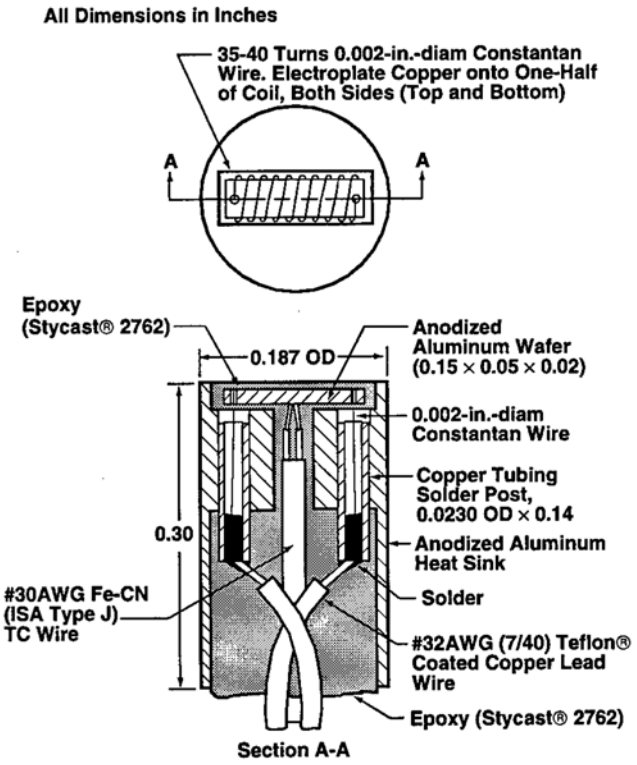

Figure 2.12 Half section sketch of Schmidt-Boelter gage [6].

In this case, the thermoelectric signal is converted with a constantan wire in electrical series with a parallel combination of constantan and copper. For a better definition of the actual gage function, the principle of operation of the Schmidt-Boelter gage can readily be divided into two separate and inherently different categories. These are the thermal and thermoelectric categories. Kidd [6] explains those categories in further detail.

2.3.1.3 Circular Foil Gages

The circular foil gage (or Gardon gage) was originated by Robert Gardon to measure radiation heat transfer (Diller [1]). Later on, it has been modified to measure heat flux in convective flows. Figure 2.13 shows the schematic of such a gage with an example of a temperature distribution on the surface of the gage.

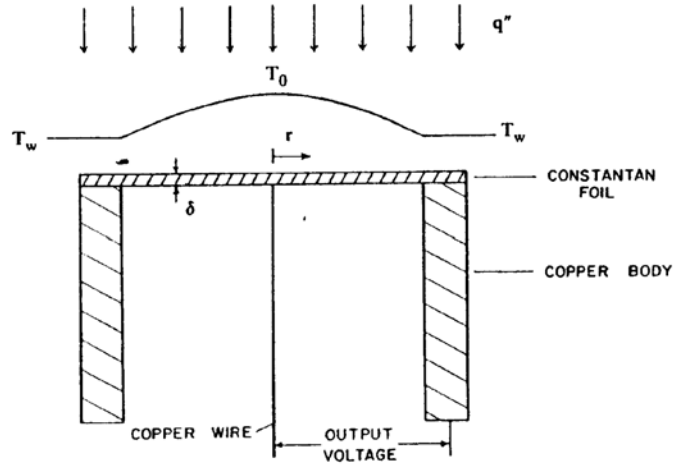

Figure 2.13: Schematic of a circular foil gage [5].

The temperature difference is measured between the center and the edge of the surface-disk using a thermocouple. In this sensor type however, thermal energy is collected by the disk and then transported to the heat sink, connected to the edge of the disk. As a result, the actual measured temperature difference is a function of both the total heat transfer to the disk and the distribution of heat flux over the disk surface. Diller [1] summarizes the solutions for this gage. For uniform radiation heat flux to the gage, the exponential time constant t', is a function of the foil radius and the thermal diffusivity α:

$$t' = \frac{R^2}{4\alpha} \tag{2.96}$$

The central question here is also: What effects appear, when the application is different than the calibration? For example, applications involving convection heat transfer can give different results due to the different temperature distributions on the disk. Unfortunately, this problem is often not addressed.

The analytical solution for the center to edge temperature (T_0 - T_{surf}) difference for radiation and the uniform heat flux case is, given by Diller [5]:

$$T_0 - T_{surf} = \frac{q''_{rad} R^2}{4\pi kd} = \frac{q''_{rad}}{4\pi kd} \tag{2.97}$$

with R as the radius of the gage. For the constant heat transfer coefficient case:

$$T_0 - T_{surf} = \frac{q''_{conv}}{4\pi kd}\left(\frac{1+\lambda^2/16}{1+\lambda^2/8}\right), \tag{2.98}$$

with: $$\lambda^2 = \frac{R^2 h}{k\delta}. \tag{2.99}$$

The additional term in equation (2.98) compared to equation (2.97) shows the influence of convection to the sensitivity. For the same total heat transfer the gage will give less output for the convection case than for radiation because of the different temperature distribution. Once the temperature difference is known, equation (2.77) can be used to obtain heat flux.

If circular foil gages are used to measure convection heat transfer, the temperature difference across the gage ($T_0 - T_{surf}$) must be kept small, because the error of the measurement is a function of the gage geometry, the fluid flow and the heat transfer coefficient. The error becomes particularly large when the convection flow has a shear flow component. This is the case for almost all convection situations.

2.3.2 Sensors based on Temperature Change with Time

There are two major types of solutions used to reduce unsteady temperature to heat flux. These are calorimeters and semi-infinite surface temperature methods.

A calorimeter measures the amount of absorbed thermal energy. The slug calorimeter is based on the assumption that the temperature throughout the sensor is constant over space. The corresponding assumption is that the internal thermal resistance is negligible. This implies a large thermal conductivity of the material. Figure 2.14 shows a slug calorimeter schematic. A is the not-insulated area of the calorimeter.

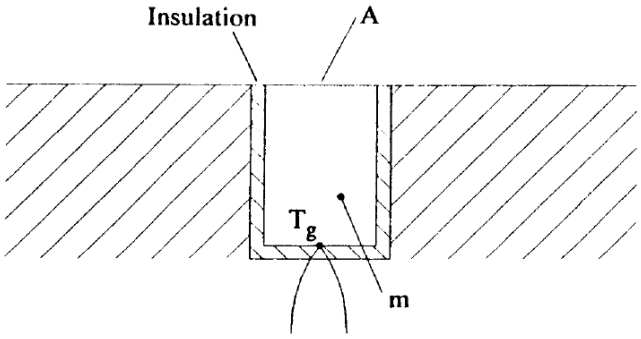

Figure 2.14: Slug calorimeter schematic [5].

Applying equation (2.5) on a control surface around the calorimeter yields

$$q_g^{"} = mc_p \frac{\partial T}{\partial t}, \tag{2.100}$$

with negligible losses, and mc_p is the thermal mass of the calorimeter. According to the type of incoming heat flux, several solutions from equation (2.100) can be obtained. For example, if the heat flux is due to convection with a uniform heat transfer coefficient, the solution is exponential:

$$T_g(t) - T_\infty = (T_i - T_\infty)e^{-t/t'}, \tag{2.101}$$

with T_i as initial temperature and *t'* as the time constant, given by:

$$t' = \frac{mc_p}{hA} \tag{2.102}$$

The assumption of negligible internal resistance is valid, when the Biot number is smaller than 0.1.

$$Bi = \frac{hL}{k} < 0.1 \tag{2.103}$$

The time constant can be found from the temperature response of the system, which can then be used to quantify h from equation (2.102). Although these calorimeters are simple in principle, it is often difficult to obtain reliable results because of heat losses and nonuniform temperatures.

Another method to determine unsteady heat flux is the semi-infinite surface temperature method. For short enough times and sufficiently thick material, it can be assumed that the transfer is one-dimensional and that the thermal effects do not reach the back surface of the material. Then, equation (2.17), will reduce to the one-dimensional, semi-infinite solution, which is simple to implement. For example, the surface temperature for a step change of heat flux at time zero is:

$$T_{surf}(t) - T_i = \frac{2q^{"}}{\sqrt{\pi k \rho c_p}} t^{1/2} \tag{2.104}$$

where T_i is the initial temperature.

There are many methods to convert the measured temperature to a heat flux signal. The easiest is to use the analytical solution with each sampled data point to recreate a heat flux. The most popular equation found by Cook and Felderman (Diller [5]):

$$q^{"}(t_n) = \frac{2\sqrt{k\rho c_p}}{\pi \Delta t} \sum_{j=1}^{N} \frac{T_j - T_{j-1}}{\sqrt{n-j} + \sqrt{n+1-j}} \tag{2.105}$$

Further methods for measuring surface temperature that can be used to determine heat flux are discussed in further detail by Diller [5] The two big groups are temperature measurements using RTDs (=Resistance Temperature Devices) and optical methods (based on interferometers, calorimeters or liquid crystals).

2.4 Radiation Calibration of Schmidt-Boelter Gages

The National Institute of Standardization and Technology (NIST) effort is to develop and validate the in-cavity technique for the calibration of sensors at high radiant heat flux levels.

Murthy [8] describes the experimental in-cavity calibration method using high-temperature, graphite-tube cylindrical cavities. Figure 2.15a shows a schematic layout of the 25- and the 51 mm diameter variable-temperature blackbodies (VTBB) used in the experiments. Both blackbodies have cylindrical cavities, with thermally insulated and electrically heated graphite walls. Direct resistance heating of the cavity walls using large ac currents at low voltages provides quick heating and cooling.

The calibration can be done by either the transfer calibration using the 25-mm-diameter VTBB with the meter outside the cavity (outside cavity calibration, Figure 2.15b) or the in-cavity calibration in both the 25 and 51 mm diameter VTBB, with the meter inserted into the heated cavity (Figure 2.15c). An optical pyrometer measures the center partition temperature by sensing radiation from tone end of the black-body. A proportional-integral-differential controller regulates the power supply to maintain the furnace temperature to within +/- 0.1 K of the set value. The meter under test and the reference radiometer receive radiant heat flux from the other side of the cavity partition. A low-velocity flow of argon gas purges the heated cavities during operation to minimize graphite erosion.

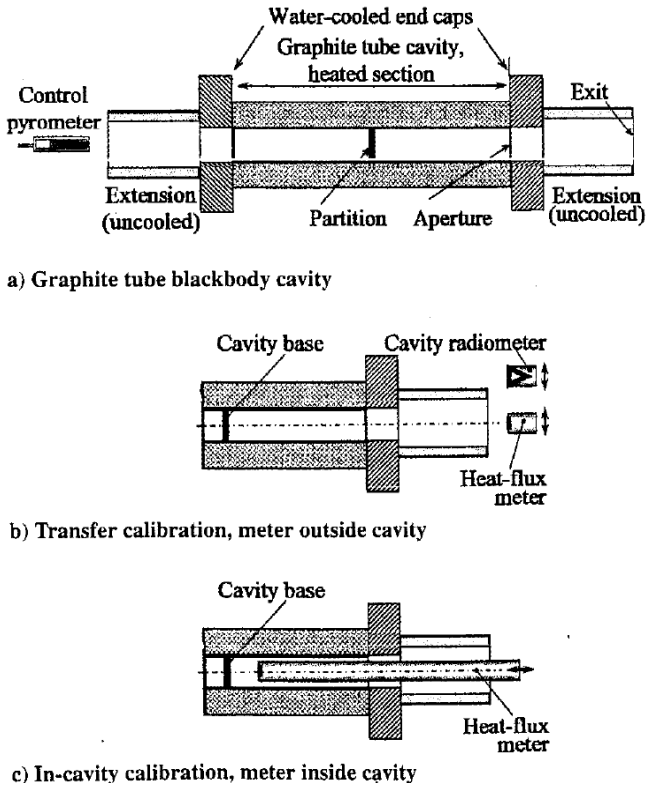

Figure 2.15: Layout of the 25- and 51-mm-diameter VTBB and heat-flux meter location for calibrations [8].

The sensor head of the Schmidt-Boelter gages is mounted at the front end of a 63.5 cm long, 12.7 mm diameter water cooled body (Figure 2.16). The sensing surface has a black coating with an absorptance value of 0.92 over the sensing area. The annular region around the high-absorptance coating is polished copper surface to achieve a high effective emissivity at the sensing surface when placed inside the blackbody cavity. The long stem of the water-cooled body facilitates placing the sensing surface of the meter inside the heated blackbody cavity. The recommended cooling water flow rate is 0.6 l/m. The long stem is made of copper with the outer surface highly polished. A type K thermocouple mounted on the tip of the sensor portion of the meter helps in monitoring the surface temperature rise when exposed to the radiant heat flux.

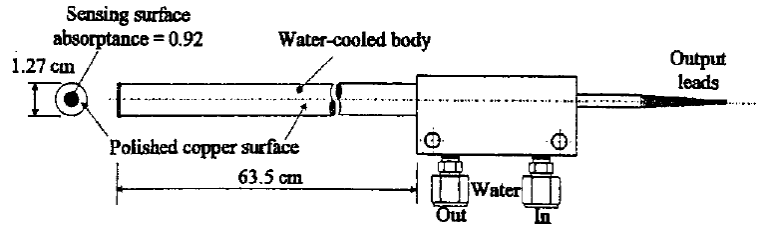

Figure 2.16: Mounting of SB gages [8].

The NIST Transfer Calibration technique in 25 mm VTBB is currently in use for calibrating heat-flux meters of 50 kW/m². The technique uses a room-temperature electrical substitution radiometer (ESR) as a transfer standard. The radiometer calibration is traceable to measurements performed with the high-accuracy cryogenic radiometer (HACR), the U.S. standard for optical power. The heat-flux meter to be calibrated and the transfer standard radiometer, placed a distance of 12.5 mm from the 25 mm VTBB exit, received equal amount of radiant heat flux from the blackbody cavity.

The in-cavity calibration requires calculation of the incident radiant heat flux at the active sensing region of the gage. Both the cavity wall and the test gage's exposed surface participate in the radiant exchange contributing to the incident radiant heat-flux level at the meter's active area. The active sensing area of the meter receives radiant heat flux over the full hemispherical field of view. The assumption of unity emissivity, used in calibrations to calculate the incident heat flux for meters mounted outside the cavity, is not valid for meter locations inside the cavity.

Calibration results usually show the measured output voltage of the test meter against the calculated blackbody radiant heat flux using the Stefan-Boltzmann equation, assuming an effective emissivity of unity. In contrast to the transfer calibration, the linear regression analysis of the in-cavity data shows a small nonzero intercept at a zero radiant heat-flux level. This intercept is attributed to heat flux arising from non-radiative effects. These effects can be very pronounced and is a major problem when calibrating at low-heat-flux levels. Convection heat transfer, in particular, can be a significant portion of the total heat flux causing nonlinearity of the gage response when plotted against the calculated radiant heat flux. However, at high-heat-flux levels, as in the present case, the effect of non-radiant contributions to the heat transfer at the meter remains nearly the same when the radiant heat flux is varied from the lowest heat-flux level of 75 kW/m² at 800°C to the highest heat-flux level of 500 kW/m² at 1450°C. Therefore, the slope calculated by the linear regression is a reliable indicator of the gage response to the radiant heat-flux.

In the NIST transfer technique, the heat-flux meter receives radiant heat flux close to normal viewing conditions. However, the same meter placed inside the cavity, in the absence of a view restricor as in the present experiment, receives radiant heat flux over the full hemispherical field of view. For a truly Lambertian meter with a cosine angular response, the responsivity measured by the two techniques should agree. the angular response of the gage

depends on the properties of the high-absorptance coating on the sensing surface and on the substrate material. For the SB-type gage with the particular coating used, the ratio of hemispherical to normal absorptance was 0.967. The in-cavity responsivity values for SB-type gages are lower than the transfer calibration results, suggesting the angular response effects in the in-cavity measurements. Assuming a correction factor of 0.967 largely accounts for the 2.7% lower responsivity of the SB meter obtained in the 25mm VTBB tests, with only effective emissivity correction.

The in-cavity technique using high-temperature cylindrical-graphite blackbody cavities is feasible. The most desirable location for the meter inside the cavity is about a cavity radius away from the cavity base. The value of the emissivity, which determines the level of incident radiant heat flux at the meter is highest in this region. The in-cavity measured responsivity values covering the full design range of the meter, when corrected for the effective emissivity and possible convections effects, show good agreement with the flux-based transfer calibration results obtained over a limited range of the meter. The good agreement between responsitivity values measured by the two different calibration methods establishes the equivalence between the temperature and radiant flux standards.

3 Convection Calibration Facility

A calibration facility has been designed and developed in order to calibrate the Schmidt-Boelter gages for heat transfer in shear and stagnation flow. This chapter gives a complete description of the convection calibration facility, the equipment used, and the experiments itself. It is divided into sections explaining the overall facility setup and the components, as there are the air heater, the stagnation test stand and the shear test stand. The data acquisition system, the experimental procedures, data reduction and error analysis is explained in detail.

3.1 Overall Facility Setup

The setup for this experiment was assembled in the Complex Thermo-Fluids Systems Laboratory at Virginia Polytechnic Institute and State University (Virginia Tech). The convection calibration facility consists of a high pressure air supply, an air heater, the stagnation flow test bed and the shear flow test bed, two data acquisition units (DAQ), as interfaces between the transducers and a computer (CPU), which is needed to sample and store the data. A schematic of the overall facility setup is illustrated in Figure 3.1. For cooling

purposes in between the tests, an ordinary box fan has been used. Figure 3.2 shows a picture of the convection calibration facility and the white box fan in the background.

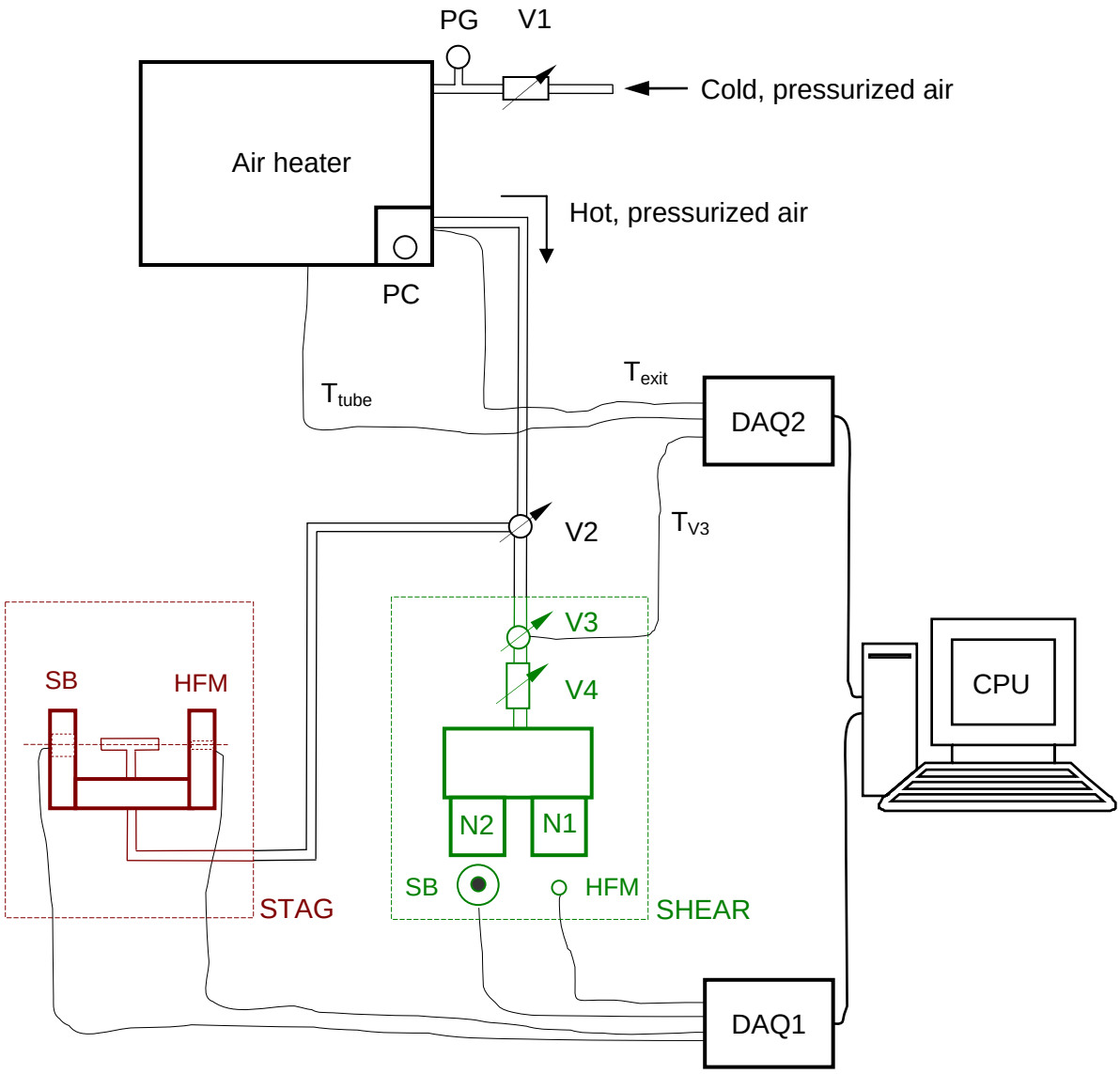

stagnation test stand (q_{HFM}, q_{SB}, T_{plate1}, T_{plate2}, T_{air})

shear test stand (q_{HFM}, q_{SB}, T_{plate1}, T_{plate2}, T_{air1}, T_{air2})

Figure 3.1: Schematic of the convection calibration facility.

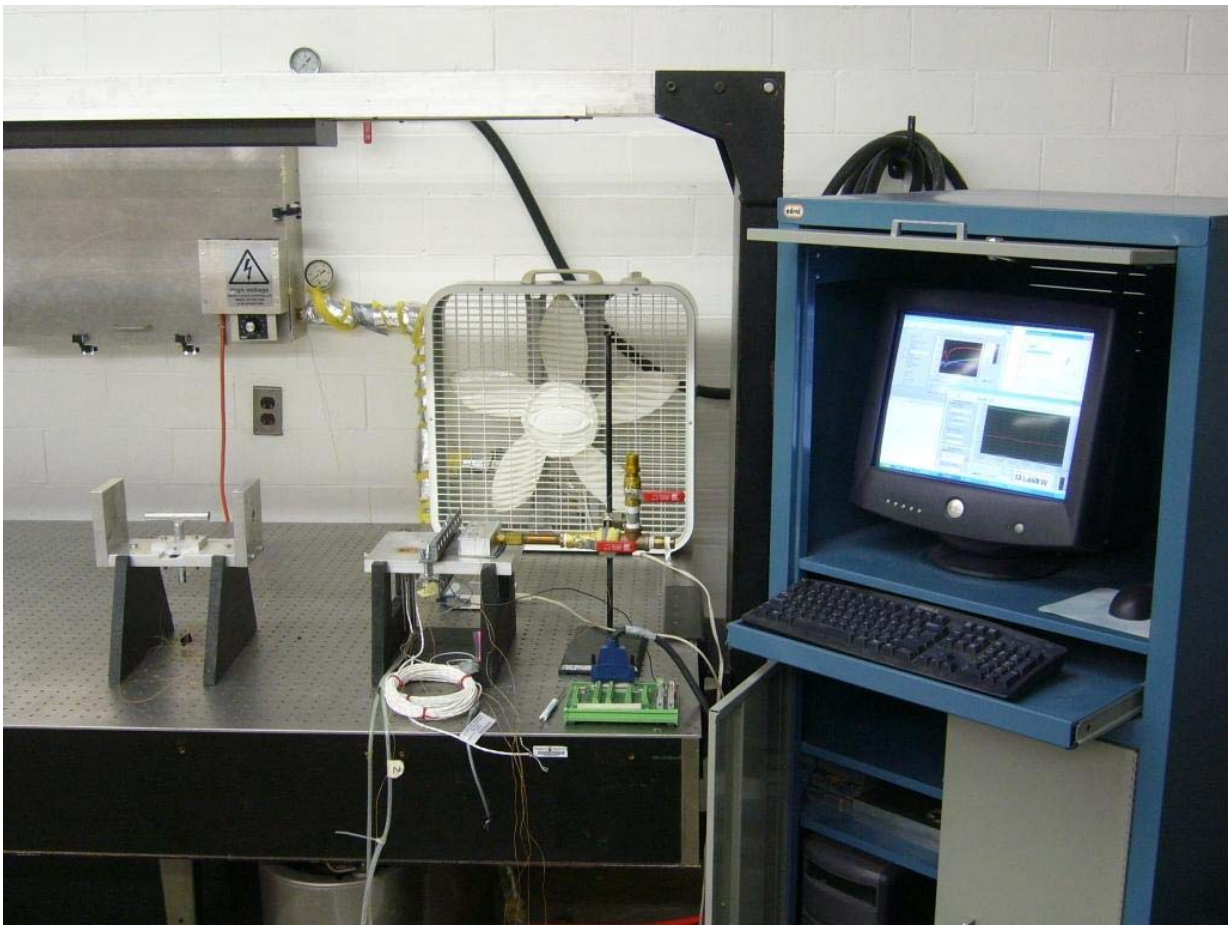

Figure 3.2: Photo of the convection calibration facility in the CTFS-Laboratory at Virginia Tech.

The compressed air supply with maximum of about 60 psi (414 kPa) is directly connected to the facility with a Valve (V1). This valve allows the user to set the desired pressure, at which the experiment will be conducted. A pressure gage (PG) helps to set the pressure accurately. After the pressure gage, the air flows into the air heater. By using the power controller (PC) of the air heater, the desired temperature of the air can be adjusted precisely. The air heater consists of a copper tube, a high temperature heater tape, which is wrapped around the tube and the power controller, as mentioned above. Valve two (V2) serves as switch to either use the shear (SHEAR) or the stagnation stand (STAG).

For the shear stand, the Schmidt-Boelter gages (SB) are surface mounted into a horizontally supported and isolated plate and precisely aligned at the middle of the exit of one of the nozzles (N1, for example). At the exit of the other nozzle (N2, for example), the reference standard, in our case the HFM (Heat Flux Micro-sensor), is mounted into the same plate. For the stagnation stand, the SB gages are mounted into one vertically supported plate on one side of the tee orifice and on the other side of the tee orifice the HFM is mounted into the second plate.

One of the data acquisition units (DAQ1), samples the data from the shear or the stagnation stand. The attained data for the shear stand included the signal of the HFM, the SB gage signal, the plate temperatures (T_{plate1}, close to the HFM and T_{plate2}, close to the SB), the temperatures in the box of the shear stand on both sides of the nozzle inlets (T_{air1} for the side of the box, at which the HFM is located and T_{air2} for the side of the box, at which the SB is located). The data for the stagnation stand was gathered analogous: the signal of the HFM, the SB gage signal, the plate temperatures (T_{plate1}, at the side of the HFM and T_{plate2}, at the side of the SB) and the air temperature (T_{air}), which was measured inside of the tee nozzle.

The other data acquisition unit (DAQ2) is a real time DAQ to monitor temperatures of the air heater directly at the copper tubing (T_{tube}), at the exit of the heater (T_{exit}) and at the overpressure valve (V3). In order to direct the air flow though the box and the nozzle of the stagnation stand, V3 has to be closed an valve four (V4) must be open. DAQ1 is connected via LPT with the CPU, DAQ2 via USB. The data sampling was carried out with LabVIEW®.

The second set of experiments, conducted with the SB gages included water cooling of the housing of the gages. This test setup is sketched in Figure 3.3. Figure 3.4 shows picture with the white water container on the ground.

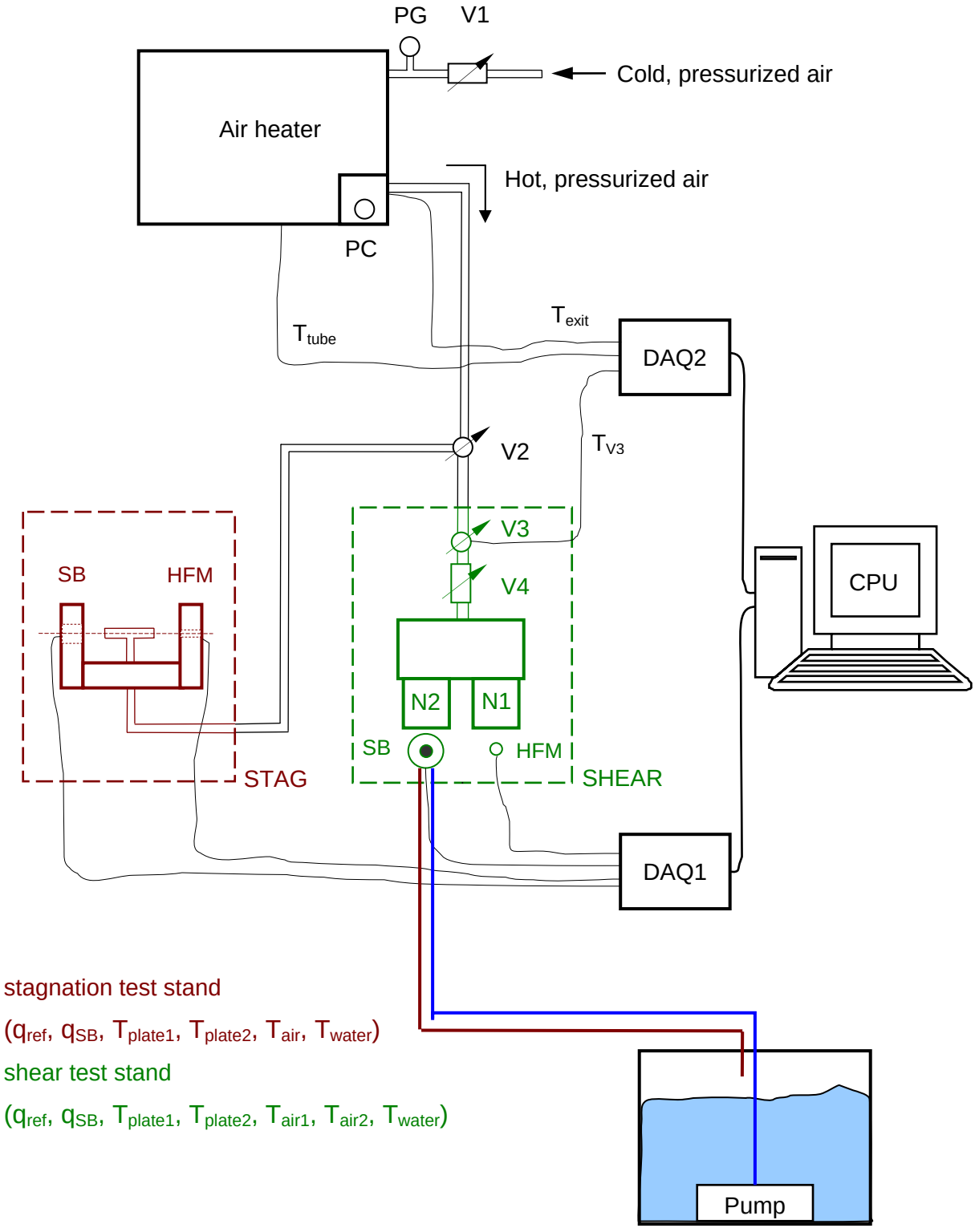

Figure 3.3: Schematic of the convection calibration facility with water cooling.

Figure 3.4: Photography of the convection calibration facility with water cooling in the CTFS-Laboratory at Virginia Tech.

3.2 Overview of Used Gages

Four different Schmidt-Boelter gages have been examined. They were provided by SANDIA National Laboratories (at Albuquerque, NM) and included two one-inch in diameter and two one-and-one-half-inches in diameter sensors. For the reference standard the in-house HFM (Heat Flux Micro-sensor) has been used, known to be little affected by convectional components of heat transfer. Since the working principle has already been explained in section 2.3.1, the following subsections and tables are to give a brief and complete overview of the data of the gages used.

3.2.1 One-inch Schmidt-Boelter Gages

Manufacturer	MEDTHERM Corporation		
Serial Number	137861		
Model Number	64-30SB-20K-6MgO-20-20747		
Window	none		
Absorptance (α)	0.94		
Incident Parameters		English	SI
	Maximum Output	20.30mV @ 30 $\frac{\text{Btu}}{\text{ft}^2\text{s}}$	20.30mV @ 34.1 $\frac{\text{W}}{\text{cm}^2}$
	Sensitivity (S)	0.677 $\frac{\text{mV}}{\text{Btu/(ft}^2\text{s)}}$	0.596 $\frac{\text{mV}}{\text{W/cm}^2}$
Absorbed Parameters		English	SI
	Maximum Output	22.07mV @ 30 $\frac{\text{Btu}}{\text{ft}^2\text{s}}$	22.07mV @ 34.1 $\frac{\text{W}}{\text{cm}^2}$
	Sensitivity (S) $S_{abs} = \frac{S_{incident}}{\alpha}$	0.736 $\frac{\text{mV}}{\text{Btu/(ft}^2\text{s)}}$	0.648 $\frac{\text{mV}}{\text{W/cm}^2}$

Table 3.1: 1.0 in. SB SN 137861 data. The highlighted value S_{abs} in SI units has been used for calibration purposes, (1Btu = 1055.06J, 1ft = 0.305m).

Manufacturer	MEDTHERM Corporation		
Serial Number	137864		
Model Number	64-50SB-20K-6MgO-20-20747		
Window	none		
Absorptance (α)	0.94		
Incident Parameters		English	SI
	Maximum Output	22.35mV @ 50 $\frac{\text{Btu}}{\text{ft}^2\text{s}}$	22.35mV @ 56.8 $\frac{\text{W}}{\text{cm}^2}$
	Sensitivity (S)	0.447 $\frac{\text{mV}}{\text{Btu/(ft}^2\text{s)}}$	0.394 $\frac{\text{mV}}{\text{W/cm}^2}$
Absorbed Parameters		English	SI
	Maximum Output	24.29mV @ 50 $\frac{\text{Btu}}{\text{ft}^2\text{s}}$	24.29mV @ 56.8 $\frac{\text{W}}{\text{cm}^2}$
	Sensitivity (S) $S_{abs} = \frac{S_{incident}}{\alpha}$	0.486 $\frac{\text{mV}}{\text{Btu/(ft}^2\text{s)}}$	0.428 $\frac{\text{mV}}{\text{W/cm}^2}$

Table 3.2: 1.0 in. SB SN 137864 data. The highlighted value S_{abs} in SI units has been used for calibration purposes, (1Btu = 1055.06J, 1ft = 0.305m).

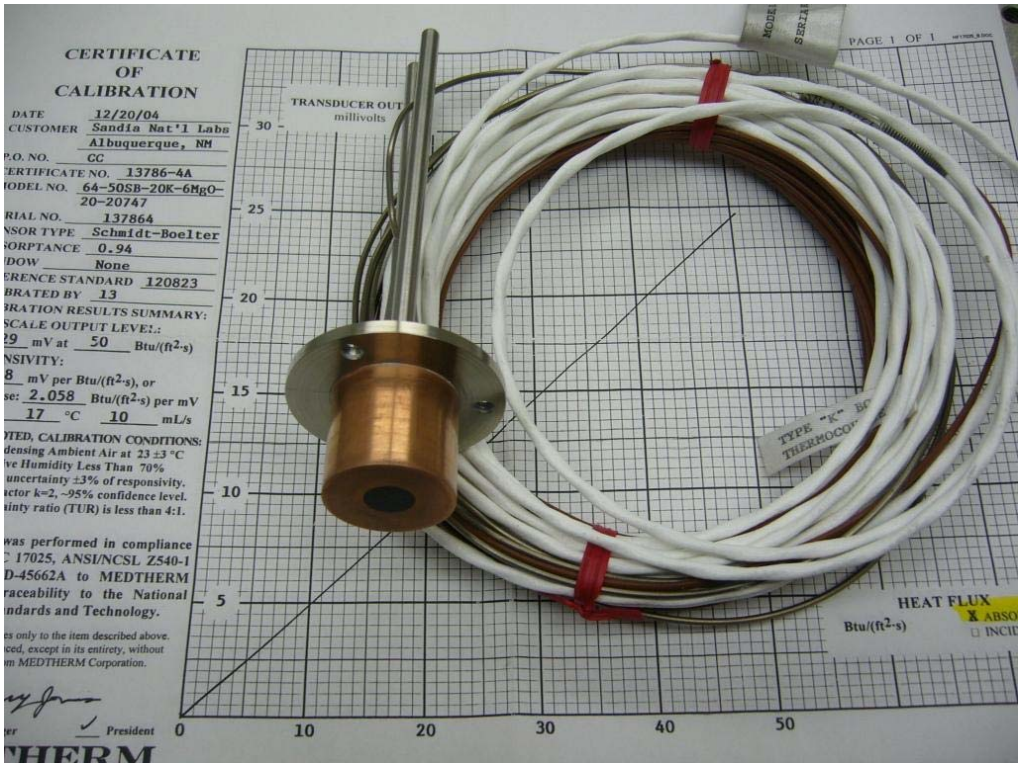

Figure 3.5: Top view of a 1.0 in. SB gage. The tubes on the bottom side of the gage are connections for the water hoses.

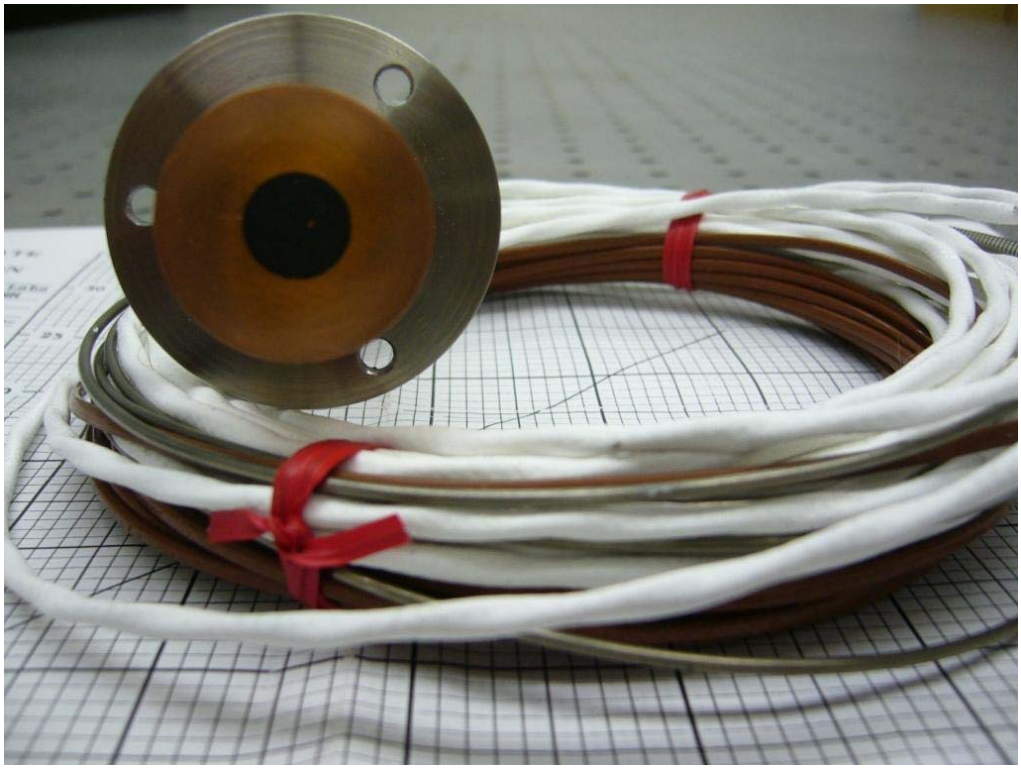

Figure 3.6: Front view of a 1.0 in. SB gage. The black area is the heat flux sensing area .

3.2.2 One-and-one-half-inch Schmidt-Boelter Gages

Manufacturer	MEDTHERM Corporation		
Serial Number	142781-T		
Model Number	96-15T-15RP(ZnSe)-360-21745		
Window	none		
Absorptance (α)	0.94		
Incident Parameters		English	SI
	Maximum Output	9.6mV @ 13.2 $\frac{\text{Btu}}{\text{ft}^2\text{s}}$	9.6mV @ 15 $\frac{\text{W}}{\text{cm}^2}$
	Sensitivity (S)	0.727 $\frac{\text{mV}}{\text{Btu/(ft}^2\text{s)}}$	0.640 $\frac{\text{mV}}{\text{W/cm}^2}$
Absorbed Parameters		English	SI
	Maximum Output	-	-
	Sensitivity (S) $S_{abs} = \frac{S_{incident}}{\alpha}$	0.773 $\frac{\text{mV}}{\text{Btu/(ft}^2\text{s)}}$	0.681 $\frac{\text{mV}}{\text{W/cm}^2}$

Table 3.3: 1.5 in. SB SN 142781T data. The highlighted value S_{abs} in SI units has been used for calibration purposes , (1Btu = 1055.06J, 1ft = 0.305m).

Manufacturer	MEDTHERM Corporation		
Serial Number	142782-T		
Model Number	96-15T-15RP(ZnSe)-360-21745		
Window	none		
Absorptance (α)	0.94		
Incident Parameters		English	SI
	Maximum Output	$11.2\text{mV} @ 13.2 \frac{\text{Btu}}{\text{ft}^2\text{s}}$	$11.2\text{mV} @ 15 \frac{\text{W}}{\text{cm}^2}$
	Sensitivity (S)	$0.834 \frac{\text{mV}}{\text{Btu/(ft}^2\text{s)}}$	$0.735 \frac{\text{mV}}{\text{W/cm}^2}$
Absorbed Parameters		English	SI
	Maximum Output	-	-
	Sensitivity (S) $S_{abs} = \frac{S_{incident}}{\alpha}$	$0.887 \frac{\text{mV}}{\text{Btu/(ft}^2\text{s)}}$	$0.782 \frac{\text{mV}}{\text{W/cm}^2}$

Table 3.4: 1.5 in. SB SN 142782T data. The highlighted value S_{abs} in SI units has been used for calibration purposes , (1Btu = 1055.06J, 1ft = 0.305m).

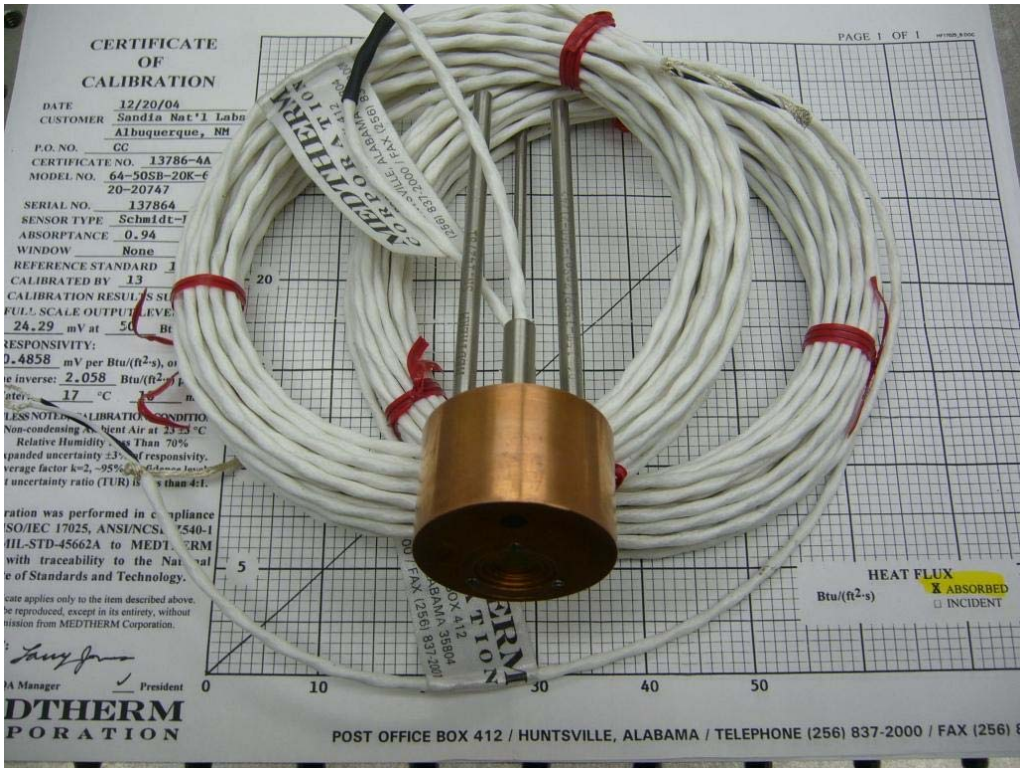

Figure 3.7: Top view of a 1.5 in. SB gage.
The tubes on the bottom side of the gage are connections for the water hoses.

Figure 3.8: Front view of a 1.5 in. SB gage. The black area is the heat flux sensing area. The black area behind the window is the heat flux sensing are for radiation.

3.2.3 Heat Flux Micro-sensor

Manufacturer			
Serial Number	2033		
Model Number			
Window	none		
Absorptance (α)	0.94		
Incident Parameters		English	SI
	Maximum Output		
	Sensitivity (S)	$0.219 \frac{\text{mV}}{\text{Btu/(ft}^2\text{s)}}$	$0.193 \frac{\text{mV}}{\text{W/cm}^2}$
Absorbed Parameters		English	SI
	Maximum Output	-	-
	Sensitivity (S) $S_{abs} = \frac{S_{incident}}{\alpha}$	$0.233 \frac{\text{mV}}{\text{Btu/(ft}^2\text{s)}}$	$0.205 \frac{\text{mV}}{\text{W/cm}^2}$

Table 3.5: HFM data. The highlighted value S_{abs} in SI units has been used for calibration purposes , (1Btu = 1055.06J, 1ft = 0.305m).

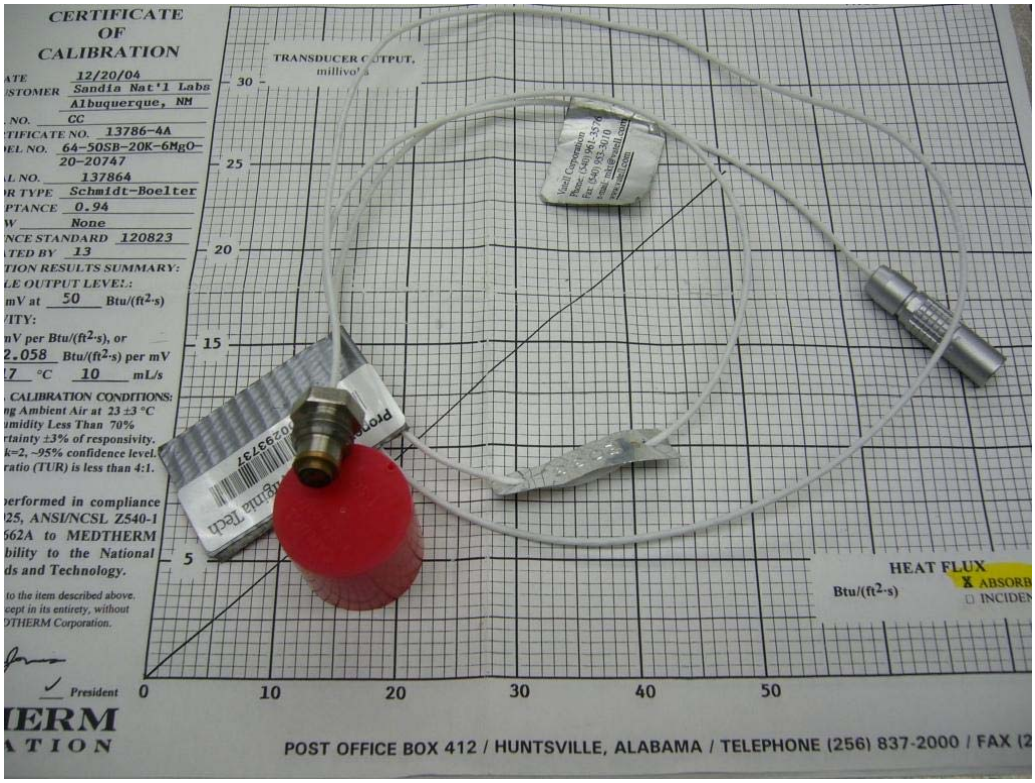

Figure 3.9: Top view of the HFM.

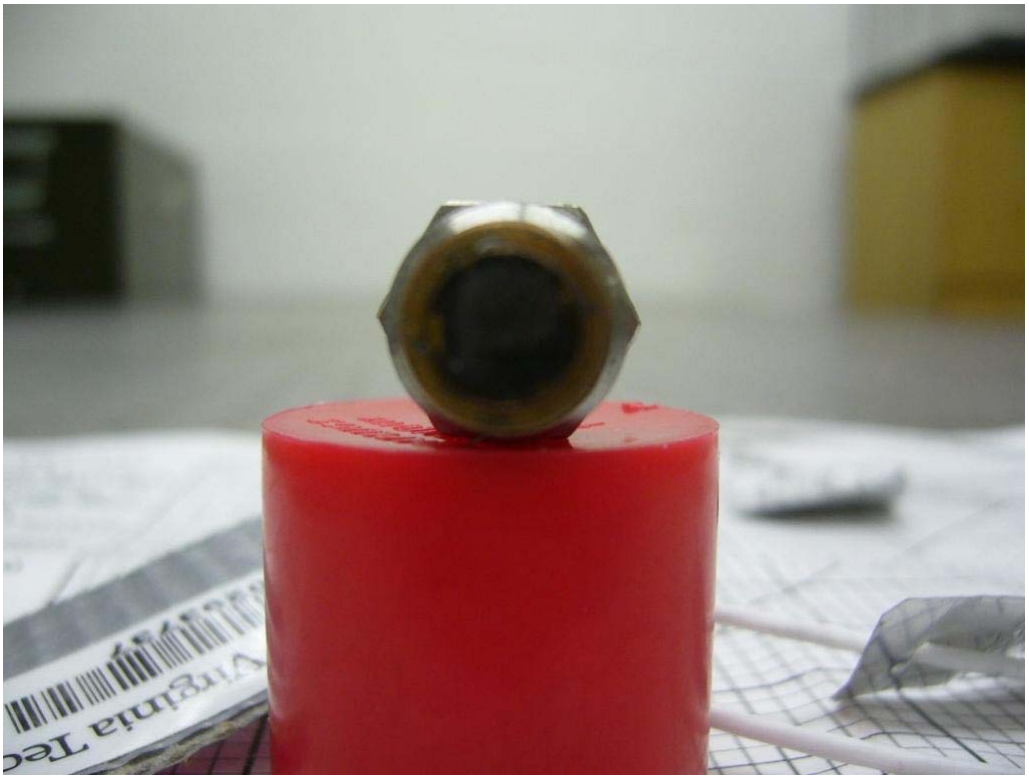

Figure 3.10: Front view of the HFM. The black area is the heat flux sensing area

3.3 Air Heater

In order to heat up the air flow, an air heater was needed that would provide an exit air temperature of at least 150 °C over a pressure range of 1 psi to at least 40 psi (6.9 kPa to at least 275.8 kPa), measured *before* the heater. In this section, the design (and the design process) of the heater is described in greater detail.

The design is simple and thus reliable. In order to achieve constant heat flux over a longer period of time, it was designed to convert electric energy directly into thermal energy, without using water as a medium, as done in the previous design [9]. The main elements of the heater were to be chosen as a 0.5 in. in inner diameter soft copper tube and a heater tape which is wrapped around the tubing (Figure 3.12).

By knowing a maximum volumetric flow rate of 65 ft^3/min (i.e. mass flow rate of 0.037 kg/s and density of air at room temperature of 1.2 kg/m^3), a specific thermal heat of air at room temperature of 1006 J/(kgK), the inlet temperature of 20 °C and an outlet temperature of 150 °C, the required thermal power was calculated to be:

$$q_{req} = \dot{m} c_p \left(T_{in} - T_{out}\right) = 1.87kW \tag{3.1}$$

As heating element, a "HTS/Amptec heavy Amox® insulated heater tape (AWH-051-080D)" was chosen, with a length of eight feet and width of 0.5 in. and is designed for 120 V (624 W). The heavy Amox® insulation allows the heater tape to be mounted on metal or other conductive surfaces and is secure to heat up to a temperature of 1400 °F (760 °C). The power density (or heat flux) provided by this heating element is thus given as:

$$q''_{tape} = \frac{P_{tape}}{L_{tape} w_{tape}} = 13 \frac{W}{in^2} = 20.15 \frac{kW}{m^2}, \tag{3.2}$$

since:

$$q_{req} = q''_{tape} L_{actual} c_{pipe} \tag{3.3}$$

the actual length of this heating element needed would then be, by using the result of (3.1) and (3.3):

$$L_{actual} = \frac{q_{req}}{q''_{tape} c_{pipe}} = \frac{q_{req}}{q''_{tape} \pi D_{pipe}} = 5.88m \approx 20\,ft\,. \tag{3.4}$$

Dividing this length, by the length of one heating element, the amount of heating tapes needed would then be 2.5; hence, three heater tapes of the type mentioned above have been installed. Because each of the tapes require the same voltage of 120 V in order to operate properly, they were connected in parallel, consuming a total current of 15.6 A.

The power module and the control potentiometer provide the control. The control potentiometer is connected in series with the load (heater tapes). The control potentiometer allows the user to set the exit temperature accurately for a given pressure (which determines mass flow rate), measured at the entrance of the air heater. Table 3.6 shows the required controller settings for a given pressure, cross listed with the exit temperatures. The user should be aware of the fact that the whole system should be at steady state to use the given settings. The time that it takes for the calibration system to be at steady state depends on the length of the air hoses. For the lower pressures, higher exit temperatures can be achieved than the values given in the table. For pressures above 25 psi, there are only exit temperatures below 100 °C provided. Besides the exit temperature, there was also the copper coil temperature monitored, it was tried not to exceed a copper coil temperature of 250 °C. By using the given table below, the tubing temperature will not exceed 180 °C.

Finally, an aluminum box was constructed around the copper tubing. Later on, the copper tubing with heater tape was insulated with glass fiber foam. Figure 3.11 shows the exterior view of the air heater with the power module; Figure 3.13 shows the copper tubing with insulation.

Pressure [psi]	Power setting [%]	Exit Temperature [°C]
1	50	100
3	58	100
5	62	100
10	70	100
15	80	100
20	88	100
25	100	88
30	100	85
35	100	82

Table 3.6: Required controller settings in per cent for a given pressure, cross listed with the achieved heater exit temperature at steady state conditions.

Figure 3.11: Exterior view of the air heater with power module and control potentiometer.

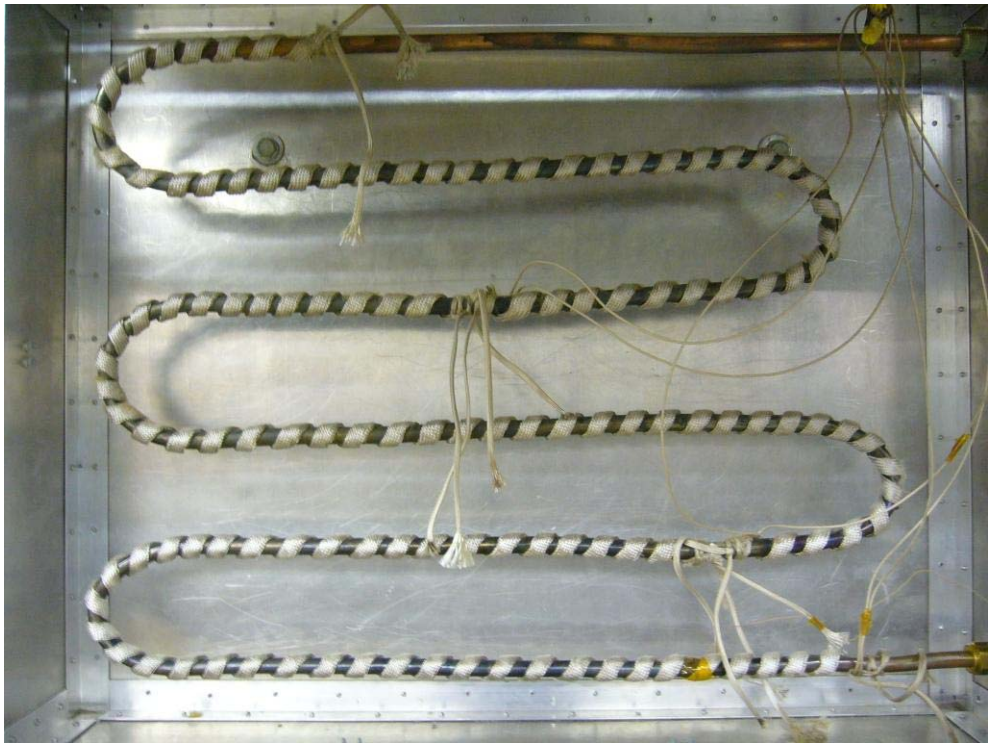

Figure 3.12: Interior view of the air heater: Copper coil with heater tape.

Figure 3.13: Heater interior with glass fiber foam.

SAFETY ADVICE

1) **The power module may not be touched at any time during operation, due to components under high voltage.**

2) **At any time during operation, there has to be a minimum air flow under at least 3 psi through the heater.**

3) **After use, the air heater has to be unplugged.**

3.4 Shear Stand

A detailed explanation of the shear stand design, performance and placement of the thermocouples is given in this section as well as the test procedure for the shear stand.

3.4.1 Shear Stand Design

The shear stand was designed to provide high convective and turbulent air flow across the SB gages mounted flush with the plate surface after the nozzle exit. The heated air coming from the air heater is directed in the shear stand box and then through the nozzles over a flat plate. The nozzle orifice dimensions were width x height = 12 mm x 2.4 mm. The box was designed to sustain a pressure of about 80 psi. A rough estimation was done (see C1 Shear Stand Design") and the required number of screws was determined to be six for the given material properties of the screws and a safety factor of 9.3. Since the nozzles were designed for a pressure of up to 143 psi with a thinnest material thickness of 0.15 in., the thickness of the front plate and the plenum was also taken to be 0.15 in. (see C2 Shear Stand Drawings). Additionally a gasket had to be used to seal the gap between the lid and the box (Figure 3.18).

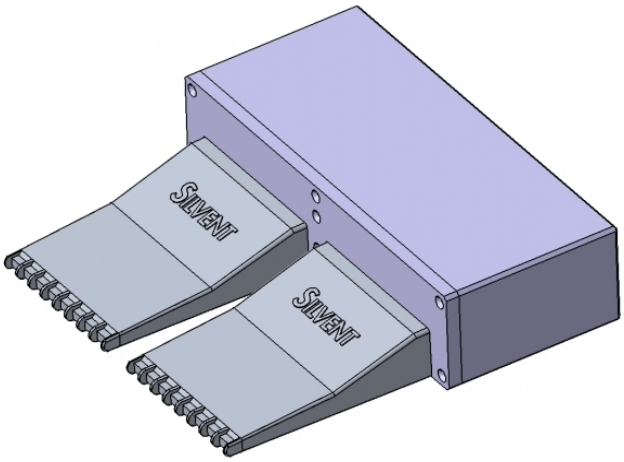

Figure 3.14: Shear stand with nozzles.

Figure 3.14 shows the shear stand box with the nozzles; Figure 3.15 shows the complete shear stand. The box was clamped on a plate with a flush surface mounted 1.5in SB gage and HFM. The support (black) is made of wood for insulation purposes.

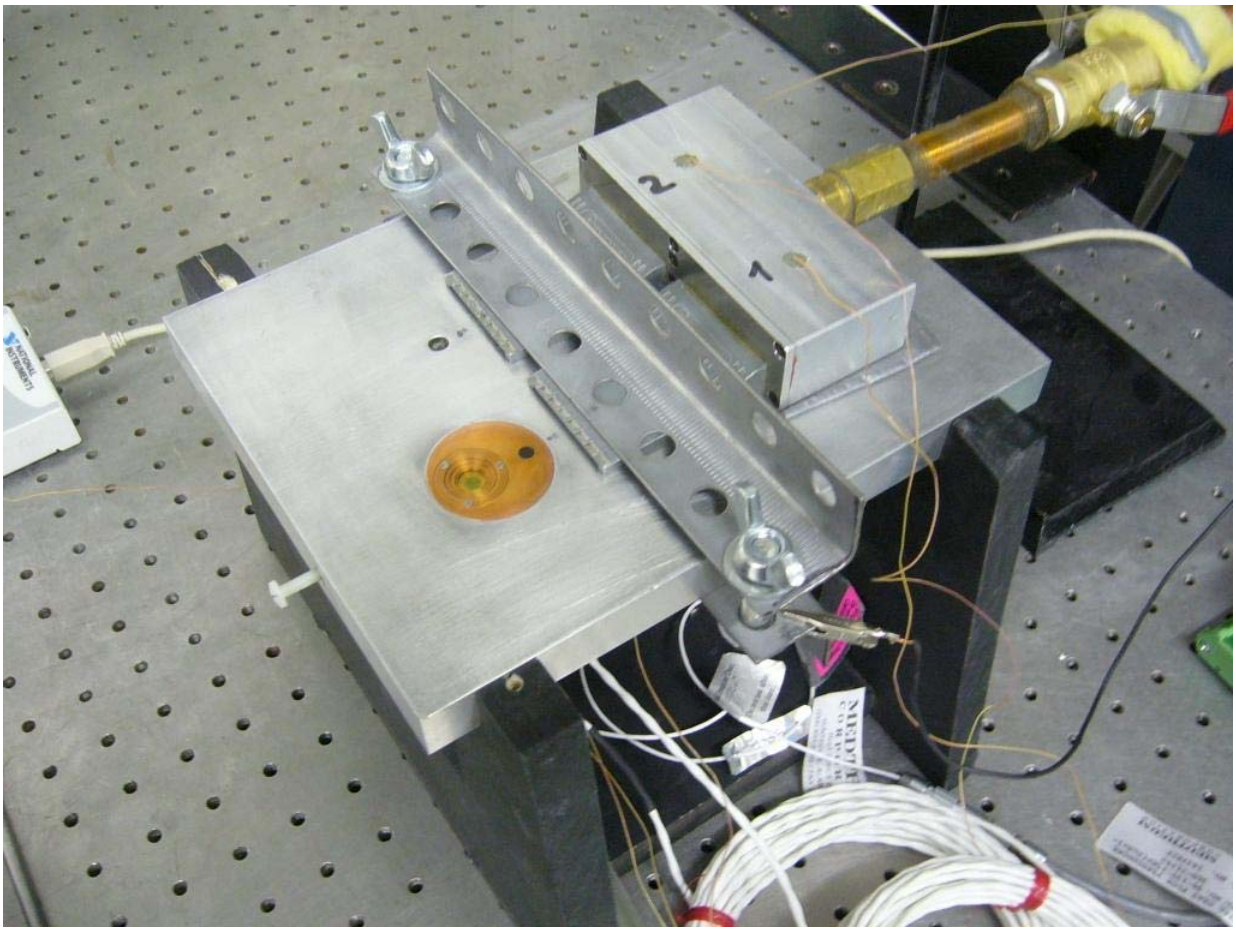

Figure 3.15: Shear stand clamped on a plate with a flush surface mounted 1.5 in. SB gage and HFM.

3.4.2 Shear Stand Performance

The stand was designed to provide the same air flow through both nozzles. After doing some initial tests, with two HFMs, it was found that the flows were different from side to side. Total pressure measurements were also done to quantify the flow differences at the nozzle exits. Figure 3.16 illustrates the setup to measure pressures at the exit of the nozzles with pressure transducers and small tubes, feeding the air into the transducers. The small tubes were moved along the nozzle cross section at positions of 25%, 50% and 75% of the width of the nozzle and at the same distance away from the nozzle of 20 mm. The tests were conducted over a range of pressures. Figure 3.17 shows the pressure variation along the nozzle cross sections compared side to side at 15 psi inlet air pressure.

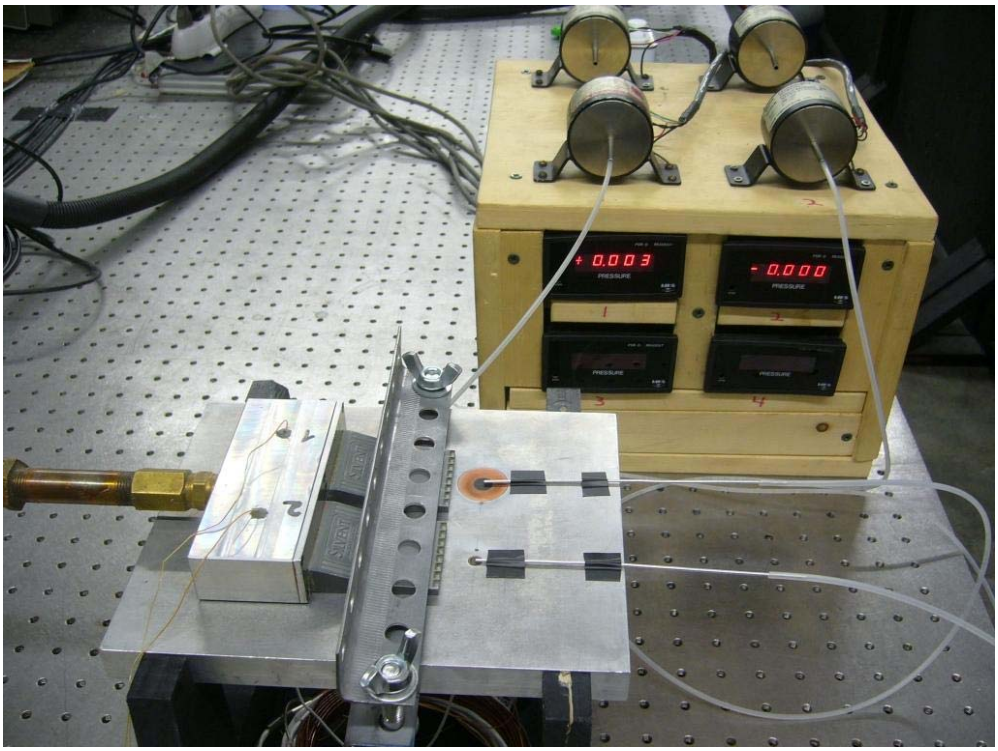

Figure 3.16: Setup to measure the nozzle exit pressures with pressure transducers and small pressure tubes. The setup has been reconstructed.

Nozzle 1 (N1) is the nozzle on the left hand side of the box in flow direction, nozzle 2 (N2) is the nozzle on the right hand side of the box in flow direction. (For labelling see Figure

3.15 or Figure 3.1 or Figure 3.3). The pressure values were averaged over a period of 90 seconds. Table 3.7 shows a quantitative comparison. The results show that there was a total pressure difference between nozzles and also within each nozzle.

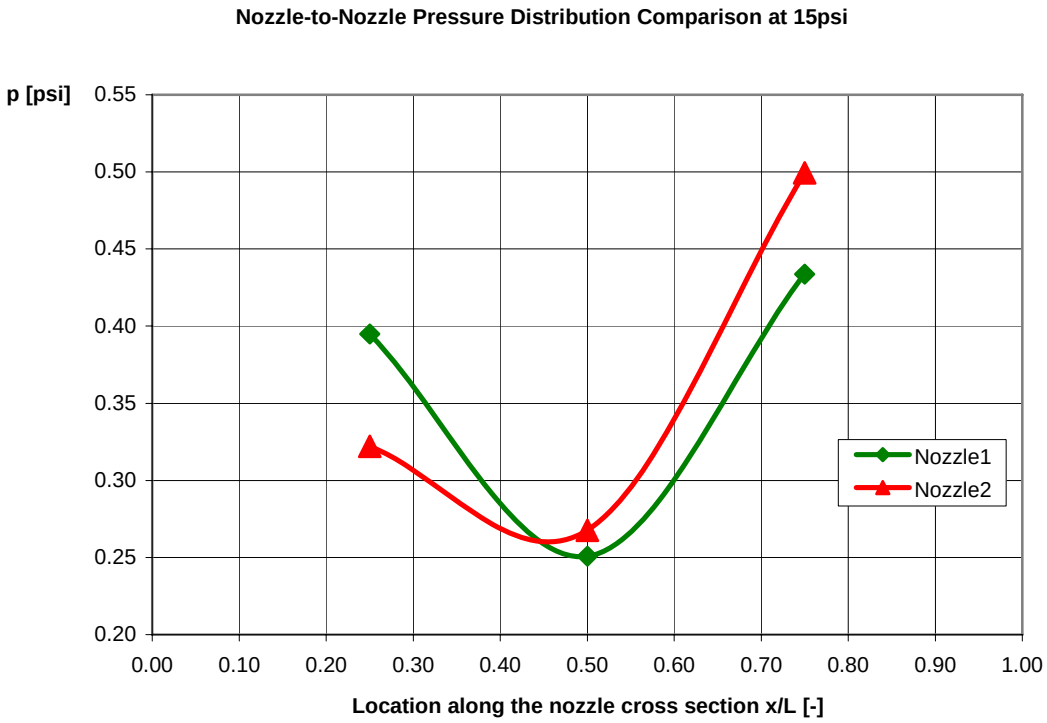

Figure 3.17: Pressure variations along the nozzles cross sections compared side to side. Detailed explanations see text.

Location x/L [-]	Pressure N1 [psi]	Pressure N2 [psi]	%Difference [-]
0.25	0.3950	0.3222	18.43
0.50	0.2508	0.2676	6.69
0.75	0.4336	0.4995	15.19

Table 3.7: Difference in pressure values. Side-to-side comparison at each nozzle location.

To address the problem of a pressure distribution across the nozzle exits, a flow resistance, made of copper foam was attached to the nozzle inlets with silicone (Figure 3.18). The results were surprisingly good (Figure 3.19 and Table 3.8).

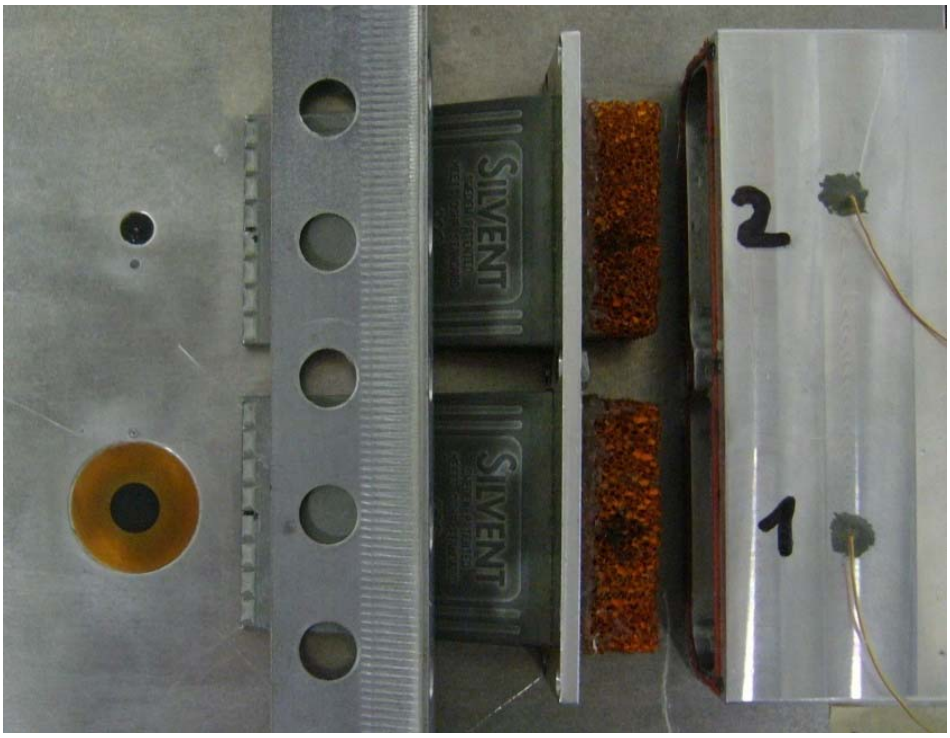

Figure 3.18: Flow resistance made of copper foam at the nozzle inlets inside of the box.

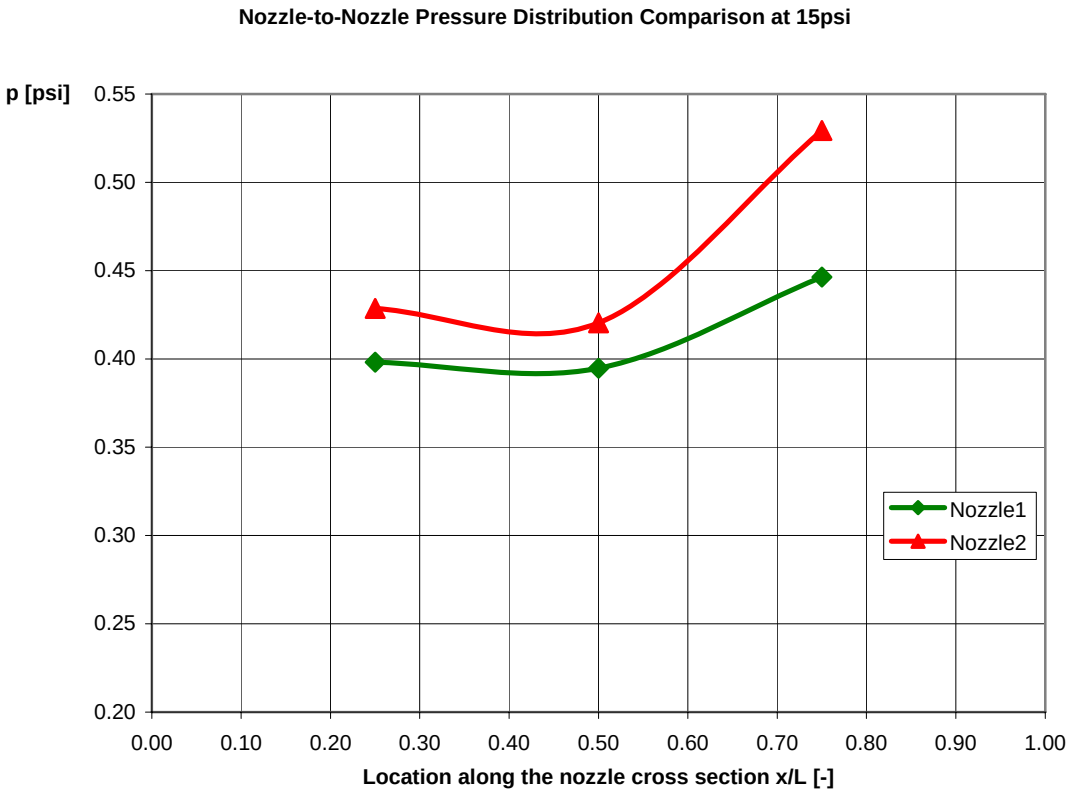

Figure 3.19: Pressure variations, AFTER attaching copper foam to the nozzle inlets, along the nozzle cross sections compared side to side. Detailed explanations see text.

Location x/L [-]	Pressure N1 [psi]	Pressure N2 [psi]	%Difference [-]
0.25	0.3982	0.4286	7.62
0.50	0.3948	0.4204	6.51
0.75	0.4464	0.5294	15.69

Table 3.8: Difference in pressure values AFTER attaching copper foam to the nozzle inlets. Side-to-side comparison at each nozzle location.

The pressure values can be easily transformed to velocity values by using the expression for the dynamic pressure, given by

$$u = \sqrt{\frac{2 \cdot p}{\rho_{100°C}}} \tag{3.5}$$

and the density for air at 100°C, which is 0.9 kg/m³, resulting in Table 3.8 and

Location x/L [-]	Velocity N1 [m/s]	Velocity N2 [m/s]	Difference % [-]
0.25	67.646	70.181	3.747
0.50	67.357	69.506	3.191
0.75	71.623	77.998	8.901

Table 3.9: Difference in velocity values AFTER attaching copper foam to the nozzle inlets. Side-to-side comparison at each nozzle location.

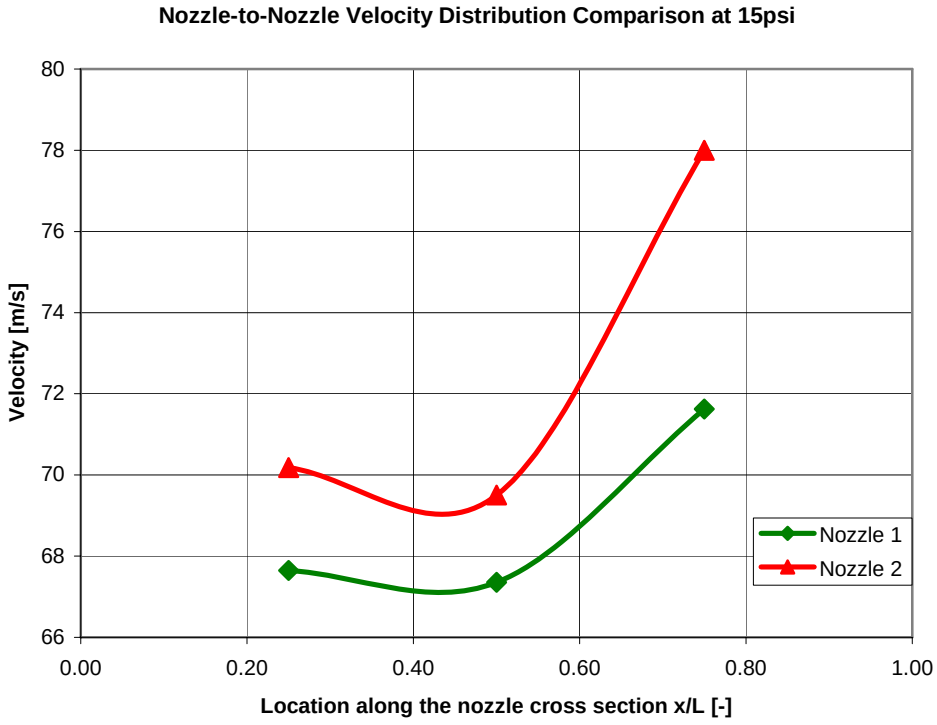

Figure 3.20: Velocity variations, AFTER attaching copper foam to the nozzle inlets, along the nozzle cross sections compared side to side. Detailed explanations see text.

The flow resistance showed dramatic performance improvements in uniformity. Because the velocity is proportional to the square root of the pressure (see equation (3.5)), the uniformity is now within about 9% (Table 3.9). However, the difference was encountered by doing two runs with the gages. The first run (run 01 or orientation 1, see Figure 3.21) with the SB gage at nozzle two (N2) and the second run (run 02 or orientation 2, see Figure 3.22) with the SB gage at nozzle one (N1).

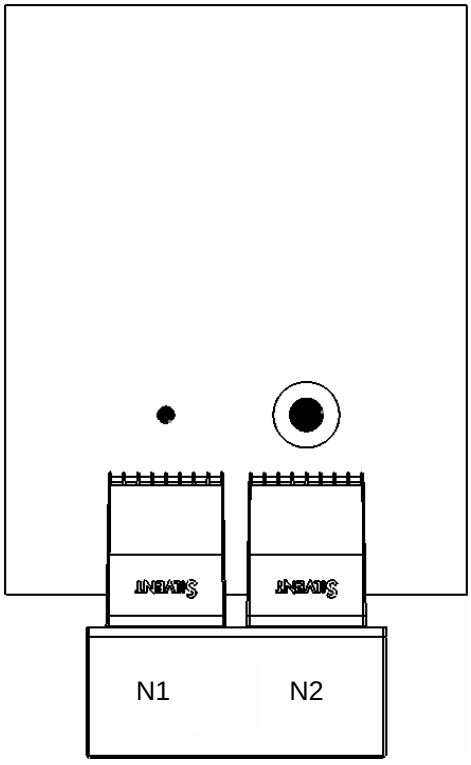

Figure 3.21: Run 01, Orientation 1, SB gage on the right nozzle, nozzle 2 (N2).

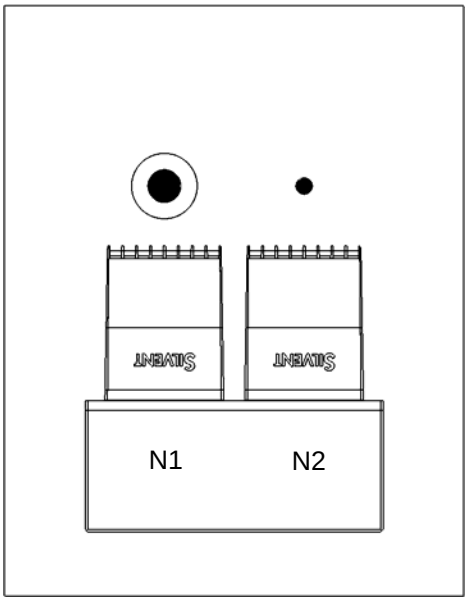

Figure 3.22: Run 02, Orientation 2, SB gage on the left nozzle, nozzle 1 (N1). Box and plate is separated by a layer of insulation.

3.4.3 Placement of Thermocouples

All of the thermocouples used were type K thermocouples. There were two thermocouples placed inside of the box, as illustrated in Figure 3.23, to measure the air temperature in the middle of the plenum. Measurements have later shown that temperatures were nearly identical, compared side to side.

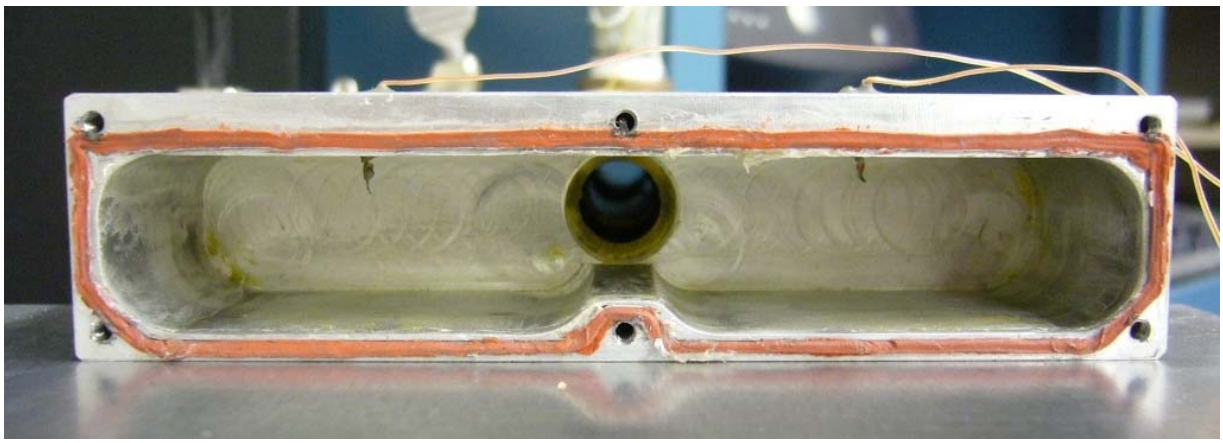

Figure 3.23: Thermocouples in the shear plenum used to measure the air temperature. Picture was taken after the PIV tests.

There were five more thermocouples used on the shear stand. Two on the plate for the 1.0 in. SB gages (Figure 3.24), two on the plate for the 1.5 in. SB gages (Figure 3.25) and one thermocouple inside of the water hose, right after the cooling water exit of the sensors (Figure 3.26).

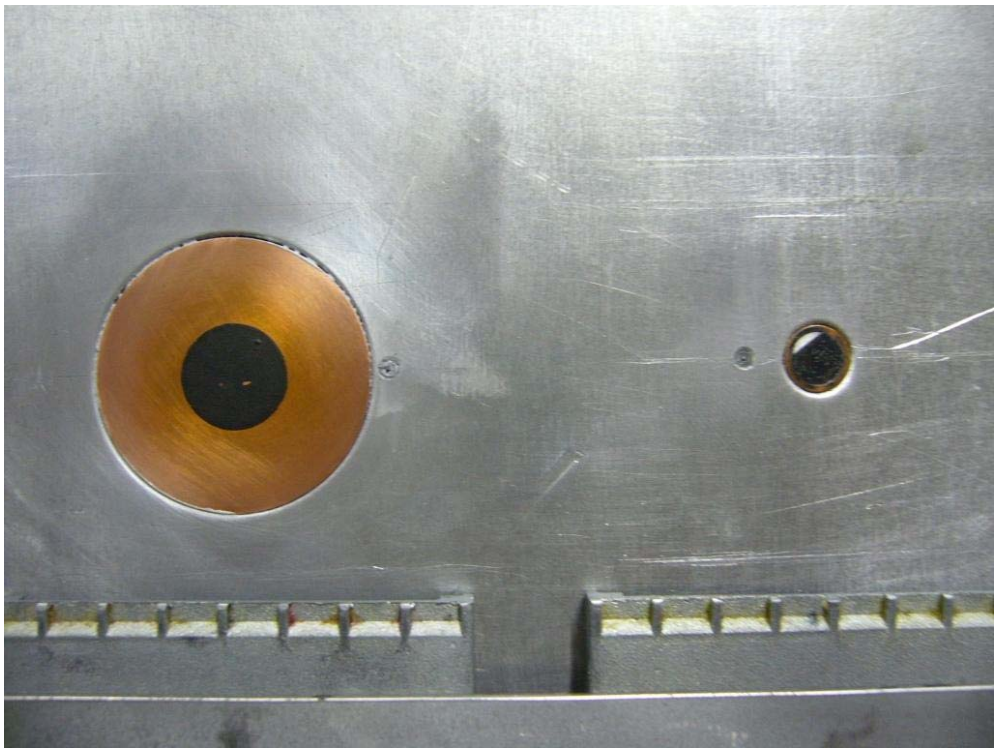

Figure 3.24: Picture of the plate for the 1.0 in. SB gages, showing the two thermocouples mounted close to SB and HFM (right).

Figure 3.25: Picture of the plate for the 1.5 in. SB gages, showing the thermocouples mounted close to the SB and HFM (right).

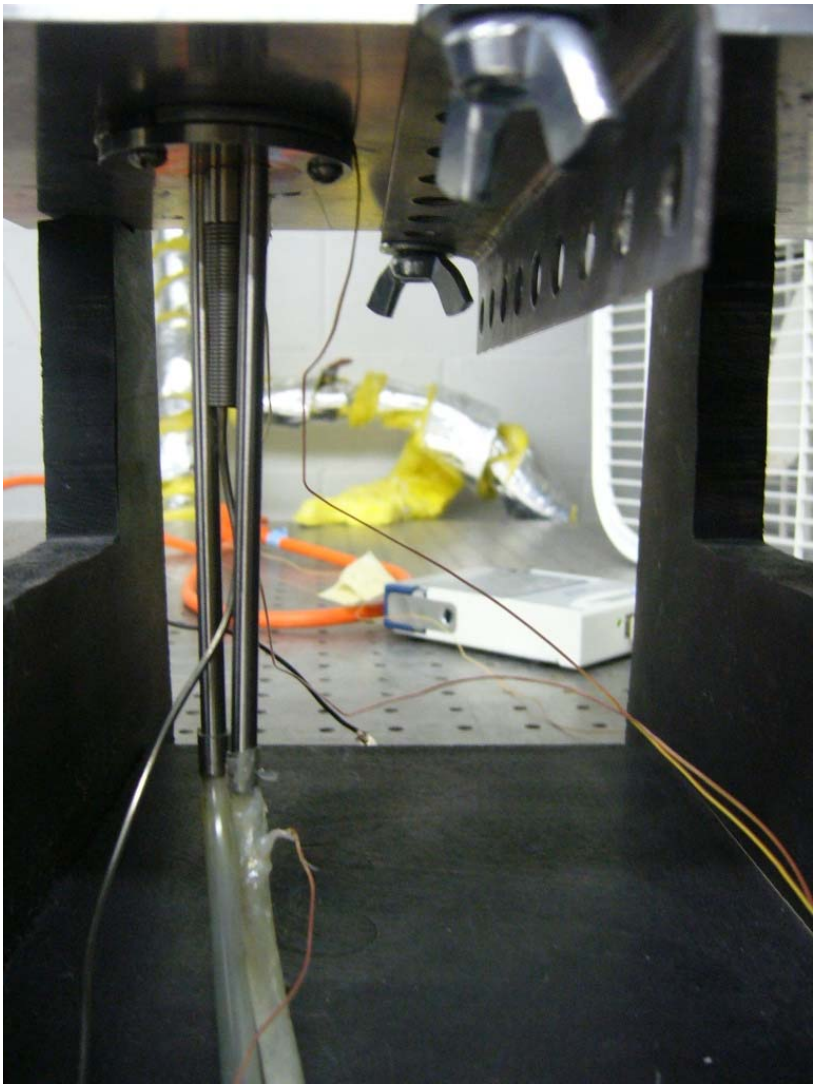

Figure 3.26: Thermocouple recording the cooling water temperature, located right after the exit.

3.4.4 Test Procedure

To perform a test run with the shear stand, the equipment has to be set up properly to produce comparable results. First, the 1 inch or the 1.5 inch SB is mounted into the suited plate. The one-inch SB is connected with three screws to the plate. A washer between the gage and plate aligns the gage surface with the plate surface. The screws and the position of the gage, relative to the plate were adjusted by using o-ring gaskets.

The 1.5 in. SB is held into the plate by using one plastic screw (Figure 3.15). The alignment of gage surface and plate surface has to be checked. To close the air gaps between gages and plate and to better align gage and plate surface, a high thermal conductivity paste is used ("Omega Therm 201"). The HFM is mounted into the plate by using a cap nut. No thermal grease is needed for the HFM.

After positioning the gages into the plate, their wires are connected with the DAQ1, the 24-bit-DAQ (Figure 3.1). Also connected to the DAQ1, are the two plate thermocouples, the two thermocouples in the shear stand box, and optionally the thermocouple for the water temperature (if water cooled). For the water cooled case, the water hoses are connected to the examined gage. The shear stand is grounded, using a cable going from a location at shear stand to the GND connection of DAQ1. Optionally, the cold junction temperature (measuring the temperature of the junctions at the DAQ, generally the room temperature) is taken by another thermocouple. However, since the experiments conducted are based on the temperature differences, the cold junction temperature is not necessary.

The second DAQ (the real time 8-bit-DAQ) is used to monitor the temperature of the copper tube inside of the air heater, the air heater exit temperature and the temperature of the air vented through valve three (V3). Both DAQs are connected to the computer.

After that, the shear stand is aligned accurately on the plate. The distance from the nozzle ends to the center of the heat sensing area for the tests undertaken, was chosen to be 20 mm. Moreover, the stand has to be aligned with the symmetry axis in the flow direction with the plate, to make sure the nozzle velocity profiles flowing over the sensors are the same and thus the results are consistent. The shear stand box and the nozzles are clamped and held in place by an L-profile. See Figure 3.15.

The next step is to enter the corresponding channels in the LabVIEW®-VI (Virtual Instrument), which samples the data of DAQ1. The sampling frequency was set to 1 Hz; the number of channels to read was six for the shear stand, seven with water cooling. The VI for DAQ2 works in a similar way to the VI sampling the data of DAQ1. Figure 3.27 shows the screen with both VI's during a typical test. The data seen on the screen shows the stand at steady-state conditions. In the DAQ2-VI, the white line represents the temperature of the copper tubes, the red line represents the air exit temperature at the air heater exit and the green line represents the temperature of the air at V3. The curves are flat due to steady-state

conditions. The DAQ2-VI shows the rest of the data discussed. It will be explained later in detail, see chapter 4: Results and Discussion.

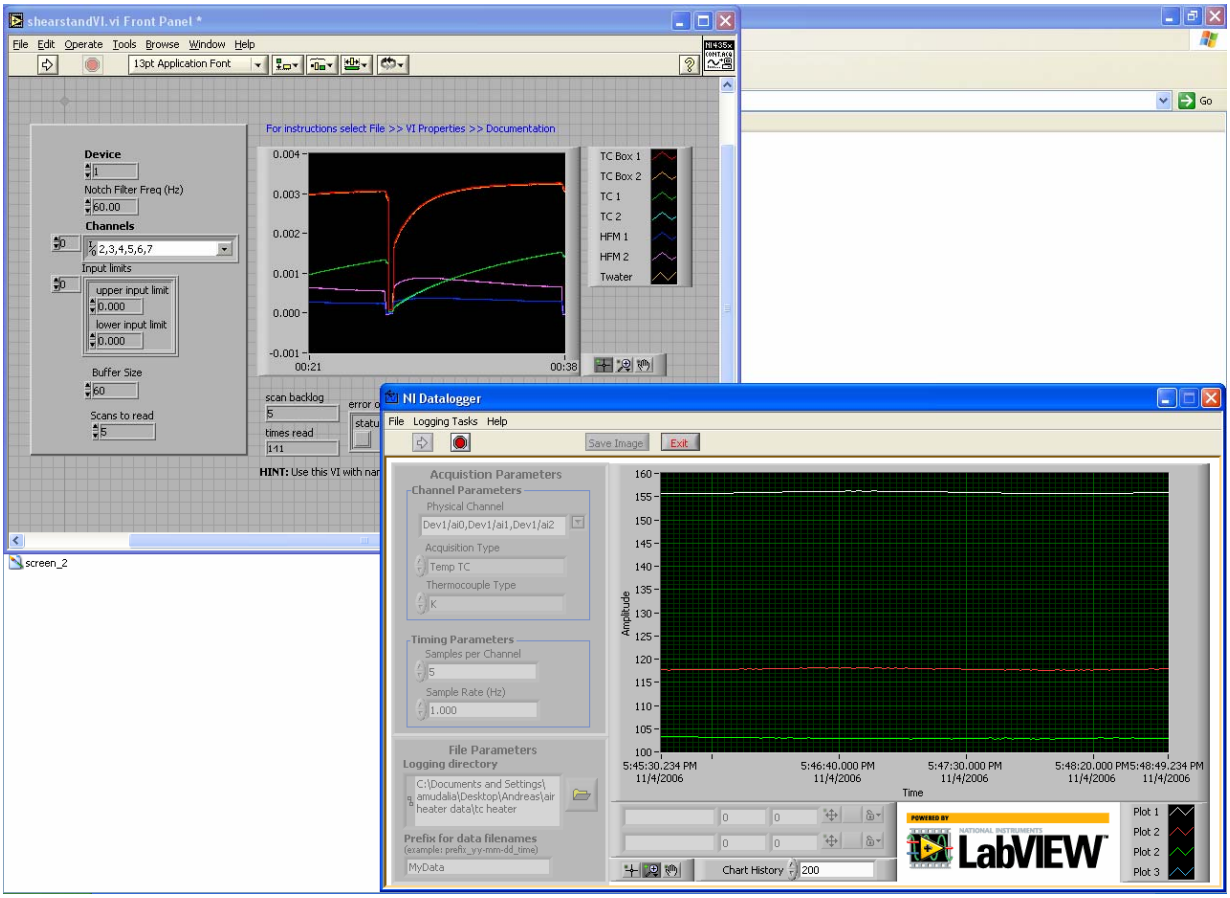

Figure 3.27: Screen during experiments, upper left window shows the VI monitoring the stand data, the lower right window shows the VI monitoring the air heater data and the temperature at V3.

After setting up the stand properly and checking if all connections work correctly, the actual experiment is accomplished very easily. The air supply is set to the desired pressure (flow rate), the air heater is set accordingly. The user has to wait until the air temperature reaches steady-state conditions at V3 (green line in Figure 3.27). After steady state is reached, V3 will be closed and V4 needs to be opened. The VI sampling data from DAQ1 needs to be started 10 seconds ahead of time in order to have reference zero values for the gages. Data will be taken, until the air flow in the shear stand box reaches steady state conditions. This takes approximately ten minutes (for lower pressures) to seven minutes (for higher pressures). Once the air going through the box reaches steady-state temperature, data is taken for another 30 seconds. After that, the air supply is turned off (V4), the shear stand VI is stopped a few

seconds later. V3 is opened again in order for the air heater not to overheat. After one test at one pressure is done, the whole stand is cooled down to room temperature in order to start from the same initial conditions. This is done with an ordinary box fan (Figure 3.2). Cooling time is about 20 to 30 minutes. The LabVIEW VI application stored the data in the specified folder in a format readable with EXCEL. The data processing and reduction is described in section 3.6 Results and Discussion.

3.5 Stagnation Stand

A detailed explanation of the stagnation stand design, performance and placement of the thermocouples is given in this section; as well as the test procedure.

3.5.1 Design, Performance and Placement of Thermocouples

The stagnation stand has been redesigned, based on a previous prototype described by Raphael-Mabel [9]. The new design is similar but has additional features. It is now possible to adjust the nozzles relative to the plates and the mounting of the stagnation plates is simplified.

The working principle is analogous to the shear stand. It was designed to provide the same convective heat flux to the reference standard and to the test gage. This was realized by simply putting a tee junction in the air supply line with a 6.3mm orifice at each end. Figure 3.28 shows the design of the stagnation stand. The gages are mounted in vertically aligned plates; which are connected with screws to the main plate, forming a U-shape and holding the tee nozzle in position. The distance between orifices and plates was designed to be 50 mm, in order to provide maximum and consistent convection heat flux. A wooden support holds the U-shaped stagnation stand in position. The heated air coming from the air heater is directly run into the tee nozzle from the bottom side of the stand.

Several tests have been performed to confirm that the heat flux from each of the impinging jets is the same. These consisted of a series of measurements that switched the

sensors from one side to the other. The results showed no difference of location on the calibration values of the gages within the three percent uncertainty of the measurements.

The placement of the type K thermocouples was done in an analogous fashion as for the shear stand. One thermocouple was inserted in the air supply of the nozzles, before the tee junction to measure the air temperature (Figure 3.29). Three more thermocouples, one for each gage used, were flush surface mounted into the plates, close to the gage location in order to represent the gage temperature, see Figure 3.30, Figure 3.31 and Figure 3.32.

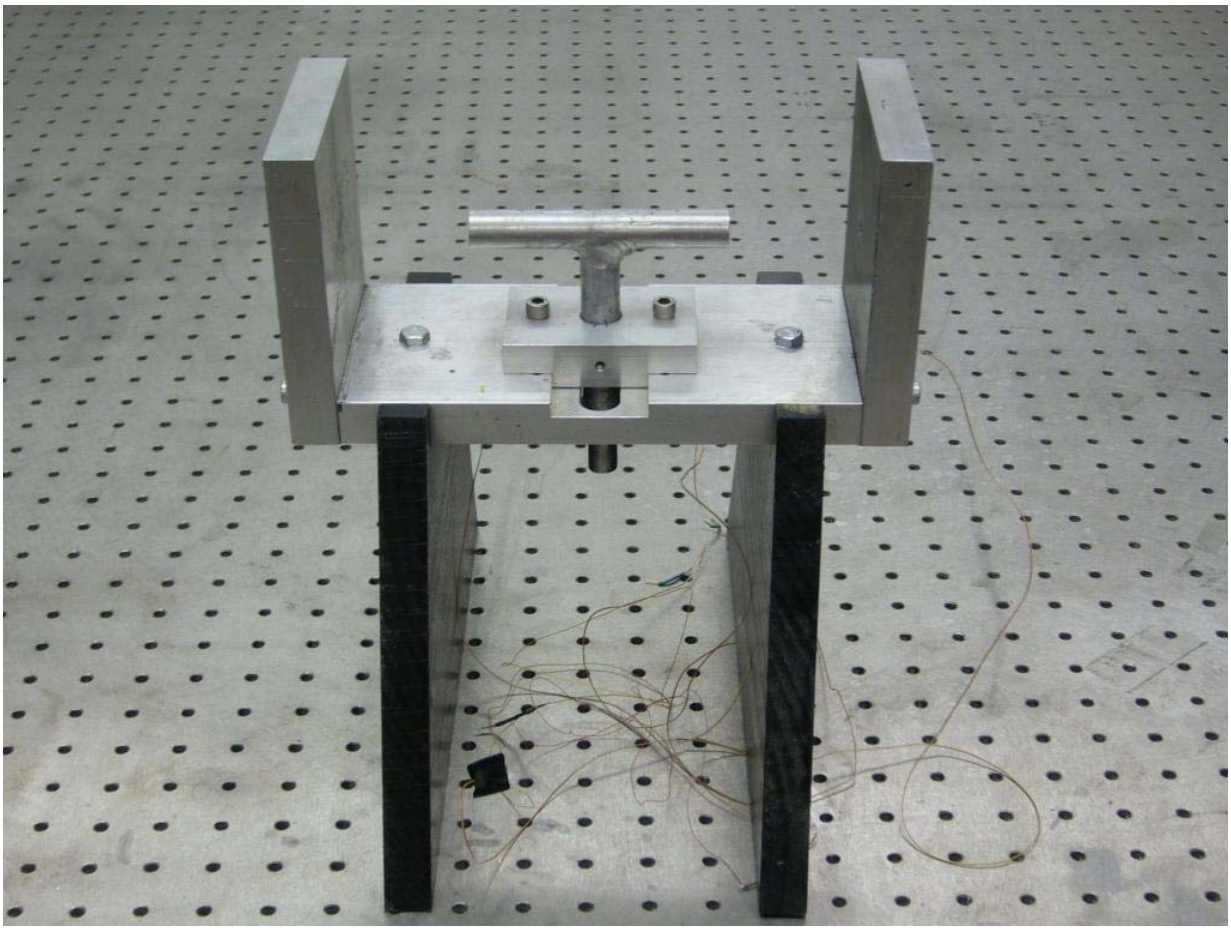

Figure 3.28: New stagnation stand design.

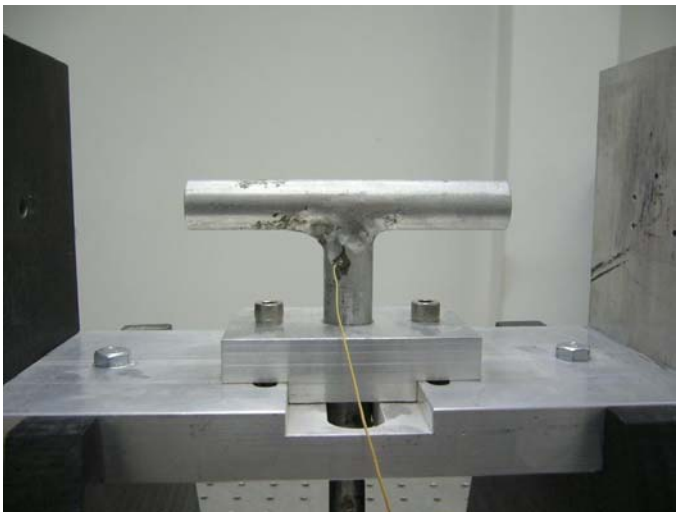

Figure 3.29: Thermocouple location to measure the air temperature.

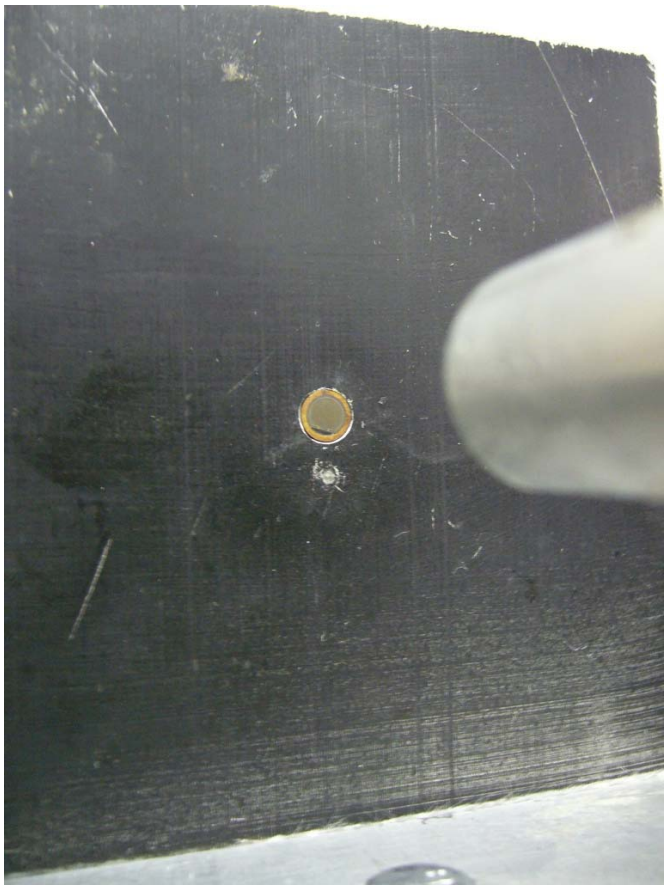

Figure 3.30: Thermocouple location for the HFM gage plate.

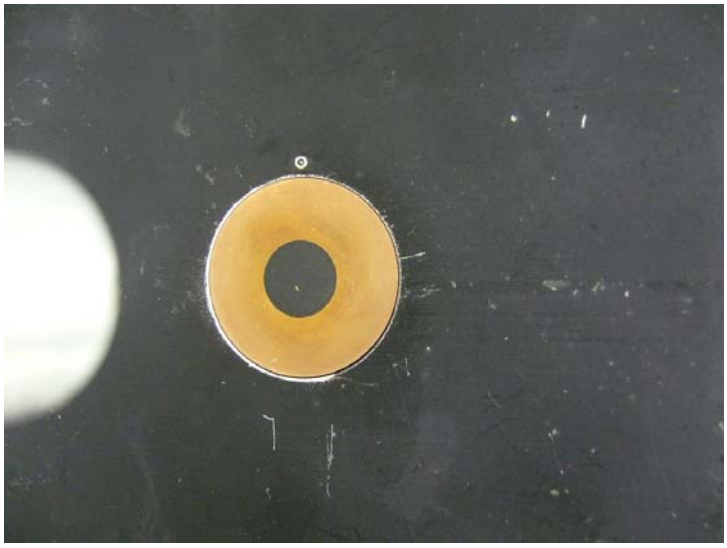

Figure 3.31: Thermocouple location for the 1 in. SB gage plate.

Figure 3.32: Thermocouple location for the 1.5 in. SB gage plate.

3.5.2 Test Procedure

The tests for the stagnation stand were done according to the test procedure for the shear stand. The gages are mounted into the plate and exactly aligned with the center line of the nozzle. This is done with the aid of a rod (see Figure 3.33). The rod is slid through the HFM hole and the nozzle, while the SB gage on the other side of the nozzle is aligned with the center line of the nozzle. After that, the HFM is mounted into the stand. Then the outputs of

the sensors are connected to the DAQ, which is connected to the CPU. The data acquisition is done with the same LabVIEW VI, the sampling frequency was one hertz.

The test starts with setting the air supply to the right pressure and temperature. The sensors are blocked by a cover from the air jets until steady-state condition is reached (i.e. constant air temperature through the tee nozzle, see Figure 3.33). At this point the data acquisition is started and a few seconds later the cover was removed. This was done to be able to calculate the reference zero for each gage and each test run. The data was taken over a time of 20 seconds. After the test is done, the stand is cooled down to room temperature again, which takes approximately 20 minutes and the next test can be performed.

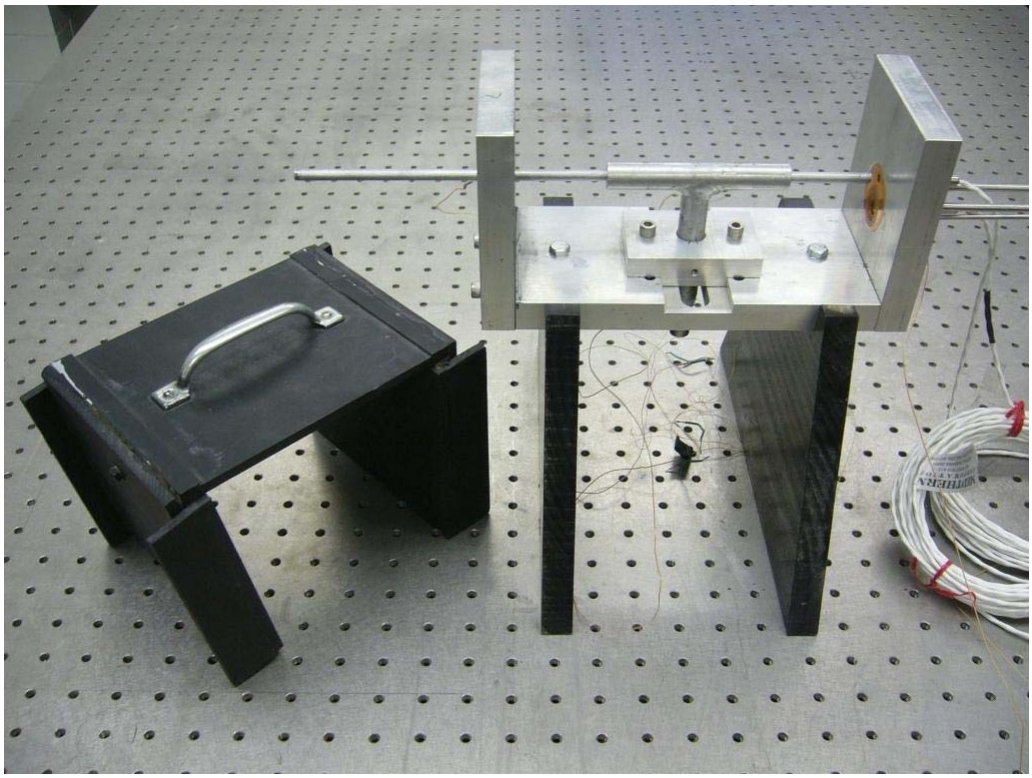

Figure 3.33: Stagnation stand, rod and cover.

3.6 Data Analysis

This section explains how the data sampled with the LabVIEW VI is processed, to produce the sensitivity curves as a function of the heat transfer coefficient, h. The LabVIEW saves its output in *.lvm files, which are readable with MS Excel. The order of the channels, written in the LabVIEW window determines the order of the output columns of the *.lvm file.

3.6.1 Data Reduction

The air flow is opened ten seconds after the LabVIEW VI is started. These first ten seconds are used to equalize the reference zero offset for each of the heat flux gages

$$q_g''(t) = \frac{E_g(t) - \frac{1}{10}\sum_{t=1s}^{10s} E_g(t)}{S_{g,abs}} \tag{3.6}$$

The LabVIEW output is in volts over time. The data has to be adapted to the units of the sensitivity or vice versa. The same is true for the conversion of the temperature signal into degrees Celsius. The constants used for conversion, given in Table 3.10 are in units of micro volts and valid for a type K-thermocouple.

Constant	Value [µV]
c0	0
c1	$2.508 \cdot 10^{-02}$
c2	$7.860 \cdot 10^{-08}$
c3	$-2.503 \cdot 10^{-10}$
c4	$8.315 \cdot 10^{-14}$
c5	$-1.228 \cdot 10^{-17}$
c6	$9.804 \cdot 10^{-22}$
c7	$-4.413 \cdot 10^{-26}$
c8	$1.058 \cdot 10^{-30}$
c9	$-1.053 \cdot 10^{-35}$

Table 3.10: Constants to convert the temperature signal in degrees Celsius.

The temperature in degrees Celsius is then obtained by calculating the polynomial, given for a type K-thermocouple and utilizing the factors given above:

$$T(t_i) = c_0 + \sum_{k=1}^{9} c_k E_i^k \tag{3.7}$$

Table 3.10 and equation (3.7) are valid for a range from zero to 500 degrees Celsius. The heat transfer coefficient is then obtained by using equation (2.27) introduced in section "2.2.3 Convection Heat Transfer and Boundary Layer Theory", as

$$h_g(t) = \frac{q_g^{"}(t)}{\left(T_{air} - T_{plate,g}(t)\right)}, \tag{3.8}$$

where T_{air} is constant for steady state conditions. Now the expected heat flux signal for the Schmidt-Boelter gage can be evaluated as

$$q_{SB}^{"} = h_{HFM}(T_{air} - T_{plate,SB}), \tag{3.9}$$

with keeping in mind, that the variables are functions of time but not T_{air}. Hence, one gets for the sensitivity of the Schmidt-Boelter gage:

$$S_{SB} = \frac{E_{SB}}{q_{SB}^{"}} = \frac{E_{SB}}{h_{HFM}(T_{air} - T_{plate,SB})} \tag{3.10}$$

Finally, using equation (3.8) with (3.10), the sensitivity for a Schmidt-Boelter gage is calibrated as:

$$S_{SB} = \frac{E_{SB}}{q_{HFM}^{"}} \frac{(T_{air} - T_{plate,HFM})}{(T_{air} - T_{plate,SB})}, \tag{3.11}$$

or:

$$\boxed{S_{SB} = \frac{E_{SB}}{E_{HFM}} S_{HFM} \frac{(T_{air} - T_{plate,HFM})}{(T_{air} - T_{plate,SB})}} \tag{3.12}$$

3.6.2 Uncertainty Analysis

3.6.2.1 Uncertainty in Sensitivity

The obtained Sensitivity was not measured directly but was determined from other quantities through a functional relation. Each quantity x_i (voltage output of SB and HFM gage, sensitivity of HFM gage and temperatures), is afflicted with an error. The combined standard error of the measurement result y, designated by $u_c^2(y)$ is obtained from [17]

$$u_c^2(y) = \sum_{i=1}^{N} \left(\frac{\partial S_{SB}}{\partial x_i} \right)^2 u^2(x_i) . \tag{3.13}$$

Dividing equation (3.13) by S_{SB}, the expressions for the partial derivatives are non-dimensionalized.

$$\left(\frac{u(y)}{S_{SB}} \right)_c^2 = \sum_{i=1}^{N} \left(\frac{1}{S_{SB}} \frac{\partial S_{SB}}{\partial x_i} \right)^2 u^2(x_i) . \tag{3.14}$$

Three different cases have been examined. The gage sensitivity based on T_{plate} not cooled (nc), based on T_{plate} water cooled (wc), and based on T_{water}, water cooled (wc). Accordingly, the equation for the sensitivity (3.11) for each case is

Based on T_{plate}, nc $$S_{SB} = \frac{E_{SB}}{E_{HFM}} S_{HFM} \frac{(T_{air} - T_{plate,HFM})}{(T_{air} - T_{plate,SB})} \tag{3.15}$$

Based on T_{plate}, wc $$S_{SB} = \frac{E_{SB}}{E_{HFM}} S_{HFM} \frac{(T_{air} - T_{plate,HFM})}{(T_{air} - T_{plate,wc,SB})} \tag{3.16}$$

Based on T_{water}, wc $$S_{SB} = \frac{E_{SB}}{E_{HFM}} S_{HFM} \frac{(T_{air} - T_{plate,HFM})}{(T_{air} - T_{water})} \tag{3.17}$$

The three cases can be considered to be the same, because it can be assumed that the thermocouples behave in the same way. However, we have to take into account that the temperatures change with the chosen test pressure, thus for each data point, the uncertainty will be different. Performing the partial derivatives, one obtains:

$$\left(\frac{u(y)}{S_{SB}}\right)_c^2 = \left(\frac{1}{E_{SB}}\right)^2 u^2(E_{SB}) + \left(\frac{-1}{E_{HFM}}\right)^2 u^2(E_{HFM}) + \left(\frac{1}{S_{HFM}}\right)^2 u^2(S_{HFM}) + \left(\frac{T_{pHFM} - T_{pSB}}{(T_a - T_{pHFM})(T_a - T_{pSB})}\right)^2 u^2(T_a) + \left(\frac{-1}{T_a - T_{pHFM}}\right)^2 u^2(T_{pHFM}) + \left(\frac{1}{T_a - T_{pSB}}\right)^2 u^2(T_{pSB}) \quad (3.18)$$

The gage sensitivity is also a function of the flow properties, i.e. the heat transfer coefficient. Considering (3.10)

$$S_{SB} = \frac{E_{SB}}{h_{HFM}(T_{air} - T_{SB})},$$

taking the partial derivative with respect to h_{HFM}, and dividing the obtained expression by S_{SB} (equation (3.10)), one obtains:

$$\frac{1}{S_{SB}} \frac{\partial S_{SB}}{\partial h_{HFM}} = \frac{1}{h_{HFM}} \quad (3.19)$$

and inserting this expression to equation (3.14), meaning adding (3.19) to equation (3.18), gives for the uncertainty for the shear stand:

$$\left(\frac{u(y)}{S_{SB}}\right)_{shear}^2 = \left(\frac{1}{E_{SB}}\right)^2 u^2(E_{SB}) + \left(\frac{-1}{E_{HFM}}\right)^2 u^2(E_{HFM}) + \left(\frac{1}{S_{HFM}}\right)^2 u^2(S_{HFM}) + 2\cdot\left(\frac{T_{pHFM} - T_{pSB}}{(T_a - T_{pHFM})(T_a - T_{pSB})}\right)^2 u^2(T_a) + \left(\frac{-1}{T_a - T_{pHFM}}\right)^2 u^2(T_{pHFM}) + \left(\frac{1}{T_a - T_{pSB}}\right)^2 u^2(T_{pSB}) + \left(\frac{1}{h_{HFM}}\right)^2 u^2(h_{HFM,shear}) \quad (3.20)$$

and for the uncertainty for the stagnation stand:

$$\left(\frac{u(y)}{S_{SB}}\right)_{stag}^2 = \left(\frac{1}{E_{SB}}\right)^2 u^2(E_{SB}) + \left(\frac{-1}{E_{HFM}}\right)^2 u^2(E_{HFM}) + \left(\frac{1}{S_{HFM}}\right)^2 u^2(S_{HFM}) + \left(\frac{T_{pHFM} - T_{pSB}}{(T_a - T_{pHFM})(T_a - T_{pSB})}\right)^2 u^2(T_a) + \left(\frac{-1}{T_a - T_{pHFM}}\right)^2 u^2(T_{pHFM}) + \left(\frac{1}{T_a - T_{pSB}}\right)^2 u^2(T_{pSB}) + \left(\frac{1}{h_{HFM}}\right)^2 u^2(h_{HFM,stag}) \quad (3.21)$$

The uncertainty in each quantity x_i is obtained from its bias and precision error, given as

$$u(x_i) = \sqrt{b^2(x_i) + p^2(x_i)} \tag{3.22}$$

The bias error is given by the uncertainty of the DAQ, the uncertainties of the thermocouples or the uncertainty in the sensitivities, so that for the voltage output signal the bias error is given as

$$b(E_i) = b(DAQ). \tag{3.23}$$

The tolerance of the HFM sensitivity is defined by a five per cent uncertainty of the absorbed sensitivity, giving a value of

$$b(S_{HFM}) = 0.05 \cdot S_{abs,HFM} = 9.62 \frac{\mu V}{W / cm^2}. \tag{3.24}$$

The total bias error of the thermocouples is given as

$$b_{tot}(T_i) = \sqrt{b(DAQ)^2 + b(T_i)^2} \tag{3.25}$$

The bias error of the DAQ is given by the manufacturer with an accuracy of 0.1°C. This can be expressed in micro volts by using the following polynomial (equation (3.26)) and Table 2.1., giving a value of 39.15 μV

$$T(t_i) = c_0 + \sum_{k=1}^{11} c_k E_i^k \tag{3.26}$$

Constant	E-Value [µV]
c00	1.760E+01
c01	3.892E+01
c02	1.856E-02
c03	-9.946E-05
c04	3.184E-07
c05	-5.607E-10
c06	5.608E-13
c07	-3.202E-16
c08	9.715E-20
c09	-1.210E-23
c10	1.186E+02
c11	-1.183E-04

Table 3.11: Constants to convert degrees Celsius in micro volts.

The actual bias error for a thermocouple read out is 0.75% of the mean value, where the data was taken. For reasons of simplicity and the assumption that each thermocouple is afflicted with the same uncertainty the bias error for all of the thermocouples was taken from the plate temperature data range, since the temperature of the water is lower and the temperature of the air is higher. Those assumptions are justified, because the error analysis should be seen as an estimate and the error can never be expressed exactly, thus with

$$b(T_i) = 0.0075 \cdot \overline{T}_i \tag{3.27}$$

a representative bias error for the thermocouples is calculated.

For the shear stand, the uncertainty in the heat transfer coefficient, *h* can be obtained by considering the difference of the *h* value from side to side, meaning the values obtained from testing the Schmidt-Boelter gage at the left and right nozzle. Taking 50% of the value will give the uncertainty in *h* for the shear stand as a function of the pressure value:

$$u_{shear}(h) = 0.5 \cdot \left(h_l(p) - h_r(p)\right) \tag{3.28}$$

For the stagnation stand, the uncertainty in *h* was obtained from previous test and determined to be as 3% difference from side to side measurements

$$u_{stag}(h) = 0.03 \cdot h(p) \tag{3.29}$$

The precision error is defined by for each of the quantity is defined by

$$p(x_i) = A\frac{\sigma_u}{\sqrt{n}}, \tag{3.30}$$

The constant A is given by the student's t distribution function, listed in Table 3.12 and can be found by a given sample set of *n* values meaning $\nu = n\text{-}1$ degrees of freedom and a usual confidence interval of 95%. The standard deviation is given as the deviation of the data from the mean value of the considered quantity [17]

$$\sigma_u = \left(\frac{1}{n(n-1)}\sum_{k=1}^{n}(x_{i,k} - \overline{x_i})^2\right)^{1/2}. \tag{3.31}$$

The results for bias and precision error and the total uncertainty for each quantity are listed in Table 3.13, Table 3.14 and Table 3.15 for shear and stagnation flow. The not cooled case based on the plate temperature has been chosen to evaluate the uncertainties. The data was taken in the range where the sensitivity data was obtained. The obtained uncertainties for the sensitivity are listed in Table 3.16 for shear flow and in Table 3.17 for stagnation flow.

A	Confidence interval										
ν	75.00%	80.00%	85.00%	90.00%	95.00%	97.50%	99.00%	99.50%	99.75%	99.90%	99.95%
1	1.000	1.376	1.963	3.078	6.314	12.710	31.820	63.660	127.300	318.300	636.600
2	0.816	1.061	1.386	1.886	2.920	4.303	6.965	9.925	14.090	22.330	31.600
3	0.765	0.978	1.250	1.638	2.353	3.182	4.541	5.841	7.453	10.210	12.920
4	0.741	0.941	1.190	1.533	2.132	2.776	3.747	4.604	5.598	7.173	8.610
5	0.727	0.920	1.156	1.476	2.015	2.571	3.365	4.032	4.773	5.893	6.869
6	0.718	0.906	1.134	1.440	1.943	2.447	3.143	3.707	4.317	5.208	5.959
7	0.711	0.896	1.119	1.415	1.895	2.365	2.998	3.499	4.029	4.785	5.408
8	0.706	0.889	1.108	1.397	1.860	2.306	2.896	3.355	3.833	4.501	5.041
9	0.703	0.883	1.100	1.383	1.833	2.262	2.821	3.250	3.690	4.297	4.781
10	0.700	0.879	1.093	1.372	1.812	2.228	2.764	3.169	3.581	4.144	4.587
11	0.697	0.876	1.088	1.363	1.796	2.201	2.718	3.106	3.497	4.025	4.437
12	0.695	0.873	1.083	1.356	1.782	2.179	2.681	3.055	3.428	3.930	4.318
13	0.694	0.870	1.079	1.350	1.771	2.160	2.650	3.012	3.372	3.852	4.221
14	0.692	0.868	1.076	1.345	1.761	2.145	2.624	2.977	3.326	3.787	4.140
15	0.691	0.866	1.074	1.341	1.753	2.131	2.602	2.947	3.286	3.733	4.073
16	0.690	0.865	1.071	1.337	1.746	2.120	2.583	2.921	3.252	3.686	4.015
17	0.689	0.863	1.069	1.333	1.740	2.110	2.567	2.898	3.222	3.646	3.965
18	0.688	0.862	1.067	1.330	1.734	2.101	2.552	2.878	3.197	3.610	3.922
19	0.688	0.861	1.066	1.328	1.729	2.093	2.539	2.861	3.174	3.579	3.883
20	0.687	0.860	1.064	1.325	1.725	2.086	2.528	2.845	3.153	3.552	3.850
21	0.686	0.859	1.063	1.323	1.721	2.080	2.518	2.831	3.135	3.527	3.819
22	0.686	0.858	1.061	1.321	1.717	2.074	2.508	2.819	3.119	3.505	3.792
23	0.685	0.858	1.060	1.319	1.714	2.069	2.500	2.807	3.104	3.485	3.767
24	0.685	0.857	1.059	1.318	1.711	2.064	2.492	2.797	3.091	3.467	3.745
25	0.684	0.856	1.058	1.316	1.708	2.060	2.485	2.787	3.078	3.450	3.725
26	0.684	0.856	1.058	1.315	1.706	2.056	2.479	2.779	3.067	3.435	3.707
27	0.684	0.855	1.057	1.314	1.703	2.052	2.473	2.771	3.057	3.421	3.690
28	0.683	0.855	1.056	1.313	1.701	2.048	2.467	2.763	3.047	3.408	3.674
29	0.683	0.854	1.055	1.311	1.699	2.045	2.462	2.756	3.038	3.396	3.659
30	0.683	0.854	1.055	1.310	1.697	2.042	2.457	2.750	3.030	3.385	3.646
40	0.681	0.851	1.050	1.303	1.684	2.021	2.423	2.704	2.971	3.307	3.551
50	0.679	0.849	1.047	1.299	1.676	2.009	2.403	2.678	2.937	3.261	3.496
60	0.679	0.848	1.045	1.296	1.671	2.000	2.390	2.660	2.915	3.232	3.460
80	0.678	0.846	1.043	1.292	1.664	1.990	2.374	2.639	2.887	3.195	3.416
100	0.677	0.845	1.042	1.290	1.660	1.984	2.364	2.626	2.871	3.174	3.390
120	0.677	0.845	1.041	1.289	1.658	1.980	2.358	2.617	2.860	3.160	3.373
∞	0.674	0.842	1.036	1.282	1.645	1.960	2.326	2.576	2.807	3.090	3.291

Table 3.12: t-distribution function, defining the "A" constant, as a function of degrees of freedom (ν) and the confidence interval, as found in [18].

Measurand	Bias Error	Precision Error	Uncertainty	Units
x_i	b	p	$u(x_i)$	
E_{SB}	39.15	1.75	39.18	μV
E_{HFM}	39.15	2.58	39.18	μV
S_{HFM}	9.62	-	9.62	$\mu V/(Wcm^2)$
T_a	0.59	0.72	0.93	$°C$
T_{pHFM}	0.32	0.88	0.94	$°C$
T_{pSB}	0.39	0.59	0.71	$°C$
$h_{HFM,shear}$	-	-	See Table 3.14	$W/(cm^2K)$
$h_{HFM,stag}$	-	-	See Table 3.15	$W/(cm^2K)$

Table 3.13: Quantity, bias error, precision error and total uncertainty for *shear* and *stagnation flow*.

Pressure Value	Heat transfer coefficient	Uncertainty
p [psi]	*h [W/(cm²K)]*	*[W/(cm²K)]*
1	0.0123	$4.29 \cdot 10^{-04}$
3	0.0161	$9.58 \cdot 10^{-04}$
5	0.0198	$4.05 \cdot 10^{-04}$
10	0.0286	$9.99 \cdot 10^{-04}$
15	0.0360	$9.89 \cdot 10^{-04}$
20	0.0426	$1.22 \cdot 10^{-03}$
25	0.0494	$2.55 \cdot 10^{-03}$
30	0.0547	$3.09 \cdot 10^{-03}$

Table 3.14: Uncertainty in *h* for the not cooled case based on T_{plate} for *shear flow*.

Pressure Value	Heat transfer coefficient	Uncertainty
p [psi]	*h [W/(cm²K)]*	*[W/(cm²K)]*
1	0.0232	$3.00 \cdot 10^{-04}$
3	0.0271	$6.94 \cdot 10^{-04}$
5	0.0313	$8.12 \cdot 10^{-04}$
10	0.0418	$9.38 \cdot 10^{-04}$
15	no data available	no data available
20	0.0617	$1.85 \cdot 10^{-03}$
25	no data available	no data available
30	0.0892	$2.68 \cdot 10^{-03}$

Table 3.15: Uncertainty in *h* for the not cooled case based on T_{plate} for *stagnation flow*.

Pressure	Sensitivity	Heat transfer coeff.	Uncertainty
p	***S***	***h***	***u(S)/S***
psi	*mV/(Wcm²)*	*W/(cm²K)*	*%*
1	0.436	0.0123	26.0
3	0.425	0.0161	24.7
5	0.421	0.0198	22.6
10	0.403	0.0286	19.3
15	0.392	0.0360	15.7
20	0.384	0.0426	14.9
25	0.383	0.0494	16.0
30	0.380	0.0547	17.7

Table 3.16: Uncertainties in the gage sensitivity values for the not cooled case based on the plate temperature for *shear flow*.

Pressure	Sensitivity	Heat transfer coeff.	Uncertainty
p	***S***	***h***	***u(S)/S***
psi	*mV/(Wcm²)*	*W/(cm²K)*	*%*
1	0.563	0.0232	7.352
3	0.597	0.0271	6.947
5	0.600	0.0313	6.765
10	0.537	0.0418	6.508
15	no data available	no data available	no data available
20	0.542	0.0617	7.152
25	no data available	no data available	no data available
30	0.511	0.0892	5.653

Table 3.17: Uncertainties in the gage sensitivity values for the not cooled case based on the plate temperature for *stagnation flow*.

3.6.2.2 Uncertainty in Thermal Resistance

The procedure to obtain the uncertainty in the thermal resistance is analogous to obtain the uncertainty in the sensitivity. The equation to obtain the thermal resistance was based on the thermal model resistance, equation (2.95)

$$S_g = \frac{S_{abs}}{1 + hR^{"}}$$

rearranging yields

$$R^{"} = \frac{S_{abs} - S_g}{h \cdot S_g}. \tag{3.32}$$

To obtain the uncertainty in per cent, one has to use the uncertainty given by

$$\left(\frac{u(y)}{R^{"}}\right)_c^2 = \sum_{i=1}^{N}\left(\frac{1}{R^{"}}\frac{\partial R^{"}}{\partial x_i}\right)^2 u^2(x_i) \tag{3.33}$$

Performing the partial derivatives and substituting into equation (3.33), one gets for the shear stand (3.34) and for the stagnation stand (3.35).

$$\left(\frac{u(y)}{R^{"}}\right)_{shear}^2 = \left(\frac{1}{S_{abs,SB} - S_g}\right)^2 u^2(S_{abs,SB}) + \left(\frac{-S_{abs}}{\left(S_{abs} - S_g\right)S_g}\right)^2 u^2(S_g) + \left(\frac{-1}{h_{HFM}}\right)^2 u^2(h_{HFM,shear}) \tag{3.34}$$

$$\left(\frac{u(y)}{R^{"}}\right)_{stag}^2 = \left(\frac{1}{S_{abs} - S_g}\right)^2 u^2(S_{abs}) + \left(\frac{-S_{abs}}{\left(S_{abs} - S_g\right)S_g}\right)^2 u^2(S_g) + \left(\frac{-1}{h_{HFM}}\right)^2 u^2(h_{HFM,stag}) \tag{3.35}$$

The tolerance of the SB sensitivity is obtained by a five per cent uncertainty of the absorbed sensitivity, likewise the tolerance for the HFM, giving a value of

$$b(S_{SB}) = 0.05 \cdot S_{abs,SB} = 0.032\,\frac{mV}{W/cm^2} \tag{3.36}$$

For the uncertainty of the gage sensitivity $u(S_g)$, the values obtained in the previous section have been used. The heat transfer coefficient h and its uncertainties for shear and stagnation

flow are taken from Table 3.14 and Table 3.15. The results for the R" uncertainty are summarized in Table 3.18 for shear and in for stagnation flow.

Pressure	**Sensitivity Value**	**Uncertainty in S**	**Thermal Resistance** (measured)	**Uncertainty**
p	***S***	***u(S)***	***R"***	***u(R")/R´´***
psi	*mV/(Wcm²)*	*mV/(Wcm²)*	*cm²K/W*	%
1	0.436	0.113	19.356	81.0
3	0.425	0.105	19.356	73.5
5	0.421	0.095	19.356	66.0
10	0.403	0.078	19.356	53.0
15	0.392	0.062	19.356	41.8
20	0.384	0.057	19.356	38.7
25	0.383	0.061	19.356	41.2
30	0.380	0.067	19.356	44.9

Table 3.18: Uncertainty in R", cross listed with the uncertainty in S for a given pressure value for *shear flow*.

Pressure	**Sensitivity Value**	**Uncertainty in S**	**Thermal Resistance** (measured)	**Uncertainty**
p	***S***	***u(S)***	***R"***	***u(R")/R´´***
psi	*mV/(Wcm²)*	*mV/(Wcm²)*	*cm²K/W*	%
1	0.563	0.041	7.344	67.7
3	0.597	0.041	7.344	109.2
5	0.600	0.041	7.344	114.9
10	0.537	0.035	7.344	48.0
15	n.a.	n.a.	n.a.	n.a.
20	0.542	0.039	7.344	53.3
25	n.a.	n.a.	n.a.	n.a.
30	0.511	0.029	7.344	35.8

Table 3.19: Uncertainty in R", cross listed with the uncertainty in S for a given pressure value for *stagnation flow*.

3.6.2.3 Summary of Uncertainties

The uncertainties in the measured gage sensitivities differ a lot between the shear and stagnation stand. For the shear stand, the uncertainty in S is in the range of 15% to 26%, for the stagnation stand the range is much smaller and below the 10% hurdle, namely from 6% to 7%, which can be seen as a very good result. The uncertainties in the thermal resistance have for both stands almost the same range from about 81% to about 39% (shear stand) and from about 115% to about 36% (stagnation stand). The two very high values with about 110% and 115% seem to be exceptional high and should not be considered with too much weight.

4 Results and Discussion

This chapter summarizes all findings obtained by the experiments undertaken. The goal was to show the influence of convectional components on the heat flux measurement. This influence arising from combined convection and conduction on the gage sensitivity was modelled by equation (2.95)

$$S_g = \frac{S_{abs}}{1 + hR''},$$

with S_g, as the gage sensitivity, S_{abs} as the absorbed sensitivity, h, the heat transfer coefficient and R'', as the conductive fraction of the thermal resistance. The sensitivity as a function of h and with a parameter R'' is plotted in Figure 4.1.

As explained in chapter 3: "Convection Calibration Facility" and subchapters; for a set pressure and steady-state temperature conditions, the sensitivity data was taken over a time of 30 seconds (stagnation stand) or 100 seconds (shear stand) and then averaged. The data taken was based on the equation (3.12)

$$S_{SB} = \frac{E_{SB}}{E_{HFM}} S_{HFM} \frac{(T_{air} - T_{plate,HFM})}{(T_{air} - T_{plate,SB})},$$

where the calibration condition $h_{SB} = h_{HFM}$ was applied and substituted in the expressions used in this subchapter. The deltas in the temperatures can be seen as adjustment factors, which are

supposed to be small in most of the cases. S_{HFM} was given and it is known that there is only little influence on convection. The rest of the values were measured and recorded.

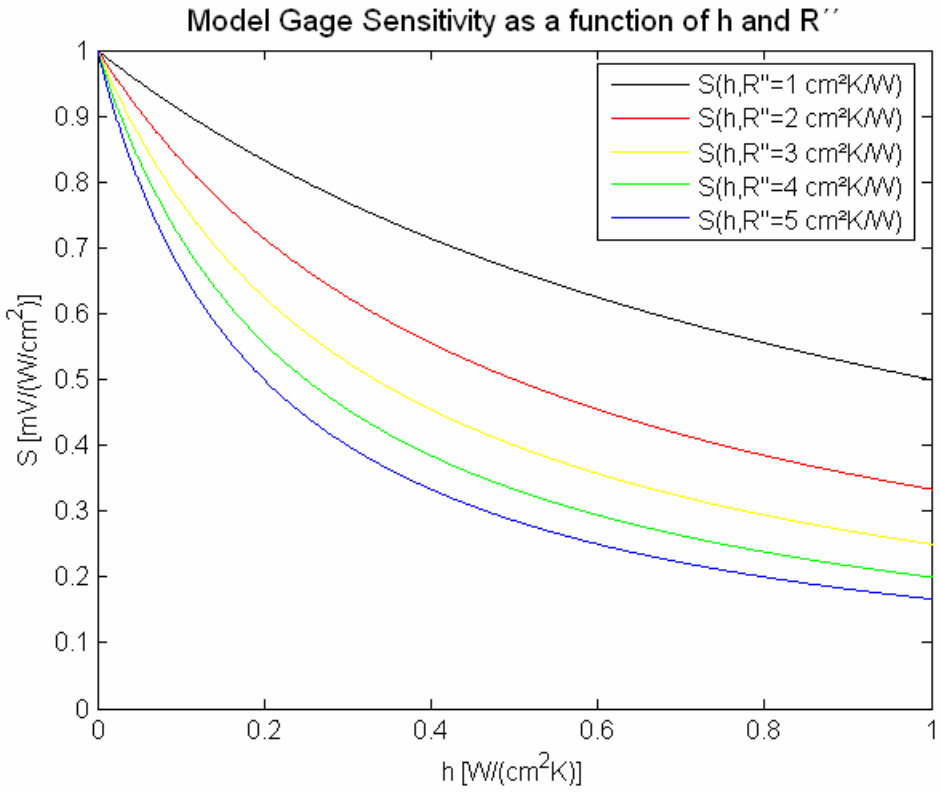

Figure 4.1: Influence of combined convection and conduction on the sensor sensitivity plotted as a function of *h* and parameter R'' with the idealistic model equation. For higher R'' values, the curve is steeper.

4.1 Not Cooled Tests Based on Plate Temperature

The first case examined was the gage sensitivity based on the plate temperature close to the gage not cooled. A typical test procedure with start section, data taking section and ending section for the *shear stand* is shown in Figure 4.2 and for the stagnation stand shown in Figure 4.3. Those examples show the tests of a 1.0 in. SB gage, with serial number 137861 at a pressure of 20 psi (measured *before* the air heater) for the not cooled case. The graph for the shear stand shows the air temperatures at each side, the SB side (blue) and the HFM side (red). Both are in the same range of about 109°C, i.e. the temperature differences from side to side

before the nozzles, measured inside of the box are negligible. The plate temperatures start from about 28°C room temperature and rise until they reach 70°C at the end of the test on both sides with negligible differences. The temperatures differ from test to test, since the flow rate changes with the set pressure. The heat flux signals are both based on the sensitivity determined by the radiation calibration. Both signals show their maximum at around 100 seconds and then decrease to a lower value at the end of the test at about 730 seconds, which was when the LabVIEW VI was stopped. The sensitivity was averaged in the range of 500 seconds to 600 seconds for the shear stand.

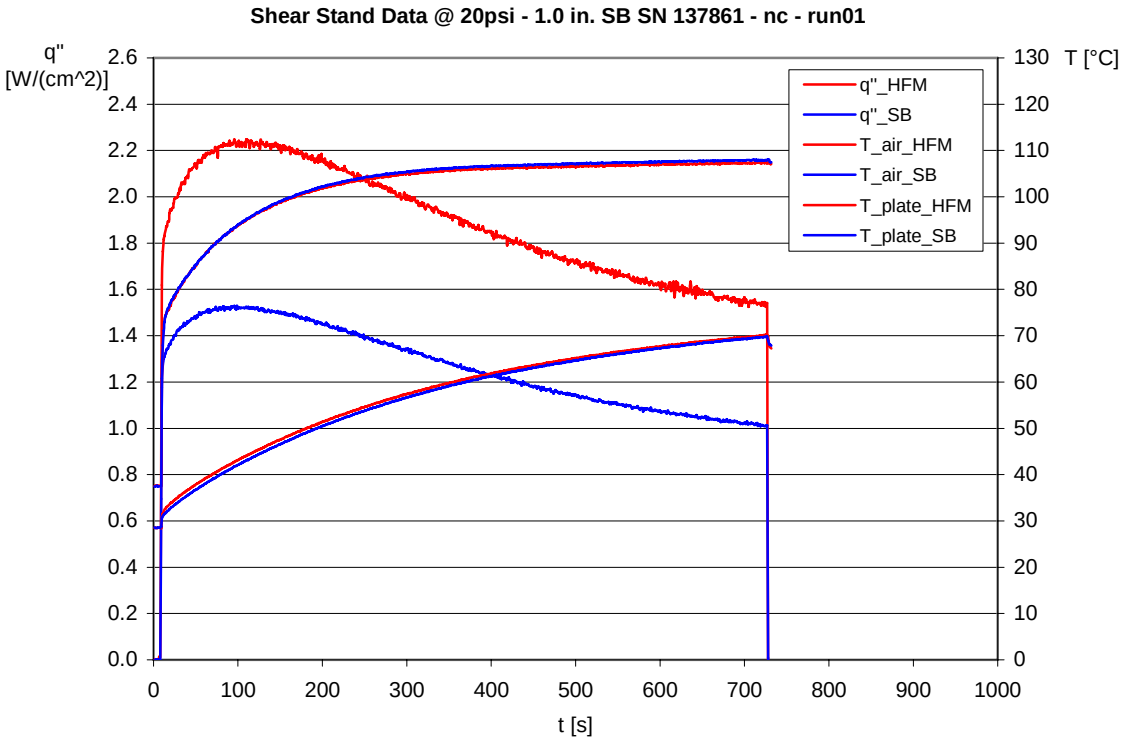

Figure 4.2: Typical data taking procedure for the *shear stand* as an example for the 1.0 in. SB SN 137861 at 20 psi and not cooled (run01). The heat flux signals of the HFM and SB as well as all of the temperatures are shown over time.

The graph for the *stagnation stand* shows the air temperature in the tee nozzle (Figure 4.3, green line), before the flow is divided into two jets. It starts at about room temperature 30°C, until it reaches 88°C at the end of the test. The plate temperature on each side starts also at about room temperature and during the 30 seconds of data taking, temporarily increases up to 40°C before the test ends. The temperatures differ from test to test, since the flow rate changes with the set pressure. The heat flux signals are both based on the sensitivity determined by the radiation calibration. Both signals show the same behavior between the

period of data taking. The HFM, however shows a higher unsteadiness because of its much higher frequency response. The sensitivity was averaged in a range of about 30 seconds.

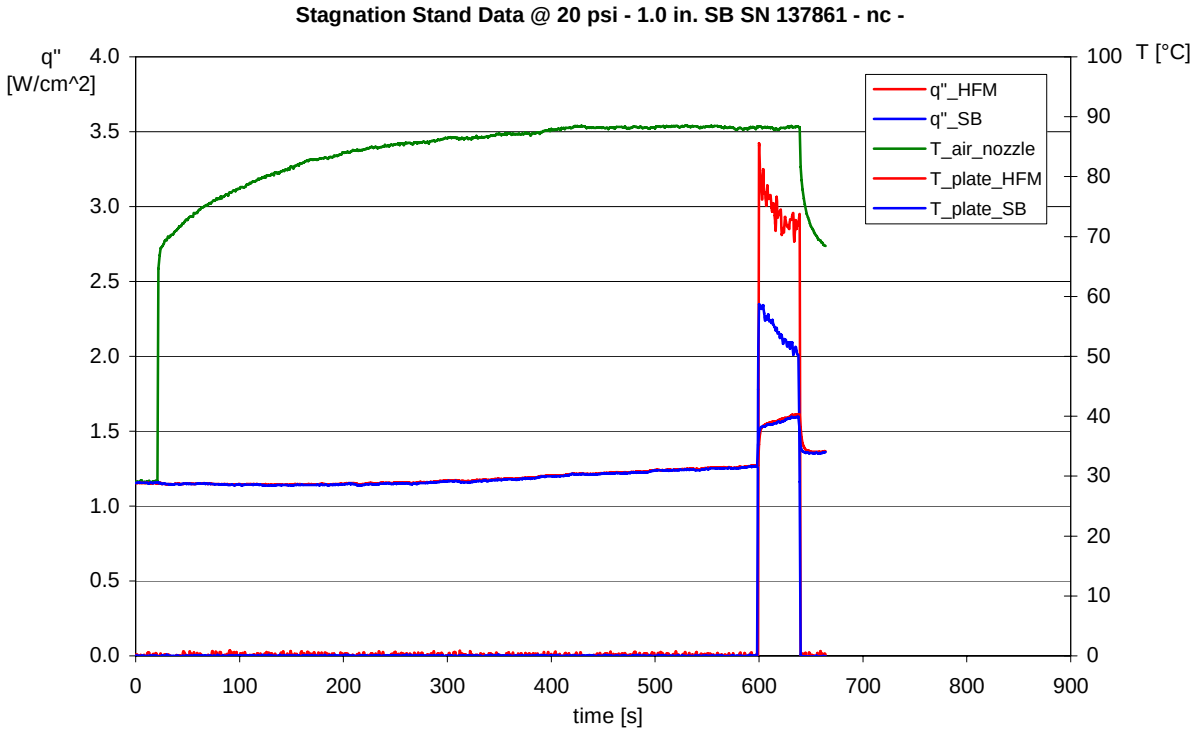

Figure 4.3: Typical data taking procedure for the *stagnation stand* as an example for the 1 in. SB SN 137861 at 20 psi and not cooled. The heat flux signals of the HFM and SB as well as all of the temperatures are shown over time.

Figure 4.4 shows the characteristic progress of *h* for *shear flow* over time during a test run. The *h* from the HFM is assumed correct. For comparison the *h* value for the Schmidt-Boelter gage (SB) is calculated from the radiation calibration, hence the *h* of the SB is different to the HFM. For steady flow conditions, i.e. steady temperature, velocity, pressure, flow rate, *h* will be constant, which indicates that the delta of the temperature and the heat flux changes in the same way.

For *stagnation flow*, Figure 4.5 indicates that *h* at the SB is not constant and hence the flow properties are not constant. Heat flux and temperatures do not change in the same way. This would explain the deviations of the measured sensitivities from the theoretical curve as shown in Figure 4.11.

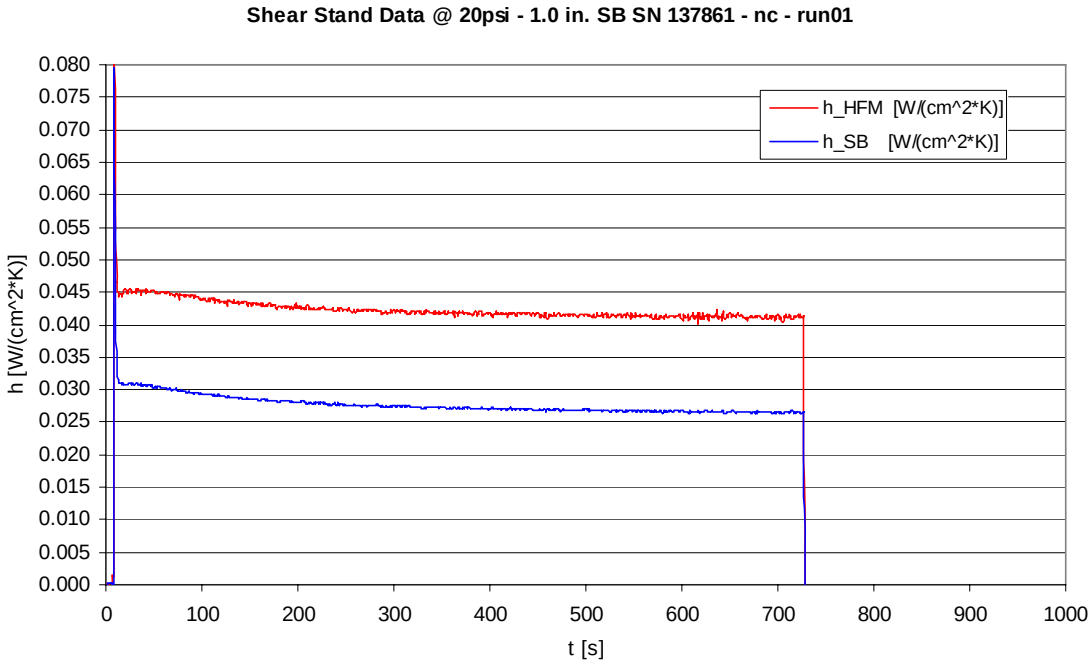

Figure 4.4: Characteristics of *h* over time for *shear flow* for the 1 in. SB SN 137861 at 20 psi and not cooled

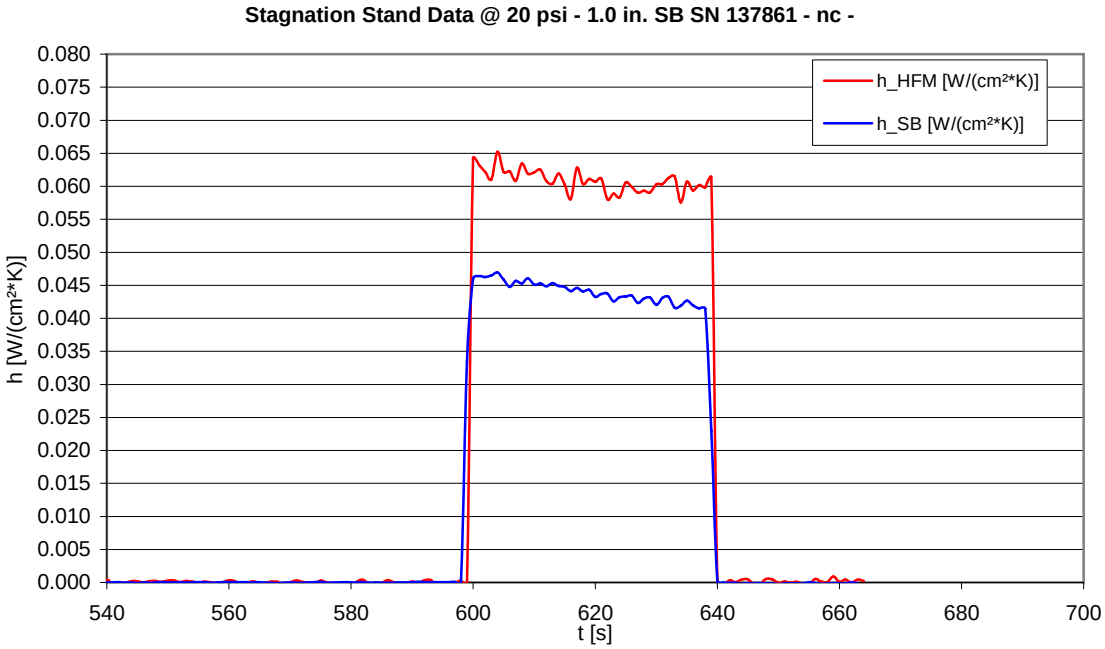

Figure 4.5: Characteristics of *h* over time for *stagnation flow* for the 1 in. SB SN 137861 at 20 psi and not cooled. Note the stretched data.

By using the sensitivity value obtained from the convection calibration, both curves for *h* will collapse to one single curve, see Figure 4.6 for shear and Figure 4.8 for stagnation flow. Also, using the convection calibration sensitivity for the heat flux signals, the results for *shear flow* from Figure 4.2 show almost a collapse of both heat flux curves, as shown in Figure 4.7. The value for the convection calibration sensitivity was obtained by averaging from 500 to 600 seconds; hence for this region the curves are matching best. Figure 4.9 shows the collapse of the *q''* for *stagnation flow*.

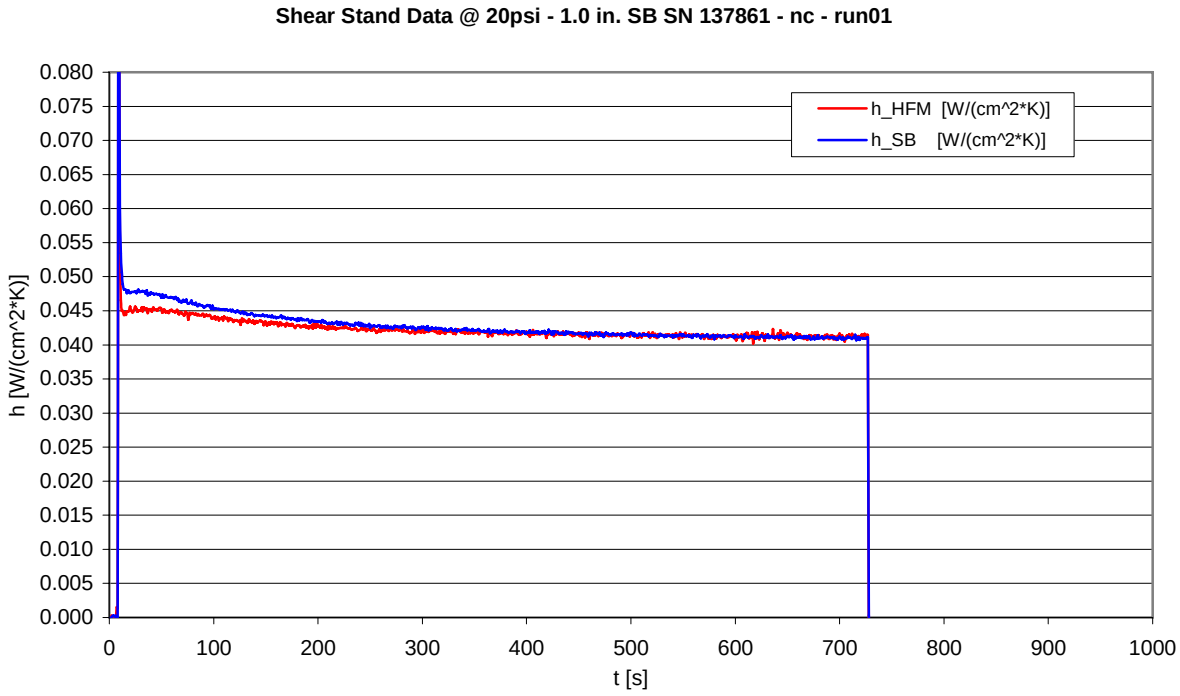

Figure 4.6: Characteristics of h over time for *shear flow* for the 1.0 in. SB SN 137861 at 20 psi and not cooled obtained by using the convection calibration sensitivity

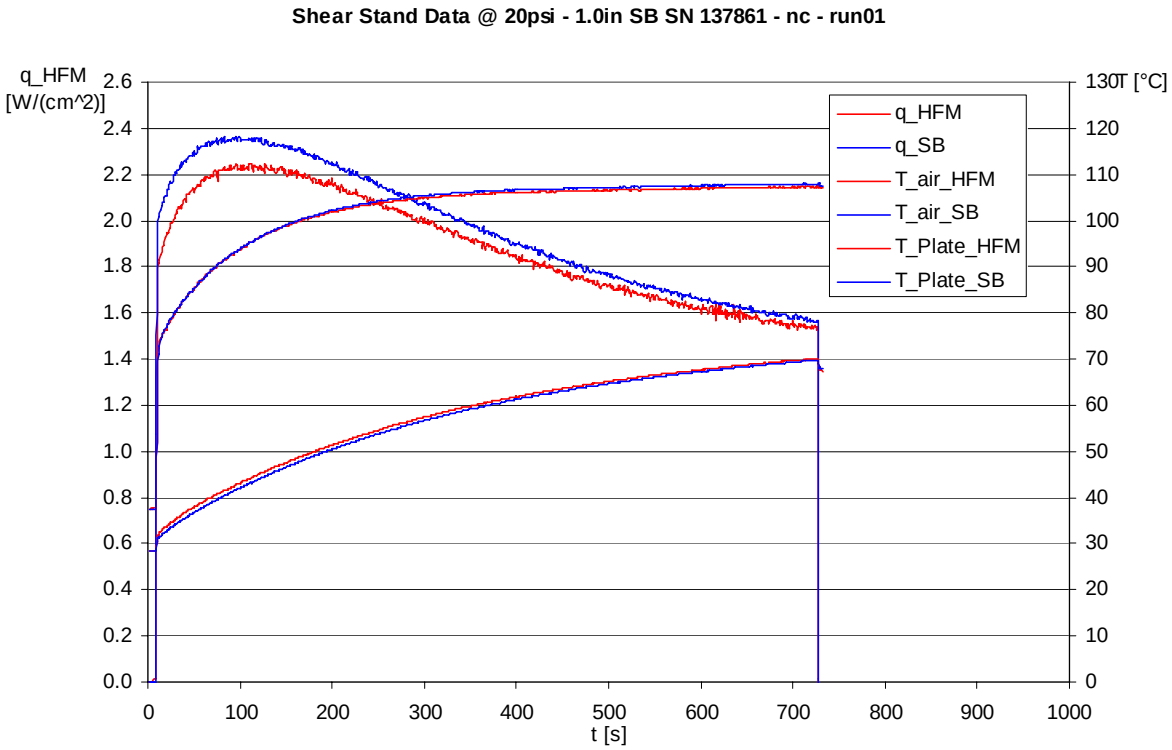

Figure 4.7: Typical data taking procedure for the *shear stand*, obtained by using the convection calibration sensitivity as well as all of the temperatures are shown over time. Further explanations see text.

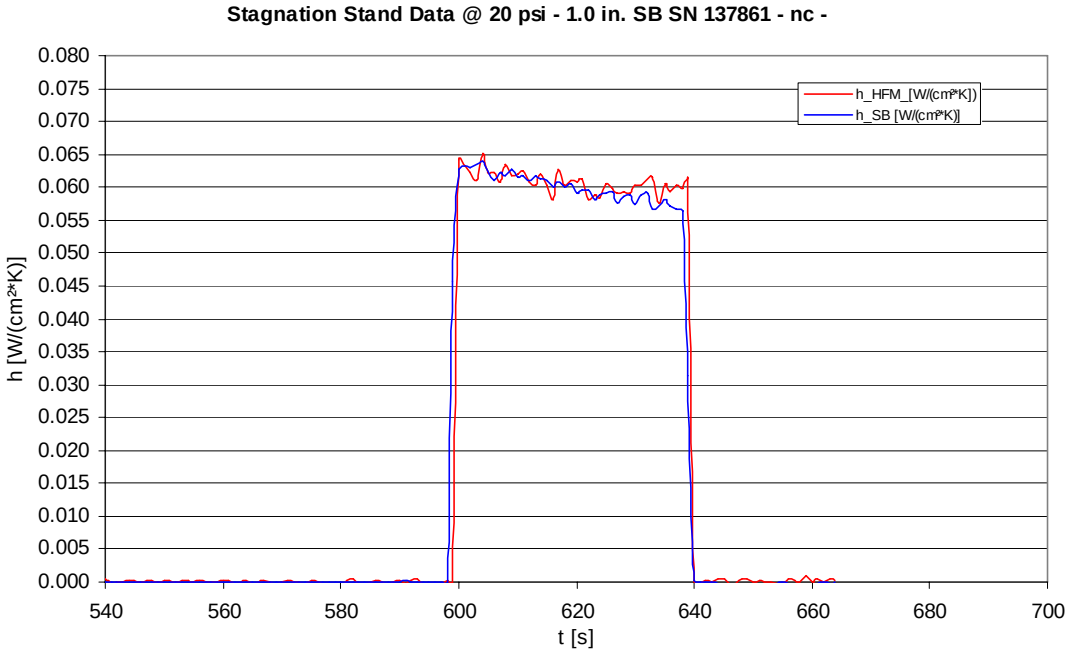

Figure 4.8: Characteristics of *h* over time for *stagnation flow* for the 1 in. SB SN 137861 at 20 psi and not cooled obtained by using the convection calibration sensitivity.

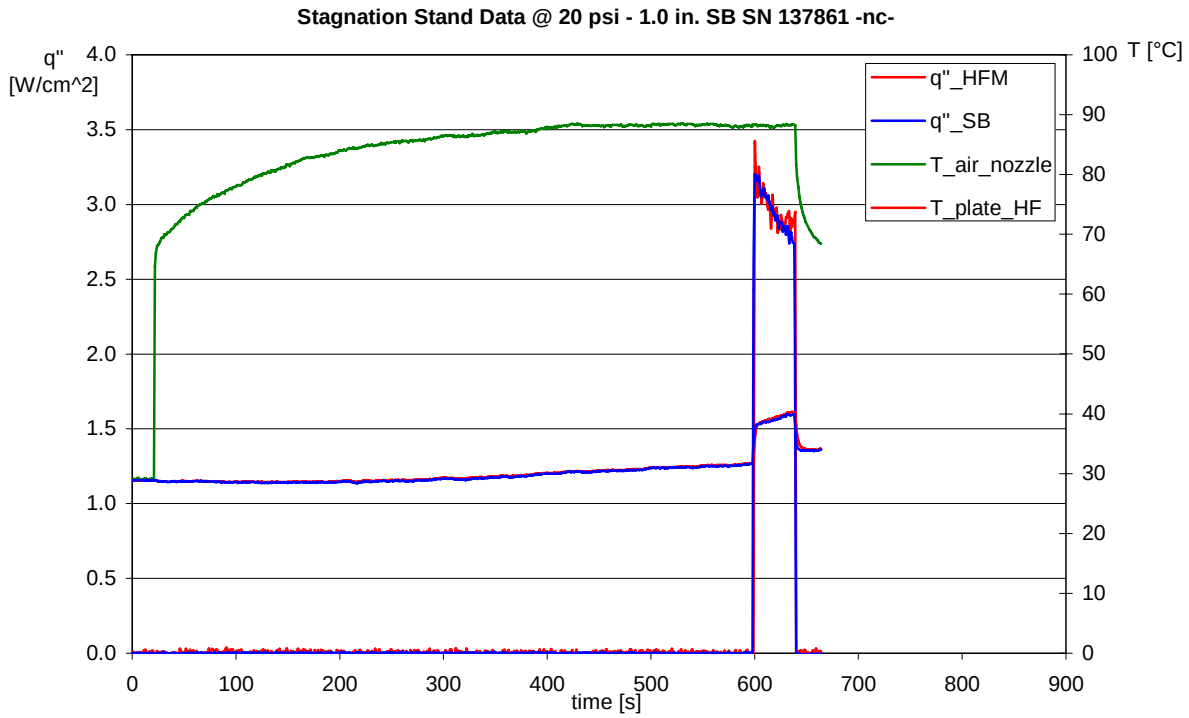

Figure 4.9: Typical data taking procedure for the *shear stand* as an example for the 1 in. SB SN 137861 at 20 psi and not cooled. The heat flux signal at HFM and SB, obtained by using the convection calibration sensitivity as well as all of the temperatures are shown over time. Further explanations see text.

Due to the different flow fields provided by the two nozzles, as shown in section 3.4.2: "Shear Stand Performance", the plate was turned around and the Schmidt-Boelter gage was tested on both nozzles. The resulting sensitivity was averaged between the tests on both sides of the shear stand. Figure 4.10 shows the sensitivity values obtained from orientation 1, which means the Schmidt-Boelter at nozzle 2 (blue) and orientation 2, meaning the Schmidt-Boelter gage at nozzle 1 (green). The red values are the average values of both measured sensitivities. There was no need to average the values obtained from the stagnation stand, since the difference from side to side was within a range of three per cent difference [9].

The bold, red solid line is obtained from a least squares curve fit based on the not cooled sensitivity data. It was obtained by minimizing the distance of the measured values to the theoretical values and forcing the curve through the radiation calibration point at $h = 0$. The MATLAB program used is attached in appendix F MATLAB Codes.

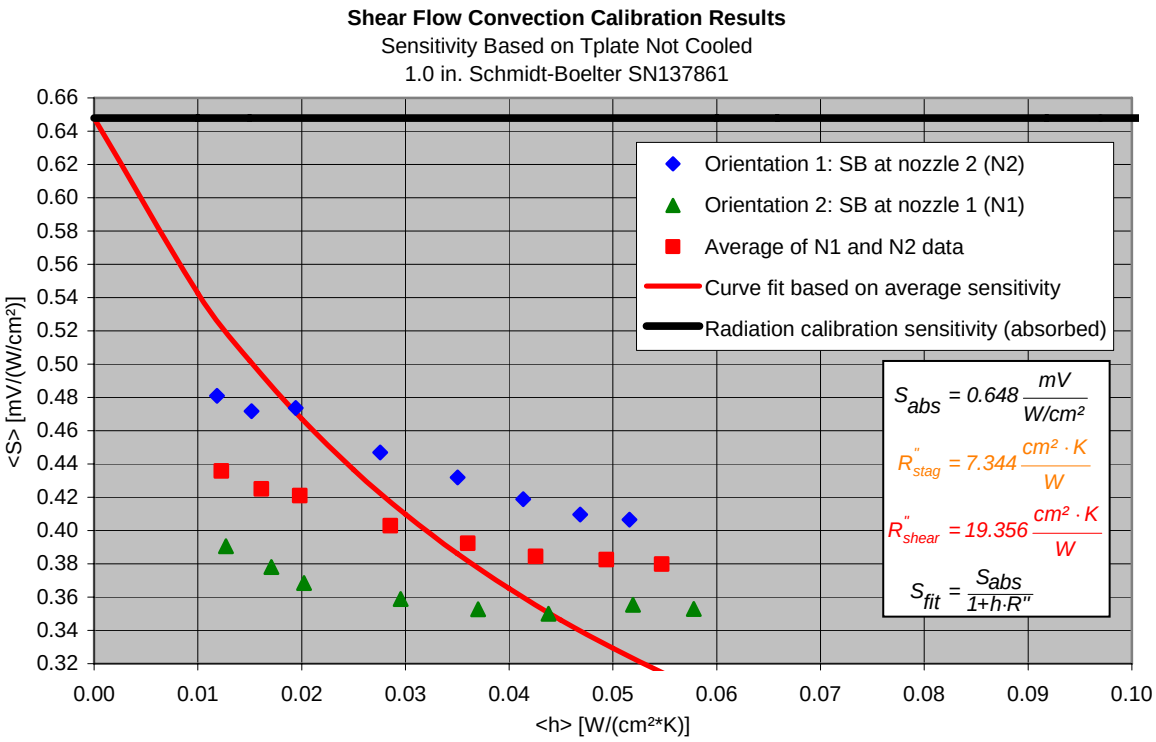

Figure 4.10: Averaged Sensitivity (red) obtained by averaging the sensitivities measured at nozzle 2, right nozzle (orientation 1, blue) and nozzle 1, left nozzle (orientation 2, green) for the 1 in. SB SN 137861 at 20 psi in *shear flow*. Each dot represents a different pressure value.

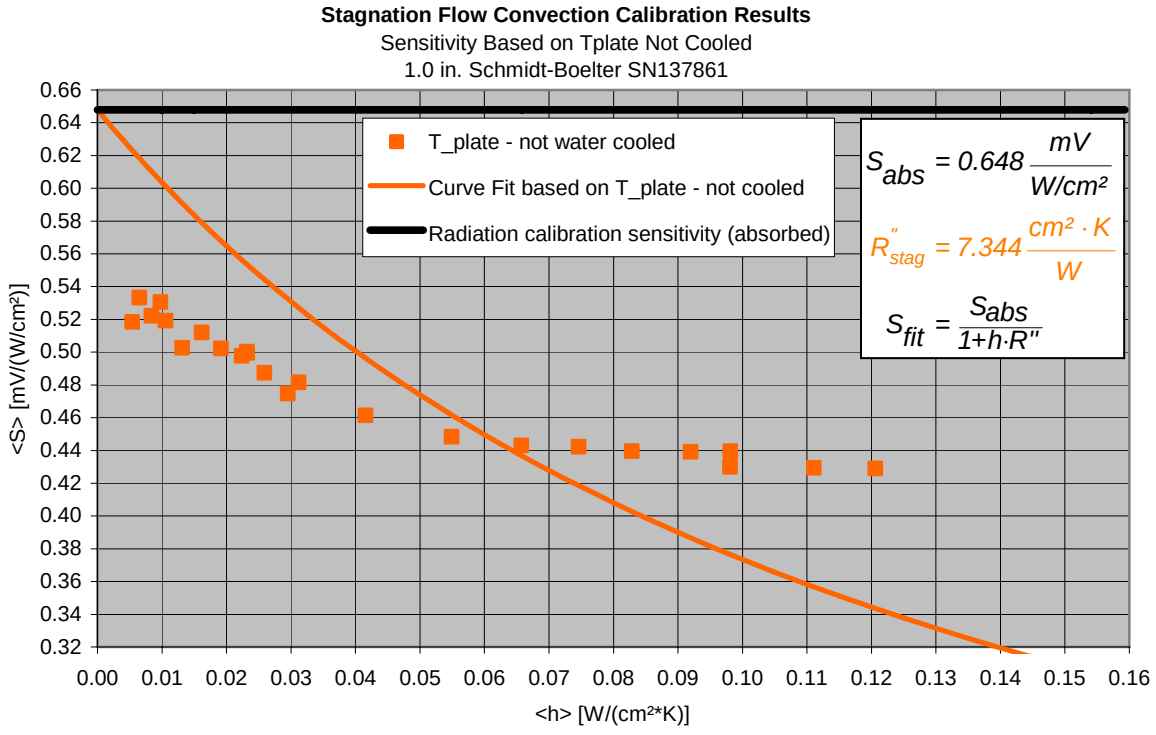

Figure 4.11: Measured sensitivities for the 1 in. SB SN 137861 at 20 psi in *stagnation flow* (not cooled, based on T_{plate}) compared to the theoretical values (orange solid line), based on a least squares curve fit. Each dot represents a different pressure value.

4.2 Water Cooled Tests Based on Plate Temperature

For a cooled SB gage, the temperature of the plate close to the SB gage will change differently than for the not cooled case.

A test run with a cooled gage for shear flow is shown in Figure 4.12 and for stagnation flow in Figure 4.13. The plate temperature at the side of the cooled Schmidt-Boelter gage shows a different progress than the temperature of the plate close to the HFM. The heat flux signal of the SB shows asymptotic behavior, which is very different than the decrease of the HFM heat flux signal. Consequently, the h is not constant over time as seen in Figure 4.14 for shear flow. The resulting sensitivities, for each run (orientation) based on the plate temperature with water cooling vary with time, which is not correct. Figure 4.16 shows the averaged sensitivities for shear flow, obtained from the values of both orientations.

For stagnation flow, Figure 4.15 indicates the same problem of a non-constant heat transfer coefficient h, meaning that the sensitivity values based on the plate temperature with a water cooled gage will deviate from the theoretical values, which can be seen in Figure 4.17.

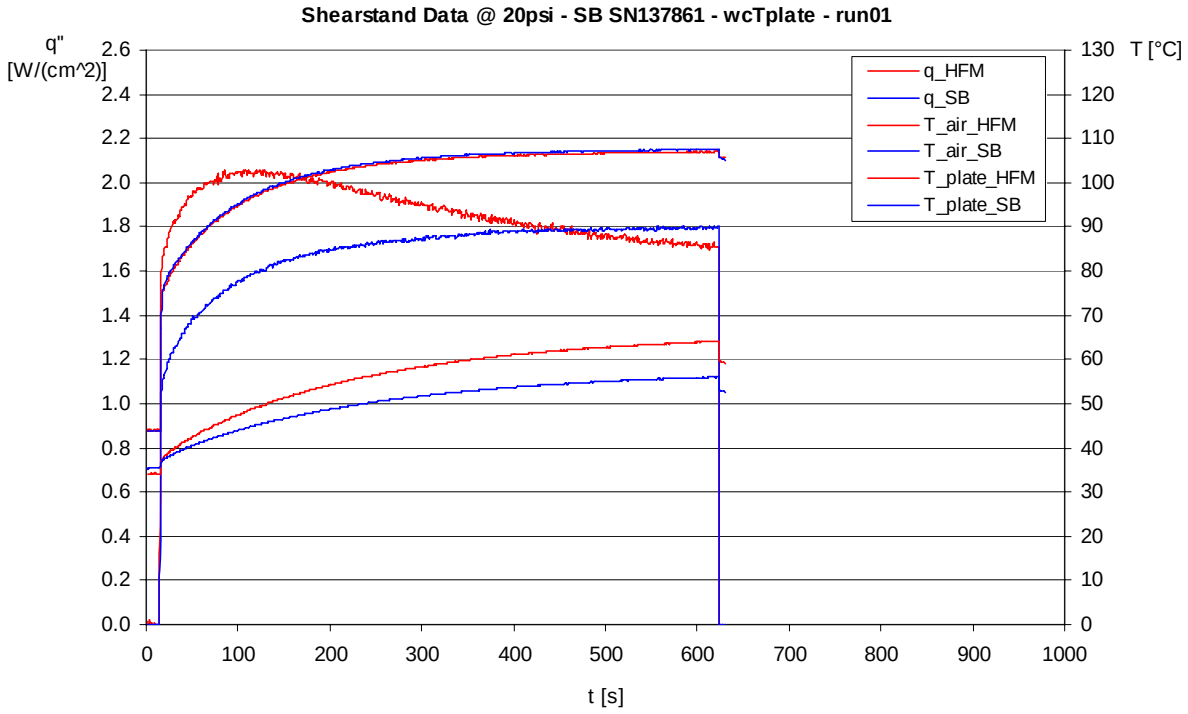

Figure 4.12: Typical data taking procedure for the *shear stand* as an example for the 1 in. SB SN 137861 at 20 psi and water cooled. The heat flux signal at HFM and SB as well as all of the temperatures are shown over time.

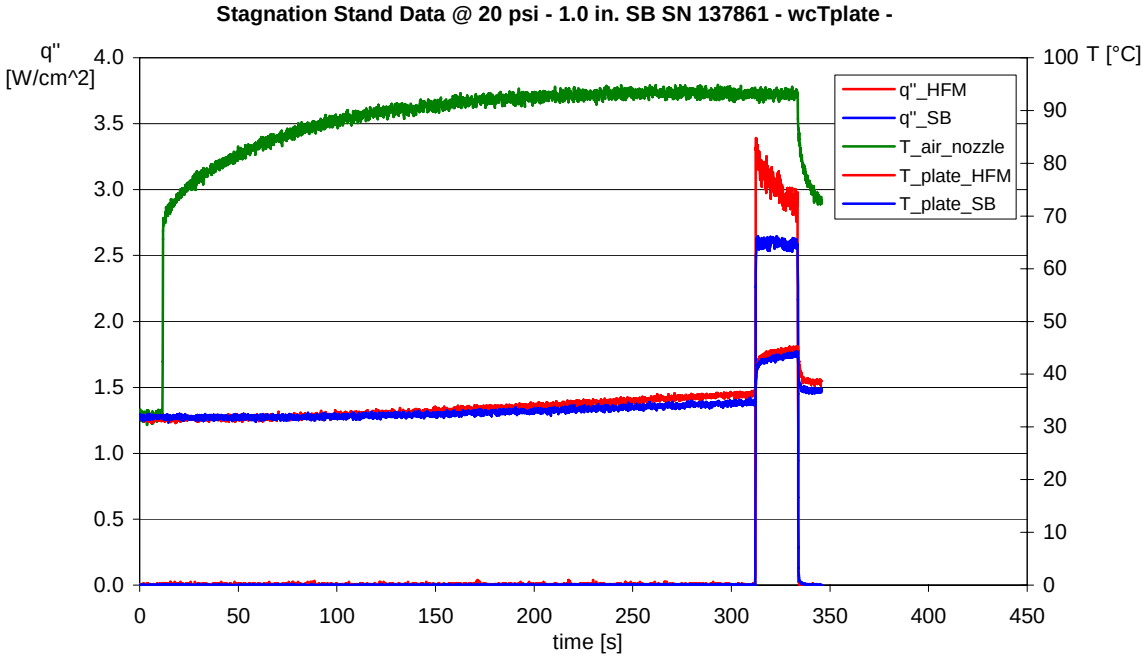

Figure 4.13: Typical data taking procedure for the *stagnation stand* as an example for the 1 in. SB SN 137861 at 20 psi and water cooled. The heat flux signal at HFM and SB as well as all of the temperatures are shown over time.

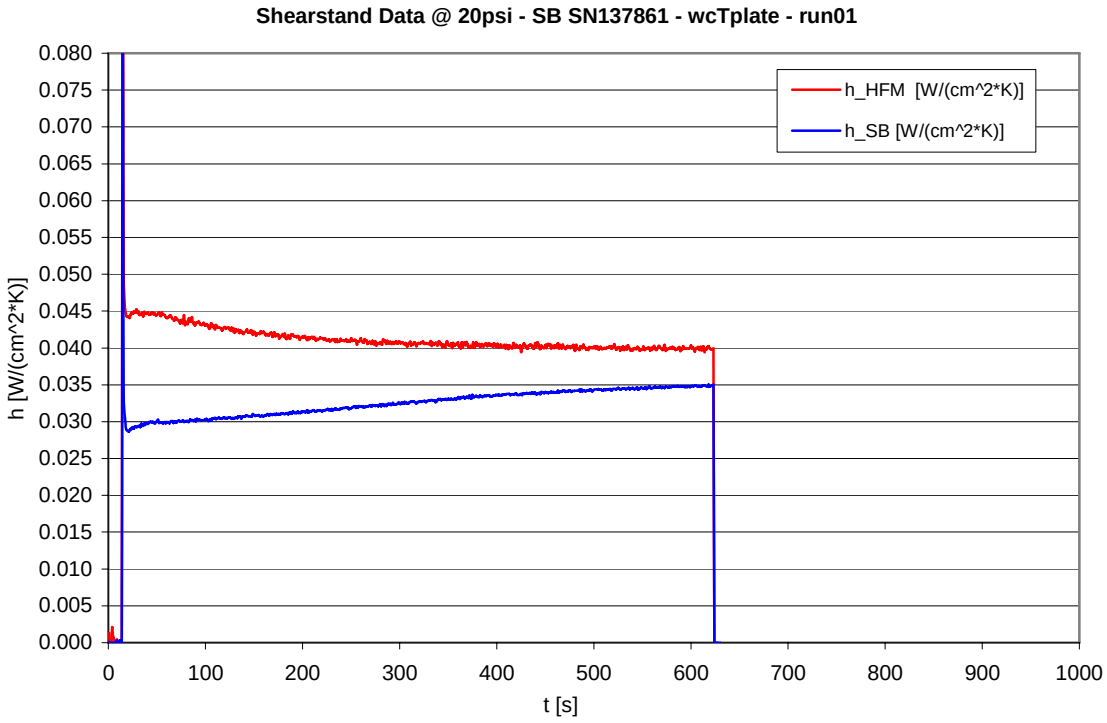

Figure 4.14: Characteristics of *h* over time for *shear flow* for the 1 in. SB SN 137861 at 20 psi and water cooled.

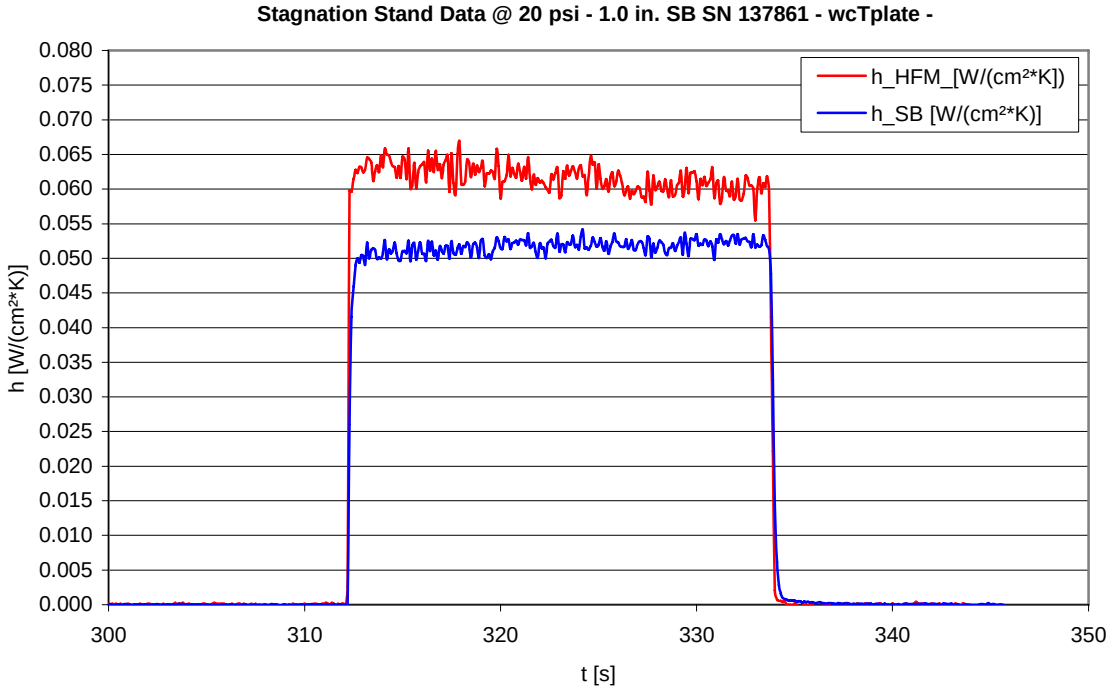

Figure 4.15: Characteristics of *h* over time for *shear flow* for the 1 in. SB SN 137861 at 20 psi and water cooled.

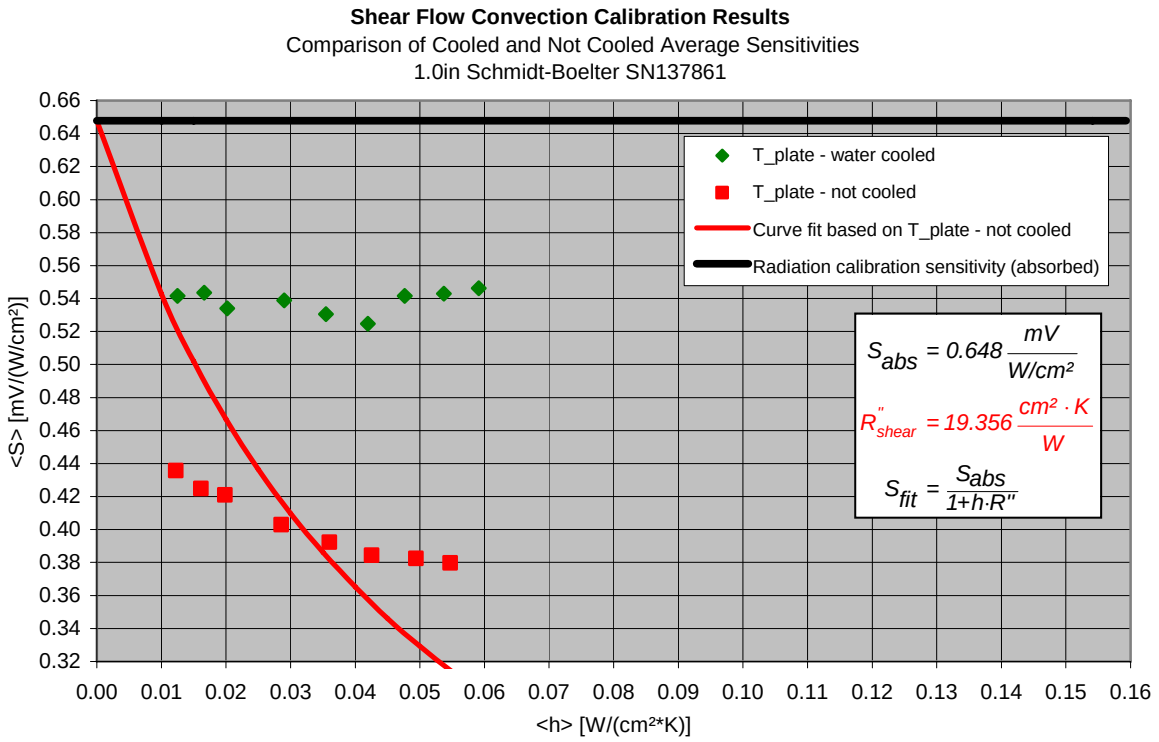

Figure 4.16: Measured sensitivities (cooled, based on T_{plate}, green) compared to the theoretical values (red solid line), based on a least squares curve fit of the data obtained from the not cooled case (red) for the 1 in. SB SN 137861 in *shear flow*.

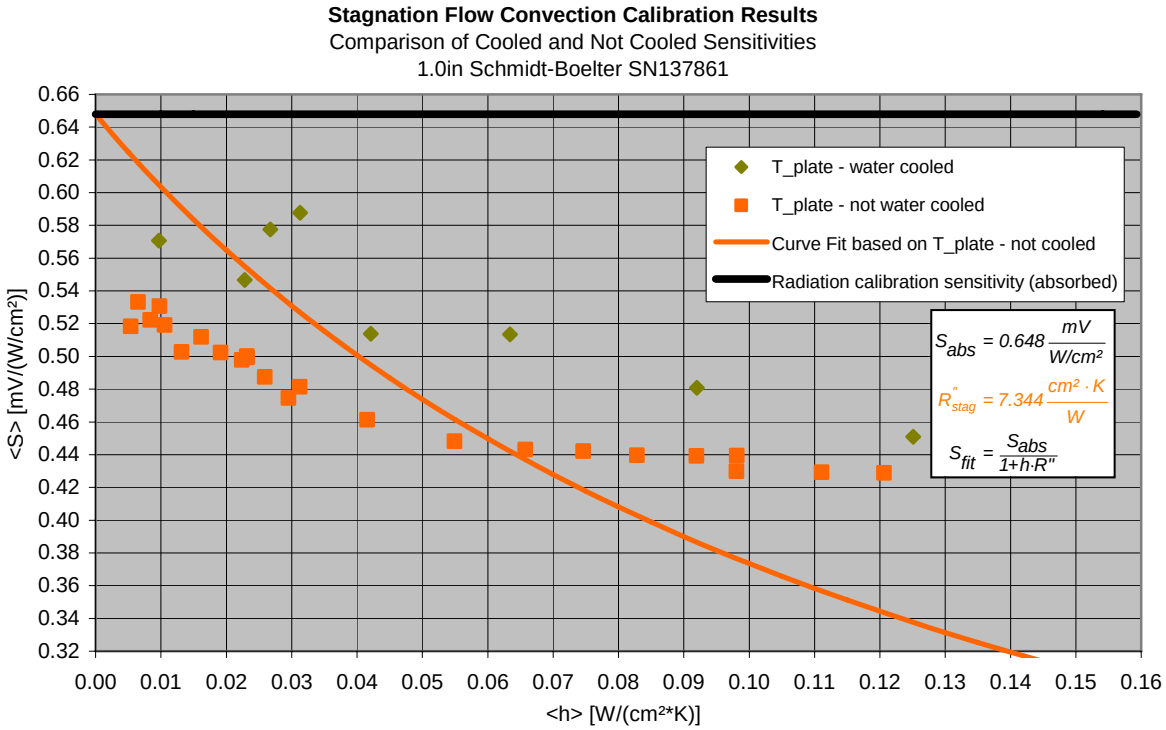

Figure 4.17: Measured sensitivities (cooled, based on T_{plate}, light green) compared to the theoretical values (orange solid line), based on a least squares curve fit of the data obtained from the not cooled case (orange) for the 1 in. SB SN 137861 in *stagnation flow*.

4.3 Water Cooled Tests Based on Water Temperature

The water cooled sensitivities based on the plate temperature did not show satisfying results, especially for shear flow. For that reason, the sensitivity data was also taken based on the water temperature of the cooling water. The test procedures for this case are shown in Figure 4.18 for shear flow and in Figure 4.19 for stagnation flow and are similar to Figure 4.12 and Figure 4.13, except for the addition of the water temperature.

For this case now the progress of *h* over time for shear *and* for stagnation flow is perfectly constant, indicating constant flow conditions on both sides (HFM and SB side). As a result, we can see the better match of the measured values with the theoretical values in Figure 4.22 for shear flow and in Figure 4.23 for stagnation flow.

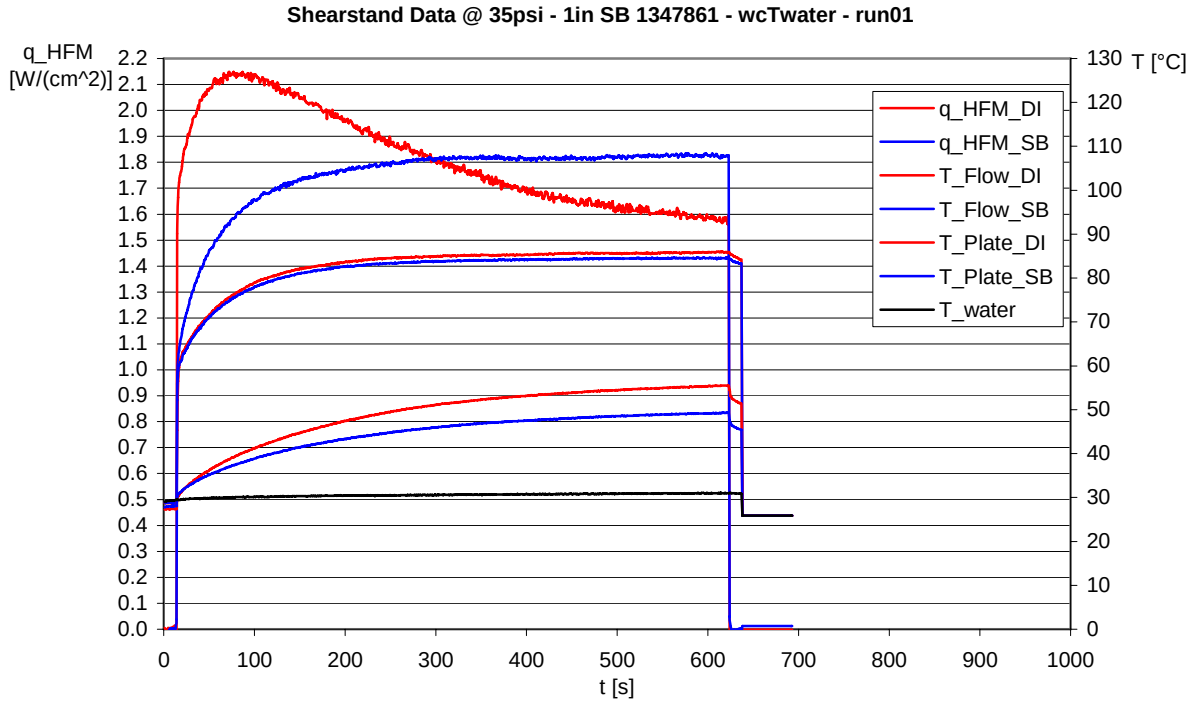

Figure 4.18: Typical data taking procedure for the *shear stand* as an example for the 1 in. SB SN 137861 at 35 psi, showing a complete test run and water cooled. The heat flux signal at HFM and SB as well as all of the temperatures, including the water temperature are shown over time. (For the chart 35 psi instead of 20 psi was chosen to show a complete test procedure with ending section).

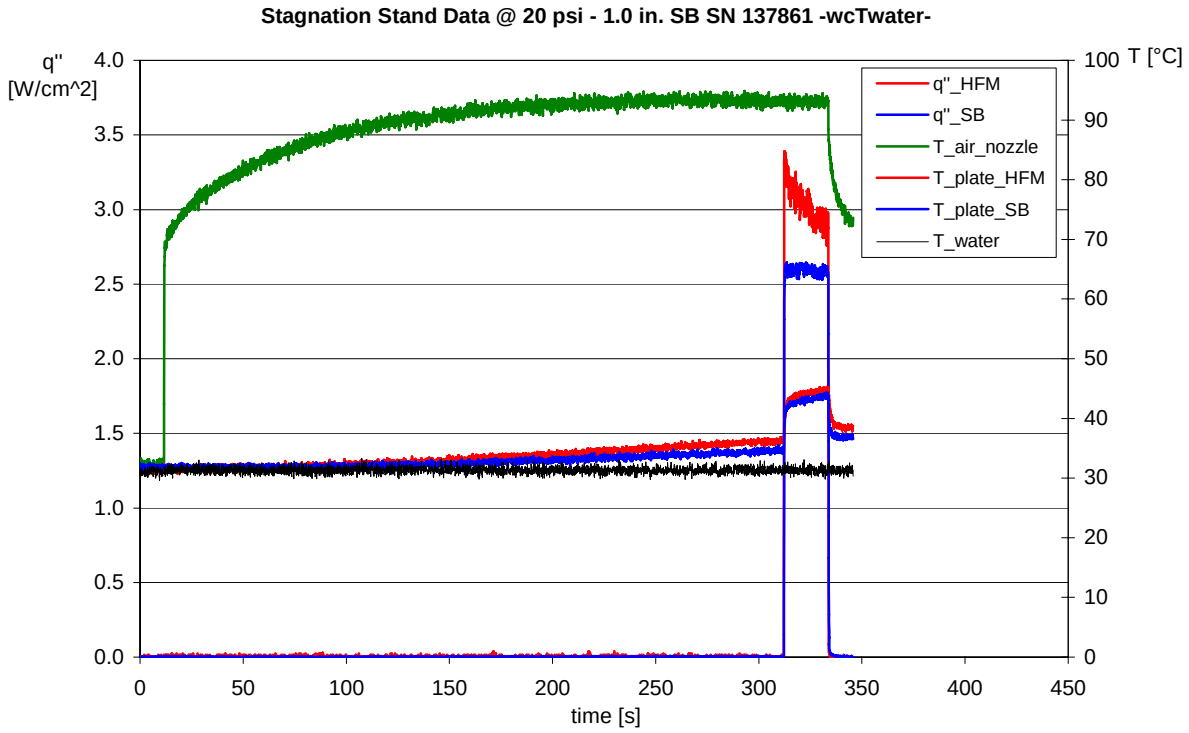

Figure 4.19: Typical data taking procedure for the *stagnation stand* as an example for the 1 in. SB SN 137861 at 20 psi, showing a complete test run and water cooled. The heat flux signal at HFM and SB as well as all of the temperatures, including the water temperature are shown over time.

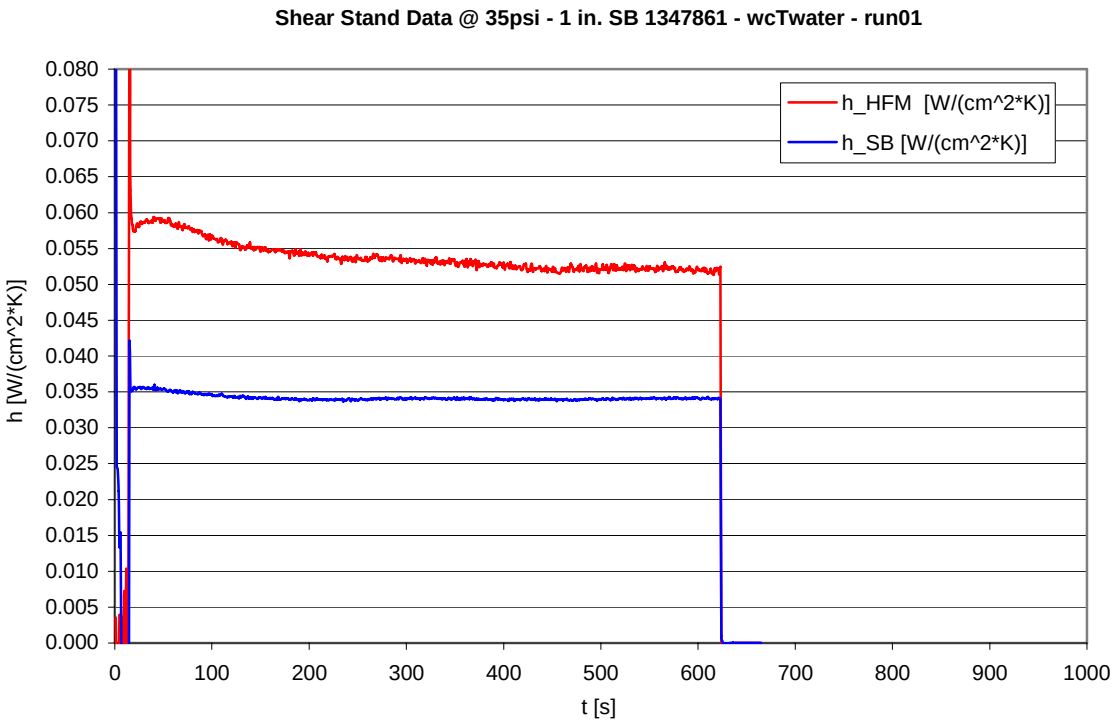

Figure 4.20: Characteristics of *h* over time for *shear flow* for the 1 in. SB SN 137861 at 20 psi and water cooled.

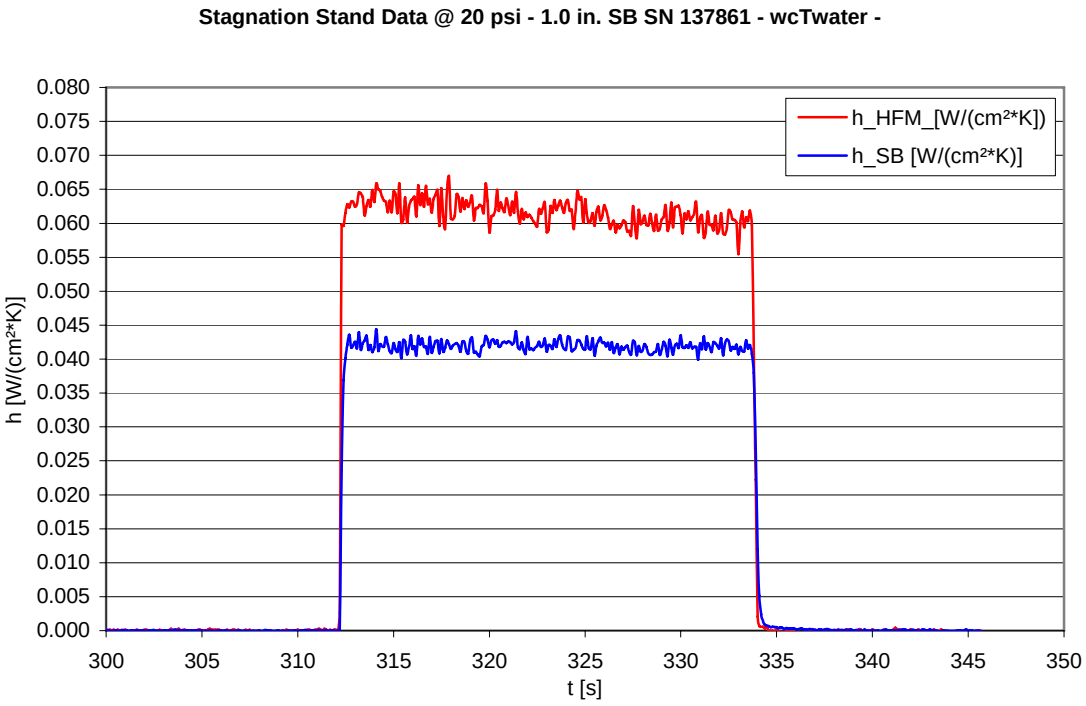

Figure 4.21: Characteristics of *h* over time for *shear flow* for the 1 in. SB SN 137861 at 20 psi and water cooled.

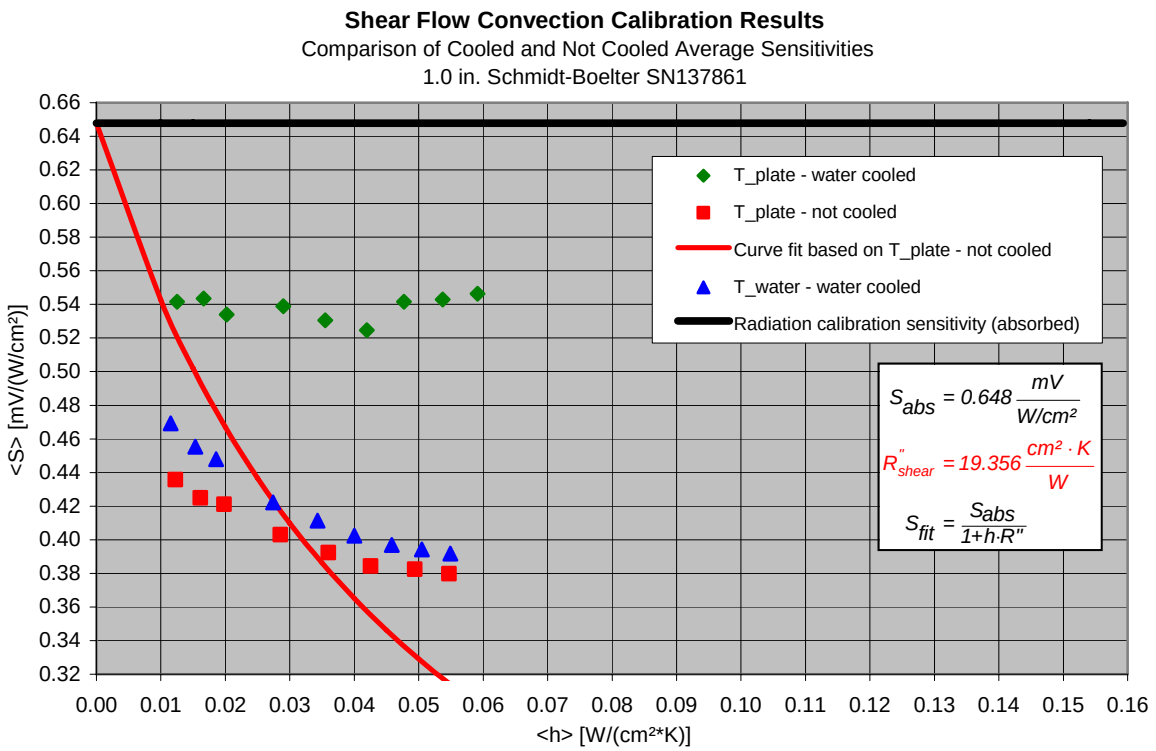

Figure 4.22: Measured sensitivities (cooled, based on T_{plate}, green) compared to the theoretical values (red solid line), based on a least squares curve fit of the data obtained from the not cooled case (red) for the 1 in. SB SN 137861 in *shear flow*.

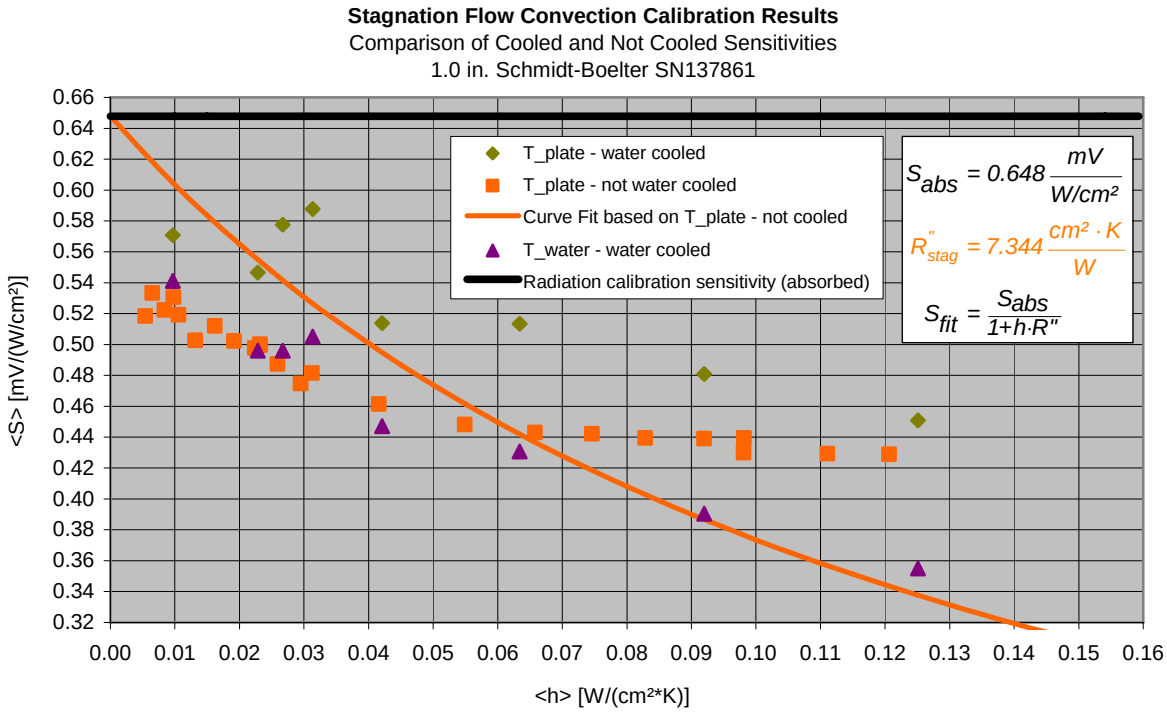

Figure 4.23: Measured sensitivities (cooled, based on T_{plate}, light green) compared to the theoretical values (orange solid line), based on a least squares curve fit of the data obtained from the not cooled case (orange) for the 1 in. SB SN 137861 in *stagnation flow*.

4.4 Turn Tests

The Schmidt-Boeleter gage consists of an aluminum wafer of rectangular shape (Figure 2.11 and chapter 2.3.1.2: "The Schmidt-Boelter Gage"). One has to assume that there may be an influence of the wafer orientation on the gage sensitivity relative to the flow direction, but only for shear flow regimes. Due to that fact, turn tests were undertaken. Figure 4.24 shows the results of these tests.

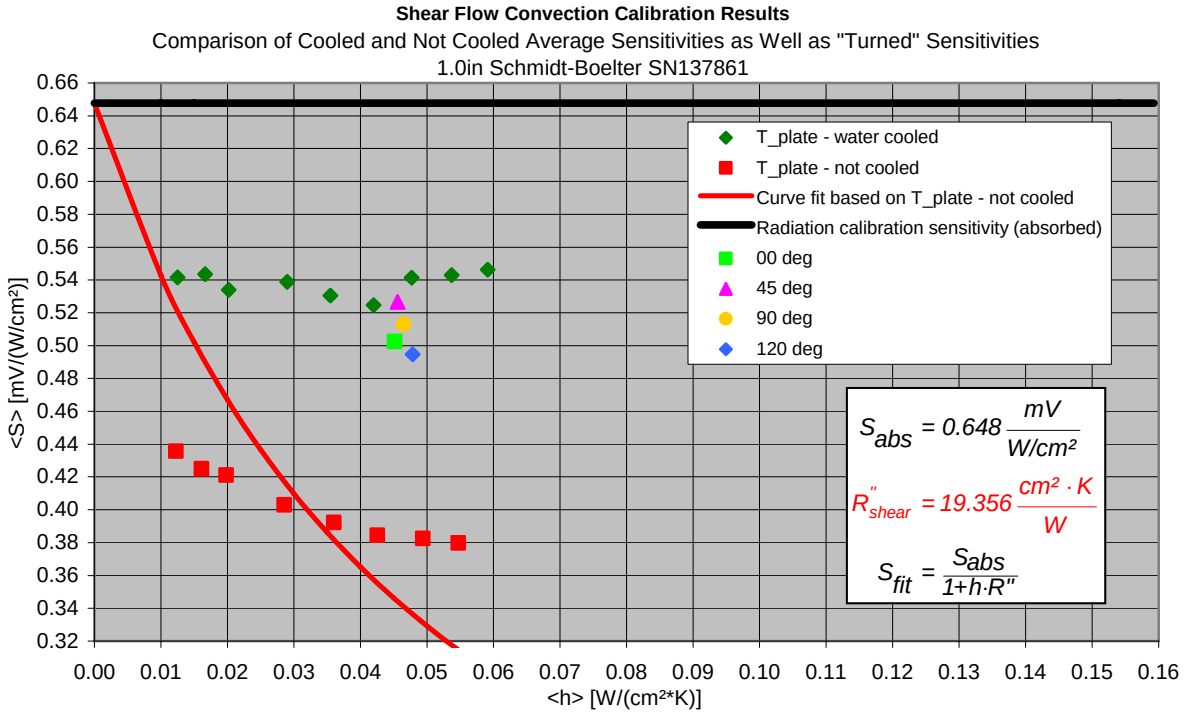

Figure 4.24: Turn tests, undertaken for the water cooled sensitivity based on the plate temperature at 20 psi in angle deltas of 45°, respectively 35° from the original position, counter clock wise.

The tests showed a small influence of the wafer orientation on the gage sensitivity. Table 4.1 summarizes the uncertainties emerging from the wafer orientation in per cent. Considering the uncertainties found in chapter 3.6.2 "Uncertainty Analysis" the differences emerging from the wafer orientation lies well within the uncertainties of sensitivities obtained from the tests, see Table 3.16 and Table 3.17.

Parameter	<S>	<h>	ΔS/S	Δh/h
Unit	$\frac{mV}{W/cm^2}$	$\frac{W}{cm^2 K}$	[%]	[%]
original	0.491	0.044	-	-
000°	0.503	0.045	**2.3**	**2.8**
045°	0.527	0.046	**7.2**	**3.7**
090°	0.513	0.047	**4.4**	**5.9**
120°	0.495	0.048	**0.7**	**8.9**

Table 4.1: Relative differences in per cent of the turned values to the original value in gage sensitivity and heat transfer coefficient.

4.5 Results Summary

4.5.1 The One-Inch Schmidt-Boelter Gages

4.5.1.1 Shear Flow Results

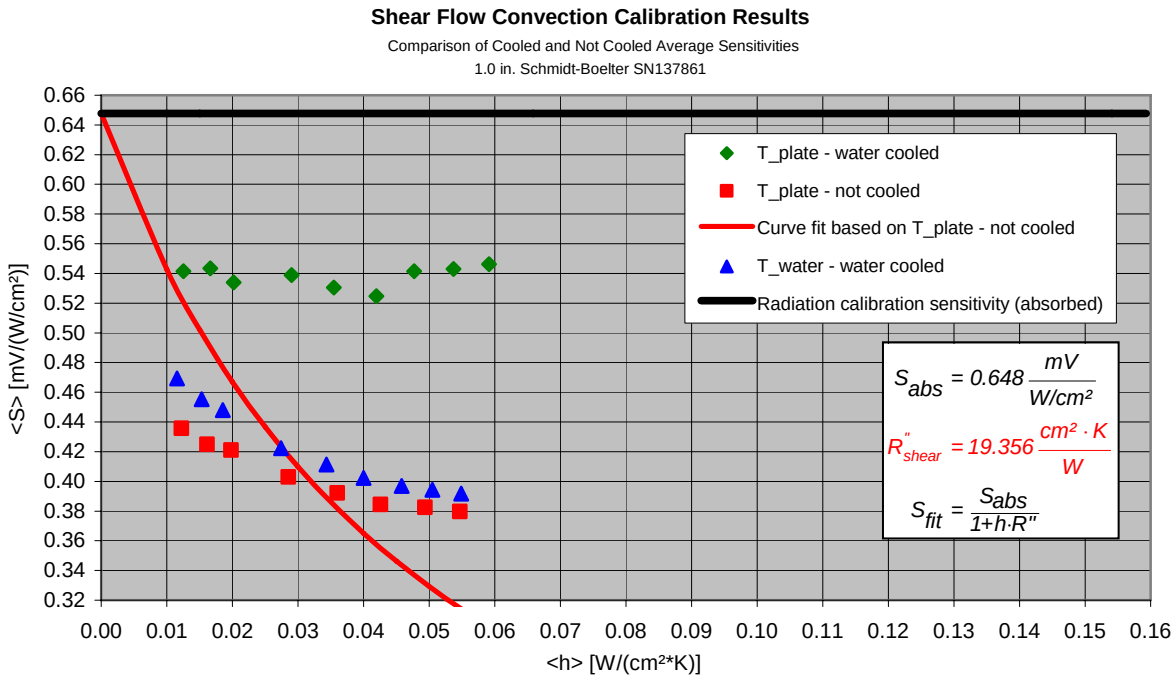

Figure 4.25: Results summary shear flow 1.0 in. SB SN 137861.

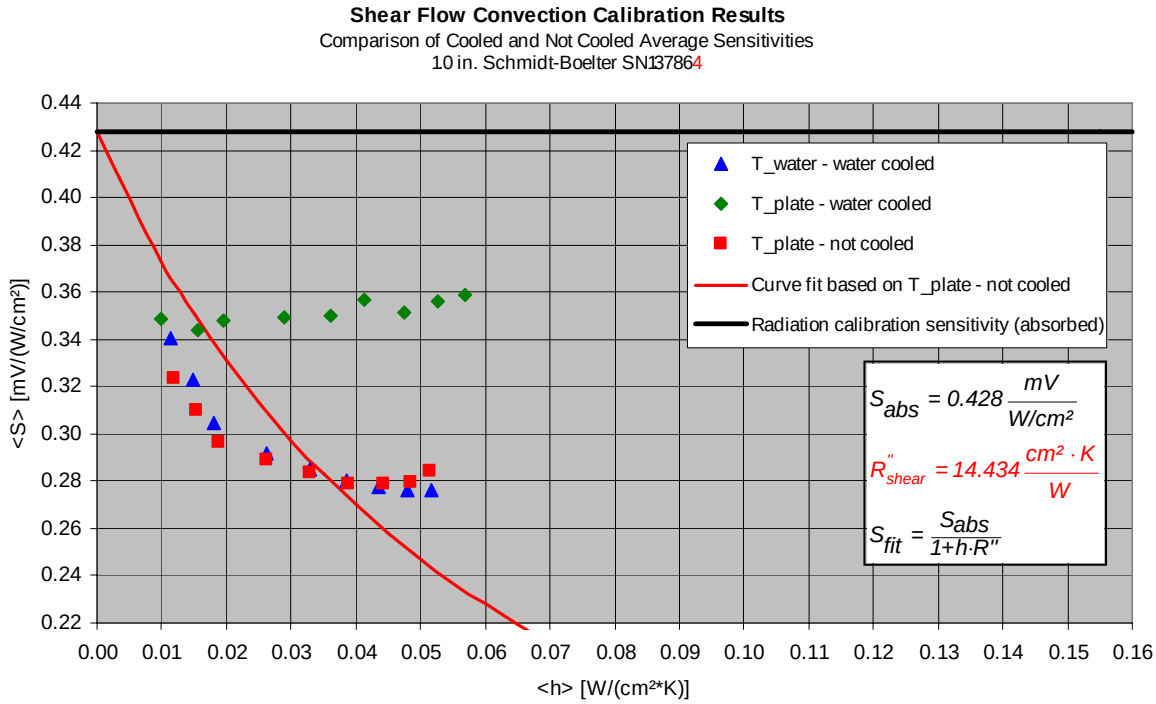

Figure 4.26: Results summary shear flow 1.0 in. SB SN 137864.

4.5.1.2 Stagnation Stand Results

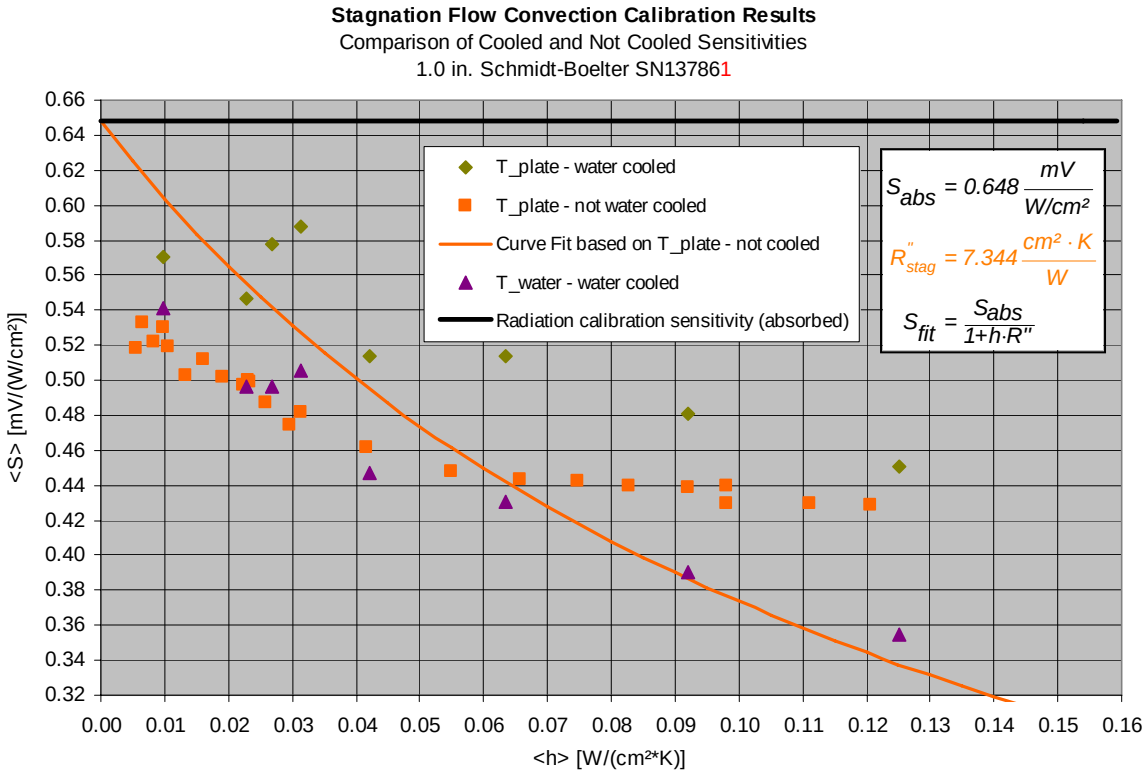

Figure 4.27: Results summary stagnation flow 1.0 in SB SN 137861.

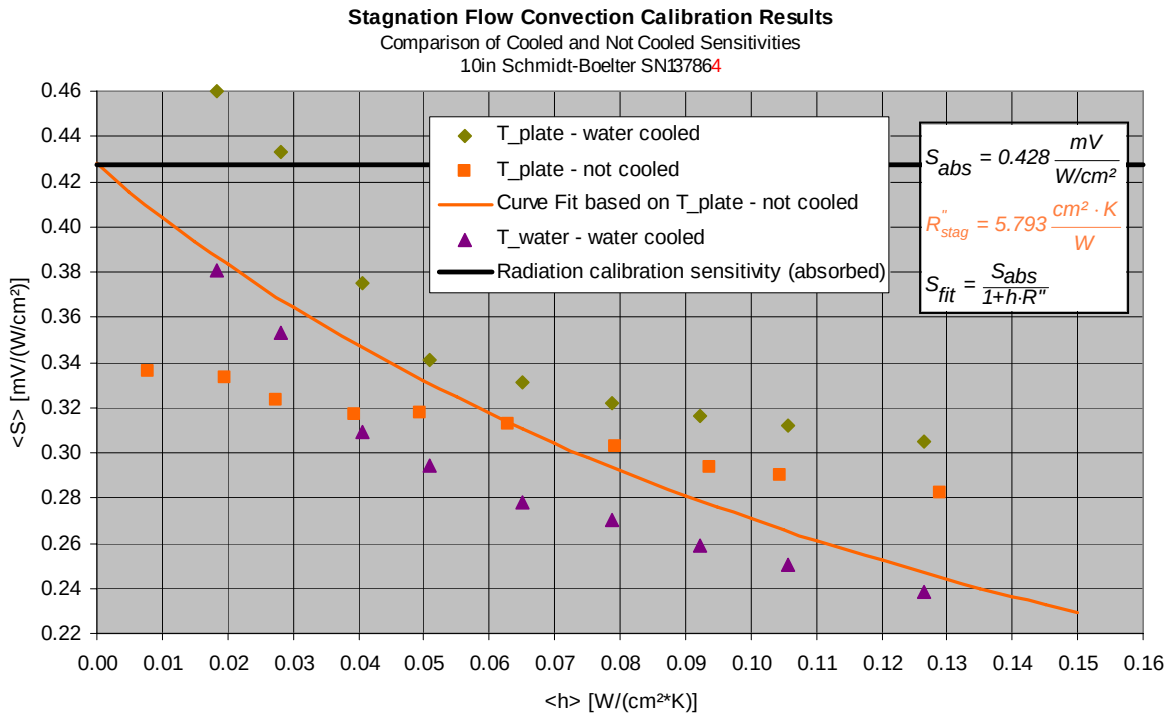

Figure 4.28: Results summary stagnation flow 1.0 in. SB SN 137864.

4.5.1.3 Comparison of Shear and Stagnation Stand Results

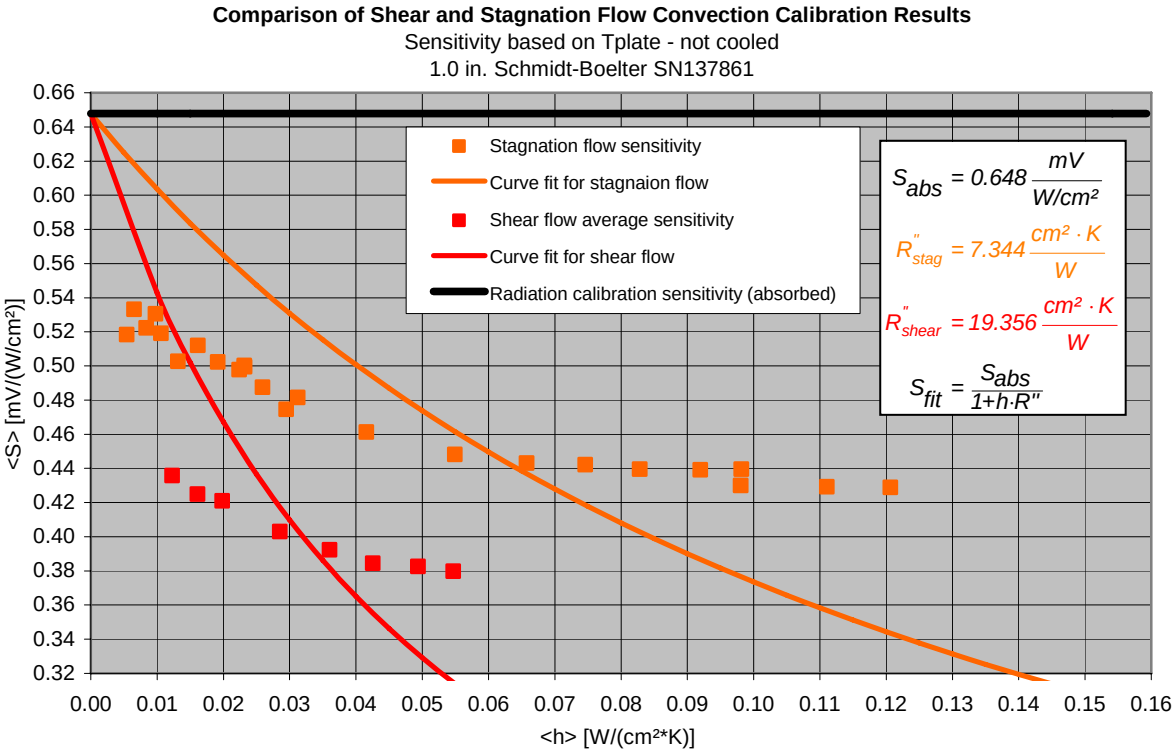

Figure 4.29: Comparison of shear and stagnation flow results, not cooled based on T_{plate} SB SN 137861.

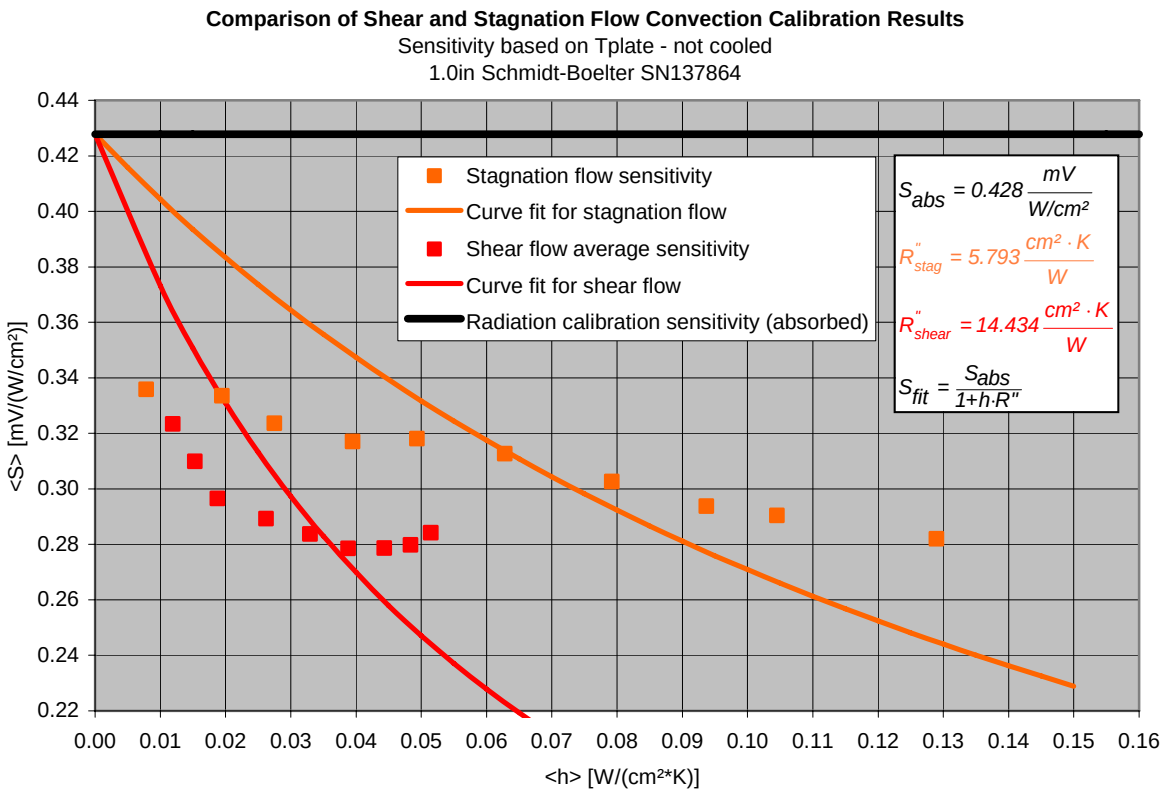

Figure 4.30: Comparison of shear and stagnation flow results, not cooled based on Tplate SB SN 137864.

4.5.2 The One-and-One-Half-Inch Schmidt-Boelter Gages

4.5.2.1 Shear Stand Results

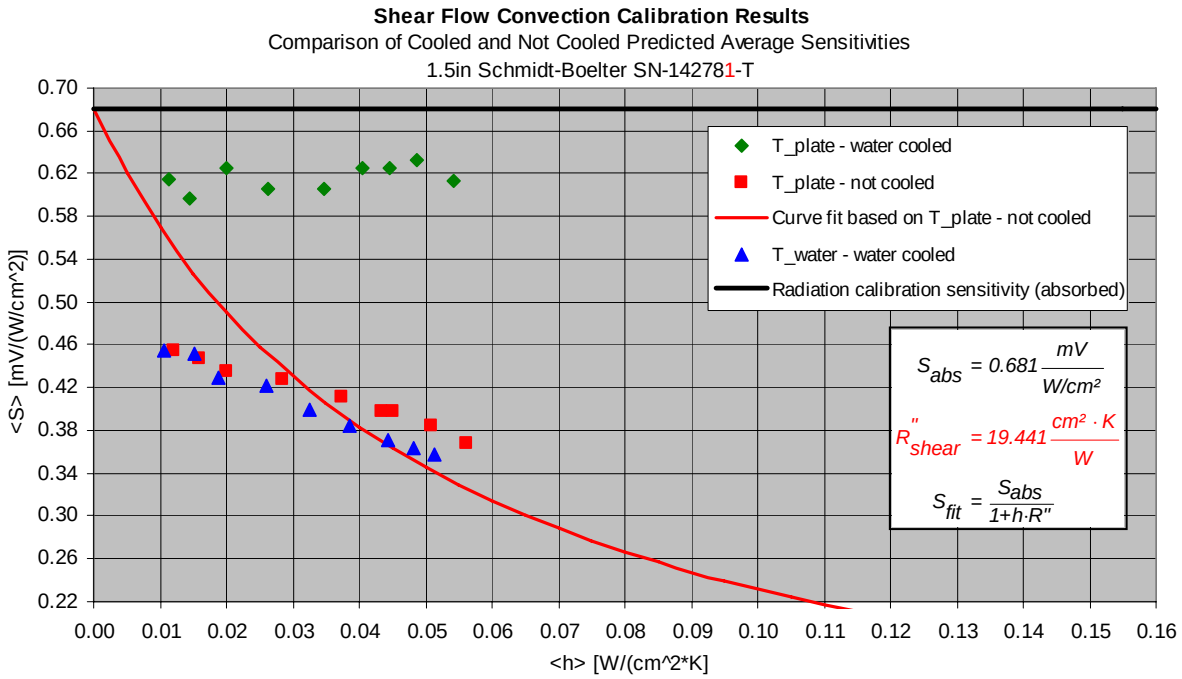

Figure 4.31: Results summary shear flow 1.5 in. SB SN 142781-T.

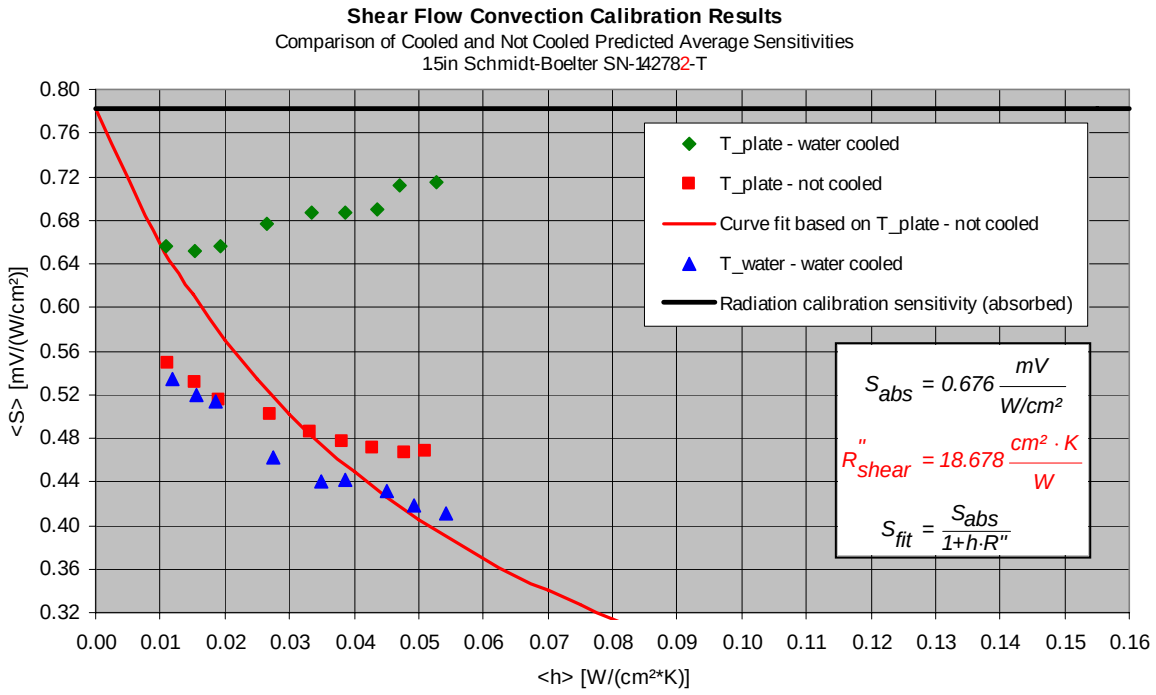

Figure 4.32: Results summary shear flow 1.5 in. SB SN 142782-T.

4.5.2.2 Stagnation Stand Results

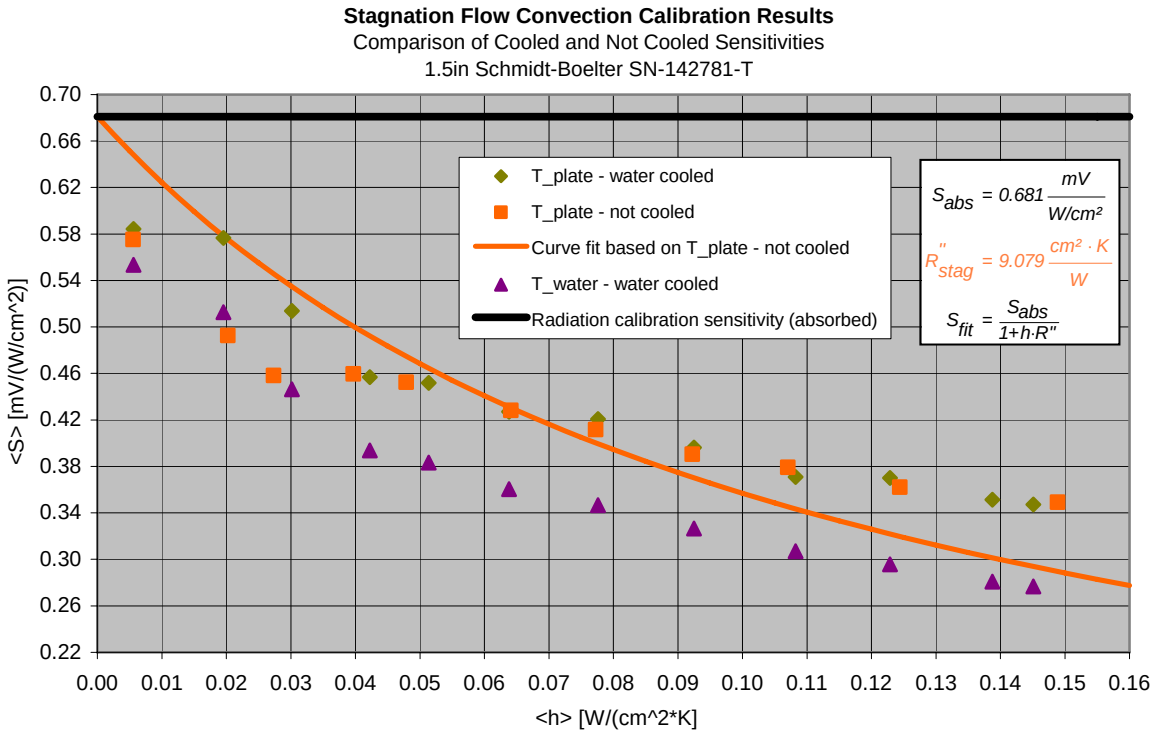

Figure 4.33: Results summary stagnation flow 1.5 in. SB SN 142781-T.

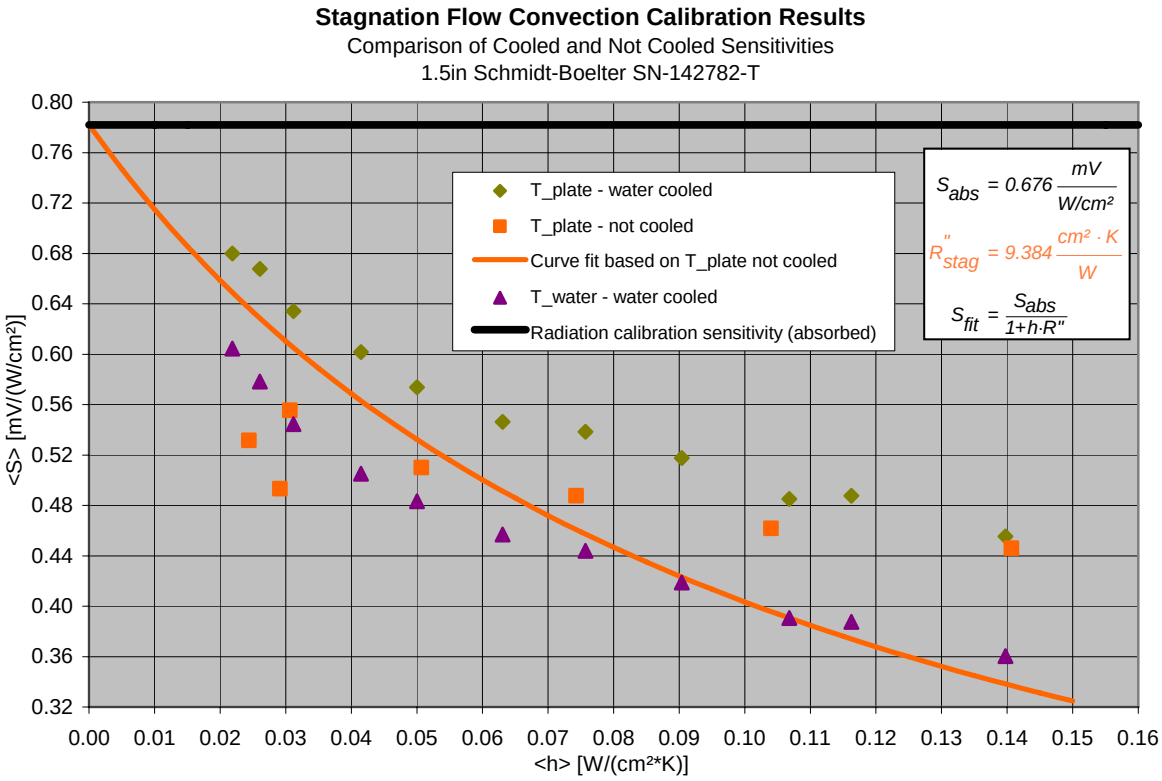

Figure 4.34: Results summary stagnation flow 1.5 in. SB SN 142782-T.

4.5.3 Comparison of Shear and Stagnation Stand Results

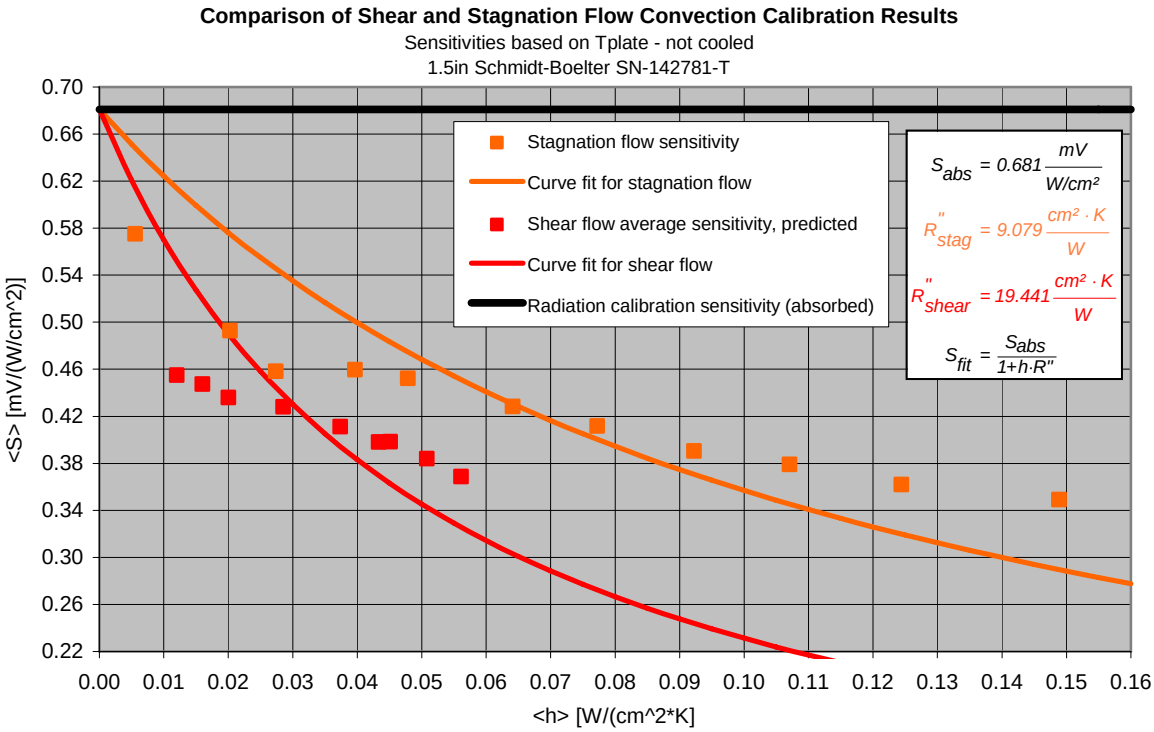

Figure 4.35: Comparison of shear and stagnation flow results, not cooled based on T_{plate} SB SN 142781-T.

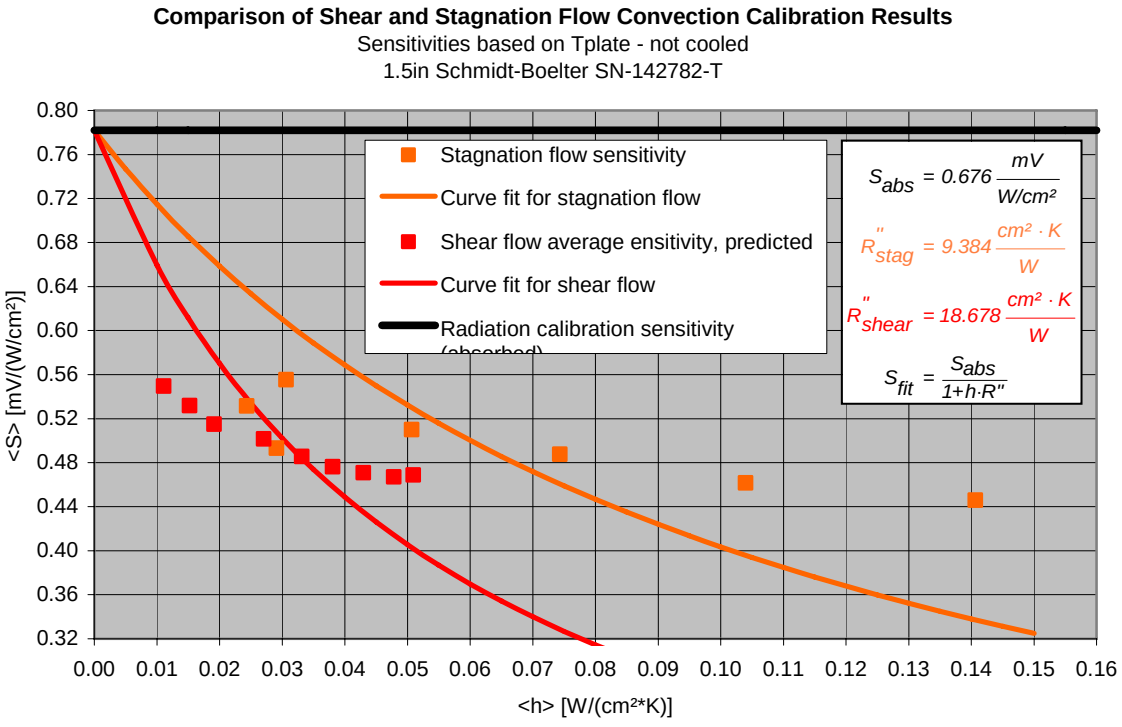

Figure 4.36: Comparison of shear and stagnation flow results, not cooled based on T_{plate} SB SN 142782-T.

4.5.4 Summary of R'' Values

The following table summarizes all of the measured R'' values. As expected, the numbers for shear flow are higher than the numbers for stagnation flow. Also, the higher the absorbed sensitivity from the radiation calibration, the higher is the R'' value.

Sensor	S_{abs}	***Shear Flow R"***	***Stagnation Flow R"***
	$\frac{mV}{W/cm^2}$	$\frac{cm^2 K}{W}$	$\frac{cm^2 K}{W}$
1.0 in. SB 137861	0.648	19.356	7.344
1.0 in. SB 137864	0.428	14.434	5.793
1.5 in. SB 142781-T	0.681	19.441	9.079
1.5 in. SB 142782-T	0.782	18.578	9.384

Table 4.2: Summary of R'' values.

5 Conclusions and Recommendations

The measurements on the shear and stagnation stand showed very clearly that the sensitivities obtained from the convection calibration are different than from the standard radiation calibration. The model equation derived in the fundamentals chapter and discussed in the results chapter provides a reasonable explanation for dependency of the sensitivity on the heat transfer coefficient. The model based on an additional thermal resistance around the gage provides a good first order approximation for the sensitivity as a function of the heat transfer coefficient.

As expected, the shear flow gave a larger convection effect than the stagnation flow, thus the apparent values for the conductive thermal resistance are larger for shear than for stagnation flow. The thermal resistances were obtained from the not cooled sensitivity values based on the plate temperature. Since the temperature of the gage (the heat sink temperature) itself is not known, one can only guess, that the sensitivity values based on the plate temperature (cooled) are too high and that the sensitivity values based on the water temperature (cooled) might be too low, so that the sensitivity values based on the plate temperature (not cooled) might the most proper ones.

The results showed also an offset. If the imaginary curve going through the measured sensitivity values is extended to the y-axis, it does not intersect with the radiation calibration value at zero heat transfer coefficient. This offset may be explained by the fact that HFM and the SB gages have been radiation calibrated in a different way. Different apparatuses have been used and different surface coating for the heat sensing area have been used.

It is thus recommended to redo the experiments by using the same apparatus, the same radiation calibration procedure and the same surface coating for the reference standard and for the Schmidt-Boelter gages in order to see if there would be an influence on the offset of the data.

A detailed understanding of the temperature distribution around the gage would be helpful to obtain an understanding of the heat paths. This would be helpful to support and confirm the model and would provide further information in case the presently used model is incomplete.

References

[1] Diller, T. E.: *"Heat Flux"*, Measurement and Instrumentation Handbook, Ch. 34 in "The Measurement, Instrumentation and Sensors Handbook", Ed. J. G. Webster, CRC Press, Boca Raton, Florida.

[2] Schetz, J. A.: *"Boundary Layer Analysis"*, Prentice Hall, Upper Saddle River, New Jersey 07458, ISBN 0-13-086885-x, 1993.

[3] Bejan, A.: *"Convection Heat Transfer"*, 3rd Edition, John Wiley & Sons., 2004, ISBN 0-471-27150-0.

[4] Pope, S. B.: *"Turbulent Flows"*, Cambridge University Press, 2000, ISBN 0 521 59886 9 (pbk).

[5] Diller, T. E.: *"Advances in Heat Flux Measurements"*, Advances in Heat Transfer, v. 23, Academic Press, Boston, 1993.

[6] Kidd, C. T. and Nelson, C. G.: *"How the Schmidt-Boelter Gage Really Works"*, Proc. 41st International Instrumentation Symposium, Research Triangle Park, NC: ISA, 1995, 347-368.

[7] Holmberg, D. G. and Diller, T. E.: *"High-Frequency Heat Flux Sensor Calibration and Modelling"*, Journal of Fluids Engineering, February 16, 1995.

[8] Murthy, A. V., Fraser, G. T. and DeWitt, D. P.: *"Experimental In-Cavity Radiative Calibration of High-Heat-Flux Meters"*, June 1, 2005, AIAA 38th Thermophysics conference, Toronto, CN.

[9] Raphael-Mabel, S., Huxtable, S., Gifford, A and Diller, T. E.: *"Design of a Novel High Temperature Heat Flux Gage"*, ASME Summer Heat Transfer Conference, Jul.17-22, 2005, San Francisco, California, USA.

[10] Barenblatt, G. I, Chorin, A. J, and Prostokishin, V. M.: *"The turbulent wall jet: A triple-layered structure and incomplete similarity"* PNAS 2005;102;8850-8853, June 9, 2005

[11] Karlsson, R. I., et al. (1991) ERCOFTAC Database: Classic Collection at Univ. of Surrey. Available at http://cfd.me.umist.ac.uk/ercoftac/database/cases/case55/case_data.

[12] Karlsson, R. I., Eriksson, J. & Persson, J. (1992) *"In Laser Techniques and Applications in Fluid Mechanics: Selected Papers from the 6th International Symposium on Applications of Laser Techniques to Mechanics"*, eds. Adrian, R. J., Durao, D. F. G, Durst, F., Asanuma, T. & Whitelaw, J. H. (Springer, Berlin-Heidelberg), pp. 311-332.

[13] Eriksson, J. (2003) Ph.D. thesis (Department of Mechanics, Royal Institute of Technology, Faxeu Laboratories, S-100 44, Stockholm).

[14] Gogineni, S. et al. *"PIV Study of a Two –Dimensional Transitional Wall Jet"*, AIAA-93-2913, Fluid Dynamics conference (1993), Orlando FL.

[15] Rodman, L. C. et al: *„Turbulence Measurements in a Plane Wall Jet"*. AIAA-86-0209, 24th Aerospace Sciences Meeting, Jan. 6-9 1986.

[16] Horne, C. and Karamcheti, K.: *"Experimental Observations of a 2D Planar Wall Jet"* AIAA, 1979.

[17] Taylor, B. B and Kuyatt, C. E.: *"Guidelines for Evaluating and Expressing the Uncertainty of NIST Measurement Results"* NIST Technical Note 1297, Edition 1994.

[18] Wikipedia, the online encyclopedia: *"Student's t-distribution"*, http://en.wikipedia.org/wiki/Student's_t-distribution, 2006

Appendix

A PIV flow field study of the rectangular wall jet

A PIV flow field study has been done on the left rectangular nozzle (N1) of the shear stand. The flow resistances described in section "3.4.2 Shear Stand Performance" (page 59) were also during the PIV test attached to the nozzles in order to have the flow field exactly the same as it seen by the heat flux gages.

Turbulent wall jets have many practical uses and have attracted the attention of many experimentalists. Thin film cooling and boundary layer control with the aid of wall jets have become an important field in fluid science. Heat transfer from a wall may be either increased or decreased by the use of surface blowing. In aeronautical applications, wall jets are primarily used on jet flaps and circulation control airfoils. The jet may be used to control flow separation from the surface, even in the presence of adverse pressure gradients. Convex stream-wise curvature of the wall enhances the entrainment capability of the jet and produces strong flow attachment by the well-known Coanda effect. There have been many attempts to find scaling laws for these flows to find dimensionless coordinates in which the velocity distributions for the various cross-sections collapse to a single curve.

The following sections describe first the theory basics of the rectangular turbulent wall jet, the PIV test setup, the data processing and the required software. The results are presented at the end of this chapter.

A1 Theory of the rectangular wall jet

Based on the analysis of the wall jet data from Karlsson and Eriksson, et al. [11], [12], [13], Barenblatt [10] develops a similarity analyisis, summarized in the first part of this section. The transitional behaviour is described in a separate section, whereas in a third subsection, the data about a LDV analysis is presented.

A1.1 Similarity Analysis

The general shape of an apparatus that produces wall jet flow is presented in Figure A1a, in Figure A1b, the distribution of the *mean* longitudinal velocity is presented schematically. Yet it is known, that the jet flow consists of two self-similar layers: a top layer and a wall layer, separated by a mixing layer, where the velocity is close to the maximum (Barenblatt [10]).

The flow develops as follows. A turbulent jet comes out a slot. The height of the slot is $\boldsymbol{h}$, and the momentum flux per unit thickness of the slot is $\boldsymbol{j}$. At large distances from the slot, the fluid is at rest. Unlike the mixing in a free jet, the mixing here is substantially influenced by the wall as well as non-symmetric.

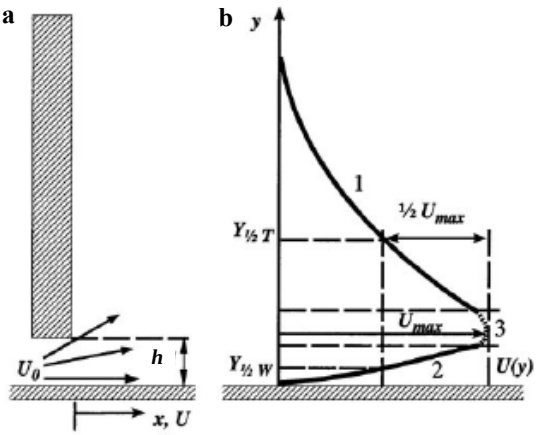

Figure A1: The schematic structure of the wall jet flow. (a) An apparatus that produces a wall jet. (b) The structure of a wall jet flow. 1: top self-similar layer, 2: wall self-similar layer, 3: mixing layer, where the velocity is close to maximum [10].

At a distance from the slot, large in comparison with the slot height $\boldsymbol{h}$, but small in comparison with the overall size of the set-up, an asymptotic flow structure is formed. Scaling laws of the form:

$$\frac{u}{u_{\max}} = f\left(\frac{y}{y_{1/2}}\right) \qquad \text{A(1.1)}$$

have been proposed for describing this structure, similarly to the free round jet, for example. $\boldsymbol{u_{max}}$ is the maximum velocity at a given section, and $\boldsymbol{y_{1/2}}$ is the coordinate, which also depends on $\boldsymbol{x}$, where the mean velocity is equal to one half of the maximum velocity, i.e.:

$$\overline{u(x, y_{1/2}(x), z)} = \frac{1}{2}\bar{u}_{\max} \qquad \text{A(1.2)}$$

This coordinate is taken, as the point where the maximum velocity is reached. The experiment has the following governing parameters: besides the mentioned height of the slot, $\boldsymbol{h}$, which scales as $\boldsymbol{\ell}$, a dimension of length ([h]~ $\boldsymbol{\ell}$) there is $\boldsymbol{L}$, a characteristic length size of the set-up, [L]~ $\boldsymbol{\ell}$; **y**, the distance of the observation point from the wall; $\boldsymbol{x}$, the longitudinal coordinate of the observation point, measured from a given origin; [x]~[y]~$\boldsymbol{\ell}$; $\boldsymbol{j}$, momentum flux through unit thickness of the slot; [j]~$\boldsymbol{m}/\boldsymbol{t}^2$; $\boldsymbol{\rho}$, the fluid density, [ρ]~$\boldsymbol{m}/\boldsymbol{\ell}^3$; **ν**, the fluid kinematic viscosity, [ν]~$\boldsymbol{\ell}^2/\boldsymbol{t}$; $\boldsymbol{m}$ and $\boldsymbol{t}$ are the dimensions of mass and time. With these parameters, four dimensionless parameters can be formed as:

$$\Pi_1 = \frac{y}{h},\ \ \Pi_2 = \frac{x}{h},\ \ \Pi_3 = \sqrt{\frac{jh}{\rho}}\frac{1}{\nu},\ \ \Pi_4 = \frac{L}{h} \qquad \text{A(1.3)}$$

Every dimensionless property of wall jet flow can be represented as a function of these parameters. With the large Π_4 characteristic of existing high-quality set-ups, it is natural to assume complete similarity in this parameter so that the value of L is immaterial. The parameter Π_3 is an analogy to the Reynolds number and can be denoted by **Re**. However, as can be easily seen from Figure A1b, the longitudinal velocity distribution of the wall jet flow has not one, but two ordinates where the mean velocity has the value $½u_{max}$. These are denoted by the variables $y_{1/2}^T$ and $y_{1/2}^W$.

Barenblatt et al. [10], using the data by Karlsson and co-workers [11], [12], [13], found, after processing the data in bi-logarithmic coordinates, that both coordinates $y_{1/2}^T$ and $y_{1/2}^W$ follow the scaling laws:

$$\begin{aligned} y_{1/2}^T &= A_T h^{1-\beta_T} x^{\beta_T} \\ y_{1/2}^W &= A_W h^{1-\beta_W} x^{\beta_W} \end{aligned}, \qquad \text{A(1.4)}$$

Barenblatt gives also values for β_T and β_W with a tolerance as to be:

$$\beta_T = 0.93 \pm 0.02 \quad \beta_W = 0.68 \pm 0.02 \qquad \text{A(1.5)}$$

Then the velocity distributions have been processed in the dimensionless coordinates:

$$\begin{aligned} U &= \frac{u}{u_{\max}}, \\ Y_T &= \frac{y}{h^{1-\beta_T} x^{\beta_T}} \text{ and} \\ Y_W &= \frac{y}{h^{1-\beta_W} x^{\beta_W}}, \end{aligned} \qquad \text{A(1.6)}$$

with convincing results. For Y_T the theory shows a clear collapse to a single curve in the top part and no collapse in the wall part. (Figure A2). For Y_W the theory shows a clear collapse of the data to a single curve in the wall part and no collapse in the top part (Figure A3). In both cases though, the collapse extended to the values of u/u_{max} close to one.

Thus, Barenblatt shows that the analysis of the data of Karlsson et al. allows us to suggest the following hypotheses concerning the structure of wall jet flow:

First Hypotheses. The flow region consists of three layers:

- *Top layer*, the region around and above the upper line $y_{1/2}^T$.
- *Wall Layer*, the region around and below the lower line $y_{1/2}^W$.

- *Intermediate Layer,* the region between the top and wall layers, where the velocity is close to maximum.

Second Hypotheses. At large Reynolds numbers in the top and wall layers, the flow has the property of incomplete similarity. This concept is explained by Barenblatt in greater detail.

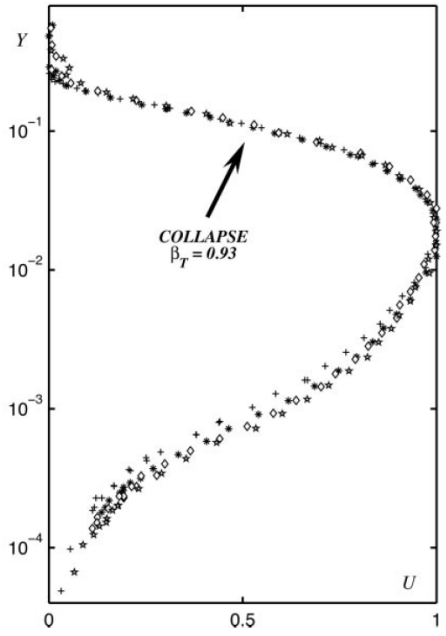

Figure A2: Collapse of the experimental curves. Y_T vs. U to different scaling laws +x/d=40; *x/d=70; ◊ x/d=100; *x/d=150 [10].

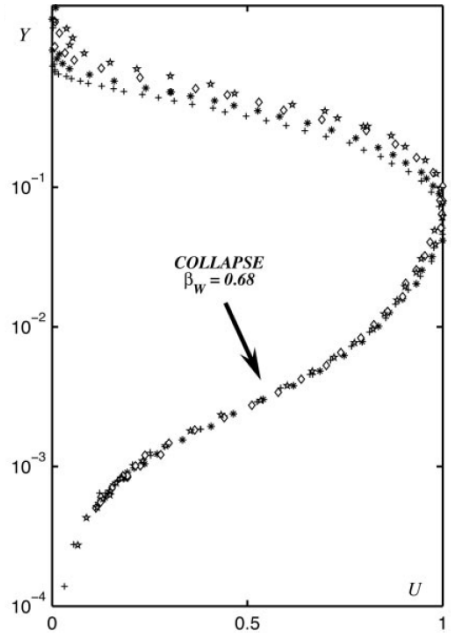

Figure A3: Collapse of the experimental curves. Y_W vs. U to different scaling laws +x/d=40; *x/d=70; ◊ x/d=100; *x/d=150 [10].

A1.2 Transitional Behaviour

As defined in the previous section, the wall jet velocity profile consists of three regions. The top layer (or referred to as the outer region), the intermediate layer (or intermediate region) and the wall layer (or inner region). Simplifying this analysis and notifying the intermediate region is small compared to the outer region and the wall region, we can declare, the turbulent wall jet is *simply composed of an inner region and an outer region*.

To get a more in depth understanding of the flow structures of the turbulent rectangular wall jet, a laminar wall jet undergoing transition is investigated experimentally using Particle Image Velocimetry (PIV). This analysis was done by Gogenini et al. in 1993

[14]. Moreover, an understanding about the boundary layer, underneath the free shear layer is desired, hence in this section, we want to look at the interactions between the free shear layer and the boundary layer. We will see that under the influence of the shear layer and the vortices arising from it, the local boundary layer separates and forms a vortex. The mutual interactions between the boundary layer and shear layer vortices dominate the transitional process. Further downstream, the emergence of three dimensional structures in the shear layer initiates the complete breakdown of the flow.

Gogenini [14] summarizes the findings from former researchers, who have investigated the transitional behaviour of wall jets. The conclusion was that there are two unstable modes. The first one, an inviscid mode that represents the large scale disturbances, has the highest mode in the free shear layer. The second, a viscous mode describing the small scale disturbances exhibits the highest amplitude near the wall. For Reynolds numbers between 100 and 600, the following stages in the transitional process have been made:

(i) Formation of discrete vortices in the free shear layer
(ii) Coalescence of adjacent vortices in the free shear layer, coupled with the vortices in the inner region wall boundary layer,
(iii) Eruption of the wall jet from near the surface of the flat plate into the ambient fluid
(iv) Dispersion of the organized flow pattern by three dimensional turbulent motions
(v) Relaminarization of the upstream flow until another vortex pairing occurs.

Consequently, the initial stages of transition are two dimensional in nature. These stages are dominated by the mechanism of vortex pairing. Forced and natural transition behaves similarly [14]. Moreover, the presence of discrete vortices has been observed in the shear layer as well as in the boundary layer.

A standard, single-channel hot-wire anemometer was used to measure mean and rms distribution of the velocity. Figure 4 shows a flow field of a forced jet from the nozzle exit to about 16 widths downstream of the exit. It can be seen that the wall jet consist of an inner region and an outer region. In the outer region, Kelvin-Helmholtz type instabilities grow and roll up into discrete vertical structures. In the inner region, a boundary layer flow structure consisting of discrete vortices that are out of phase with respect to the corresponding structures can be seen. This well organized double row vortex structure convects downstream and becomes indistinguishable from each other at a certain downstream location.

Figure A4: Streamwise flow visualization for a forced jet. Transition from Laminar to turbulent flow can be seen [14].

Gogenini et al [14] found out that the flow remains two-dimensional before it breaks down. Based on the observations, the transition process for the Reynolds number considered in this experiment, consist of formation and development of discrete vortices in both inner and outer regions before the flow becomes three dimensional and turbulent.

By using the single normal hot wire anemometer, the mean velocity distributions at several downstream locations for normalized mean velocity profiles at the nozzle exit could be produced. Figure A5 shows the normalized and mean velocity profiles at the nozzle exit. The mean velocity is normalized with the maximum exit velocity. The cross stream distance y is normalized with $y_{1/2}$. It was found that the self-similar mean velocity profiles for both cases agree well with the theoretical profile, provided in the first part of this paper.

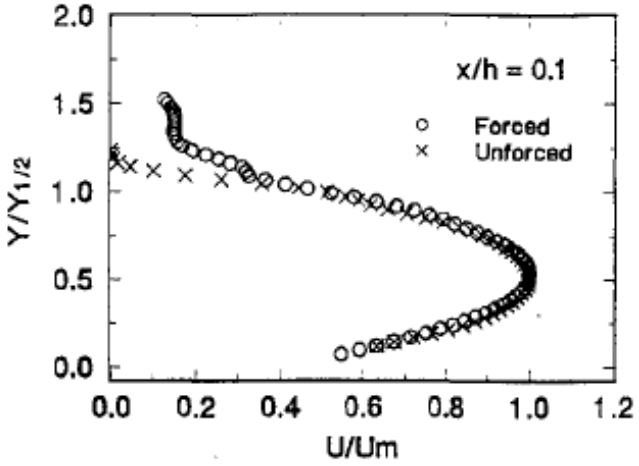

Figure A5: Mean velocity profile at nozzle exit [14].

The flow field has been divided into four sections to accommodate PIV measurement with each section covering approximately four nozzle exit widths. The data for the first section

describe vortex induced separation process and the subsequent formation of a vortex in the inner region. The data from the later sections describe the interactions between the free shear layer and developing boundary layer vortices and the emergence of the three dimensional structure that leads to breakdown of the flow.

The instantaneous vorticity data was obtained at 40 different phases and 30 instantaneous velocity fields are obtained at one specific phase. The phase-averaged vorticity field is shown in Figure A6.

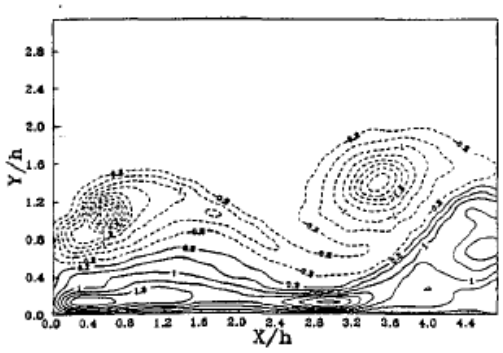

Figure A6: **Phase averaged vorticity [14].**

The data clearly depict two discrete vortices in the free shear layer. Under the upstream vortex, the boundary layer is thickening with no apparent separation yet. Further downstream of the flow, the boundary layer detaches from the surface and rolls into a vortex.

Figure 7 shows the temporal development of the instantaneous vorticity field in the region extending from the nozzle exit to 4.6 nozzle widths downstream. At the nozzle exit, the shear layer vorticity coalescences immediately into a vortex (Figure A7 a-d). Under the influence of this vortex, the local boundary layer is thickening and eventually separates from the surface and forms a discrete vortex that has the opposite circulation compared to the shear layer vortex. The boundary layer vortex moves away from the surface toward the center of the jet, from where it experiences higher convection and appears to move ahead of the shear layer vortex. These two counter-rotating vortices later convect together forming a vortex pair (Figure A7 e-h). After two vortices pair, their mutual induction propels the pair to move further away from the surface as shown by the downstream vortex pair from Figure A7 a-d.

The recirculation bubble grows in size and pushes the boundary layer flow away from the wall. This separating boundary layer is subject to inviscid instability as usually experienced by a free shear layer, and coalesces into a vortex with positive vorticity in the inner region, commonly known as the boundary layer vortex. Note that the free shear layer

vortex has negative vorticity. As the vortices in shear layer continuously convects downstream, the local boundary layer therefore experiences cyclic detachment and reattachment. As the boundary layer vortex moves away from the surface, it experiences higher convection jet stream and also stronger induction from the shear layer vortex, as a result it moves faster than the shear layer vortex. Eventually, the boundary layer vortex moves into a position approximately midway between two shear layer vortices. The downstream shear layer vortex now has increasing influence on the boundary vortex and slows down its convection. Consequently, the whole arrays of vortices, including several shear layer and boundary layer vortices, start to move as group (Figure A8 a, b). This arrangement persists downstream until the downstream shear layer vortex is weakened by the emergence of three-dimensional structure. As a result, the boundary layer vortex is lifted up from the wall as shown in Figure A8c.

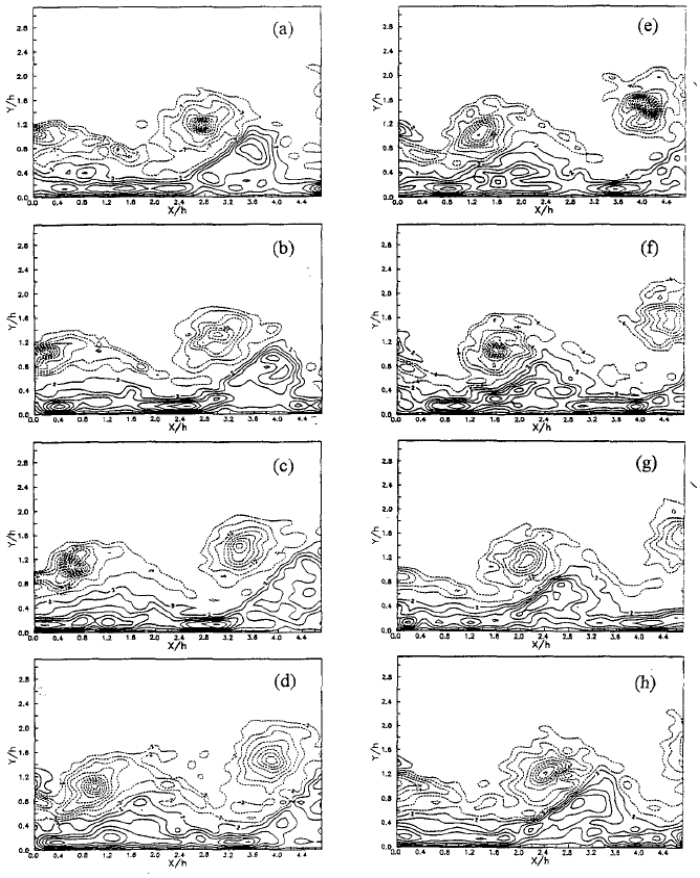

Figure A7: Temporal development of the instantaneous vorticity fields at several phases [14].

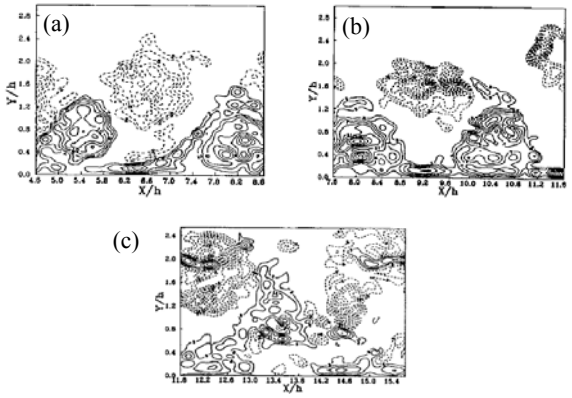

Figure A8: Spatial evolution of the instantaneous vorticity field [14].

A1.3 Results from a LDV Analyis

LDV (Laser Doppler Velocimetry) measurements of the turbulent normal and shear stresses in the wall jet are presented by Rodman et al. [15]. In the following experiment, a two-dimensional plane wall jet flow is simulated by having a jet blow axially over a cylinder (Figure A9). Although the wall jet in this case is axisymmetric, adequate "two-dimensional" flow can be obtained as long as the ratio of the jet width to the cylinder radius is small. The annular wall jet has several advantages over wall jets issuing from finite rectangular slots. Since the slot has no ends, three-dimensional effects caused by sidewall interference are eliminated. For further details, how three-dimensional and wall effects can be reduced, see proper sections in [15].

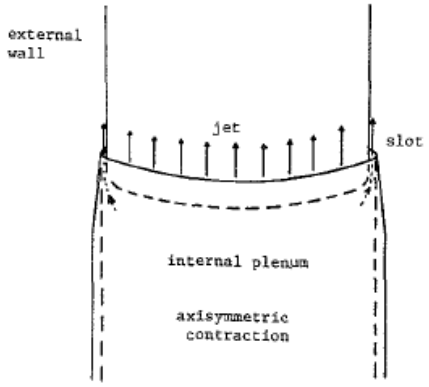

Figure A9: Axi-symmetric plane wall jet model [15].

As mentioned above, the wall jet resembles half of a free jet (free shear flow) with a wall boundary layer (wall bounded flow) imposed, and the effect of the wall is felt throughout the jet width. Due to the wall damping on the size of the large eddies, entrainment is lower for a wall jet than for a free jet, which results in a slower decay rate of the maximum velocity, Rodman [15]. The jets over plane walls achieve some degree of self-similariy, which may simplify their calculation, as described in the first part of this paper. But standard mixing length models do not accurately predict the shear profile of a wall jet, because the location of the zero mean velocity gradient dows not correspond to the location of zero turbulent shear stress.

LDV measurements allowed measurements to be taken of high turbulence intensities, without probe interference and with improved spatial resolution compared to cross wires, i.e. hot wire anemometry. The model cylinder was approximately 20cm in radius, which allows laser access to within 0.4mm from the wall. The slot height was 1.3mm, and the wall extended 23cm downstream. With a jet exit velocity of 100m/s, the Reynolds number based on slot heigt was 9000.

Mean flow measurements in the wall jet were taken using a pitot pressure tube and turbulence measurements were made with a two-component LDV system, a single hot wire, and a split film probe. The LDV system used in this study was comprised of a 2-color 4-beam matrix produced from a 4 Watts Argon Ion laser. Bragg cell shifting at a fixed frequency of 40 MHz was incorporated into each spectral line. The receiving optics was in the forward scatter off-axis mode. Both, the transmitting and the receiving optics were placed on separate 2D traversing mechanisms which were moved synchronously. Smoke particles from burning mineral oil were used to seed the flow.

As a comparison to the LDV data, single hot wire data was taken to measure the longitudinal stream wise turbulence intensity $\overline{u'^2}$, and a split film probe was used to measure both normal stresses $\overline{u'^2}$ and $\overline{v'^2}$, and the shear stresses $\overline{u'v'}$. The wall jet air was typically about 20°C above the room temperature. A simple temperature correction was applied to the single wire data, although its validity was questionable for the large temperature range of the experiment. A heat exchanger was later used to cool the jet during the split film tests, and the temperature difference compared to ambient conditions was reduced by almost 50%. An alternative air supply was also available that typically ran about 15°C cooler than room temperature. Split film measurements in the two air supplies showed that although the absolute

mean and RMS velocity measurements varied with temperature, the normalized turbulence intensities remained constant for the warm and cool jets (Figure A10).

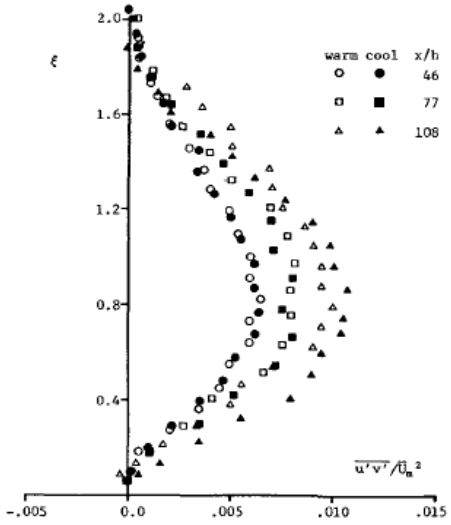

Figure A10: Temperature Effects on Split Film Measurements of Turbulent Shear Stresses [15].

The only noticeable effect due to temperature was a slight skew of the profiles, caused by the opposite temperature gradients across the jet.

The mean velocity profiles of the flow field were measured with pitot probes at several positions about the circumference of the cylinder. These results showed good flow uniformity and "two-dimensionality" along the jet span. In two-dimensional flow, loss of streamwise momentum should be small, due to only skin friction. Thus, the ratio of jet momentum J(x) relative to the slot momentum is

$$\frac{J(x)}{J_0} = \left(\frac{u_{\max}}{u_j}\right)^2 \frac{y_{1/2}}{h} \int_0^\infty \left(\frac{u}{u_{\max}}\right) d\xi, \qquad \text{A(1.7)}$$

whereas for a frictionless flow we have:

$$\frac{J(x)}{J_0} = 1 \text{ for all x.}$$

For the jet width growth rate and the velocity decay rate was obtained:

$$\frac{\partial y_{1/2}}{\partial x} = 0.074$$
$$\frac{u_{\max}}{u_j} = 4.9\left(\frac{x}{h} + 0.96\right)^{-0.55} \qquad \text{A(1.8)}$$

The mean velocity profiles measured using a pitot probe exhibited the self-similar shape typical of plane wall jets after 15 slot heights downstream (Figure A11). A 2-component LDV system was used to measure the flow field in detail. Longitudinal and lateral turbulence intensities, shear stresses and selected triple components were measured in addition to the mean velocities. Figure A11 to Figure A14 show turbulence measurements taken with the LDV. The profiles were taken at x=6, 8, 10, and 12 cm downstream of the slot, or x/h=46 to 92. These data were compared to cross wire measurements taken by previous researchers. [15] It was deemed impractical to take cross wire measurements in the present experiment, since the jet width was small and significant temperature gradients existed in the flow. The normalized longitudinal turbulence intensity $\overline{u'^2}/\bar{u}^2_{max}$ profiles agreed with previous hot wire results in general shape and position of the peak intensity. The position of the minimum $\overline{u'^2}/\bar{u}^2_{max}$ was clearly seen in all the profiles.

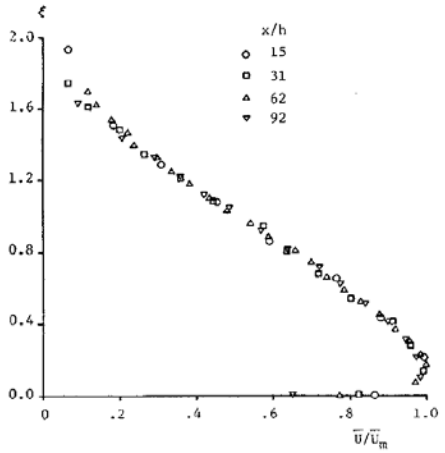

Figure A11: Self-similar wall jet mean velocity profiles [15].

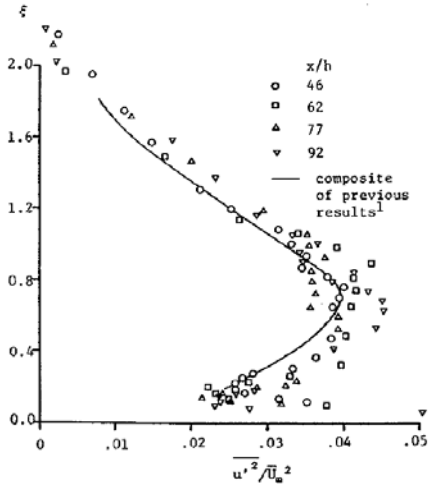

Figure A12: LDV measurements of longitudinal normal stress compared with previous crosswire results [15].

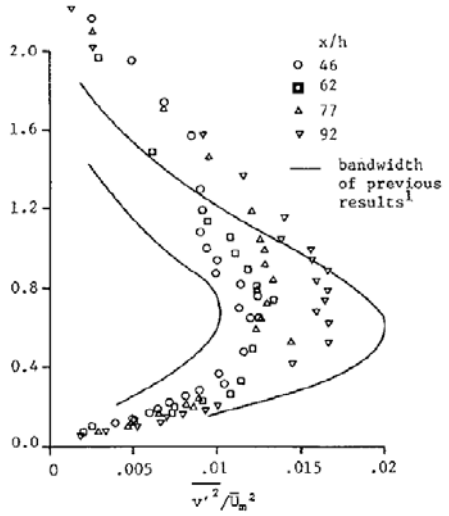

Figure A13: LDV measurements of lateral and normal stress compared with previous crosswire results [15].

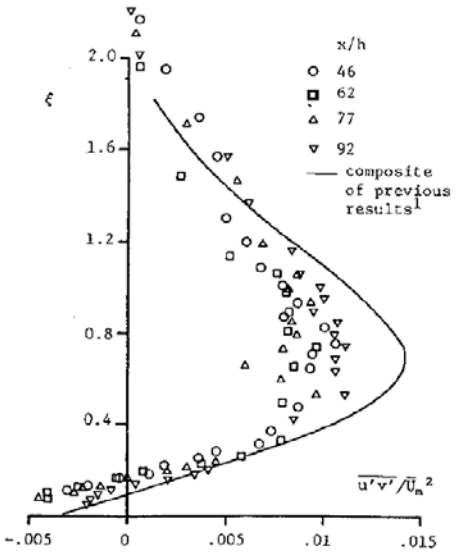

Figure A14: LDV measurements of shear stress compared with previous crosswire results [15].

The results were convincingly good. The measurement of the normalized lateral turbulence intensity $\overline{v'^2}/\bar{u}_{\max}^2$ showed only small scatter at x/h=62 and 77, but exhibited an increase in magnitude at x/h=92. Unlike the longitudinal turbulence intensity, the profiles repeated very well at the same x location. Previous measurements of the longitudinal velocity intensity showed considerable scatter. The turbulent shear stress $\overline{u'v'}/\bar{u}_{\max}^2$ profiles also showed a slight increase in magnitude with downstream distance. The scatter among the profiles was comparable to that of normal turbulent stresses.

In order to calculate the shear stresses in the self-similar wall jet, the momentum integral method can be used. The analysis was performed on a wall jet blown axially over a Cylinder. The equation for continuity and momentum for a body of revolution were used [15]:

$$\frac{\partial(r\bar{u})}{\partial x}+\frac{\partial(r\bar{v})}{dy}=0$$
$$\bar{u}\frac{\partial\bar{u}}{\partial x}+\bar{v}\frac{\partial\bar{u}}{dy}=-\frac{1}{\rho}\frac{dp}{dx}+\frac{1}{\rho r}\frac{\partial}{\partial y}\left[r\left(\mu\frac{\partial\bar{u}}{\partial y}-\rho\overline{u'v'}\right)\right] \qquad \text{A(1.9)}$$

the pressure gradient can be neglected, if the curvature is small. For dr/dy=0, this problem will reduce to the 2D case. The assumed velocity profile was (where $\xi_{max}=y_{max}/y_{1/2}$, $u_{max}=u(y_{max})$):

$$\frac{\bar{u}}{\bar{u}_{\max}}=2\left(\frac{\xi}{\xi_{\max}}\right)^{1/n}-\left(\frac{\xi}{\xi_{\max}}\right)^{2/n}=f(\xi),\quad \xi\le\xi_{\mathrm{m}}$$
$$\frac{\bar{u}}{\bar{u}_{\max}}=\operatorname{sech}^2\left(\frac{k(\xi-\xi_m)}{(1-\xi_{m)}}\right)\qquad =f(\xi),\quad \xi>\xi_{\mathrm{m}} \qquad \text{A(1.10)}$$

Setting: $\bar{u}/\bar{u}_{\max}=1/2$ at ξ=1 , the constant k was found to be 0.8814. The constant n is typically equal to 7 for a boundary layer (Prandtl's 1/7-power-law). Matching the second derivatives of the two profiles at $\xi=\xi_{max}$ gives ξ_{max}=0.159, which is constant for all downstream locations. Writing the integral form of the equation and substituting the assumed velocity profiles, gives:

$$-\frac{r}{r_0}\frac{\tau}{\rho u_{\max}^2}=\frac{dy_{1/2}}{dx}\left[\frac{1}{2}f(\xi)\int_0^{\xi}f(\xi)d\xi\right]$$
$$+\frac{1}{u_m^2}\frac{d(y_{1/2}u_{\max}^2)}{dx}\left[\int_{\xi}^{\infty}f^2(\xi)d\xi+\frac{1}{2}f(\xi)\int_0^{\xi}f(\xi)d\xi\right]$$
$$+\frac{y_{1/2}}{r_0}\left[\left(\frac{1}{u_{\max}^2}\frac{d(y_{1/2}u_{\max}^2)}{dx}+\frac{dy_{1/2}}{x}\right)\int_{\xi}^{\infty}f^2(\xi)d\xi\right] \qquad \text{A(1.11)}$$
$$+\frac{y_{1/2}}{r_0}f(\xi)\left[\left(\frac{1}{u_{\max}}\frac{d(y_{1/2}u_{\max})}{dx}+\frac{dy_{1/2}}{x}\right)\int_0^{\xi}f(\xi)d\xi\right]$$

Evaluation at the wall: $\xi=0$, yields:

$$-\frac{1}{2}c_f=\left(\frac{1}{u_{\max}^2}\frac{d(y_{1/2}u_{\max}^2)}{dx}\right)\int_0^{\infty}f^2(\xi)d\xi$$
$$+\frac{y_{1/2}}{r_0}\left[\left(\frac{1}{u_{\max}^2}\frac{d(y_{1/2}u_m^2)}{dx}+\frac{dy_{1/2}}{x}\right)\int_0^{\infty}\xi f^2(\xi)d\xi\right] \qquad \text{A(1.12)}$$

The momentum equation can now be rewritten as:

$$-\frac{r}{r_0}\frac{\tau}{\rho u_{\max}^2} = \frac{1}{2}c_f F(\xi) + \frac{dy_{1/2}}{dx}G(\xi) + \frac{y_{1/2}}{r_0}\left(\frac{1}{u_{\max}^2}\frac{d(y_{1/2}u_{\max}^2)}{dx} + \frac{dy_{1/2}}{dx}\right)H(\xi) + \frac{y_{1/2}}{r_0}\left(\frac{1}{u_{\max}}\frac{d(y_{1/2}u_{\max})}{dx} + \frac{dy_{1/2}}{dx}\right)J(\xi) \qquad \text{A(1.13)}$$

with:

$$A = \int_0^\infty f^2 d\xi \qquad A = \int_0^\infty \xi f^2 d\xi$$

$$J(\xi) = f\int_0^\xi \xi f d\xi \qquad G(\xi) = \frac{1}{2}f\int_0^\xi f d\xi \qquad \text{A(1.14)}$$

$$F(\xi) = 1 - \frac{1}{A}\left[\int_0^\xi f^2 d\xi - G(\xi)\right]$$

$$H(\xi) = -\int_0^\xi \xi f^2 d\xi + \frac{B}{A}\left[\int_0^\xi f^2 d\xi - G(\xi)\right]$$

The effects of transverse curvature were characterized by the ratio of the jet half width to cylinder radius (b/r_0)-parameter. As b/r_0 tends to zero, the flow becomes 2D, but as b/r_0 becomes large, the flow becomes axisymmetric.

In order to calculate the shear stress throughout the jet, the skin friction coefficient c_f must be known. Since c_f was notmeasured in the present experiment, the term was computed from equation (11) using the measured momentum derivative $1/u_{\max}^2 d(y_{1/2}u_{\max}^2)/dx$ and growth rate $dy_{1/2}/dx$. This method was subjected to error, however, since small inaccuracies in the measured growth an decay rates would produce large inaccuracies in c_f.

The shear stress profile can then be calculated by a computer program for various $y_{1/2}/r_0$. Figure 15 shows the near shear stress profile for various $y_{1/2}/r_0$.

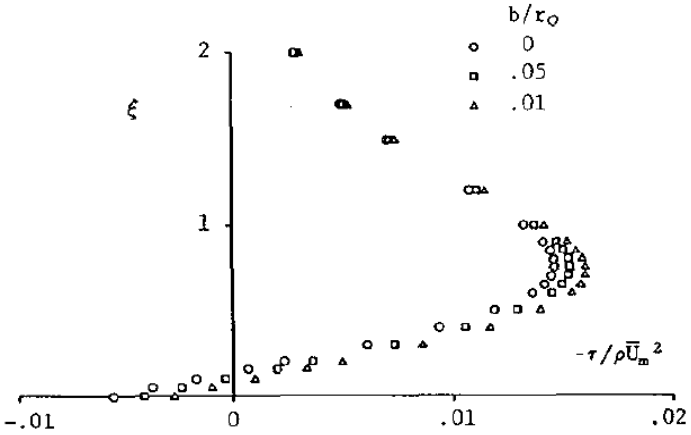

Figure A15: Shear stress profiles computed from integral technique, as a function of transverse curvature [15].

A1.4 Summary of the findings for the rectangular wall jet

We have seen that the turbulent rectangular wall jet consists of three layers. The top layer or free shear region, the intermediate layer and the wall layer or inner region. For purposes of simplicity, we can say the turbulent rectangular wall jet consists of an inner region, represented by a wall bounded boundary layer flow and the outer region, representing a free shear flow.

The analysis of the transitional wall jet has shown that, under the influence of the shear layer vortex, the local boundary layer separates and forms a discrete vortex. Once this vortex is formed, the interactions between the shear layer and boundary layer vortices dominate the transition process. The emergence of three-dimensional structure inside the shear layer triggers the complete breakdown of the flow.

The profiles obtained from LDV showed the same trends as the data, obtained from the hot wire anemometry. Axisymmetric models can give adequate 2D flow up to a b/r_0 of 0.1. LDV provides good turbulence data which is a supplement to hot wire anemometry, since it offers the potential for increased frequency response, improved spatial resolution, and no probe interference. However, great care is necessary to ensure that noise levels are minimized, so that confidence in the data may be obtained.

A2 PIV Setup and Experiment

To understand the unsteady flow characteristics, it is necessary to study the spatial velocity distribution at each instant of time. The PIV technique provides instantaneous, two-dimensional velocity field measurements in a selected plane with sufficient spatial accuracy so that the instantaneous velocity field can be obtained. The main parameters governing the incompressible transitional wall jet are the Reynolds number (based on the nozzle width and the exit mean velocity), the disturbance characteristics at the nozzle exit, the aspect ratio of the nozzle, and the length of the wall. The height of the nozzle is 2.4 mm. The mean velocity was determined to be 40 m/s. In the present experiment the Reynolds number was 4200. The exit mean velocity profile was parabolic. The aspect ratio of the nozzle was 16.

The air was supplied through the shear plenum. By adding an additional valve in the duct, the seeding was inserted into the air stream. As seeding, baby powder was used, with a diameter of one micron. The Yag laser (λ=535nm, green light) provided double illuminating pulses. The double pulse frequency or laser pulse separation (LPS), i.e. the time between a double frame was between 12-15 micro seconds. The pair frequency or pair separation (PS), i.e. the time that separates two double pulses was set to be 1 MHz. Figure A16 illustrates the coherence between LPS and PS. The laser sheet was created by forcing the laser light to go through the focal point (FP) and by using a combination of spherical and cylindrical lenses. The light scattered by the seed particles generates a particle image pattern. This pattern is recorded using a CMOS camera. The camera is controlled by a CPU which coordinates LPS and PS with the camera shutter time. The images were saved on the computer. A schematic of the experimental setup is shown in Figure A17. Figure A19 and Figure A20 show photos of the experimental setup. The back scattered laser light by the particles can be seen in Figure A21. One of the 40 000 digital images taken by the CMOS camera is shown in Figure A 22.

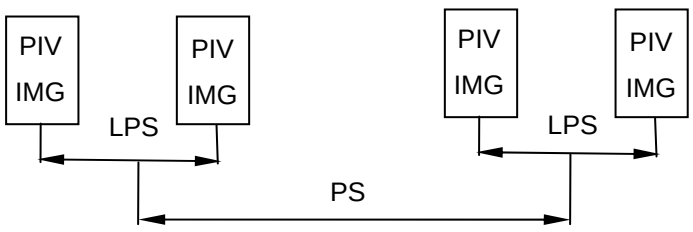

Figure A16: LPS and PS. Explanations see text.

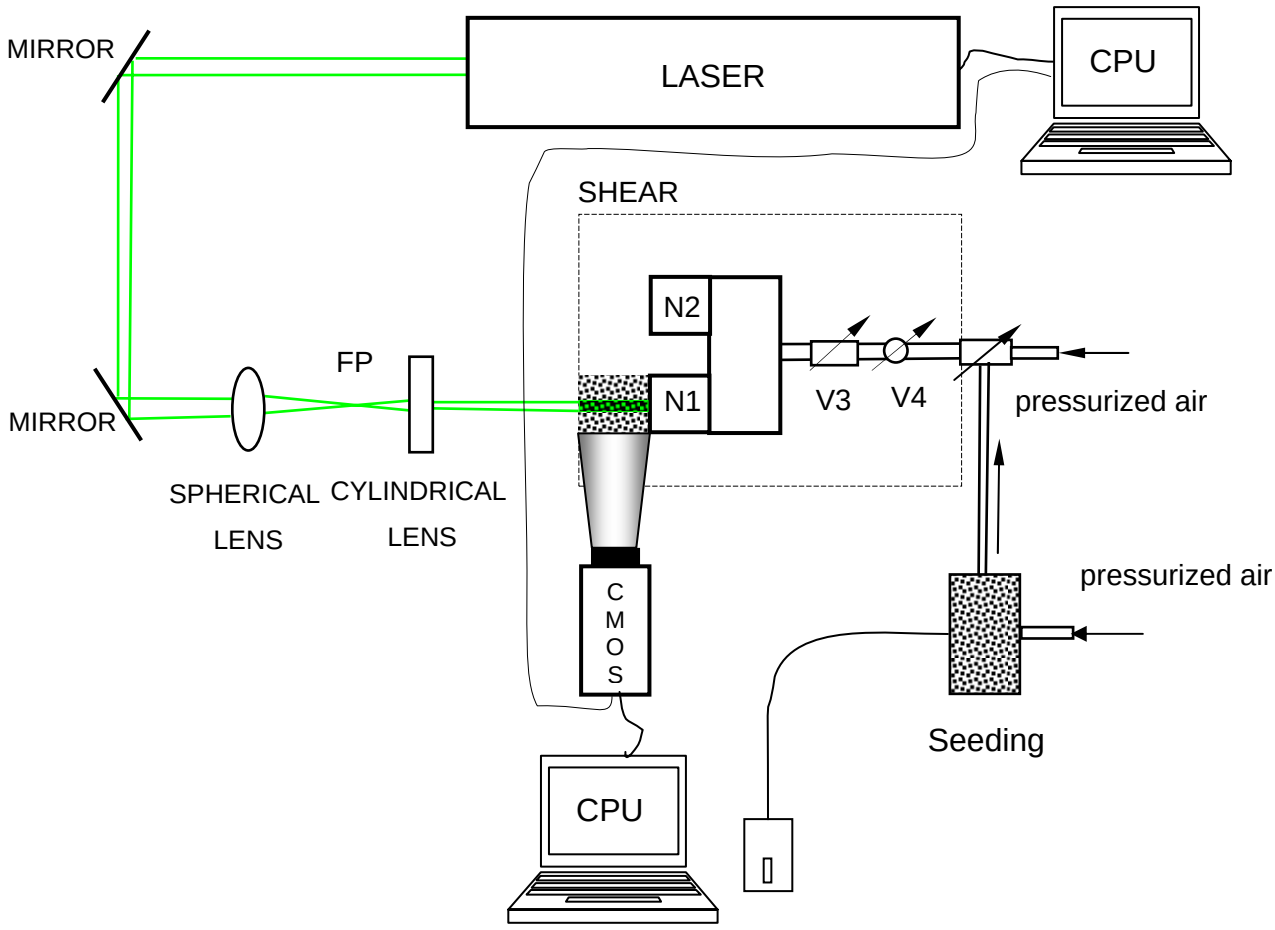

Figure A17: Schematic of the PIV Experiment setup.

Figure A18: Photo of the PIV Experiment Setup in the CTFS at the VT ME department. Laser, lenses, camera and shear stand.

Figure A19: Photo of the PIV Experiment Setup in the CTFS at the VT ME department. Laser, lenses, camera, shear stand and seeder.

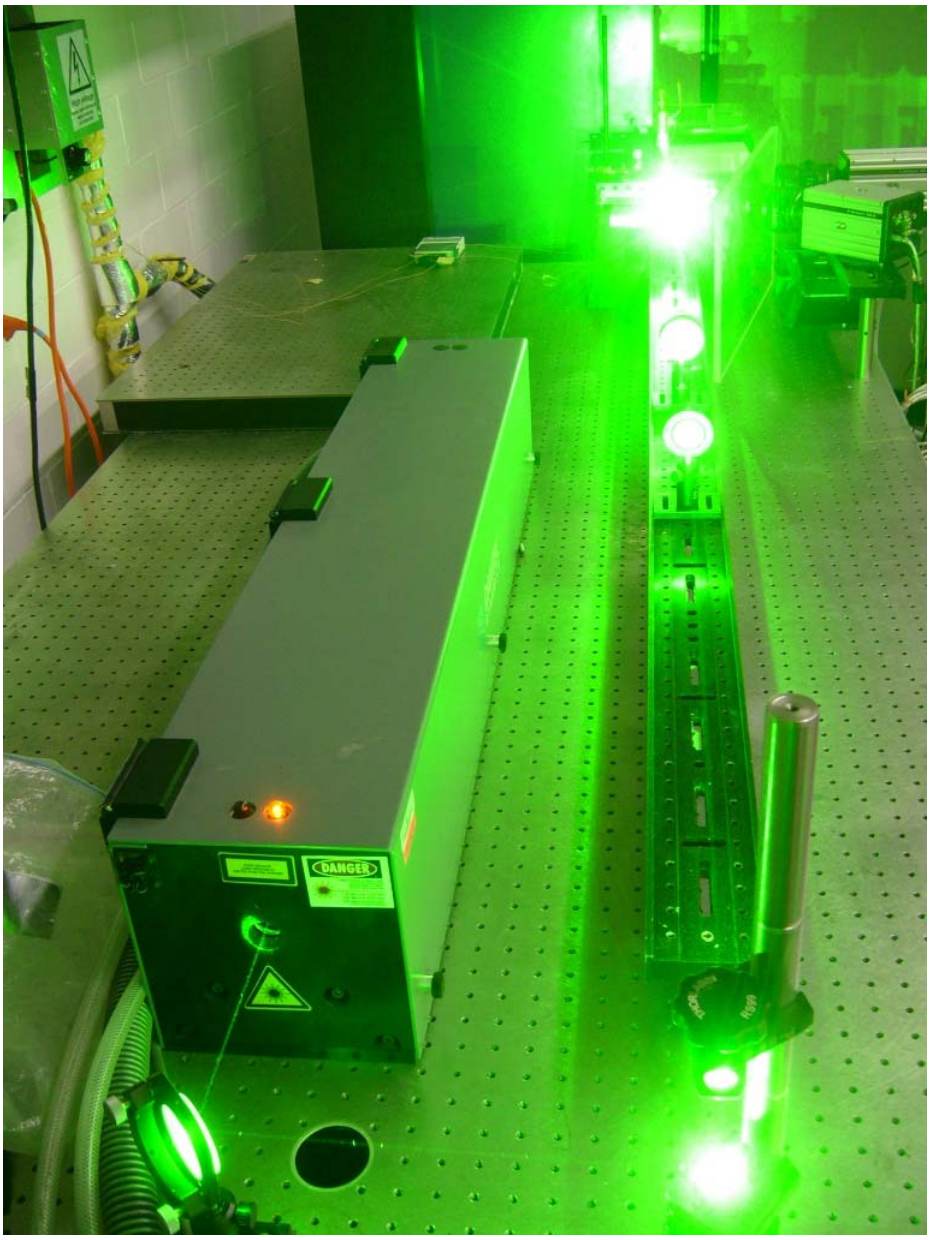

Figure A20: Photography of the PIV Experiment Setup in the CTFS at the VT ME department. Laser in operation.

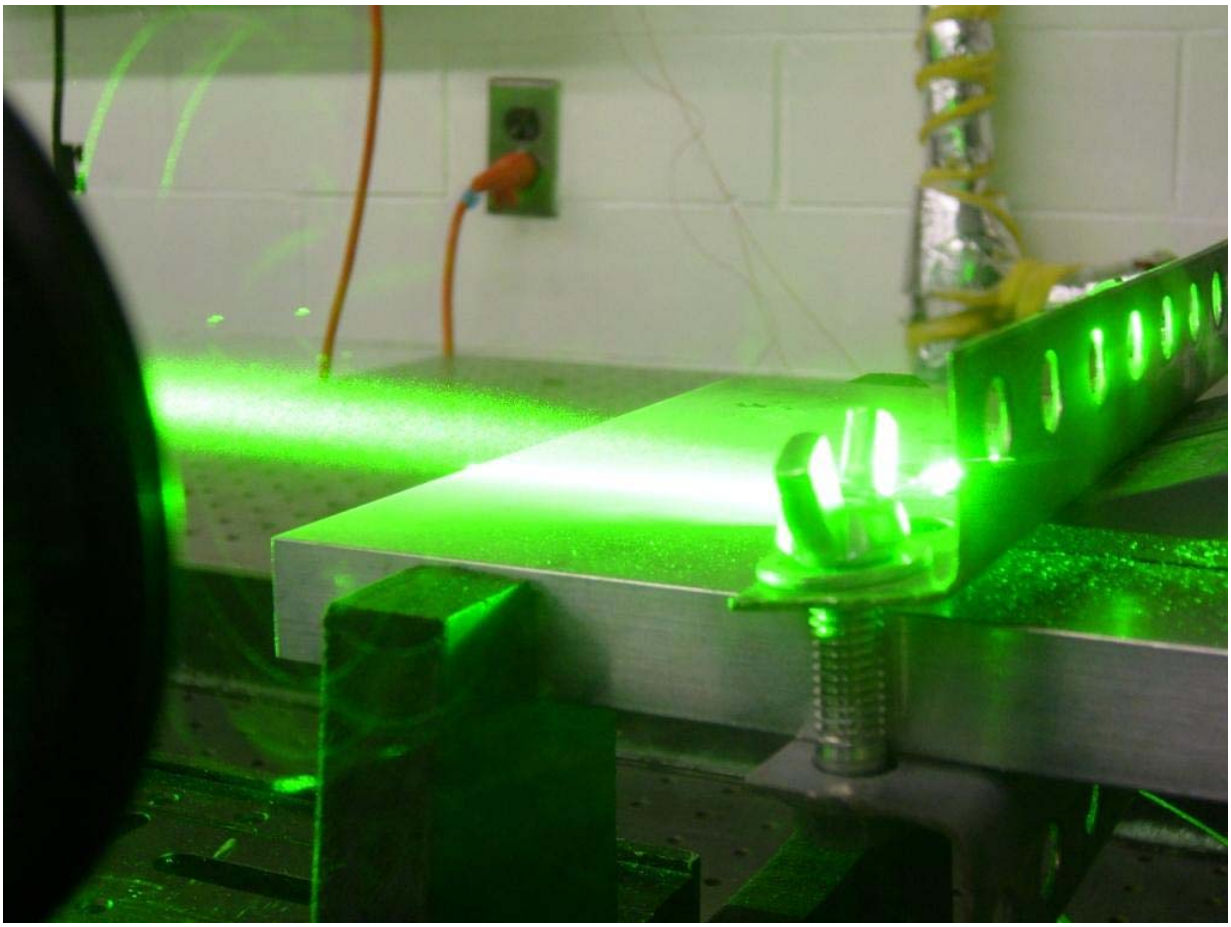

Figure A21: Scattered laser light on the particles.

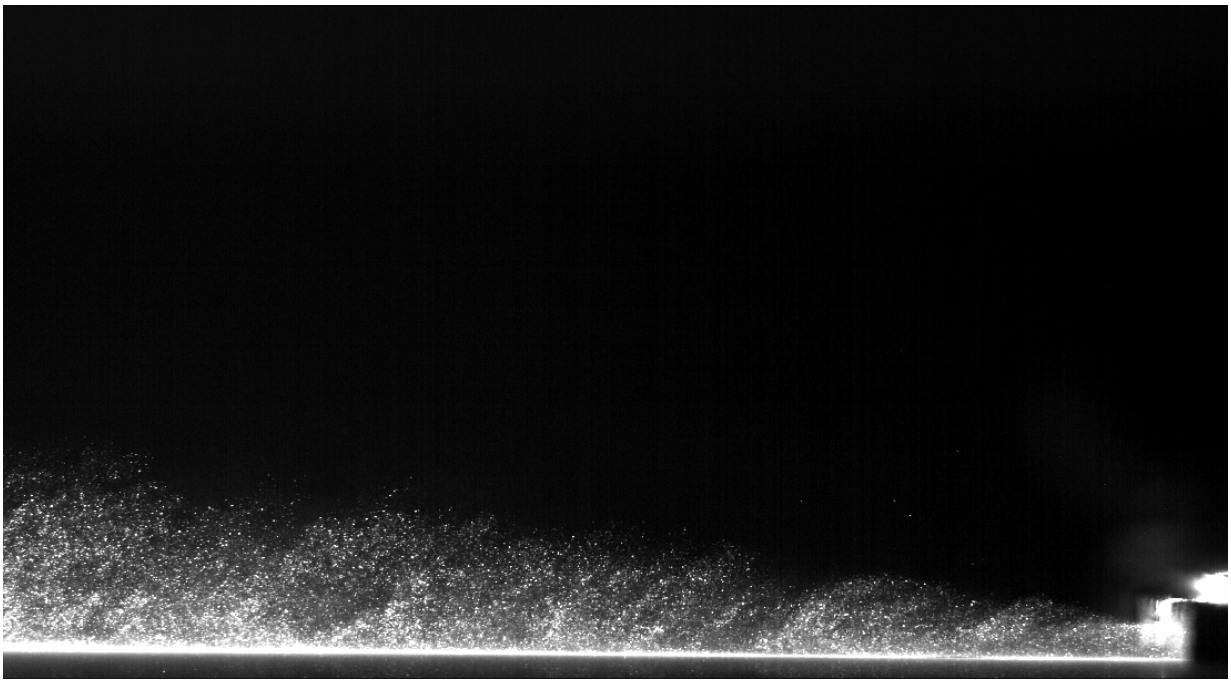

Figure A 22: One of 40 000 CCD images of the flow field.

Two tests were made at five different locations along the nozzle cross section (see Figure A23). Thus ten data sets were obtained containing an amount of 40 000 frames, equivalent to 25 GB of data. But only 50% of the data was processed due to long computational times. The locations relative to the nozzle and HFM were non-dimensionalized by the height, h (2.4 mm) of the nozzle.

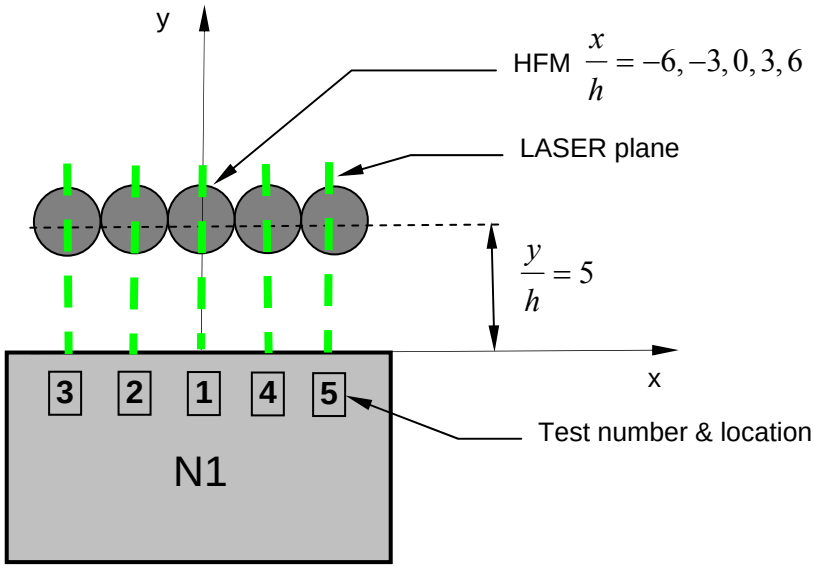

Figure A23: Locations of the laser beam relative to the nozzle cross sectional area.

A3 Data Processing

The raw data was first processed with FlowIQ. Each pair of images (*.tif) resulted in one FlowIQ output file (*.plt), containing the velocity vector field. Hence, the number of files for each data set was reduced to 2,000 images, resulting in a total number of 10,000 files. The FlowIQ output files were then further processed with TechPlot, to visualize the vector field. To obtain the time averaged flow field and quantities, the 3PI was used.

In order to compute the vector field with FlowIQ, several parameters had to be entered. Those values are summarized in Table A1. The FlowIQ interface is shown in Figure A 24: FlowIQ experiment settings interface.

Parameter		Value
Input values	Physical pixel size (magnification)	75 µm/pixel
	Camera pixel size	11 µm/pixel
	Exposure time	0.5 ms
	Aperture	2.8
	Wave length	535 µm (green light)
	Flow tracer density (seeding density)	100 %
	Flow tracer diameter (seeding diameter)	1 µm
	Characteristic length (h)	2.4 mm
	Characteristic velocity	40 m/s
	Density	0.946 kg/m³
	Kinematic viscosity	$2.3 \cdot 10^{-5}$ m²/s
	Laser pulse separation	12µs…15µs
Derived values	Dynamic viscosity, $\mu = \nu\rho$	$2.2 \cdot 10^{-5}$ kg/(ms)
	Reynolds number	~ 4200
	Stokes number	~ 158 000

Table A1: Parameters for flow IQ.

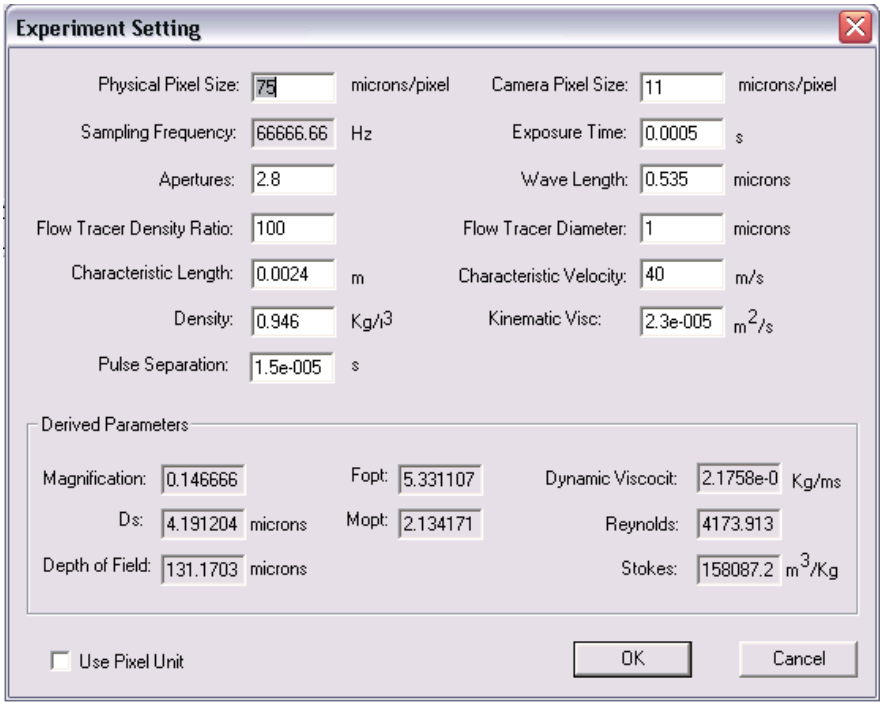

Figure A 24: FlowIQ experiment settings interface.

After the experimental data is entered in FlowIQ one has to create a PIV task. The PIV dialog box asks for grid parameters and computing methods. Those parameters are listed in Table A2. The FlowIQ PIV dialog is shown in Figure A25. The rule of thumb for a window size says the window should be greater or equal to four times the particle displacements, see equation A(1.15). The rule of thumb for the grid spacing suggests, the grid size should be 25% of the size of the smaller window, so that 75% overlap is secured, equation A(1.16).

$$
\begin{aligned}
WS &\geq 4 \times \frac{DISP}{frame} \\
WS &\geq 4 \times u_{char} \Delta t_{LPS} \cdot RES \cdot frame \\
WS &\geq 4 \times 40 \frac{m}{s} \cdot 15 \frac{\mu s}{frame} \cdot \frac{1}{75.062} \frac{pix}{\mu m} \cdot frame \\
WS &\geq 4 \times 7.934\, pix \\
WS &\geq 31.74\, pix \quad => \quad WS \approx 32 pix
\end{aligned}
\qquad \text{A(1.15)}
$$

$$
GS = \frac{1}{4} WS = 8\, pix \qquad \text{A(1.16)}
$$

Parameter	Value
Method	Second order DWO PIV (Center Difference Method)
Peak detection method	Three Point Gaussian Fit
Multi pass type	Standard
Correlation method	FFT based + fast
Window size	(64 32),(32 16), [rectangular, 1st, 2nd pass, 1st and 2nd window]
Grid Spacing	8 x 4
Validation task	Threshold high: 1.2 Threshold low: 1.0 Filer: Mean Loops: 8
Area selection	Optional (not used)
Input file selection	Double frame
Output file info	Specify ….

Table A2: PIV task parameters.

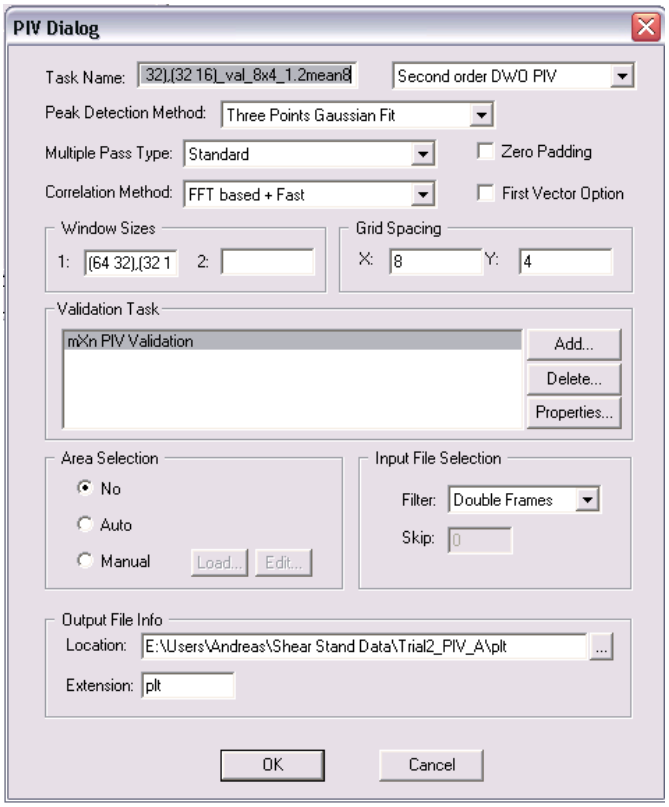

Figure A25: PIV task dialog. Explanation see table and text.

After specifying the processing parameters and the output file location, one has to specify the input file and the sequence of files to read. The next step is to associate the specified file sequence with the processing task. If all parameters are entered correctly and if every necessary step is done, the process can be executed.

To compute the 13 GB of data (1/2·25 GB) the computer cluster provided in the CTFS was used (Figure A26). The cluster is built up of five AMD Athlon^{tm} Dual Core 3800+ processors with a speed of 2 GHz and 2 GB of RAM. The five computations performed are listed in Table A3. Test run (number), workstation, length of computation and processing per double frame is compared.

Figure A26: Workstation cluster in the CTFS at VT.

Test	Workstation	Time per double frame	Date	Time	Computing time
1	Valkyrie	~30.0s	start: 11/18/06	09:00pm	18h00m
			end: 11/19/06	15:00pm	
2	Valkyrie	~20.0s	start: 11/20/06	05:16pm	11h:50m
			end: 11/21/06	05:06am	
3	Domino	~20.0s	start: 11/20/06	05:32pm	11h:50m
			end: 11/21/06	05:22pm	
4	Kitsune	19.4s	start: 11/20/06	07:05pm	11h:30m
			end: 11/21/06	06:35am	
5	Nereid	19.7s	start: 11/20/06	09:30pm	11h:40m
			end: 11/21/06	09:10am	
Total effective computing time:					**64h:50m**

Table A3: Test run, workstation, computing time.

After processing the data with FlowIQ, the time-averaged data was obtained by computing the FlowIQ output with 3PI. After unpacking the data, however, it was found out that a good amount of the *.tif – files were corrupt (Figure A27). Thus, for each test run, the data had to be processed in groups. after having processed each group with 3PI, in order to get the time-averaged quantities over the whole test run, the data had to be merged and time averaged with a 3PI merger (see section F MATLAB Codes).

In order to get the job done faster, a batch file was written, which would call for each data set and each test number the 3PI program. Another Matlab program then calls the 3PI merger and merge the steady output files from 3PI to one coherent big file for each test run (see section F MATLAB Codes). The 3PI input face is shown in Figure A28. Each of the necessary parameters can be seen in this figure as well. Figure A29 illustrates the data processing procedure.

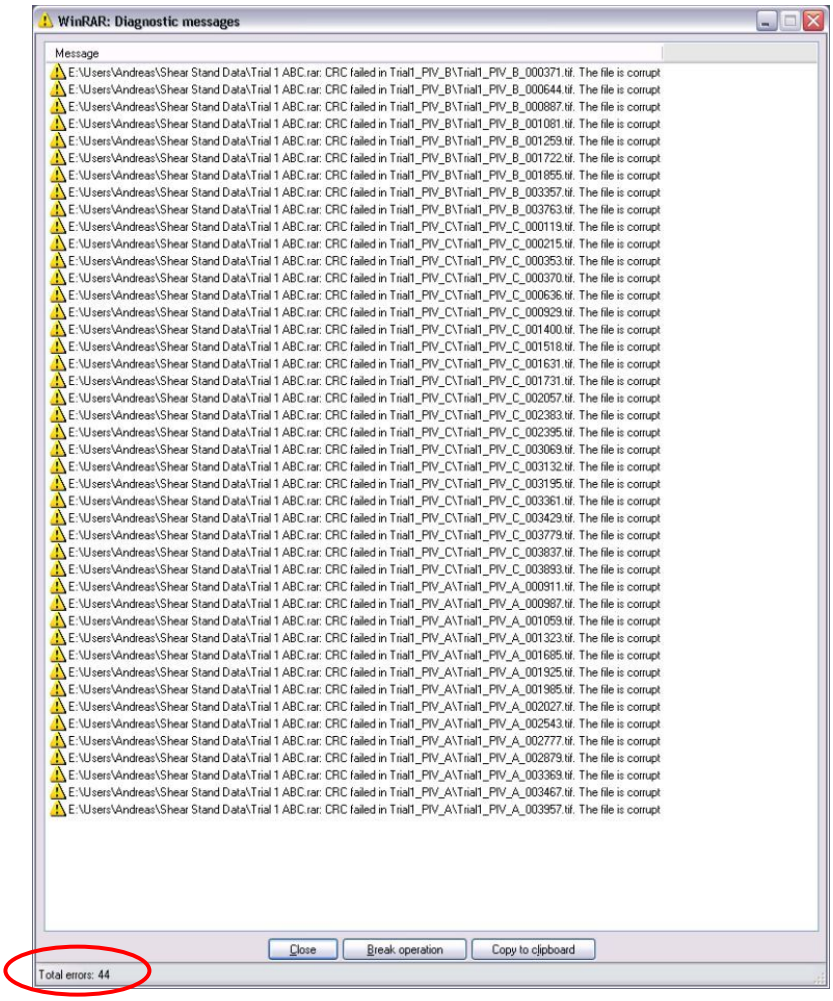

Figure A27: WinRAR corrupt messages warnings. The total errors for test 1 was 44, the total amount of errors for all five tests was 124.

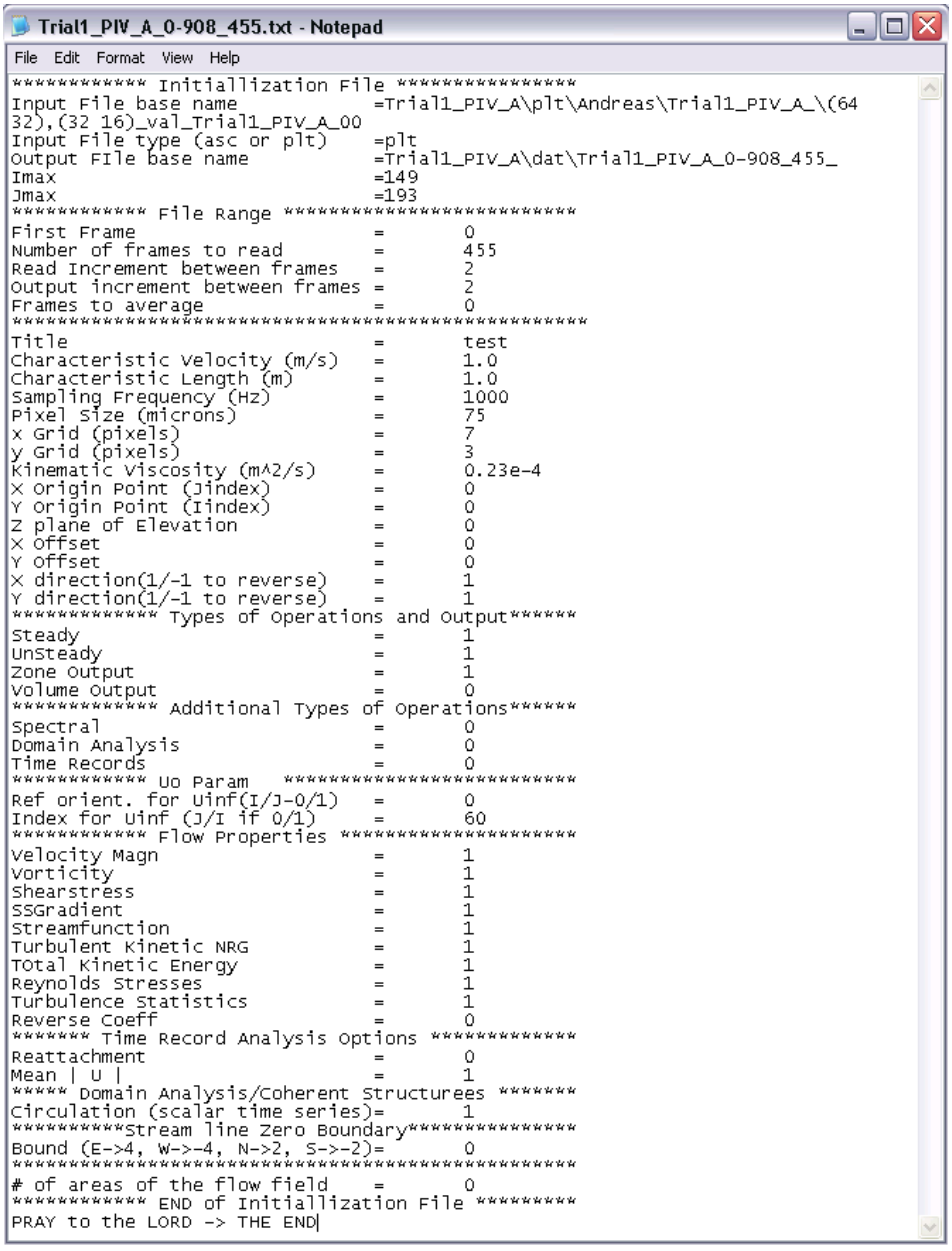

Trial1_PIV_A_0-908_455.txt - Notepad

File Edit Format View Help

```
************* Initiallization File *****************
Input File base name            =Trial1_PIV_A\plt\Andreas\Trial1_PIV_A_\(64
32),(32 16)_val_Trial1_PIV_A_00
Input File type (asc or plt)    =plt
Output FIle base name           =Trial1_PIV_A\dat\Trial1_PIV_A_0-908_455_
Imax                            =149
Jmax                            =193
************* File Range ****************************
First Frame                     =       0
Number of frames to read        =       455
Read Increment between frames   =       2
Output increment between frames =       2
Frames to average               =       0
*********************************************************
Title                           =       test
Characteristic Velocity (m/s)   =       1.0
Characteristic Length (m)       =       1.0
Sampling Frequency (Hz)         =       1000
Pixel Size (microns)            =       75
x Grid (pixels)                 =       7
y Grid (pixels)                 =       3
Kinematic Viscosity (m^2/s)     =       0.23e-4
X Origin Point (Jindex)         =       0
Y Origin Point (Iindex)         =       0
Z plane of Elevation            =       0
X Offset                        =       0
Y Offset                        =       0
X direction(1/-1 to reverse)    =       1
Y direction(1/-1 to reverse)    =       1
************** Types of Operations and Output******
Steady                          =       1
UnSteady                        =       1
Zone Output                     =       1
Volume Output                   =       0
************** Additional Types of Operations******
Spectral                        =       0
Domain Analysis                 =       0
Time Records                    =       0
************* Uo Param    ***************************
Ref orient. for Uinf(I/J-0/1)   =       0
Index for Uinf (J/I if 0/1)     =       60
************* Flow Properties ***********************
Velocity Magn                   =       1
Vorticity                       =       1
Shearstress                     =       1
SSGradient                      =       1
Streamfunction                  =       1
Turbulent Kinetic NRG           =       1
TOtal Kinetic Energy            =       1
Reynolds Stresses               =       1
Turbulence Statistics           =       1
Reverse Coeff                   =       0
******* Time Record Analysis Options ***************
Reattachment                    =       0
Mean | U |                      =       1
***** Domain Analysis/Coherent Structurees *******
Circulation (scalar time series)=       1
***********Stream line Zero Boundary****************
Bound (E->4, W->-4, N->2, S->-2)=       0
*********************************************************
# of areas of the flow field    =       0
************* END of Initiallization File *********
PRAY to the LORD -> THE END
```

Figure A28: 3PI interface. Each parameter can be seen.

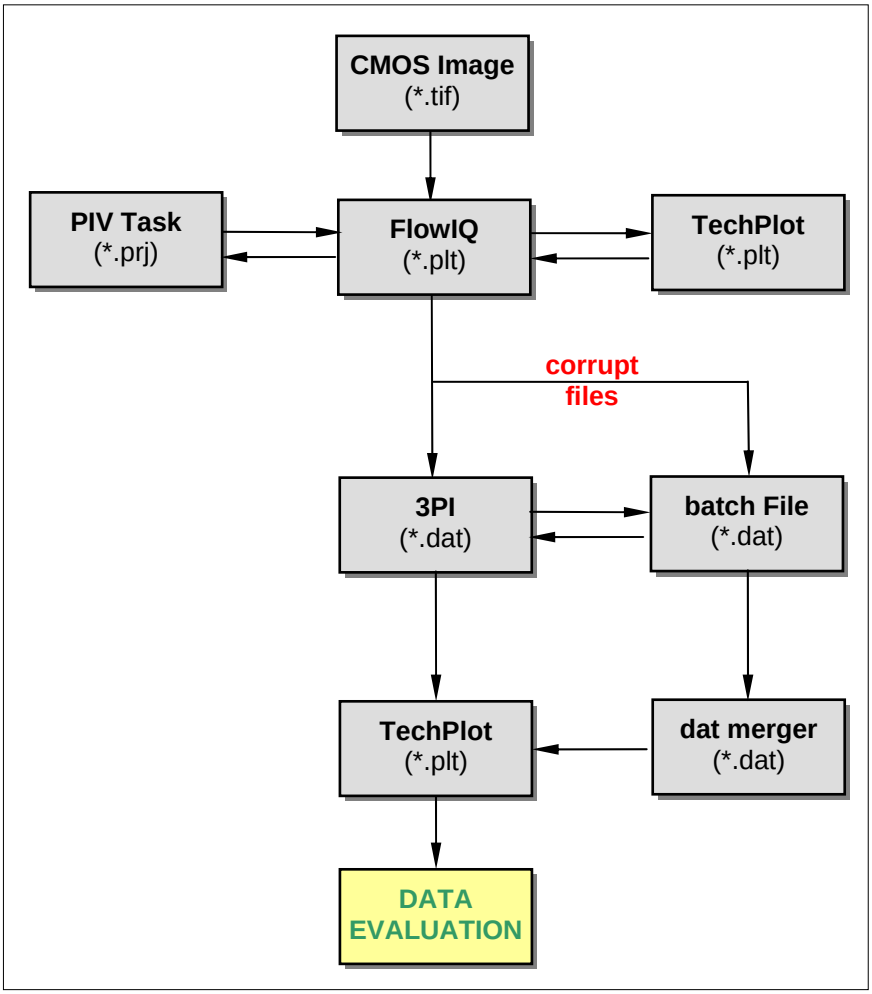

Figure A29: Data processing procedure. For corrupt and non-corrupt raw data. File extensions in brackets is the output format of the according program.

A4 Results

A4.1 Time averaged flow field for location 1 (test 1 at 5 psi)

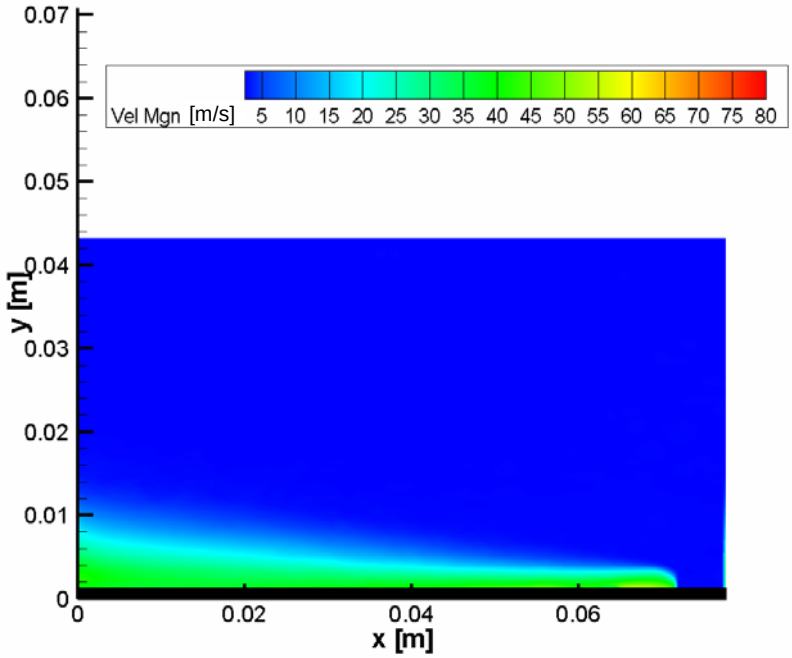

Figure A30: Time averaged flow field at location one at 5 psi. The color is mostly green, meaning the mean velocity is around 40 m/s. The black solid line is the plate.

A4.2 Time averaged flow field for location 2 (test 2 at 5 psi)

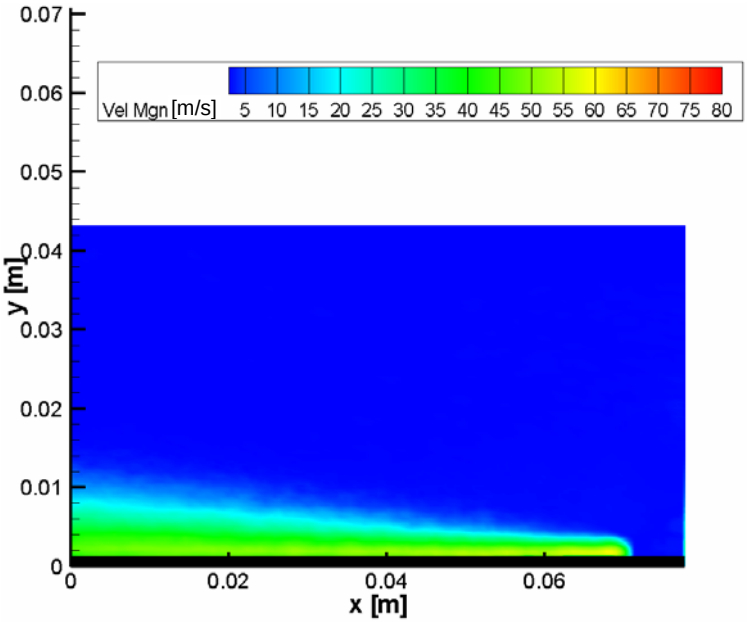

Figure A31: Time averaged flow field at location two at 5 psi. The color is mostly green, meaning the mean velocity is around 40 m/s. The black solid line is the plate.

A4.3 Time averaged flow field for location 3 (test 3 at 5 psi)

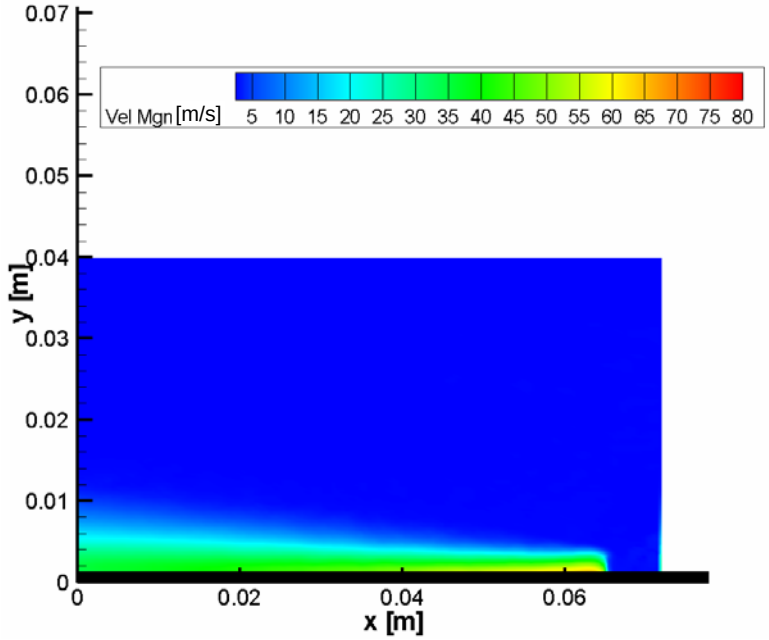

Figure A32: Time averaged flow field at location three at 5 psi. The color is mostly green, meaning the mean velocity is around 40 m/s. The black solid line is the plate.

A4.4 Time averaged flow field for location 4 (test 4 at 5 psi)

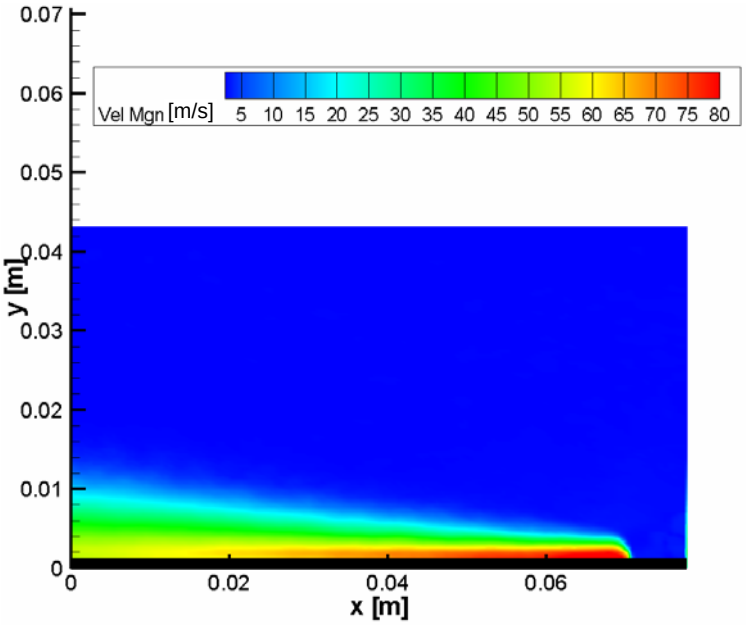

Figure A33: Time averaged flow field at location four at 5 psi. The color is mostly green, meaning the mean velocity is around 40 m/s. The black solid line is the plate.

A4.5 Time averaged flow field for location 5 (test 5 at 5 psi)

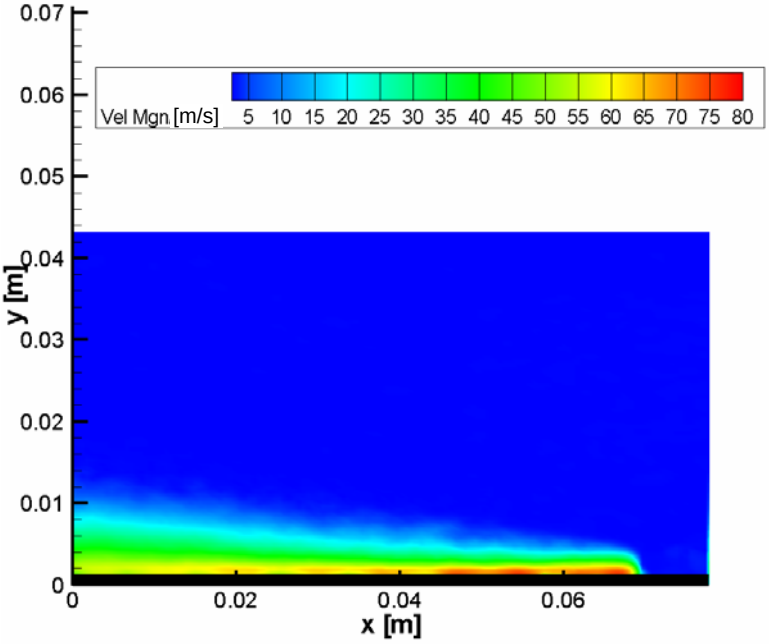

Figure A34: Time averaged flow field at location five at 5 psi. The color is mostly green, meaning the mean velocity is around 40 m/s. The black solid line is the plate.

A4.6 Time averaged flow field for location 1 through 5 (test 1 through 5 at 5 psi)

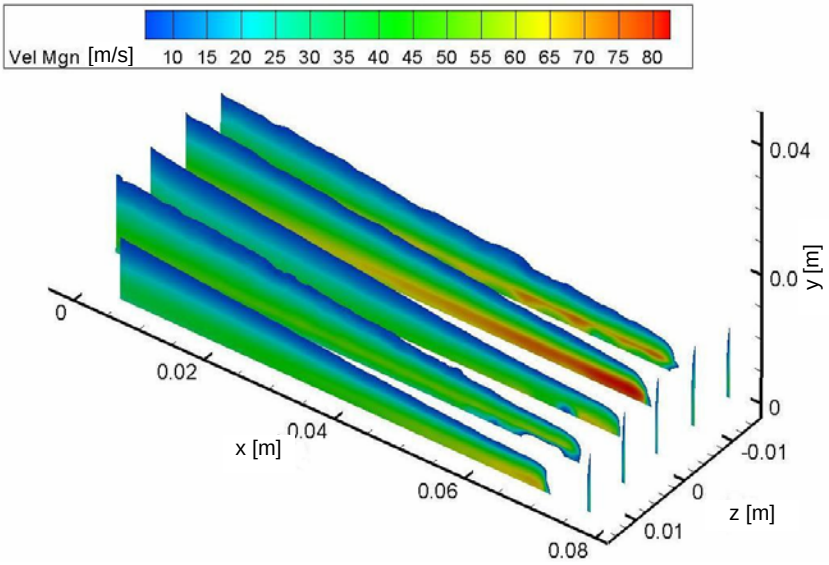

Figure A35: Time averaged flow field at 5 psi. The color is mostly green, meaning the mean velocity is around 40 m/s. The black solid line is the plate.

The velocity field shown in Figure A35 shows a composition of all five tests taken. The picture is misleading, because the tests were not taken at the same time. The velocity field is skewed, because the velocities on the right edge are higher than on the left edge. The red color is indicating high velocities the blue color is indicating low velocities, the mean velocity is in the green colors, around 45 m/s.

B1 Air Heater Design

Properties of air at STP (300K, 1.013bar)

$\rho := 1.205 \frac{kg}{m^3}$ $c_p := 1006 \frac{J}{kg \cdot K}$

Material Properties of Copper

$k := 372 \frac{W}{m \cdot K}$

Boundary Conditions

Input Data:

Temperature in °C

$T_{inC} := 20\,°C$

$T_{outC} := 150\,°C$

Mass Flow Rate in kg/s:

$V_{dot} := 65 \frac{ft^3}{min}$ $m_{dot} := \rho \cdot V_{dot}$ $m_{dot} = 0.037 \frac{kg}{s}$

Temperature Conversion

°C	**°F**	**K**
– –	$T_{inF} := \frac{9}{5} \cdot T_{inC} + 32$	$T_{inK} := 273.15 \cdot K + T_{inC} \cdot K$
– –	$T_{outF} := \frac{9}{5} \cdot T_{outC} + 32$	$T_{outK} := 273.15 \cdot K + T_{outC} \cdot K$
$T_{inC} = 20\,°C$	$T_{inF} = 68\,°F$	$T_{inK} = 293.15\,K$
$T_{outC} = 150\,°C$	$T_{outF} = 302\,°F$	$T_{outK} = 423.15\,K$

Energy Balance

$Q := m_{dot} \cdot c_p \cdot (T_{outK} - T_{inK})$ $Q = 4.834 \times 10^3 W$

Heat Tape (Mc Master, oder no 4550T14, T12)

$q'' := 13 \frac{W}{in^2}$ $w := 0.5in$

Length of tape

$D := 0.5in$ $D = 0.013m$

$c := \pi \cdot D$ $c = 0.04m$

$L_{tape} := \frac{Q}{q'' \cdot c}$ $L_{tape} = 6.013m$ $L_{tape} = 19.728ft$ $L_{tape} = 236.74in$

Total Energy Output of Heat Tape

$Q_{out} := q'' \cdot L_{tape} \cdot c$ $Q_{out} = 4.834 \times 10^3 W$ OK

Length of pipe

14 in tape ----> 5 in pipe

$L_{pipe} := \frac{5}{14} \cdot L_{tape}$ $L_{pipe} = 2.148m$ $L_{pipe} = 7.046ft$ $L_{pipe} = 84.55in$

Price:

$P_{8ft} := 64.69$

$P_{4ft} := 41.66$

$P := 2 \cdot P_{8ft} + P_{4ft}$ $P = 171.04$

Current needed

$I_1 := 5.2A$ $I_2 := 2.6A$ $U := 120V$

$R_1 := \frac{U}{I_1}$ $R_1 = 23.077\Omega$

$R_2 := \frac{U}{I_2}$ $R_2 = 46.154\Omega$

$I := \frac{U}{2R_1 + R_2}$ $I = 1.3A$

B2 Air Heater Box Design

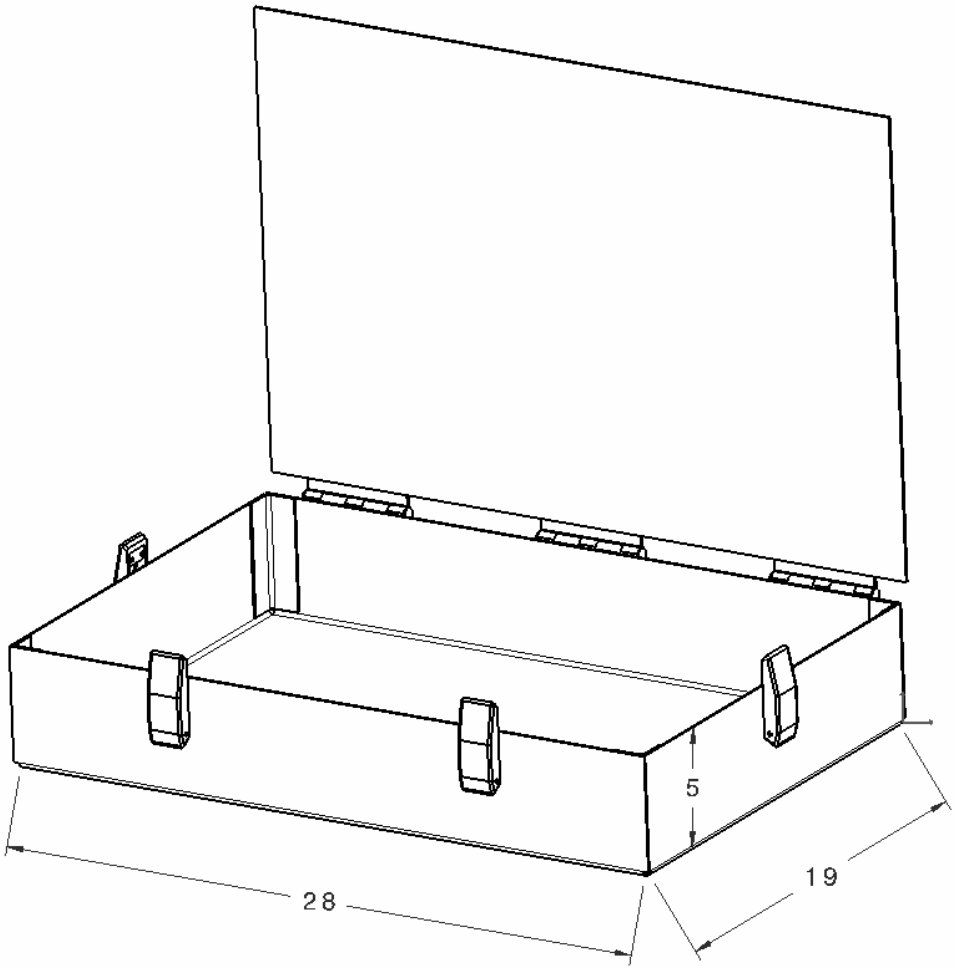

Figure B2- 1: Air heater box.

C1 Shear Stand Design

Pressure Vessel

Design of Pressure Vessel Cap and Screws

		Brit.:	ISO:
Number of screws:	$n := 6$		
Parameters:		$p := 80psi$	$p = 0.552 \frac{N}{mm^2}$
		$w := 4.3in$	$w = 109.22mm$
		$h := 0.723in$	$h = 18.364mm$
Cap Area:	$A_c := w \cdot h$	$A_c = 3.109in^2$	$A_c = 2005.738mm^2$
Total force on cap:	$F_c := p \cdot A_c$		$F_c = 1106.326N$
Force on one screw:	$F_s := \frac{F_c}{n}$		$F_s = 184.388N$

Select screws:		$d_s := 0.06in$	$d_s = 1.524mm$
Length:		$l_s := \frac{3}{8}in$	$l_s = 9.525mm$
Tensile strength:		$R := 144000psi$	$R = 992.845 \frac{N}{mm^2}$
Safety factor:	$\nu := 3$		
Allowable stress:	$R_{max} := \frac{R}{\nu}$		$R_{max} = 330.948 \frac{N}{mm^2}$

Cross section area of screw:	$A_s := \frac{\pi \cdot d_s^2}{4}$		$A_s = 1.824mm^2$
Tension on one screw:	$\sigma_s := \frac{F_s}{A_s}$		$\sigma_s = 101.082 \frac{N}{mm^2}$

$R_{max} < \sigma_s$.. OKAY

Actual safety factor: $\nu_a := \frac{R}{\sigma_s}$ $\nu_a = 9.822$

C2 Shear Stand Drawings

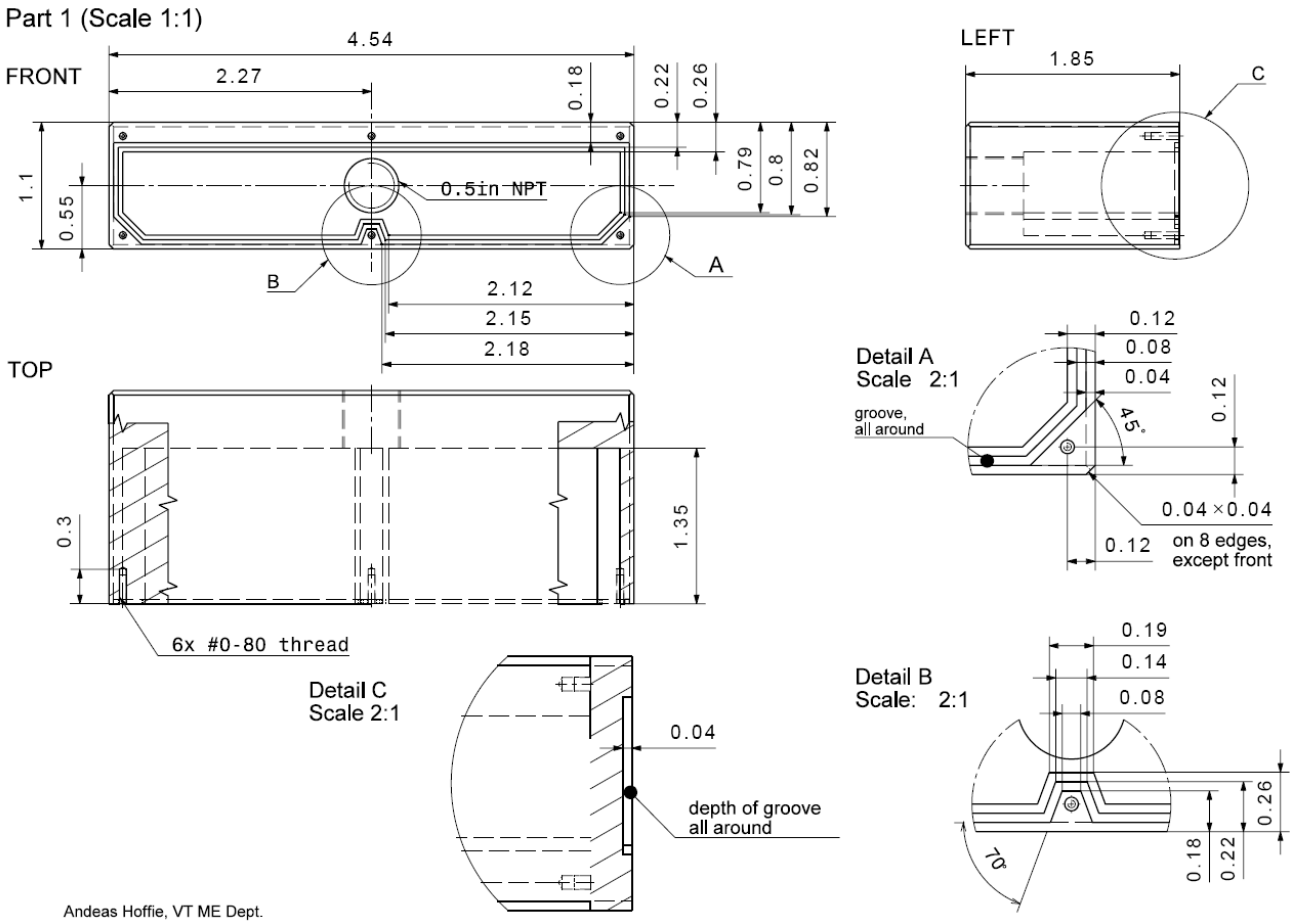

Figure C2- 1: Shear stand plenum.

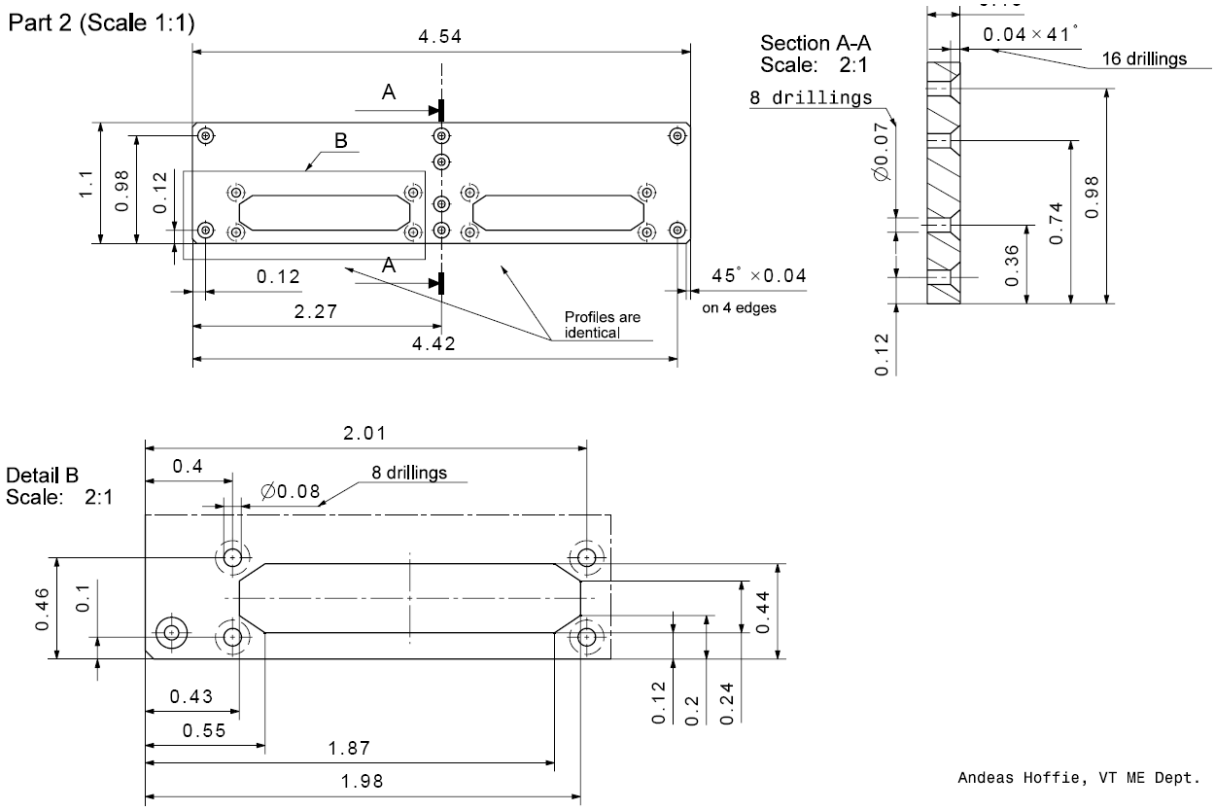

Figure C2- 2: Shear stand front plate.

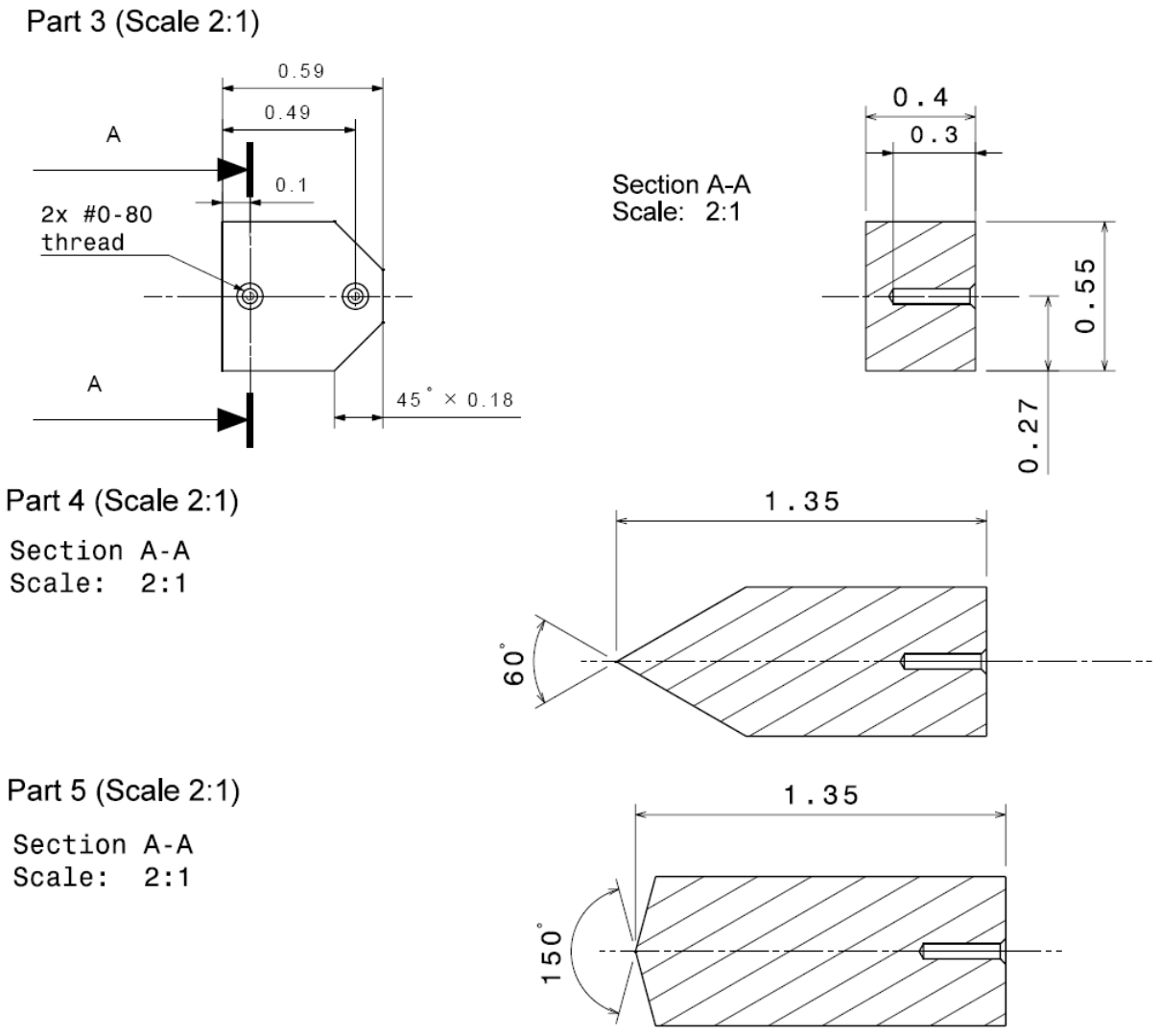

Figure C2- 3: Shear stand flow splitter.

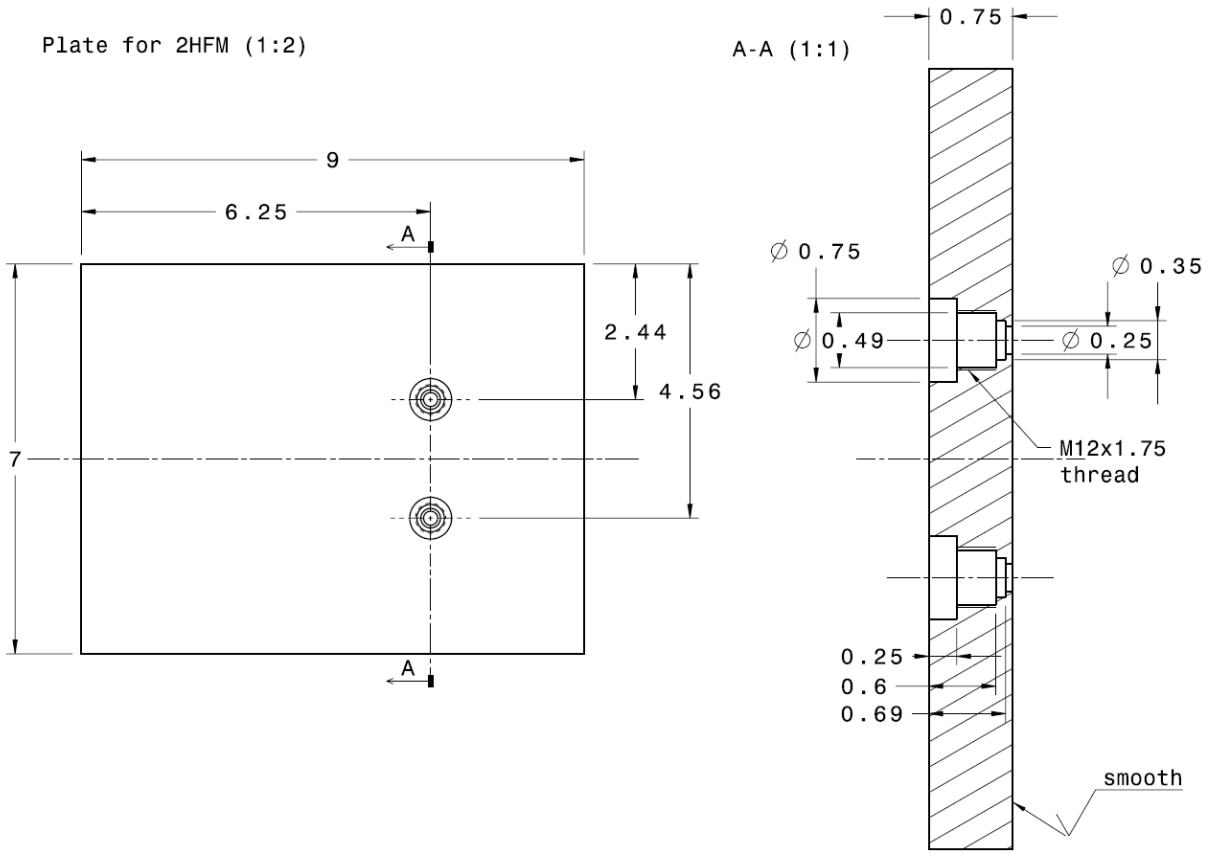

Figure C2- 4: Shear stand plate for 2 HFM.

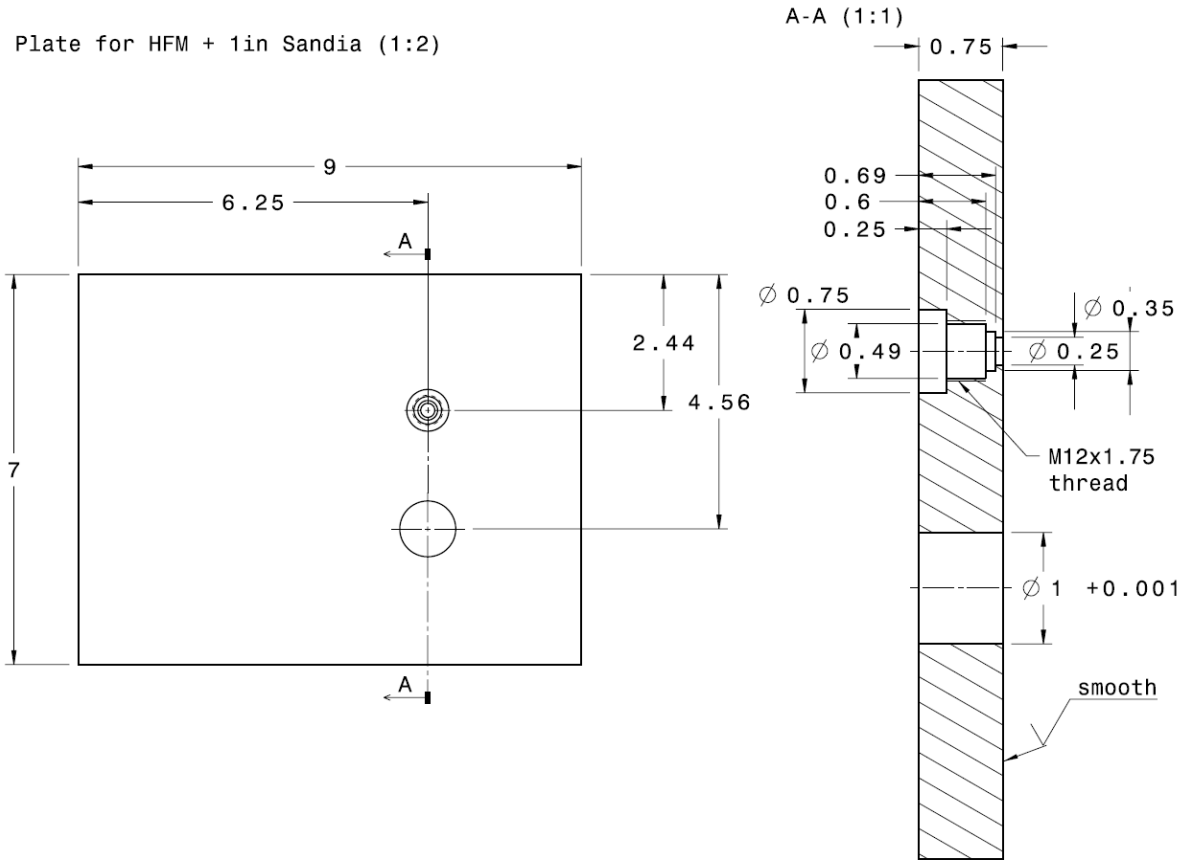

Figure C2- 5: Shear stand plate for HFM and 1 in. SB gage.

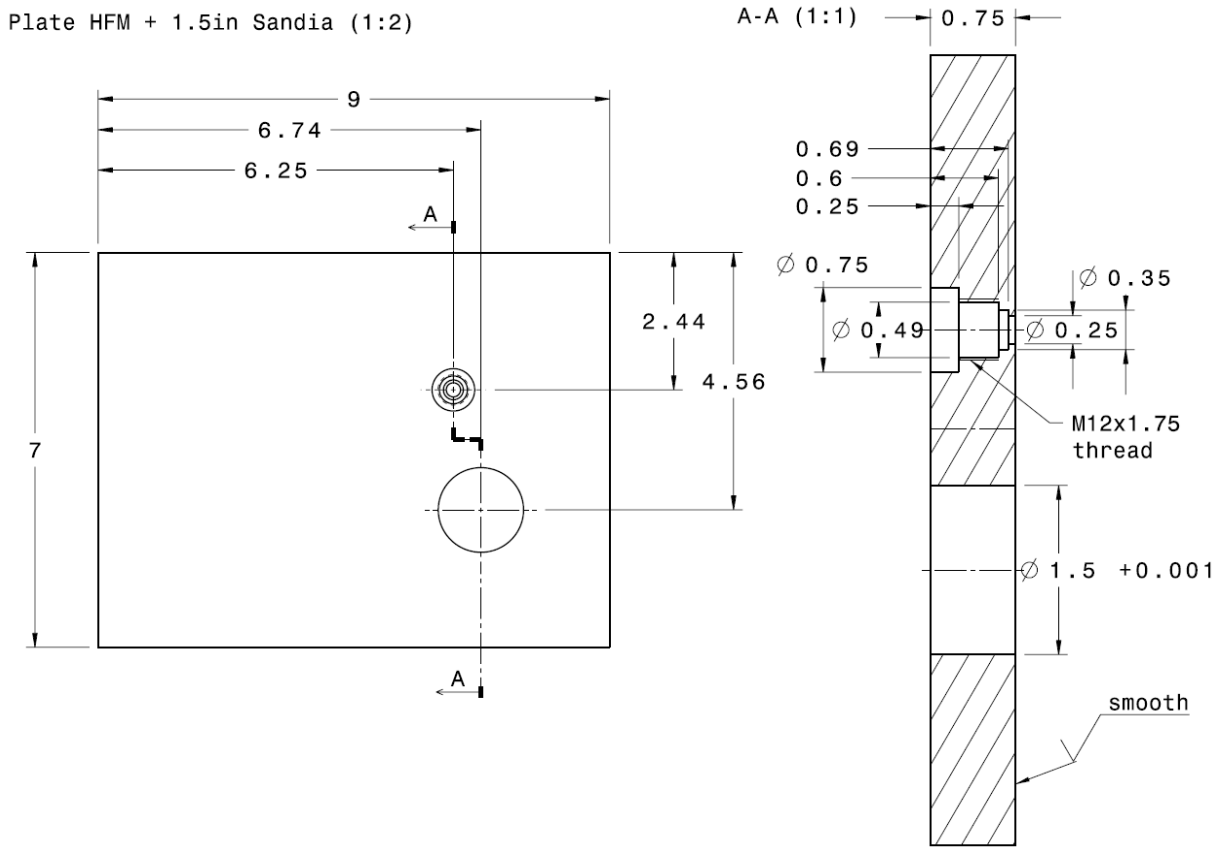

Figure C2- 6: Shear stand plate for HFM and 1.5 in. SB gage.

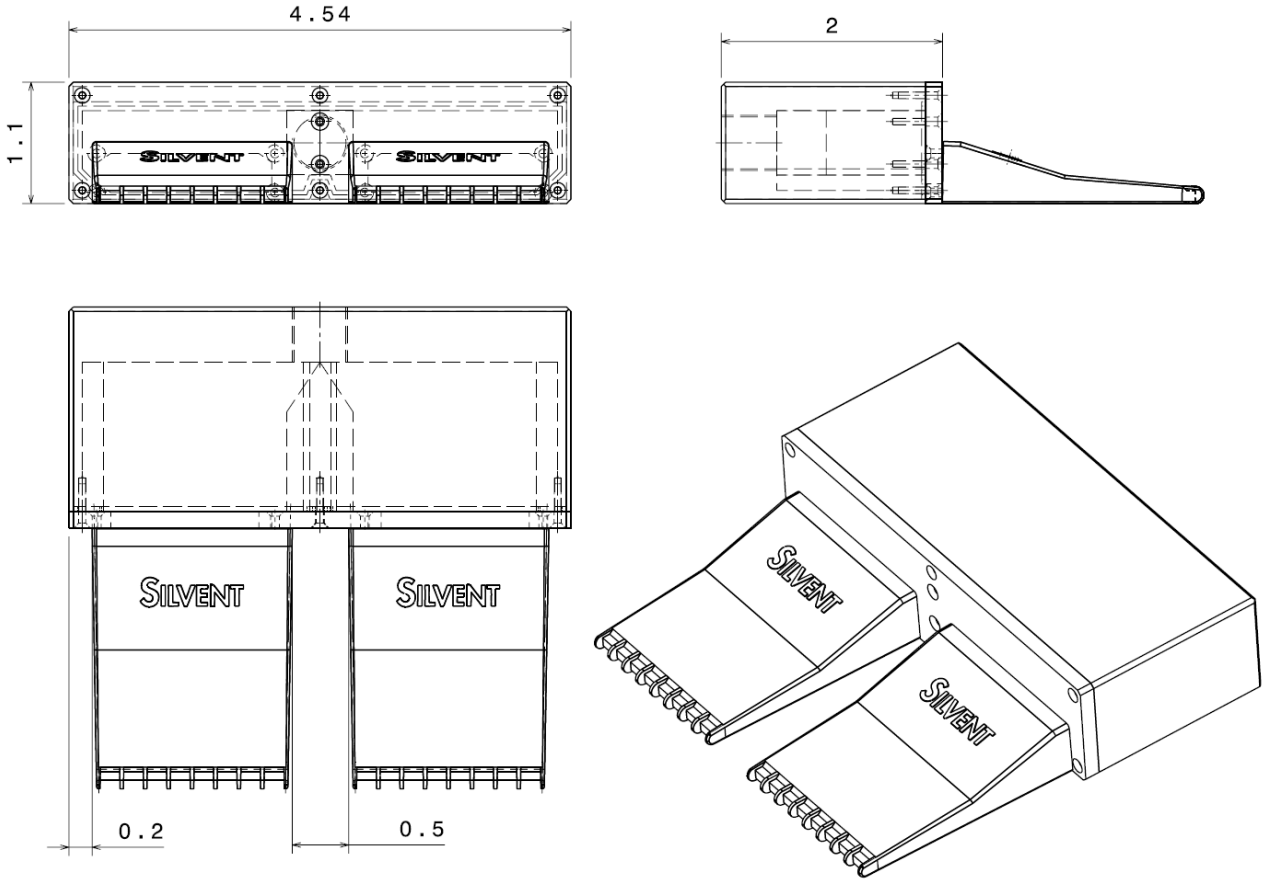

Figure C2- 7: Shear stand, front, top, left and iso view.

D Stagnation Stand Drawings

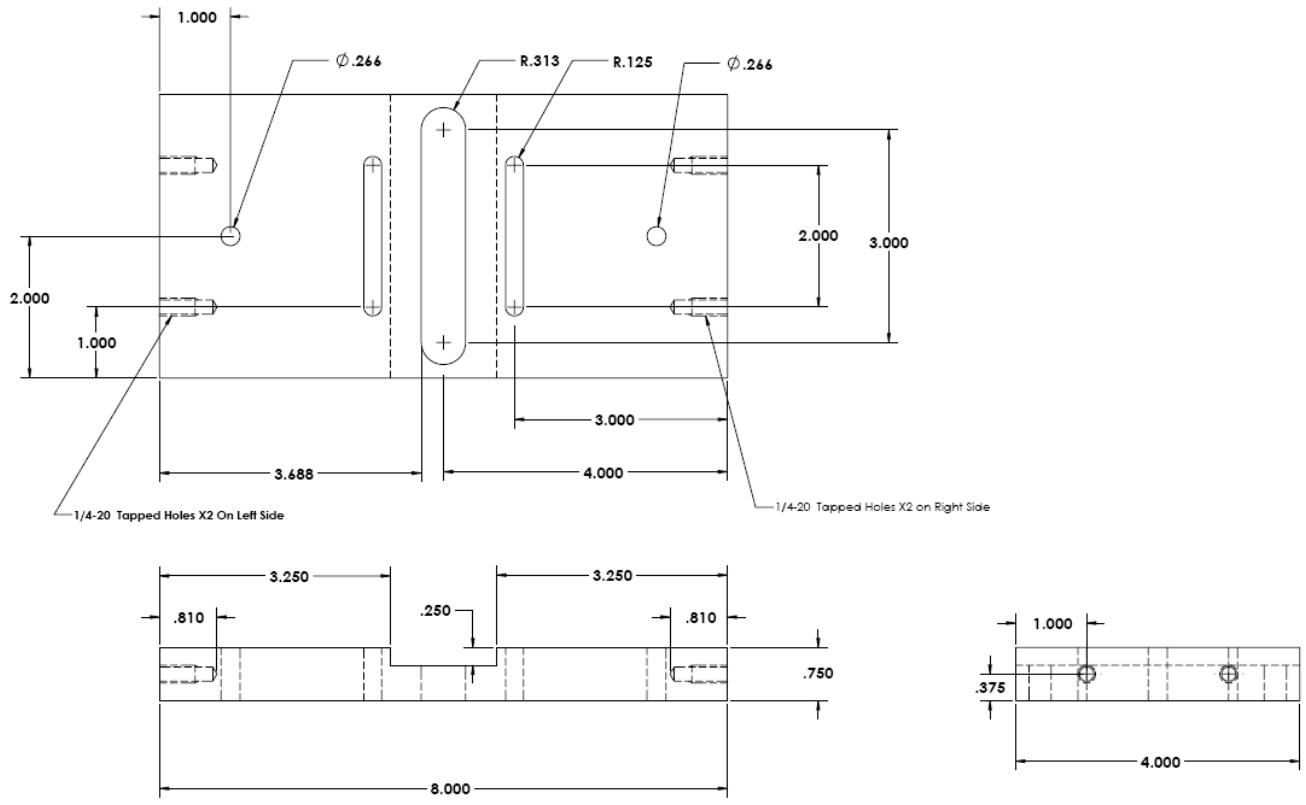

Figure D 1: Stagnation stand, horizontal plate.

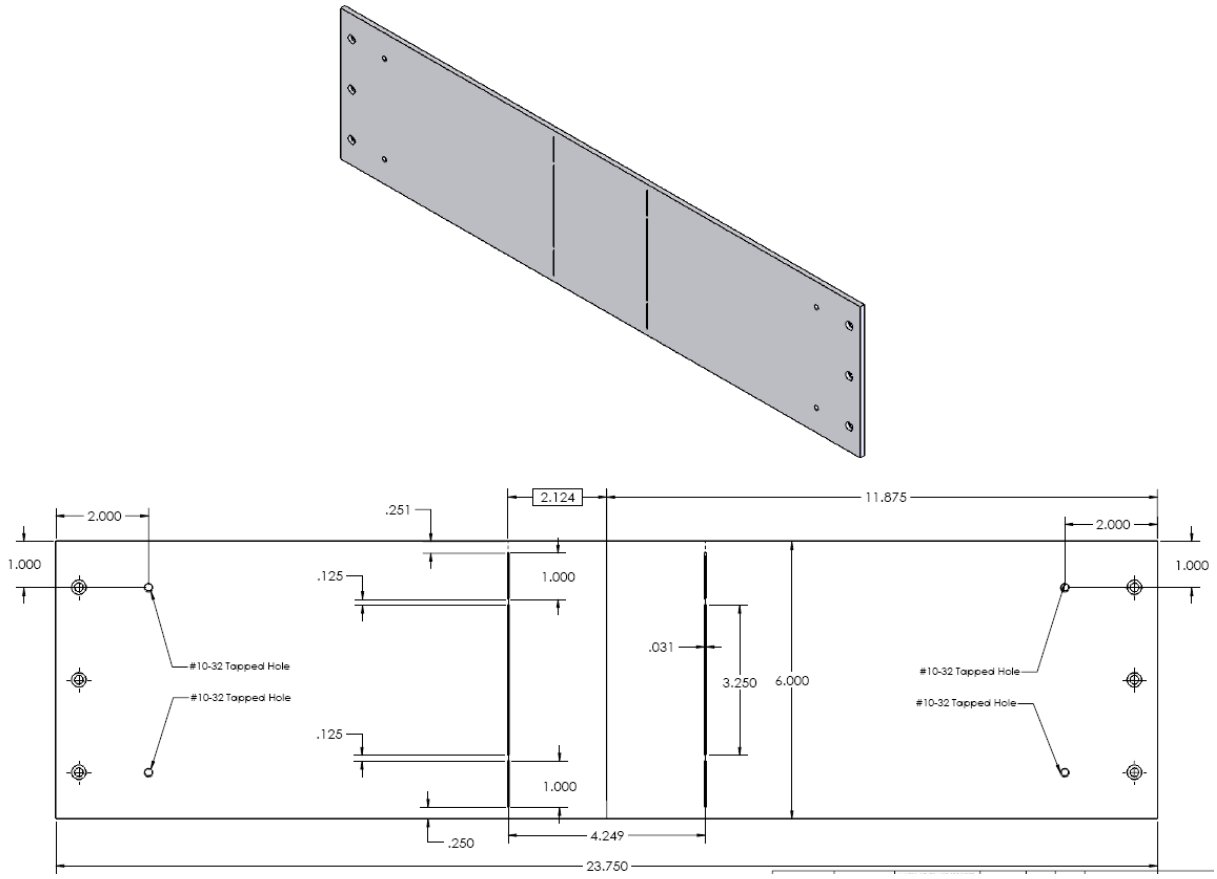

Figure D 2: Stagnation stand, vertical plates.

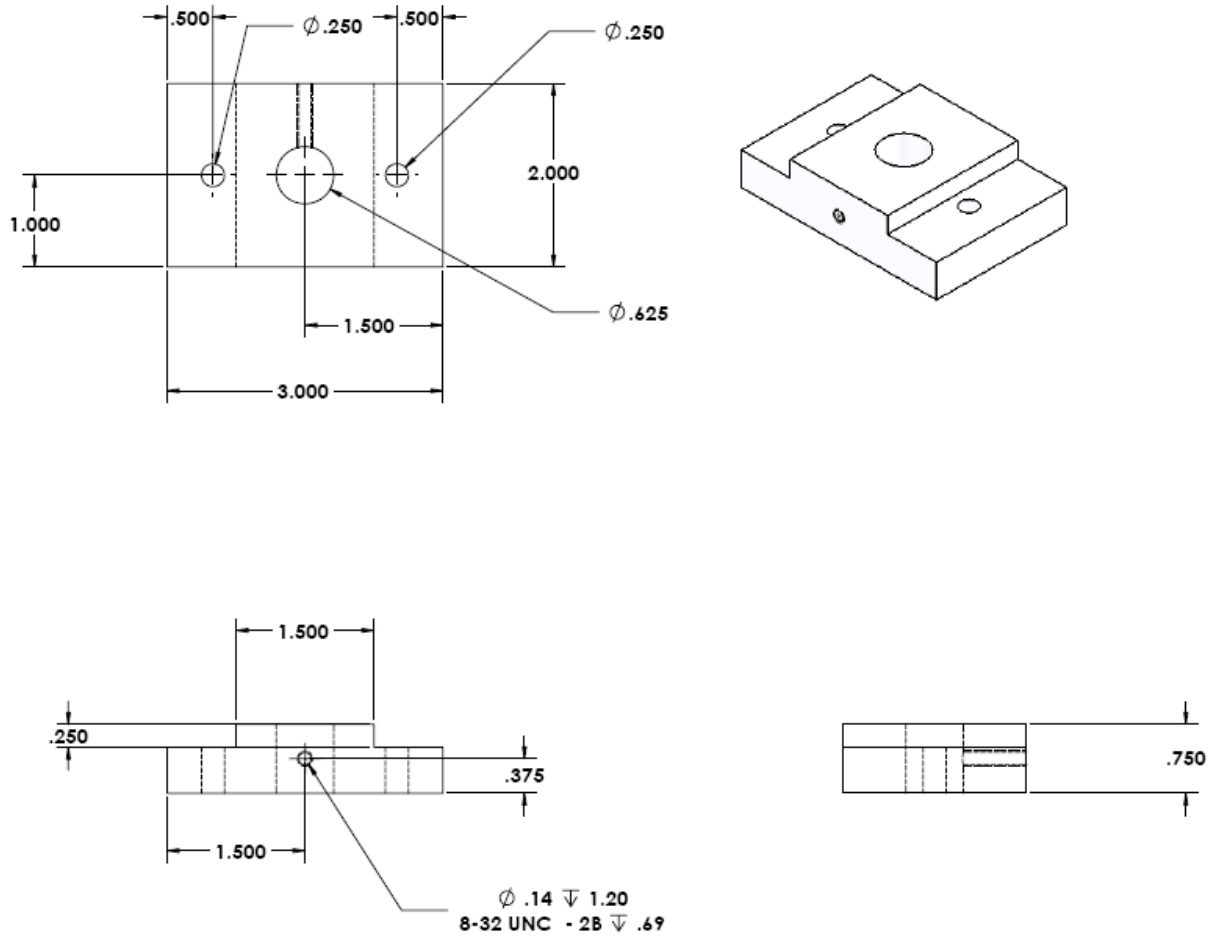

Figure D 3: Stagnation stand, attachment for air supply.

E Property Table for Air

T	ρ	c_p	μ	ν	k	α	Pr
°C	kg/m³	kJ/(kgK)	kg/s·m	cm²/s	W/m·K	cm²/s	-
0	1.293	1.006	$1.71 \cdot 10^{-5}$	0.123	0.024	0.184	0.72
10	1.247	1.006	$1.76 \cdot 10^{-5}$	0.141	0.025	0.196	0.72
20	1.205	1.006	$1.81 \cdot 10^{-5}$	0.150	0.025	0.208	0.72
30	1.165	1.006	$1.86 \cdot 10^{-5}$	0.160	0.026	0.223	0.72
60	1.060	1.008	$2.00 \cdot 10^{-5}$	0.188	0.028	0.274	0.70
100	0.964	1.011	$2.18 \cdot 10^{-5}$	0.230	0.032	0.328	0.70
200	0.746	1.025	$2.58 \cdot 10^{-5}$	0.346	0.039	0.519	0.68
300	0.616	1.045	$2.95 \cdot 10^{-5}$	0.481	0.045	0.717	0.68

Table E 1: Dry air at atmospheric pressure. Source: Bejan [3].

F MATLAB Codes

F1 Least Squares Curve Fit

```
%Developed by Andrew Gifford to provide a viable way
%of fitting an empirical data curve to Sandia Heat
%Flux Gage Results where the unknown parameter
%is R'' , a thermal resistance.
clc
clear all
close all

format long

%Enter an initial guess for the value of the thermal resistance R''
R=[100];      %cm^2-C/W

%Find the minimum R that minimizes the distance from the experimental data
%and a curve fit using the form S0/(1+h*R'')
[Ropt, fval]=fminimax(@ObjectiveFunction,R)


%%%%%%%%%%%%%%%%%%%%%%%%%%%%%%%%%%%%%%%%%%%%%%%%%%%%%%%%%%%%%%%%%%%%%%%%%%%%%%%
%Objective Function
function F=ObjectiveFunction(R)
%Enter the known vector of measured heat transfer coefficients (W/cm^2-C):
hexp=[
0.024371969
0.029112376
0.030616217
0.050698512
0.074301685
0.104010731
0.140685138
];
%Enter the known vector of measured gage senstivities (mV/W/cm^2-C):
```

```
Sexp=[
0.531511413
0.493212239
0.555317816
0.509917317
0.487666524
0.461618051
0.445928387

];
%Enter the accepted value of S at h=0 W/cm^2-C:
S0=0.78200; %mV/W/cm^2-C

for i=1:1:length(hexp)
    F1(i,1)=(abs([Sexp(i)-S0/(1+R*hexp(i))]))^2;
end
F=sum(F1);
%%%%%%%%%%%%%%%%%%%%%%%%%%%%%%%%%%%%%%%%%%%%%%%%%%%%%%%%%%%%%%%%%%%%%%%%%%%%%%%
```

F2 3PI Merger

```
% By Mike Brady
% steady3pifiles is a cell array containing the file names (no directory)
% Idat and Jdat from dat files
% numvars is number of variables in dat files, scalar
% numframes is the number of frames in each set (vector)

function mergedatfiles(steady3pifiles,direc,Idat,Jdat,numvars,numframes);
            % read file
            for j=1:length(steady3pifiles)
            fid = fopen([direc steady3pifiles{j}]);
            line1=fgetl(fid);
            line2=fgetl(fid);
            line3=fgetl(fid);
            xmat=[];
            for k=1:numvars
            xmat=[xmat;fscanf(fid,'%g',[Idat Jdat])'];
            end
            xmatall(:,:,j)=xmat*numframes(j);
            fclose(fid);
            size(xmatall)
            end

            % do average, weighted based on number of frames in each set

            xmatallave=sum(xmatall,3)/sum(numframes);

            % output file

fid = fopen([direc 'all-' steady3pifiles{1}], 'w');
strg=[];
for j=1:Idat
    strg=[strg '%+10.3e '];
end
```

```
strg=[strg '\n'];
fprintf(fid,'TITLE="DPIV Data File"\n');
fprintf(fid,'VARIABLES =     "X/L",  "Y/L",  "Z/L",  "U/Uo",  "V/Uo",  "W/Uo",
"boundary",   "Vel   Mgn/Uo",   "Vorticity",   "Shearstress",   "SSGradient",
"StreamFunction",    "TKE/Uo^2",    "KE/Uo^2",    "u´^2/Uo^2",    "v´^2/Uo^2",
"u´v´/Uo^2",   "(Urms)/Uo",   "U  Skew/Uo^2",   "U  Curt",   "(Vrms)/Uo",   "V
Skew/Uo^2", "V Curt", "E_i", "E_j", "E",\n');
fprintf(fid,'Zone T= "1", I=%3.0f J=%3.0f F="BLOCK"\n',Idat,Jdat);
fprintf(fid,strg,xmatallave');
fclose(fid);
disp('done');
```

VITA

Andreas Hoffie was born on August 5th 1980 in "Geislingen an der Steige", close to Stuttgart in South West Germany. He grew up in a rural area. His parental business of gastronomy and farming incorporated him already at an early age and accompanied him throughout his youth during school and college. In his free time he showed interest in sports (soccer and athletics), farming technology but later also in astronomy and aerospace technology. These interests finally, determined his decision to study aerospace engineering at Stuttgart University with beginning of October 2001 and received his Bachelor equivalent status in aerospace engineering in 2004.

In the middle of 2004, he decided to apply for an exchange program between the University of Stuttgart and Virginia Tech, USA. In August 2005 he started his studies abroad. The desire to obtain an American M.S. degree brought him the opportunity to work as a graduate research assistant for Dr. Thomas Diller for over one year. He defended successfully his work on December 19th 2006 and received his Master of Science in mechanical Engineering.

With beginning of 2007 he will return to Stuttgart University and continue his studies towards his Master of Science equivalent degree in aerospace engineering ("Diploma-Engineer in aerospace engineering"). His plan is to finish his second Masters at the latest by middle of 2008. He also intends to obtain a Doctor of Philosophy in Engineering and he also considers coming back to the U.S. to obtain this degree.

Andreas Hoffie can imagine working as a research or systems engineer for the space industry (Lockheed Martin, EADS) as well as for government space agencies (NASA, ESA). His secondary goal is to obtain a flight licence and to apply for a position as an astronaut board engineer in one of the present or future manned space flight programs.